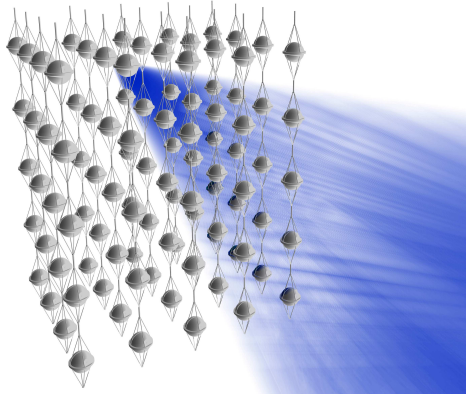


# All-flavor based Searches for solar Dark Matter with the IceCube Neutrino Observatory



Dissertation zur Erlangung des Grades  
"Doktor der Naturwissenschaften"

am Fachbereich Physik, Mathematik und Informatik  
der Johannes Gutenberg–Universität in Mainz

vorgelegt von

**Klaus Wiebe**  
geboren am 01. Juli 1984 in Orenburg

Mainz, den 26. September 2016

Datum der mündlichen Prüfung: 19.01.2017

Klaus Wiebe  
Institut für Physik  
Johannes Gutenberg–Universität  
D-55128 Mainz

---

[klaus.wiebe@uni-mainz.de](mailto:klaus.wiebe@uni-mainz.de)

*Für Johanna  
und Emily.*



---

This work is licensed under a  
Creative Commons Attribution-NonCommercial 4.0 International License.



## Abstract

Dark matter particles may be trapped in large celestial bodies as the sun and by self-annihilation can produce a detectable neutrino flux on Earth. Well shielded volumes of natural media are used to register neutrinos by means of their Cherenkov signatures after they undergo charged or neutral-current interactions. One of these detectors, the IceCube neutrino observatory, is located in the clear glacial ice beneath the geographic South Pole, comprising a volume of one cubic kilometer which is monitored by 5160 photomultiplier modules. While traditional studies with the IceCube detector have concentrated on the good angular resolution of muon neutrino events and neglected other flavors of active neutrinos, this work attempts to achieve better sensitivities through an all-flavor based approach which increases the expected signal rate in the detector by a factor of two. The worse directional resolution of cascade-shaped events is improved by computationally intensive reconstructions and a newly developed uncertainty estimator enables the classification of individual events according to their reconstruction quality. Machine learning is applied at the final step of a multi-level event selection which aims at extracting the signal from the abundant background of atmospheric muons and neutrinos. Sensitivity limits on the annihilation rate are then obtained by means of a likelihood analysis using energy and directional information including the angular uncertainty. These sensitivities are finally interpreted as spin-dependent cross-section bounds within the supersymmetric framework of the pMSSM for which 100 billion possible models were scanned. Compared to present track-based searches with IceCube, the sensitivity for low dark matter masses could be improved by up to one order of magnitude.

*Begin at the beginning, the King said, very gravely,  
and go on till you come to the end: then stop.*

---

Lewis Carroll, *Alice in Wonderland*

# Contents

<b>Introduction</b>	<b>9</b>
<b>1. Dark Matter and its Particle Candidates</b>	<b>11</b>
1.1. Cosmology and the $\Lambda$ CDM Model . . . . .	11
1.2. Dark Matter Evidence . . . . .	14
1.3. WIMP Candidates from Supersymmetric Extensions of the Standard Model . . . . .	19
1.4. Interaction and Detection of Dark Matter . . . . .	27
<b>2. Neutrinos</b>	<b>33</b>
2.1. Neutrinos in the Standard Model of Particle Physics . . . . .	34
2.2. Neutrino Oscillations . . . . .	35
2.3. Cosmic Messengers . . . . .	40
2.4. Interaction and Detection of Neutrinos . . . . .	44
<b>3. The IceCube Detector</b>	<b>49</b>
3.1. Detector Layout and Detector Components . . . . .	49
3.2. Data Acquisition, Filtering and Transmission . . . . .	52
3.3. Ice Properties and Modeling . . . . .	56
3.4. Event Topologies and Energy Losses . . . . .	57
<b>4. A Resolution Estimator for Cascades</b>	<b>61</b>
4.1. Event Reconstruction . . . . .	61
4.2. Likelihood-based Resolution Estimation for Cascades . . . . .	63
4.3. Implementation of the Resolution Estimator . . . . .	66
4.4. Performance and Validation of the Resolution Estimator . . . . .	68
<b>5. All-Flavor Solar Dark Matter Search</b>	<b>71</b>
5.1. Neutrinos from Dark Matter Annihilation in the Sun . . . . .	72
5.2. Experimental and Monte-Carlo Datasets . . . . .	75
5.3. Event Selection . . . . .	76
5.4. BDT Training . . . . .	96
5.5. Likelihood Analysis . . . . .	101
5.6. Sensitivities on the Spin-Dependent WIMP-Proton Scattering Cross-Section . . . . .	109
5.7. Systematic Uncertainties . . . . .	112
<b>6. Supersymmetric Model Scans</b>	<b>119</b>
6.1. Motivation . . . . .	120
6.2. Prior Ranges and Distribution . . . . .	121
6.3. Model Characteristics and posterior Constraints . . . . .	121
6.4. Cross-Section Exclusion Complementarity between Direct and Indirect Measurements . . . . .	124
<b>Summary and Outlook</b>	<b>129</b>
<b>A. Signal Energy Spectra</b>	<b>131</b>
<b>B. Low-level Production of Signal Simulation</b>	<b>135</b>

<b>C. Cascade and Track Signatures</b>	<b>137</b>
<b>D. BDT Input Variables Distribution</b>	<b>139</b>
<b>E. BDT Results</b>	<b>145</b>
<b>F. BDT Cut Score Optimization</b>	<b>153</b>
<b>G. Event Rates at the various Selection Levels</b>	<b>155</b>
<b>List of Figures</b>	<b>163</b>
<b>List of Tables</b>	<b>167</b>
<b>Bibliography</b>	<b>169</b>

# Introduction

The particle nature of dark matter is among the most striking mysteries of contemporary physics. While strong evidence from the observation of gravitationally bound systems points towards the existence of this non-luminous form of matter, no dark matter particle except for the neutrino has been discovered so far. Supersymmetry offers a suitable particle candidate in the form of the lightest neutralino which is both stable and neutral. Being massive and having interaction strengths at the weak scale, it naturally qualifies as a Weakly Interacting Massive Particle (WIMP) which is predicted as a generic dark matter candidate when considering the conditions at thermal freezeout of the dark matter.

The search is pursued by means of various channels: dark matter can be produced and observed in accelerators, it can be detected directly through nuclear recoils in well-shielded detectors filled with heavy noble gases or solid-state materials. Another approach is provided by the indirect detection through a signal of Standard Model particles which are created as the result of pairwise self-annihilations of dark matter particles. The latter search is also pursued with the IceCube Neutrino Observatory, a Cherenkov based neutrino detector which is located in the antarctic glacier beneath the geographic South Pole. A volume of one cubic kilometer is instrumented with optical modules which are mounted on strings leading to a surface data acquisition laboratory. About 1,500 meters of ice overburden serve as a shielding for atmospheric muons. IceCube was originally designed to detect high-energy point sources and has recently produced results of a diffuse neutrino flux originating from astrophysical sources. However, the science potential reaches much further and a dark matter induced neutrino signal can also be efficiently probed.

WIMP particles can lose energy via weak interactions and thus become trapped in gravitational wells like the sun after subsequent scatterings. Assuming a Majorana nature they can self-annihilate and produce a detectable flux of neutrinos at the earth.

Solar dark matter searches at large-volume Cherenkov detectors have traditionally only considered track-shaped events from charged-current muon neutrino interactions due to their better angular reconstruction. However, with increased computing power and new reconstruction tools, the angular reconstruction of cascade-shaped events can now be performed with decent resolutions. This work, for the first time, includes signal neutrinos of all flavors and employs a state-of-the-art event selection with the aid of machine learning, computationally intensive event reconstructions and a novel resolution estimator which has been developed in the scope of this analysis. A reliable resolution estimation plays a crucial role in categorizing events depending on whether they could be well reconstructed or not. The code developed has a modular design and its result – in conjunction with the reconstructed direction and the energy – is used as an input

for a sophisticated likelihood analysis which determines the sensitivity to the number of signal events. The obtained results are expected to be competitive to previous IceCube searches in the energy region below a few hundred GeV, because, at lower energies, track-like signatures cannot be reconstructed very well due to the limited photon deposition in the detector.

Sensitivities on the neutrino flux can be converted into solar dark matter annihilation rates which – assuming capture-annihilation equilibrium – correspond to sensitivities on the spin-dependent cross-section for elastic dark matter scattering off solar hydrogen nuclei. These sensitivities can be compared to scattering cross-sections of actual supersymmetric models. For this purpose, a large number of models (about  $10^{11}$ ) have been scanned in the framework of the phenomenological supersymmetric extension of the Standard Model (pMSSM). This allows for exclusions on a model by model basis and furthermore is very helpful in complementarity studies of direct, indirect and accelerator bounds.

Chapter 1 introduces the dark matter phenomenology in the standard cosmological framework and discusses popular candidates from Supersymmetry and their interaction types. Chapter 2 is about the elusive particle known as the neutrino, in particular its place in the Standard Model of particle physics, the transformation of its flavor eigenstates, its role as a cosmic messenger and its detection in large transparent volumes. The setup of the IceCube detector, the data acquisition, the properties of the glacial medium and neutrino event signatures in the fiducial detector volume are presented in chapter 3. Chapter 4 discusses event reconstructions in IceCube as well as the algorithm and the performance of the novel resolution estimator for cascade-shaped events.

The data analysis is presented in chapter 5, starting with the formalism of the dark matter induced neutrino signal and the corresponding simulations. After the discussion of the background Monte-Carlo datasets used in the analysis and the characteristics of experimental data, the event filtering as well as the likelihood analysis are presented and the sensitivities so obtained are compared to other studies. The chapter concludes with a discussion of the systematic errors, which originate mainly from detector-related and cosmological uncertainties. The results obtained in this thesis are interpreted in a supersymmetric framework. By means of massive parallelization, billions of individual supersymmetric models are scanned. The used code, input priors, Standard Model parameters as well as complementarity studies with both direct and indirect searches are presented in chapter 6.

This work is merely one example for an intriguing nature of astroparticle physics: the fact that the study of cosmological particles and processes is deeply tied to a thorough understanding of fundamental particles and their interactions.

# 1

## Dark Matter and its Particle Candidates

For all is like an ocean, all flows and connects;  
touch it in one place and it echoes at the other  
end of the world.

---

F. Dostoyevsky, *The Brothers Karamazov*

Despite the compelling evidence for dark matter and an extensive search effort by means of several detection techniques, no experimental confirmation for the existence of dark matter particles exists at the time of this writing and its nature thus remains unknown. Following a brief introduction of the cosmological framework in section 1.1, the measurements and observations pointing towards dark matter are presented in section 1.2. The WIMP concept as well as the supersymmetric extension of the Standard Model which gives rise to an intriguing dark matter candidate are introduced in section 1.3. This supersymmetric particle, the neutralino, will be further studied in chapter 6 and is consequently assumed as a potential source for a solar neutrino signal, as described in the data analysis in chapter 5. Finally, section 1.4 concludes with a comparison of common dark matter detection approaches and the interaction types which they exploit.

### 1.1 Cosmology and the $\Lambda$ CDM Model

Our universe can be observed by means of various cosmic messengers, including X-rays, radio waves, high-energy nuclei and neutrinos. The first observations, however, exploited characteristic lines in the known spectra of visible light. While complex three-dimensional structures can be observed in the surrounding space, the distant universe – a few hundred Mpc and beyond – seems to be rather uniform. Therefore, the large-scale universe may be considered isotropic and homogeneous. This assumption is often referred to as the *Cosmological Principle*. These two properties do not necessarily imply each other. However, if we require isotropy at any arbitrary point in space, then the universe must also be homogeneous. The Cosmological Principle is well supported by precise

observations of the *Cosmic Microwave Background* (CMB)<sup>1</sup>, which contains information about various cosmological quantities, as discussed in section 1.2.

Building on the concept of isotropy and homogeneity, an equation that connects the energy density, expansion and curvature of the universe can be derived. In the framework of General Relativity, a metric can be defined by an invariant line element  $ds$ :

$$ds^2 = g_{\mu\nu} dx^\mu dx^\nu \quad . \quad (1.1)$$

The main difference, when compared to a Minkowski line element, is the position-dependent metric tensor  $g_{\mu\nu}$ , which describes the geometry of the universe. The most general form of such a metric is called the *Robertson-Walker-Metric* [1, 2], yielding

$$ds^2 = c^2 dt^2 - R^2(t) \left[ \frac{dr^2}{1 - kr^2} + r^2 d\theta^2 + r^2 \sin^2\theta d\varphi^2 \right] \quad . \quad (1.2)$$

Two important quantities are introduced in this relation: the curvature  $k$  (which will be discussed in more detail below) and the scale factor  $R(t)$ , which represents a relative expansion and relates the proper distance between two points in space for a given time  $t$ . The only important property of  $R$  is its time dependence, it can thus be scaled arbitrarily, e.g. by setting  $R(0) = 1$ .

The Robertson-Walker metric allows one to analytically solve *Einstein's Field Equations*

$$G^{\mu\nu} = -\frac{8\pi G}{c^4} T^{\mu\nu} + \Lambda g^{\mu\nu} \quad , \quad (1.3)$$

where the energy-momentum tensor  $T^{\mu\nu}$  respects the Cosmological Principle and the Einstein tensor  $G^{\mu\nu}$  is of the form

$$G^{\mu\nu} = \mathcal{R}^{\mu\nu} - \frac{1}{2} g^{\mu\nu} \mathcal{R} \quad , \quad (1.4)$$

$\mathcal{R}^{\mu\nu}$  and  $\mathcal{R}$  being the Ricci curvature tensor and scalar. The 00-component of this solution is called the (first) *Friedmann Equation*:

$$\frac{\dot{R}^2}{R^2} = \frac{8\pi G}{3} \rho - \frac{kc^2}{R^2} + \frac{\Lambda c^2}{3} \quad . \quad (1.5)$$

$\Lambda$  is the *Cosmological Constant* and was originally introduced by Albert Einstein to his field equations (equation 1.3) in order to achieve a static universe. The corresponding density  $\rho_\Lambda = \Lambda c^2 / 8\pi G$  is regarded as the density of a vacuum energy (also known as *dark energy*) that now makes up a major part of the total energy content of the universe.

---

<sup>1</sup>The Cosmic Microwave Background is a relic radiation that decoupled from matter when the universe became cool enough for electrons and protons to form hydrogen and thus became transparent for photons at an age of about 380,000 years. Due to the subsequent expansion of space its characteristic wavelength became shifted by three orders of magnitude to the microwave region of the electromagnetic spectrum. The CMB is essentially isotropic – anisotropies occur only at the  $10^{-5}$  level.

$\rho_\Lambda$  can be absorbed in  $\rho$ , which then represents the combined density of all forms of matter and energy. With  $\rho \rightarrow \rho + \rho_\Lambda$ , equation 1.5 reads:

$$\frac{\dot{R}^2}{R^2} = \frac{8\pi G}{3}\rho - \frac{kc^2}{R^2} \quad . \quad (1.6)$$

The Friedmann equation is an essential part of the  $\Lambda$ -Cold Dark Matter ( $\Lambda$ CDM) model, a six-parameter model that successfully describes the basic properties of our universe and is thus called the standard model of modern Big Bang cosmology. Besides the above introduced cosmological constant  $\Lambda$ , a crucial ingredient of this model (and of the universe) is *dark matter*, which will be the focus of the following considerations. The  $\Lambda$ CDM model itself is established on the assumptions that the Cosmological Principle applies and that gravity on cosmological scales can be described by general relativity. Its free parameters, however, have to be determined by means of various kinds of observations.

In 1929, Edwin Hubble discovered that the speed  $v$  of receding galaxies is proportional to their (proper) distance  $D$ .  $v$  can be determined through the redshift  $z = \lambda_{\text{obs}}/\lambda_{\text{em}} - 1$  of the observed light signal and  $D$  from observation of stellar objects with constant light output, so-called *Standard Candles*<sup>2</sup>. The linear relation between recession speed and distance is known as *Hubble's Law*:

$$v = H_0 \cdot D \quad . \quad (1.7)$$

$H_0$  is called the *Hubble Constant* and is only a constant in space, but not in time. The currently most precise value of  $H_0$  was measured to be  $67.27 \pm 0.66$  (km/s)/Mpc [3], where the subscript denotes the value of the Hubble constant today ( $t = 0$ ).

Hubble's law (equation 1.7) can equally be used to link the scale parameter  $R(t)$  to its derivative

$$\dot{R}(t) = H(t) \cdot R(t) \quad , \quad (1.8)$$

simplifying Friedmann's equation (1.6) to the form:

$$H^2 = \frac{8\pi G}{3}\rho - \frac{kc^2}{R^2} \quad . \quad (1.9)$$

Setting the curvature  $k$  to zero, one can subsequently derive the critical density required for a flat universe,

$$\rho_c = \frac{3H^2}{8\pi G} \quad , \quad (1.10)$$

and define the ratio of the actual density and the critical density as *density parameter*  $\Omega$ :

$$\Omega = \frac{\rho}{\rho_c} = 1 + \frac{kc^2}{H^2 R^2} \quad . \quad (1.11)$$

---

<sup>2</sup>Popular standard candles are supernova explosions of type Ia. The progenitor of such a supernova is believed to be a binary star system where a star orbits a carbon-oxygen white dwarf that constantly pulls matter from its companion. When the white dwarf's mass reaches the Chandrasekhar limit (1.39 solar masses), the electron degeneracy pressure can no longer withstand the gravitational pressure, causing the white dwarf to collapse to a neutron star after rapidly fusing carbon and oxygen to heavier elements. The thermonuclear explosion produces an isotropic light signal of constant intensity, which is reduced by a factor of  $4\pi D^2$  after traveling for a distance  $D$ .

It is obvious that a vanishing curvature will effect  $\Omega$  to be 1. A positive  $k$  corresponds to a spherical (closed) universe and will produce an  $\Omega$  value larger than 1, while an open hyperbolic universe has negative curvature and a density parameter smaller than 1. Observational evidence suggests that we indeed live in a universe with zero curvature (on large scales) and the density is exactly given by the critical density. Interestingly enough, only a small deviation of  $\mathcal{O}(10^{-24})$  from the critical density is sufficient to produce a universe that would have collapsed or flown apart at present time. The fact that the actual density is fine-tuned to the critical density with such a high precision – although it could have an arbitrary value – is known as the *Flatness Problem* and is commonly accepted to be solved by the concept of *Cosmic Inflation*<sup>3</sup>.

The density parameter (equation 1.11) can be split into its components, the relative contributions of radiation, baryonic matter, (cold) dark matter, dark energy, and other eventual contributions not known to us so far:

$$\Omega = \Omega_{\text{rad}} + \Omega_{\text{b}} + \Omega_{\text{c}} + \Omega_{\Lambda} + \dots \quad , \quad (1.12)$$

where  $\Omega_{\text{c}}$  corresponds to cold (non-relativistic) dark matter. The total  $\Omega$  and contributions from dark and baryonic matter can be determined from measurements of the CMB. To avoid the dependence on the Hubble constant (equation 1.10) and thus on its fairly large error, the  $\Omega_i$  values are usually multiplied with the square of the dimensionless *Hubble Parameter*:

$$h = \frac{H_0}{100 \text{ (km/s)/Mpc}} \approx 0.67 \quad . \quad (1.13)$$

It is worth noting that, while  $\Omega$  will always be 1 for a flat universe, the contributions of the various components do change over time. For the first 40,000 years, radiation was the most abundant form of energy, but decreased so rapidly due to expansion and absorption that matter began to dominate. Only at the age of four billion years, the matter density fell below the (constant) density of dark energy, which dominates the present universe.

Many of these insights would not be possible without the study of the Cosmic Microwave Background, which contains valuable information about the structure and matter portions of the universe, including dark matter – which we will turn to in next section.

## 1.2 Dark Matter Evidence

Shortly after Edwin Hubble found a linear relation between recession velocities of distant galaxies and their distance (equation 1.7), swiss astronomer Fritz Zwicky made use of this technique and discovered that galaxy motions inside the Coma galaxy cluster cannot be explained by luminous matter alone. Zwicky applied the virial theorem<sup>4</sup> to eight galaxies

<sup>3</sup>Cosmic Inflation posits that about  $10^{-36}$  seconds after the Big Bang, an extreme expansion, lasting  $10^{-34}$  s, stretched the universe by a factor of  $10^{43}$  [4] and in this process flattened out all anomalies and curvature.

<sup>4</sup>The virial theorem relates the time-averaged total kinetic energy to the averaged total potential in a stable n-body system:  $2 \langle E_{\text{kin}} \rangle = - \langle E_{\text{pot}} \rangle$  .

at the edge of the cluster in order to infer the cluster's total mass. He discovered that the velocities were much larger than expected and thus a massive amount of additional non-luminous matter must contribute, which he called *dark matter* [5]. Zwicky's quantitative results were off by more than an order of magnitude (due to the inaccurate value of the Hubble constant at his time), but he correctly concluded that a major part of the matter content was indeed dark. It is worth noting that the term *dark matter* in its modern sense refers to non-baryonic matter, whereas in Zwicky's times *dark* just meant *non-luminous*.

In the same decade, a radial increase of the mass-to-light ratio in the Andromeda nebula was observed by H. B. Babcock (now interpreted as a halo<sup>5</sup> of dark matter), but was not attributed to missing matter at that time. Over 30 years later, in 1970, Vera Rubin and Kent Ford studied orbital velocities of Andromeda and other spiral galaxies with greater precision and found these velocities to remain more or less constant for larger radii, quite in contrast to the decrease expected from Keplerian motion [7, 8]. More detailed reviews of the historical results can be found in [9, 10].

In the 1980s, a variety of measurements could confirm the cosmological impacts of non-luminous matter, including gravitational lensing effects near galaxy clusters and anisotropy patterns in the Cosmic Microwave Background. Large-scale structures in the universe are believed to arise from small primordial fluctuations of the energy density, presumably caused by vacuum fluctuations. Over time, such small mass aggregations are amplified by gravity and collect more and more matter, leading to the large-scale structures today which evolved from the tiny temperature and density variations in the CMB.

When the universe was less than 380,000 years old, it was so dense and hot that atoms could not yet exist: whenever an electron was captured by a hydrogen nucleus, it was immediately kicked out by a photon, since the mean photon energy exceeded the hydrogen bonding energy of 13.6 eV. More precisely, since photons were a billion times more abundant than electrons, the photons in the high-energy tail of the Boltzmann distribution were sufficient to immediately re-ionize any forming hydrogen atoms. So electrons, photons and nuclei existed in an equilibrium, forming a hot plasma. Due to the short mean free path of photons (caused by frequent Thomson scattering) the universe used to be opaque. Subsequent cooling and expansion made ionization more and more difficult, because photons with energy below the bonding threshold were not able to kick out electrons from hydrogen atoms, no matter how numerous they were (quite similar to the situation of the photoelectric effect). The sudden condition where photons were able to travel unimpeded is known as *photon decoupling* and happened when the temperature of the universe had reached about 3000 K. Over time, these photons were subject to a

---

<sup>5</sup>In contrast to the disk-shaped form of luminous matter in spiral galaxies, the dark matter distribution of galaxies is of spherical shape. Recent observations suggest this halo of dark matter to extend a few times beyond the visible boundaries. These halos are subject to gravitational kinematics and thus can have non-spherical shapes. For the case of our host galaxy, the *Milky Way*, the halo is slightly stretched perpendicular to the spiral disk [6].

redshift and can be detected today with a temperature<sup>6</sup> of about 2.7 K, which puts them in the microwave region of the electromagnetic spectrum and they are consequently denoted as the *Cosmic Microwave Background*. It is worth noting that this relic radiation constitutes most of the radiation density in the universe,  $\Omega_{\text{rad}}$ .

Since we know the photon temperature at decoupling, we also know the distance in space (and hence time) to their origin, which is of order  $6000 h^{-1}$  Mpc. Assuming isotropy, the spherical surface corresponding to this radius is known as the *surface of last scattering*. There is however, as mentioned earlier, a slight temperature dependence on the arrival direction of the CMB which allows one to make statements about cosmological parameters.

The CMB temperature can be measured as a function of incident direction  $T(\theta, \varphi)$ , where  $\theta$  and  $\varphi$  are spherical coordinates. Like any directional function, the temperature anisotropy can be expanded in spherical harmonics  $Y_l^m(\theta, \varphi)$ :

$$\frac{\Delta T}{T}(\theta, \varphi) = \sum_{l=0}^{\infty} \sum_{m=-l}^l a_{lm} Y_l^m(\theta, \varphi) \quad , \quad (1.14)$$

where coefficients  $a_{lm}$  quantify the amplitude of the irregularities on different scales. Larger  $l$  correspond to smaller angular structures and the corresponding terms are called *multipole moments*, like the terms in the multipole expansion of electromagnetic fields. So the  $l = 0$  term is called *monopole*, the  $l = 1$  term is called *dipole*, and so on. In the case of the CMB, the monopole term gives the overall temperature average of 2.72548(57) K. There is a dipole term at a relative order of  $10^{-3}$  which is caused by the motion of our solar system through a reference frame in which the CMB has no dipole moment.

Based on observations of large-scale structure in the universe, small-angle anisotropies are expected at a level of  $10^{-5}$ . These were first measured by the COBE<sup>7</sup> spacecraft in 1992 and later with much higher precisions by the WMAP<sup>8</sup> (2001-2010) and PLANCK (2009-2013) satellites. The latter was able to measure the angular power spectrum up to  $l \approx 2500$  (see figure 1.1), which corresponds to an angular accuracy of less than 0.1 degree [3]. The distinct structures at  $l \approx 220$  and above are known as *acoustic peaks*, since they are linked to sound waves in the ionized plasma that existed prior to photon decoupling. Density fluctuations caused matter to accumulate and through gravity to aggregate even more matter, causing compression and heating. Through photon radiation, this local concentrations were able to cool and expand, leaving the possibility to gravitationally clump together once again. This alternating process caused longitudinal acoustic oscillations in the photon-baryon fluid. The knowledge of the particle horizon (the largest distance that could be in causal contact at the time of photon decoupling) and the proper distance to the surface of last scattering allows us to obtain today's angular separation of the particle horizon distance, which is about 1 degree for a flat universe. This corresponds to a multipole moment of about 220, which is the location of the first

---

<sup>6</sup>The energy spectrum follows the shape of black body radiation (i.e. Planck's Law) for  $T=2.725$  K.

<sup>7</sup>*Cosmic Background Explorer*.

<sup>8</sup>*Wilkinson Microwave Anisotropy Probe*.

peak. If the universe had non-zero curvature ( $\Omega \neq 1$ , see equation 1.11), there would be a significant impact on this angular separation and thus on  $l$ . In fact, the position of the acoustic peaks is proportional to  $\Omega^{-1/2}$  and thus allows one to deduce the density parameter. The positions of peaks in PLANCK data are consistent with  $\Omega = 1$  within error ranges. The intervals and amplitudes of the various peaks strongly depend on the oscillation dynamics in the photon-baryon fluid and as such on the amounts of dark and baryonic matter. For example, odd-numbered peaks are associated with the compression and heating part of the acoustic oscillations mentioned above and are thus amplified by the amount of baryons. A formal description of the acoustic peak characteristics and their connection to cosmological parameters can be found in [11].

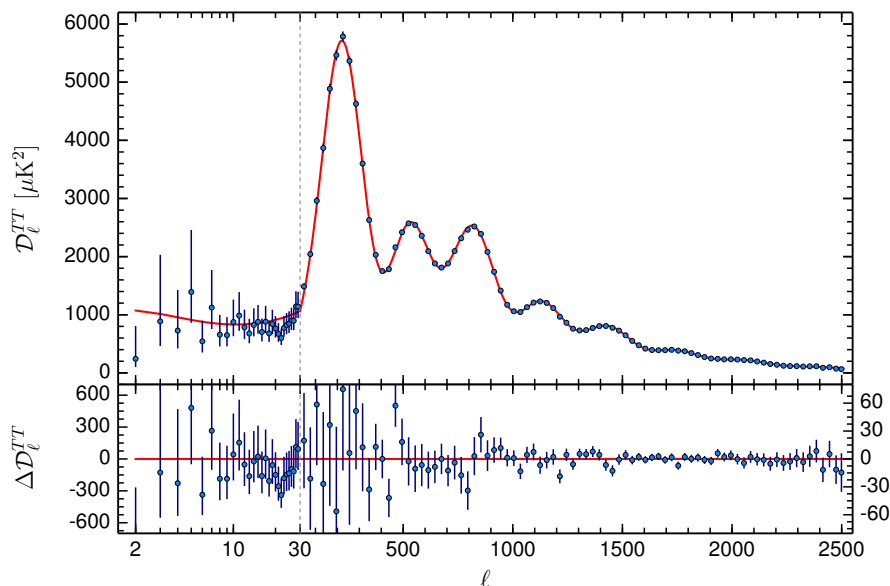


Figure 1.1.: Temperature fluctuation dependence on multipole moment as measured by the PLANCK satellite. The continuous prediction from the  $\Lambda$ CDM parametrization is shown for reference (red). Note the change in horizontal scale at  $l = 30$  (from [3]).

Measurements of the power spectrum (as shown in figure 1.1) thus constrain matter densities and curvature – in the case of PLANCK data alone – up to a precision of a few percent [3]. However, due to partial degeneracy with other parameters (e.g. the Hubble constant) the precision of the constraints is limited. Relative baryon and dark matter densities can therefore be better determined by including further observational results, such as data from high-redshift supernova searches [12, 13].

A current value for the relic density of (cold) dark matter is [3]

$$\Omega_c h^2 = 0.1199 \pm 0.0027 \quad . \quad (1.15)$$

In the course of the last ten years, sufficient computational power became available to compare CMB observations to predictions of structure formation made by the  $\Lambda$ CDM

model including the effects of cosmic inflation. The *Millennium Run* was such an N-body simulation [14, 15], which confirms the necessary contribution of (cold) dark matter to large-scale structure formation. The simulation also confirmed the possibility of black hole candidates in very bright quasars at large distances – which was a challenging discovery made shortly before by the *Sloan Digital Sky Survey*<sup>9</sup> observatory.

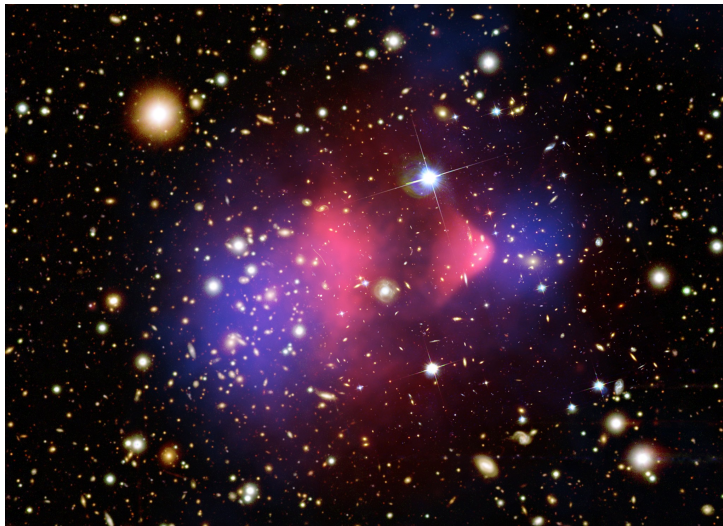


Figure 1.2.: Composite image of the matter distribution in the galaxy cluster 1E 0657-56 (better known as the “Bullet Cluster”). X-ray emitting gas clouds are shown in red, while the clearly separated dark matter is pigmented in blue (from [16]).

Another impressive hint towards the existence of dark matter comes from X-ray and optical astronomy: the observation of a galaxy cluster merger, the *Bullet Cluster*, reveals that the weakly interacting dark component is rather unaffected by the collision, while there is a large impact on the motion of its baryonic (luminous) matter, whose X-ray emission could be well detected by the *Chandra Observatory* [17]. The position of dark matter within the cluster could be determined by the effects of gravitational lensing<sup>10</sup> on the location of surrounding galaxies. Figure 1.2 shows the Bullet cluster, overlaid with a pigmented density of dark and baryonic matter. Independent observations of the merging cluster MACS J0025.4-1222 suggest a similar separation of luminous and non-luminous matter [18], which is considered yet another indirect evidence for dark matter, disfavoring alternative theories, e.g. models that are based on modified gravity<sup>11</sup>.

---

<sup>9</sup>Ground-based optical telescope, located in New Mexico (USA). In a recent extension (2014), an additional telescope was built in Chile, which allows for the observation of the southern hemisphere.

<sup>10</sup>According to General Relativity, space-time is bent by the presence of mass and hence light traveling on a straight line will be significantly diverted and refocused when passing large accumulations of matter (e.g. galaxy clusters) and thus will seem to arrive from different directions when observed. Since the lensing effect is stronger for larger masses, the total mass of the passed matter can be inferred.

<sup>11</sup>Modified Newtonian Dynamics (MOND): Originally introduced to explain the non-Keplerian distribution of galaxy (cluster) rotation curves. According to MOND, Newton’s second law ( $F = m \cdot a$ ) is modified for small accelerations in a way that  $F$  will be proportional to  $a^2$ . Flat rotation curves can

## 1.3 WIMP Candidates from Supersymmetric Extensions of the Standard Model

Observational cosmology poses constraints concerning the nature of suitable dark matter candidates. They have to be stable, electrically neutral and sufficiently massive to be non-relativistic, hence being able to explain the structure formation in the universe. Also, the (self-)annihilation cross-section has to be on the right order of magnitude to account for today's observed matter content and its structure formation. No standard model particle fits these requirements.

Assuming such a new stable particle exists, it must have been quite abundant and in thermal equilibrium in the early universe. This equilibrium can be maintained through annihilation to (and from) other particle-antiparticle pairs:

$$\chi\bar{\chi} \leftrightarrow l\bar{l} \quad , \quad (1.16)$$

where the new stable particle is called  $\chi$  (and in the Majorana case is its own antiparticle). Since the universe expands and cools, the equilibrium abundance drops exponentially until the expansion rate reaches the annihilation rate. From this point forward, annihilation partners get separated too far and the interactions sustaining the thermal equilibrium freeze out, leaving behind a relic abundance of  $\chi$  particles.

The time evolution of the total number density  $n_\chi$  can be described by the Boltzmann equation:

$$\frac{dn_\chi}{dt} = -3Hn_\chi - \langle\sigma_A v\rangle \left[ (n_\chi)^2 - (n_\chi^{\text{eq}})^2 \right] \quad , \quad (1.17)$$

with  $\langle\sigma_A v\rangle$  being the velocity-averaged annihilation cross-section. In equilibrium (see equation 1.16), the right-hand side is zero, due to the equilibrium density  $n_\chi^{\text{eq}}$  being exactly the number density  $n_\chi$ , which at this early stage is only reduced by Hubble expansion. Once the temperature drops below the  $\chi$  mass, the creation of  $\chi\bar{\chi}$  pairs requires ordinary matter particles from the hot tail of their thermal distribution and so  $n_\chi^{\text{eq}}$  is Boltzmann-suppressed and decreases exponentially:

$$n_\chi^{\text{eq}} \propto \left( \frac{m_\chi T}{2\pi} \right)^{3/2} \exp\left( \frac{-m_\chi c^2}{k_B T} \right) \quad . \quad (1.18)$$

This exponential fall-off is ultimately interrupted by the above-mentioned freeze-out (see figure 1.3), which takes place earlier in case of smaller annihilation cross-sections.

While there is no analytic solution to equation 1.17, an approximation can be derived [20, 21], which is good to about 10%:

$$\Omega_\chi h^2 = \frac{m_\chi n_\chi}{\rho_c} \simeq \frac{3 \cdot 10^{-27} \text{ cm}^3/\text{s}}{\langle\sigma_A v\rangle} \quad . \quad (1.19)$$

---

thus be explained without the need for yet undiscovered particles. However, among other inconsistencies, such a theory has severe problems explaining the observed separation in the Bullet Cluster (see figure 1.2) and the initial formation of large-scale structures.

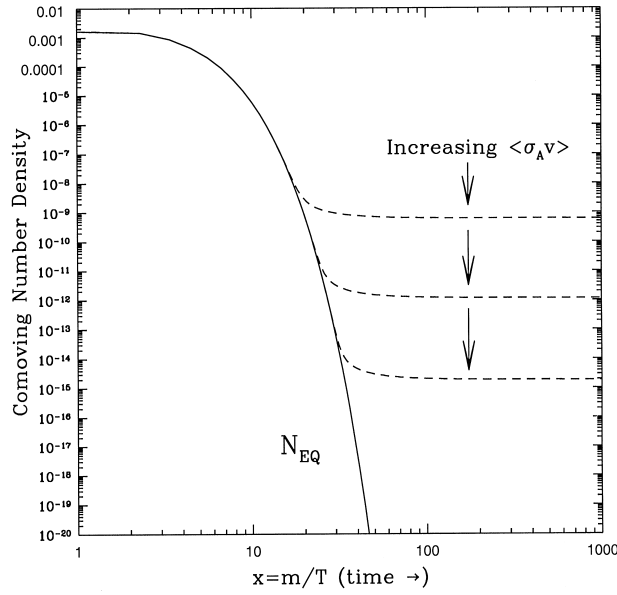


Figure 1.3.: Comoving WIMP number density in the early universe. Dashed lines show the cross-section dependent actual abundances, while the solid line represents the equilibrium abundance (from [19]).

Apart from logarithmic corrections, this approximation is independent of the particle's mass. Taking into account the measured relic density today (equation 1.15), the corresponding velocity-averaged annihilation cross-section is around  $3 \cdot 10^{-26} \text{ cm}^3/\text{s}$ .

It is remarkable that this cross-section is in the region of the weak scale, especially since there is no reason why the scale of electroweak interaction should in any way be related to the relic dark matter density in the universe. So if a new particle with weak-scale interactions existed, it would seem likely that this particle indeed makes up (or significantly contributes to) dark matter. Mass and annihilation cross-section can then be related by the fine-structure constant  $\alpha$ :

$$\langle\sigma_A v\rangle \sim \alpha^2 (100 \text{ GeV}/c^2)^{-2} \sim 10^{-25} \text{ cm}^3/\text{s} \quad . \quad (1.20)$$

Therefore such  $\chi$  particles are consequently called *Weakly Interacting Massive Particles* (WIMPs) [22].

The WIMP, despite being a well motivated dark matter candidate, is merely a generic construct without a theoretical framework. A popular candidate that naturally qualifies as a WIMP and has been postulated long before, is the lightest *neutralino*, a fermion that arises from a theory called *Supersymmetry*. There is truly a variety of other particle dark matter candidates [23]; however, in this work the focus will be on this popular supersymmetric candidate.

Supersymmetry can formally be expressed as an extension of the *Standard Model of Particle Physics* (SM), which tries to describe the to-date known elementary particle

and their fundamental interactions. The SM is a *Quantum Field Theory* (QFT), which generally aims at unifying quantum mechanics and special relativity on the basis of continuous fields, and as such sees particles and interactions as field quanta, with no a-priori limit on the number of degrees of freedom<sup>12</sup>.

After a brief presentation of the SM formalism and the relevant aspects regarding this work, the supersymmetric extension and its newly arising particles will be introduced. A more extensive overview of quantum field concepts can e.g. be found in [24, 25].

Analog to classical Lagrangian mechanics, QFTs use the field formulation of the *Euler-Lagrange-Equation*:

$$\frac{\partial \mathcal{L}}{\partial \phi} - \partial_\mu \left( \frac{\partial \mathcal{L}}{\partial (\partial_\mu \phi)} \right) = 0, \quad L = \int \mathcal{L} d^3x \quad , \quad (1.21)$$

where  $\phi$  is a scalar field which replaces the generalized coordinates. The Lagrangian density  $\mathcal{L}$  (colloquially also referred to as *Lagrangian*) controls the field's dynamics and – as indicated before – each particle and coupling is described by a dynamic field that pervades spacetime. In QFTs, fields are operator-valued and act upon quantum states.

The Standard Model Lagrangian can be composed of a mass term, a coupling term that allows for interactions between gauge and fermion fields (typically denoted by Dirac spinors  $\psi$ ), a kinetic term for the gauge fields (since fermion fields are usually consistently treated in the coupling part), and a Higgs field that by interaction gives mass to fermions and gauge bosons:

$$\mathcal{L}_{\text{SM}} = \mathcal{L}_{\text{mass}} + \mathcal{L}_{\text{coupling}} + \mathcal{L}_{\text{kinetic}} + \mathcal{L}_{\text{Higgs}} \quad , \quad (1.22)$$

where the coupling term can be further decomposed into electroweak and strong<sup>13</sup> components ( $\mathcal{L}_{\text{coupling}} = \mathcal{L}_{\text{EW}} + \mathcal{L}_{\text{QCD}}$ ). The QCD sector will not be discussed in this frame; a short glimpse at the quark mixing is, however, provided in the context of section 6.2. The leptonic fermion content and neutrino properties will be treated in section 2.1.

Interactions in the SM are described by a local  $U(1) \times SU(2) \times SU(3)$  symmetry. Being a gauge field theory, each generator of these groups is attributed a gauge vector field. This field, since it is quantized, corresponds to a vector boson, which has to be massless to retain the field's gauge invariance. For  $U(1)$ , this is the  $B$  boson (with the weak hypercharge  $Y$  as generator),  $SU(2)$  is generated by the three-component weak isospin  $I$  (with associated bosons  $W^1, W^2, W^3$ ) and  $SU(3)$  constitutes eight gluons, the mediators of color charge (which they also carry themselves). The electroweak part  $U(1) \times SU(2)$  is subject to spontaneous symmetry breaking caused by the *Higgs field* (discussed below),

---

<sup>12</sup>The assumptions of particles being quantized excitations of a field leads to the possibility of systems with an arbitrary amount of created particles with an infinite amount of degrees of freedom. In a perturbation series this results in the divergence of higher-order contributions, thus producing infinite values for calculated quantities, as e.g. the self-energy of the electron. Possible solutions include the renormalization of QFT and the discretization of spacetime.

<sup>13</sup>Quantum Chromodynamics (QCD) is the theory of strong interaction. *Chroma* (greek for “color”) refers to the color charges of strongly interacting particles; red, green and blue.

which gives rise to the known carriers of the weak ( $W^\pm, Z^0$ ) and electromagnetic ( $\gamma$ ) force:

$$W^\pm = \frac{1}{\sqrt{2}}(W_1 \mp iW_2) \quad , \quad \begin{pmatrix} \gamma \\ Z^0 \end{pmatrix} = \begin{pmatrix} \cos \theta_W & \sin \theta_W \\ -\sin \theta_W & \cos \theta_W \end{pmatrix} \begin{pmatrix} B \\ W_3 \end{pmatrix} \quad , \quad (1.23)$$

where  $\theta_W$  is the *Weinberg angle*, that also relates the  $Z^0$  to the  $W^\pm$  mass ( $m_Z = m_W / \cos \theta_W$ ). So the symmetry breaking causes these two bosons to acquire mass, while the  $\gamma$  is massless. The reason is the emerging (unbroken)  $U(1)_{\text{em}}$  symmetry with a generator

$$Q = Y/2 + I_3 \quad (1.24)$$

which does not interact with the Higgs field, because the latter is an eigenstate of both the weak hypercharge  $Y$  and the third component of the weak isospin,  $I_3$ . This unification of the weak and electromagnetic interactions is known as the *Glashow-Weinberg-Salam model* [26, 27]. An instructive approach to the electroweak sector can be found in [28].

The Higgs field, which allows fermions and gauge bosons to acquire mass, can (prior to symmetry breaking) be described as a complex scalar doublet

$$\phi = \frac{1}{\sqrt{2}} \begin{pmatrix} \phi^+ \\ \phi^0 \end{pmatrix} \quad , \quad (1.25)$$

where  $+$  and  $0$  denote the components' electric charges - their weak hypercharge  $Y$  being 1. Choosing a particular gauge, the unitary gauge, this doublet field assumes the simple form

$$\phi = \frac{1}{\sqrt{2}} \begin{pmatrix} 0 \\ v + H \end{pmatrix} \quad , \quad (1.26)$$

with  $H$  being a real field describing neutral scalar particles, the Higgs bosons, and  $v = 2\mu\lambda^{-1/2}$  constituting the (non-zero) vacuum expectation value  $\langle \phi \rangle = 1/\sqrt{2}(0, v) \approx 246 \text{ GeV}/c^2$  which is determined by the gauge sector – and is the only non-dimensionless parameter of the Standard Model. The constants  $\mu$  and  $\lambda$  originate from the Higgs potential

$$V = -\mu^2 \phi^\dagger \phi + \frac{\lambda}{4} (\phi^\dagger \phi)^2 \quad . \quad (1.27)$$

The Higgs boson was first measured at the *Large Hadron Collider* in 2012 [29] and its mass was later more precisely determined to be  $125.09(32) \text{ GeV}/c^2$  [30].

Fermions gain mass through (*Yukawa*) interactions with the Higgs field, with coupling constants being proportional to their mass. Originally only designed to couple with charged fermions, Yukawa couplings with neutrinos can also be introduced to the SM Lagrangian to account for the observed effect of neutrino flavor oscillations and thus the fact that neutrinos must have mass. Lepton families, the chiral aspect of electroweak interaction and neutrino oscillations will be discussed in chapter 2.

One problem with the Higgs potential is, however, its sensitivity to any new physics that may be incorporated into the Standard Model. The latter is assumed to be the

low-energy limit of a more fundamental theory located at or near the Planck scale ( $M_{\text{P}} = (\hbar c/G)^{1/2} \approx 1.22 \cdot 10^{19} \text{ GeV}/c^2$ ), at which quantum gravitational effects become significant. The squared Higgs mass parameter  $m_H^2 = \mu\sqrt{2}$  receives significant quantum corrections from every particle that couples to the Higgs field and therefore merely the severe discrepancy of the electroweak energy scale and the Planck scale poses a problem for consistently incorporating physics at higher energies. Given a fermion  $f$  with Higgs field coupling yields a Lagrangian term

$$- \lambda_f H \bar{\Psi}_f \Psi_f \quad (1.28)$$

and thus a  $m_H^2$  correction of

$$\Delta m_H^2 = - \frac{|\lambda_f|^2}{8\pi^2} \Lambda^2 + \dots \quad , \quad (1.29)$$

where  $\Lambda$  is a high-energy cutoff scale. If  $\Lambda$  were of the order of the Planck scale, such quantum corrections would make  $m_H^2$  about thirty orders of magnitude larger than the value required by the Standard Model;  $m_H^2 \approx -(100 \text{ GeV})^2$ . Although SM fermions and gauge bosons do not directly share this quadratic sensitivity (equation 1.29), they all obtain their masses from  $H$ , and these are hence sensitive to the cutoff scale  $\Lambda$ .

While the actual picture of this so-called *hierarchy problem* is more complex (details can for instance be found in [21, 31]), the above outline provides a first motivation for a solution that eliminates the quadratic radiative corrections: low-energy *Supersymmetry*. Unlike fermionic terms, scalar correction terms (from a Lagrangian  $-\lambda_S |H|^2 |S|^2$ ) have a positive sign:

$$\Delta m_H^2 = \frac{\lambda_S}{16\pi^2} \Lambda^2 + \dots \quad , \quad (1.30)$$

suggesting a symmetry between fermions and bosons: if every quark and lepton in the SM had two corresponding complex scalars with couplings strengths  $\lambda_S = |\lambda_f|^2$ , the quadratic contributions (see equations 1.29 and 1.30) would cancel out.

Introducing an operator  $Q$ , which is a Majorana spinor with spin 1/2, fermions can directly be related to their bosonic (super)partners and vice versa:

$$Q |\text{fermion}\rangle = |\text{boson}\rangle \quad , \quad Q |\text{boson}\rangle = |\text{fermion}\rangle \quad . \quad (1.31)$$

In supersymmetric extensions of the Standard Model, like the *Minimal Supersymmetric Standard Model* (MSSM), all SM gauge fields (gluons,  $B$  and  $W$  bosons) thus receive fermionic partners called *gauginos*, or more specifically *gluinos*, *binos* and *winos*. Scalar partners (*sfermions*) are associated with Standard Model fermions, where superpartner names are equipped with an *s*- prefix, like *slepton*, *squark* and *sneutrino*. In order to preserve Supersymmetry, it is also necessary to additionally introduce one Higgs field, yielding a total of two SM Higgs doublets and four supersymmetric Higgsinos. The total particle content of such a minimal supersymmetric extension of the SM is summarized in table 1.1. *Minimal* refers to the minimum field content which is necessary to give rise to the known fields of the Standard Model [32].

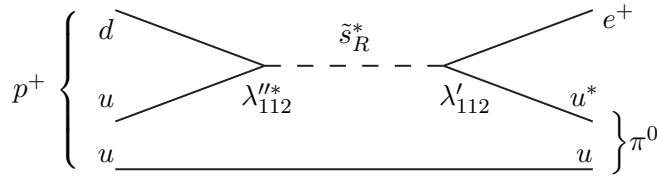
Standard Model particles and fields		Supersymmetric partners			
Symbol	Name	Interaction eigenstates	Symbol	Mass eigenstates	Name
$q = d, c, b, u, s, t$	quark	$\tilde{q}_L, \tilde{q}_R$	squark	$\tilde{q}_1, \tilde{q}_2$	squark
$l = e, \mu, \tau$	lepton	$\tilde{l}_L, \tilde{l}_R$	slepton	$\tilde{l}_1, \tilde{l}_2$	slepton
$\nu = \nu_e, \nu_\mu, \nu_\tau$	neutrino	$\tilde{\nu}$	sneutrino	$\tilde{\nu}$	sneutrino
$g$	gluon	$\tilde{g}$	gluino	$\tilde{g}$	gluino
$W^\pm$	$W$ -boson	$\tilde{W}^\pm$	wino	} $\tilde{\chi}_{1,2}^\pm$	chargino
$H^-$	charged Higgs boson	$\tilde{H}_1^-$	higgsino		
$H^+$	charged Higgs boson	$\tilde{H}_2^+$	higgsino	} $\tilde{\chi}_{1,2,3,4}^0$	neutralino
$B$	$B$ -field	$\tilde{B}$	bino		
$W^3$	$W^3$ -field	$\tilde{W}^3$	wino		
$h$	light Higgs boson	$\tilde{H}_1^0$	higgsino		
$H$	heavy Higgs boson	$\tilde{H}_2^0$	higgsino		
$A$	pseudoscalar Higgs boson				

Table 1.1.: Standard Model particles and their MSSM superpartners (adapted from [33]).

In the Lagrangian, a part containing the superpotential  $W$  is added:

$$\mathcal{L}_{\text{SUSY}} = -\frac{1}{2}(W^{ij}\psi_i\psi_j + W_{ij}^*\psi^{i\dagger}\psi^{j\dagger}) - W^i W_i^* \quad , \quad (1.32)$$

where  $W^i \equiv \partial W / \partial \phi_i$ ,  $W_i^* \equiv \partial W / \partial \phi^{i*}$ ,  $W^{ij} \equiv \partial^2 W / \partial \phi_i \partial \phi_j$  and  $\phi_i, \psi_i$  are scalar and fermion fields. This superpotential contains supersymmetrizations of Yukawa couplings, a bilinear Higgs term and – in its most general gauge-invariant and renormalizable form – also terms that allow lepton ( $L$ ) and baryon number ( $B$ ) violating processes. If the respective couplings were unsuppressed, proton decay (e.g.  $p \rightarrow e^+ \pi^0$ ) would be possible with a lifetime of far less than a second [31], for instance by the process shown in figure 1.4.


 Figure 1.4.: Proton decay to  $\pi^0$  and  $e^+$ , mediated by a  $t$ -channel strange squark with couplings  $\lambda''_{112}$  and  $\lambda'_{112}$  (from [31]).

The remedy in avoiding the possible (and fast) proton decay is to simply introduce<sup>14</sup> a

<sup>14</sup>This introduction may seem artificial from a theoretical point of view, since Supersymmetry without  $R$ -parity would not suffer any internal inconsistencies. However, the stable nature of the proton and the necessity for a dark matter candidate provide a strong phenomenological motivation. The alternative, postulating  $L$  and  $B$  conservation in the MSSM, is clearly a step backward compared to

new discrete symmetry called *R-parity*:

$$R \equiv (-1)^{3B+L+2s} \quad , \quad (1.33)$$

where  $s$  is the particle spin. By requiring the conservation of *R-parity*, decays of superpartners ( $R = -1$ ) to any SM particles ( $R = +1$ ) are also forbidden and as a consequence the lightest supersymmetric particle (LSP) is absolutely stable and sparticles can only be produced (or destroyed) in pairs. This quality makes Supersymmetry interesting in the context of the search for a suitable dark matter candidate, since in many<sup>15</sup> scenarios this LSP is the lightest *neutralino*. Supersymmetric binos, winos and neutral higgsinos share the same quantum numbers and thus mix into Majorana fermionic mass eigenstates, called neutralinos (see table 1.1). The mass mixing matrix in the basis of  $(\tilde{B}, \tilde{W}_3, \tilde{H}_1^0, \tilde{H}_2^0)$  can be written as:

$$\mathcal{M} = \begin{pmatrix} M_1 & 0 & -M_Z \cos\beta \sin\theta_W & M_Z \sin\beta \sin\theta_W \\ 0 & M_2 & M_Z \cos\beta \cos\theta_W & -M_Z \sin\beta \cos\theta_W \\ -M_Z \cos\beta \sin\theta_W & M_Z \cos\beta \cos\theta_W & 0 & -\mu \\ M_Z \sin\beta \sin\theta_W & -M_Z \sin\beta \cos\theta_W & -\mu & 0 \end{pmatrix} \quad , \quad (1.34)$$

where  $M_1$  and  $M_2$  are the bino and wino mass parameters,  $\mu$  is the higgsino mass parameter,  $M_Z$  is the  $Z$  mass,  $\theta_W$  the Weinberg angle (as in equation 1.23) and  $\tan(\beta)$  is the ratio of the vacuum expectation values of the two Higgs doublets. In its role as a dark matter candidate the lightest neutralino  $\tilde{\chi}_1^0$  is usually referred to as *the* neutralino and simply denoted as  $\chi$  [23]. Its linear composition in terms of the interaction eigenstates  $(\tilde{B}, \tilde{W}_3, \tilde{H}_1^0, \tilde{H}_2^0)$  can be read off from equation 1.34:

$$\begin{aligned} \chi &= \mathcal{M}_{11}\tilde{B} + \mathcal{M}_{12}\tilde{W}_3 + \mathcal{M}_{13}\tilde{H}_1^0 + \mathcal{M}_{14}\tilde{H}_2^0 \\ &= M_1\tilde{B} + M_Z \sin\theta_W \left( \sin\beta\tilde{H}_2^0 - \cos\beta\tilde{H}_1^0 \right) \quad . \end{aligned} \quad (1.35)$$

The neutralino certainly is one of the most well-motivated particle dark matter candidates; it can satisfy cosmological requirements, i.e. being neutral, stable over cosmological timescales and – as a WIMP – it can naturally account for the required abundance in the early universe. Throughout the next chapters, the terms *WIMP* and *neutralino* ( $\chi$ ) will be used interchangeably, which is common practice in the community. Many dark matter searches (direct and indirect) use the more general term *WIMP dark matter* and then choose to interpret their results in a supersymmetric framework. Also, in many cases, WIMPs are denoted as ' $\chi$ ', without any explicit reference to Supersymmetry.

While the neutralino WIMP is a very popular dark matter candidate, it should also be noted that there is a whole variety of particle candidates, even several neutral ones

---

the Standard Model, where  $B$  and  $L$  conservation is not artificially imposed, but arises quite naturally through the absence of renormalizable Lagrangian terms that would violate these numbers.

<sup>15</sup>Depending on the prior choice the lightest *chargino* can also be the LSP, but it is not convenient as a dark matter candidate and therefore will not be treated further in this context.

from Supersymmetry, such as the *gravitino*, *axino* or *sneutrino* [21, 23]. The sneutrino has been excluded by direct dark matter searches while gravitinos and axinos have very weak interactions and are thus hard to detect – effectively making them less interesting as dark matter candidates.

There is one further important aspect of Supersymmetry which provides more flexibility, but also makes the theory harder to assess. It is a phenomenological fact that Supersymmetry must be a broken symmetry. If it were not, superpartners would have the same mass as their SM counterparts and as such meanwhile would have been detected or excluded. The Lagrangian is thus enriched with terms breaking supersymmetry, however, this needs to be done carefully, keeping in mind that the hierarchy between the Planck scale and the electroweak scale must stay intact. These new (*soft*) breaking terms introduce a variety of mass parameters which contribute to the total of 105 supersymmetric MSSM parameters (masses, phases and mixing angles) [34], in addition to the 26 free parameters of the Standard Model [35] (19 conventional and 7 due to neutrino masses and mixing).

In order to computationally scan the viable region of this vast parameter space it seems appropriate to somehow reduce the number of free parameters in a sensible way. There are a few approaches that provide a significant reduction of the parameter number, one of them being *Minimal Supergravity* (mSUGRA). This model assumes that all couplings, gaugino masses and scalar masses unify at the Grand Unification scale ( $\approx 10^{16}$  GeV) and has “4.5” free parameters, four being continuous and one discrete (the sign of the higgsino mass parameter  $\mu$ ). The corresponding model, where  $\mu$  is allowed to be continuous, making a total of 5 free parameters, is called *Constrained MSSM* (CMSSM) [36]. The parameter space can be well probed with collider searches. Recent data make it difficult to reconcile the measurement of the Higgs mass with the needed dark matter density by means of any mSUGRA/CMSSM scenario [37].

A more flexible approach is the *phenomenological MSSM* (pMSSM). Not being a fixed model like mSUGRA, but rather a flexible framework, there are implementations with 7, 10, 19 or 25 free parameters [23]. The assumptions leading to this parameter reduction (compared to the MSSM) are motivated by supersymmetric phenomenology, not by theory. Usual requirements include:

- the absence of new sources for *CP*-violation,
- no flavor-changing neutral currents,
- a first and second generation superpartner universality.

With the equivalent of 300 years of runtime on a single processor, a quantitative exploration of the 19-parameter realization [32, 38] is attempted in chapter 6. The numerous resulting scenarios are required to be compatible with laboratory and cosmological constraints and are used as a supersymmetric interpretation of the indirect exclusion sensitivities obtained in chapter 5. Furthermore, the complementarity with results from direct detection experiments is studied.

Finally, it is worth noting that the bound on the relic density (equation 1.15) can be filled by more than one single type of dark matter particle. For instance, Standard Model neutrinos contribute to dark matter, but cannot account for all of it. Indirect detection prospects of multi-component dark matter are e.g. discussed in [39].

## 1.4 Interaction and Detection of Dark Matter

Neutralino-like dark matter can be detected in several ways: it can be pair-wise produced in colliders [40, 41] and it can deposit energy in earth-based (*direct detection*) experiments by elastically scattering off ordinary matter [42]. A completely different way is to detect a signal of Standard Model particles stemming from pair-wise dark matter annihilation in gravitationally bound objects (*indirect detection*) [43]. None of these methods has as yet produced a solid discovery, however, experiments are rapidly gaining in sensitivity. For the indirect detection scenario, close-by gravitational wells are suited as observational sources, like the cores of the earth [44] and the sun [45, 46] and furthermore our galaxy's center or halo [47, 48]. Annihilation products include  $\gamma$ -rays and neutrinos, each having their (dis)advantages. While  $\gamma$ -rays cannot penetrate opaque matter and thus are not suited to probe accumulated matter near the earth's or solar core, neutrinos are interacting rarely and require large-volume detectors. Also, for energies above a few 100 GeV, due to an increasing scattering cross-section, the sun becomes opaque for neutrinos as well (see figure A.6: even for a 1000 GeV/ $c^2$  candidate the neutrino energy spectrum is not able to peak above 200 GeV). So for candidate masses larger than  $\gtrsim 1$  TeV/ $c^2$  sensitivities get significantly worse. This is even more impaired by the fact that the expected signal for larger candidate masses is initially smaller, because fewer dark matter particles are needed to account for the dark matter relic density, making it harder to accumulate in the sun and find one another to undergo self-annihilation (compare to section 5.1).

Direct-detection experiments are preferably located in a well-shielded environment underground to avoid hiding the rare WIMP signal in the overabundant background of atmospheric muons. Former mines make popular locations, e.g. for the XENON and LUX experiments, which make use of cylindrical time-projection chambers filled with liquid xenon. A particle interaction in the detector volume produces direct scintillation light and ionization electrons which, by an electric field, are guided to the gaseous part of the detector to produce delayed scintillation light. The time difference of these two scintillation signals is used for spatial reconstruction along the electric field – the two remaining coordinates are reconstructed from the photomultiplier hit pattern – whereas the ratio of their amplitudes allows for a distinction of nuclear recoils and such induced by  $\gamma$  and  $\beta$  backgrounds, because the latter produce a larger delayed component [49]. Since the spatial reconstruction works at centimeter-precision, additional background rejection can be achieved through fiducial volume cuts, requiring potential signal events to be reconstructed near the center of the detector [50].

To evaluate the number of WIMP interactions in such detectors, the local WIMP density and their velocity distribution – due to the rotation of our spiral arm within the galaxy – as well as the strength of the interaction have to be known. The latter is quantified by the WIMP-nucleon scattering cross-section, which depends on the distribution of quarks in the nucleon and fundamentally on the WIMP-quark interaction strength. In the scope of Supersymmetry, the according neutralino couplings with the six<sup>16</sup> quarks and gluons are determined by the parameters of a given supersymmetric model. However, such parameters are manifold, as discussed in the previous section and as will be further assessed in chapter 6. This situation results in a large model uncertainty and thus even the fundamental elastic scattering cross-sections cannot be determined uniquely. Once modeled for a specific (supersymmetric) scenario, interactions with quarks have to be transferred to interactions with nucleons: hadronic matrix elements for quark and gluon operators inside a nucleon can be obtained from appropriate scattering data. In the resulting effective<sup>17</sup> Lagrangian, several interaction types arise; axial-vector, vector, scalar and tensor parts – named after their respective behaviors when subject to a Lorentz transformation. For a composed nucleus, these components have to be added coherently using nuclear wave functions, which are yet another source of uncertainty. A more concrete discussion of the relevant nuclear physics can be found in [51]. Such treatment of WIMP-nucleus scattering is necessary because WIMPs are slow-moving particles and as such cannot resolve the nucleus' internals and perceive it in its entirety. Due to the non-relativistic energies, the mentioned tensor and vector currents – for Majorana particles the latter vanish anyway – assume the same form as the scalar part. The axial-vector part essentially becomes an interaction between neutralino spin and quark spin [21]; leaving the WIMP to couple to the mass of the nucleus via scalar interaction and to the spin of the nucleus via axial-vector interaction.

The scalar contribution to the Lagrangian (omitting the one-loop amplitudes for neutralino interactions with gluons) is given by

$$\mathcal{L}_{\text{scalar}} = f_q \bar{\chi} \chi \bar{q} q \quad , \quad (1.36)$$

where  $f_q$  is the neutralino-quark coupling. Being fermion fields, the neutralino and quark are represented by Dirac *spinors*  $\chi$  and  $q$ . Spinors are four-component objects, much like four-vectors, except that they behave differently under Lorentz transformations: they are only turned by half the angle when compared to a vector.  $\bar{\psi}$  denote adjoint spinors ( $\bar{\psi} = \psi^\dagger \gamma^0$ ) and  $\gamma^\mu$  are the Dirac matrices:

$$\gamma^0 = \begin{pmatrix} \mathbb{1}_2 & 0 \\ 0 & -\mathbb{1}_2 \end{pmatrix}, \quad \gamma^k = \begin{pmatrix} 0 & \sigma^k \\ -\sigma^k & 0 \end{pmatrix}, \quad \gamma^5 = \begin{pmatrix} 0 & \mathbb{1}_2 \\ \mathbb{1}_2 & 0 \end{pmatrix} = i\gamma^0\gamma^1\gamma^2\gamma^3 \quad , \quad (1.37)$$

---

<sup>16</sup>Due to the arising quark loops at such scattering processes, all quark and gluon couplings have to be known, not only the ones for up- and down-type quarks.

<sup>17</sup>For the purpose of describing a specific process or set of processes, effective Lagrangians come into play. Their application is restrained to the given process or energy regime, but with less applicability comes less complication.

where  $\sigma^k$  are the three Pauli matrices, defined as

$$\sigma_k = \begin{pmatrix} \delta_{k3} & \delta_{k1} - i\delta_{k2} \\ \delta_{k1} + i\delta_{k2} & -\delta_{k3} \end{pmatrix} . \quad (1.38)$$

$\gamma^5$  is also useful in the context of chiral theories; namely for the division of a Dirac field into left- and right-handed components (this aspect will be further discussed in section 2.1). The corresponding cross-section can be written as

$$\frac{d\sigma_{\text{scalar}}}{d|\mathbf{q}|^2} = \frac{1}{\pi v^2} [Zf_p + (A - Z)f_n]^2 F^2(Q) , \quad (1.39)$$

where  $|\mathbf{q}|$  denotes the absolute value of the momentum transfer  $\mathbf{q}$  and  $F(Q)$  is the nuclear form factor<sup>18</sup>, which is dependent on the energy transferred from the neutralino to the nucleon.  $v$  is the velocity of the incident neutralino and  $f_{p,n}$  are the neutralino couplings to protons and neutrons, whose values only differ slightly. Hence, the scalar cross-section effectively becomes independent of the proton number  $Z$  and is quadratically dependent on the mass number  $A$ . For zero momentum transfer, the cross-section then assumes the simplified form:

$$\sigma_{0,\text{scalar}} = \int_0^{4m_r^2 v^2} \frac{d\sigma_{\text{scalar}}(q=0)}{d|\mathbf{q}|^2} d|\mathbf{q}|^2 = \frac{4m_r^2}{\pi} [Zf_p + (A - Z)f_n]^2 \approx \frac{4m_r^2}{\pi} A^2 f_p^2 . \quad (1.40)$$

Here  $m_r = m_\chi m_N / (m_\chi + m_N)$  is the reduced mass of the neutralino-nucleus system. While scalar interactions are not relevant in the frame of the performed study (chapter 5), they are presented as the counterpart of the spin-dependent interaction. Typically, for nuclei with  $A \gtrsim 30$ , the scalar interaction becomes dominant and is thus an important aspect of direct detector designs. The choice of xenon in the aforementioned detectors, for example, is not only driven by xenon's low intrinsic radiation, but also by the large mass number of about 130 (depending on isotope).

Axial-vector (spin-dependent) interactions on the other hand are the dominant reason for neutralino WIMPs to accumulate in the center of the sun by subsequent scattering and associated energy loss [45]. The sun mostly consists of hydrogen, which has non-zero total spin and is thus the perfect target for axial-vector coupling. The spin-dependent cross-section is therefore the quantity that can be probed and constrained by searches for neutralino self-annihilation products, namely neutrinos. More precisely, in the first step, the neutralino self-annihilation rate can be deduced and by the assumption of capture-annihilation equilibrium (the appropriate formalism and validity will be discussed in section 5.1) the capture rate and the associated scattering cross-section are probed. For axial-vector currents, the Lagrangian equivalent to equation 1.36 can be written as

$$\mathcal{L}_A = d_q \cdot \bar{\chi} \gamma^\mu \gamma_5 \chi \bar{q} \gamma_\mu \gamma_5 q , \quad (1.41)$$

<sup>18</sup>The form factor commonly assumes an exponential form [52]:

$$F(Q) = \exp(-Q/2Q_0) , \quad F(Q=0) = 1 ,$$

where  $Q_0$  is the *coherence energy* and depends on the mass and radius of the nucleus.

where repeated indices are implicitly summed over.  $d_q$  is a combined coupling, which can be broken down to more fundamental contributions. As shown in figure 1.5, the spin-dependent scattering is mediated by  $Z^0$  or squark exchange and  $d_q$  is hence composed of seven terms (one from the  $Z^0$  and one from each of the six squarks).

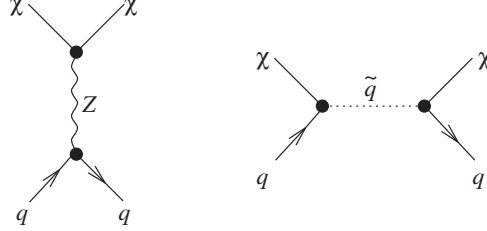


Figure 1.5.: Neutralino-quark spin-dependent elastic scattering processes (from [21]).

In a similar fashion as in equation 1.39, the spin-dependent cross-section can be written as

$$\frac{d\sigma_A}{d|\mathbf{q}|^2} = G_F^2 \frac{8}{\pi v^2} \Lambda^2 J(J+1) F^2(|\mathbf{q}|) \quad , \quad (1.42)$$

where  $J$  is the total angular momentum of the nucleus and  $G_F$  is the Fermi constant.  $\Lambda$  is defined as

$$\Lambda \equiv \frac{1}{J} (a_p \langle S_p \rangle + a_n \langle S_n \rangle) \quad , \quad (1.43)$$

where  $\langle S_{p,n} \rangle$  are expectation values of the spin content in the nucleus, originating from protons – or neutrons, respectively. These values significantly depend on the target nucleus. The  $a_{p,n}$  are proportional to the quark spin contents  $\Delta q^{p,n}$ :

$$a_{p,n} = \sum_{q=u,d,s} \frac{d_q}{\sqrt{2} G_F} \Delta q^{p,n} \quad . \quad (1.44)$$

It is worth noting that the apparent quadratic cross-section dependence on  $J$  in equation 1.42 is canceled by the  $1/J$  normalization in  $\Lambda$  (see equation 1.43). And, again assuming zero momentum transfer, the simplified version reads [21]

$$\sigma_{0,A} = \int_0^{4m_\tau^2 v^2} \frac{d\sigma_A(q=0)}{d|\mathbf{q}|^2} d|\mathbf{q}|^2 = \frac{32}{\pi} G_F^2 m_\tau^2 \Lambda^2 J(J+1) \quad . \quad (1.45)$$

In the solar case, neutralino scattering and capture would only be the first step towards an (indirect) detection via a neutrino signal. When accumulated at the center of the sun, neutralinos can eventually find one another and – since they would be Majorana particles – undergo self-annihilation<sup>19</sup>. Annihilation channels include the pair-wise production of  $W$  bosons,  $Z$  bosons,  $t$ -quarks,  $b$ -quarks,  $\tau$  leptons and quite a few other possibilities [21]. Feynman diagrams contributing to the neutralino annihilation into fermions are shown in figure 1.6.

<sup>19</sup>A magnitude for the self-annihilation cross-section can be found in equation 1.19.

These first Standard Model annihilation products will subsequently decay and in the process also produce neutrinos of all flavors. Whether the neutrinos have a rather hard or soft energy spectrum, however, depends on the annihilation channel. Annihilation channel branching further depends on the specific choice of supersymmetric parameters. Since a whole range of parameters is allowed for modeling a suitable neutralino WIMP, it is desirable to be independent of individual branching fractions. So neutralinos undergoing self-annihilation are assumed to fully branch into one channel. To assess the full possible sensitivity range, a generic hard channel (typically  $\tau^+\tau^-$ ) and a generic soft channel (typically  $b\bar{b}$ ) are chosen and sensitivity to these two scenarios is calculated separately. Any sensitivity to models with branching mixtures of hard, soft and intermediate channels would then necessarily lie within the bounds of these generic hard and soft channel sensitivities.

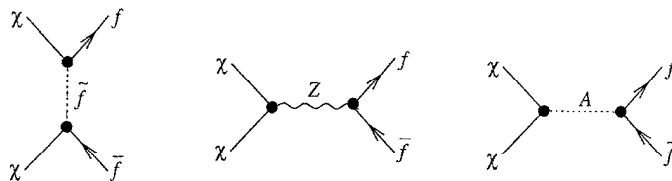


Figure 1.6.: Possible neutralino self-annihilations into fermions.  $A$  is the pseudoscalar Higgs boson which (in supersymmetric extensions) arises in addition to the other neutral Higgs bosons; the CP-even  $h$  and  $H$  (see table 1.1), from [21].

More details about the WIMP capture and annihilation in the sun, the equilibrium condition and input from cosmological quantities will be discussed in section 5.1.

Apart from the spin-(in)dependent scattering cross-sections, which can be probed by the presented detection types, the neutralino self-annihilation cross-section can be assessed by indirect detection of  $\nu$  or  $\gamma$  stemming from the galactic halo or center.  $\sigma_A$ , being dependent on the relative velocity of the two annihilation partners, is usually given in the velocity-averaged form as  $\langle\sigma_A v\rangle$ . In this more general case, where a signal from a defined region with a dark matter density  $\rho$  is expected, the differential flux (here for neutrinos) is given by:

$$\frac{d\Phi}{dE}(E, \phi, \theta) = \frac{1}{4\pi} \frac{\langle\sigma_A v\rangle}{2m_\chi^2} \sum_f \frac{dN}{dE} B_f J(\Delta\Omega) \quad , \quad (1.46)$$

where  $(\theta, \phi)$  is the source direction and  $dN/dE$  is the differential neutrino multiplicity, which is weighted by the branching fraction  $B_f$ . The astrophysical factor  $J$  depends on the spatial distribution of the dark matter and also on the beam size. It consists of a *line-of-sight* integration of the squared density over the solid angle  $\Delta\Omega$  [43]:

$$J(\Delta\Omega) = \int_{\Delta\Omega(\phi, \theta)} d\Omega' \int_{\text{l.o.s.}} \rho^2(r(l, \phi')) dl(r, \phi') \quad . \quad (1.47)$$

In this vein, the annihilation cross-section can be constrained and experiments have presented results on several signal regions, like nearby galaxy clusters and dwarf galaxies, as well as the galactic halo and center. Searches with the *Fermi Large Area Telescope* [53] can even reach down to the cross-section region predicted in the scope of the WIMP freezeout, also denoted as the *natural scale* (see equation 1.19). Neutrinos and  $\gamma$ -rays are best suited for such studies due to their spectral and directional information. However, with more extensive efforts on diffusion and propagation modeling, also charged particles, like electrons and protons (and their respective antiparticles), can be used as cosmic messengers for dark matter searches [23].

# 2

## Neutrinos

A billion neutrinos go swimming: one gets wet.

---

Michael Kamakana

The detection of neutrinos and unraveling the mystery of their oscillations is certainly among the greatest achievements of modern particle physics. Originally postulated by Wolfgang Pauli in 1930, who himself claimed it could never be detected<sup>1</sup>, the neutrino is still subject to fundamental investigations. Due to its elusive nature, well shielded detectors with a large number of photo sensors are required for the high-statistics detection of a natural neutrino flux.

The reason for suggesting the existence of the neutrino was the observed continuous energy spectrum of electrons from beta decay. Building on the concept of energy conservation, Pauli invented a neutral particle (he called it “neutron”) which would carry away the missing energy in an unhindered way. Pauli’s friend Walter Baade made a bet that this particle would be detected some day [54] – and Wolfgang Pauli had to pay up when free neutrinos could finally be observed in 1956 [55].

When the Standard Model was developed, neutrinos entered with zero mass. However, the discovery of neutrino oscillations made it apparent that neutrinos are required to carry a mass – oscillations will be further discussed in section 2.2. Bounds on the lightest mass eigenstate could be established by groups in Mainz and Troitsk in the late 90s, when they carefully studied the endpoint of the tritium beta decay spectrum [56]. A statement about neutrino mass can also be obtained through the yet unsuccessful measurement of neutrinoless beta decay<sup>2</sup>, since the corresponding decay rate is related to the square of a combination of neutrino masses [57].

---

<sup>1</sup> “Ich habe etwas Schreckliches getan. Ich habe ein Teilchen postuliert, das nicht nachgewiesen werden kann.”

<sup>2</sup>Neutrinoless beta decay is possible in the case where neutrinos have Majorana character, i.e. they are their own antiparticles.

The following sections introduce neutrinos in the framework of the Standard Model of Particle Physics, discuss the oscillation of their flavor eigenstates, lay out their role as cosmic messengers and finally introduce the detection possibilities on earth.

## 2.1 Neutrinos in the Standard Model of Particle Physics

Neutrinos, together with the charged leptons; the electron, muon and tau, can be organized in three generations of weak isospin doublets with left-handed chirality (also denoted as *flavors*). Being a chiral theory, the weak interaction only couples to left-handed particles and right-handed antiparticles. Thus, under the assumption that neutrinos are massless, they have no interacting right-handed counterparts – leaving three right-handed singlets for the charged leptons:

$$\begin{pmatrix} \nu_e \\ e \end{pmatrix}_L, \quad \begin{pmatrix} \nu_\mu \\ \mu \end{pmatrix}_L, \quad \begin{pmatrix} \nu_\tau \\ \tau \end{pmatrix}_L, \quad e_R, \quad \mu_R, \quad \tau_R \quad . \quad (2.1)$$

Quarks can be arranged in a similar way, with the difference that all of them have mass, resulting in six right-handed singlets:

$$\begin{pmatrix} u \\ d \end{pmatrix}_L, \quad \begin{pmatrix} c \\ s \end{pmatrix}_L, \quad \begin{pmatrix} t \\ b \end{pmatrix}_L, \quad u_R, \quad d_R, \quad c_R, \quad s_R, \quad t_R, \quad b_R \quad . \quad (2.2)$$

By means of the Dirac matrices, introduced in equation 1.37, fermion spinors  $\psi$  can be decomposed into left- and right-handed components:

$$\psi = \psi_L + \psi_R, \quad \psi_L = \frac{1 - \gamma_5}{2} \psi, \quad \psi_R = \frac{1 + \gamma_5}{2} \psi \quad . \quad (2.3)$$

Under weak isospin rotation such left-handed spinors transform to isospin doublets, while right-handed spinors transform to singlets. For example, a left-handed muon could be rotated to a muon-neutrino by the concurrent emission of a  $W^-$  boson, but no equivalent transformation would be possible for a right-handed muon.

The total weak isospin  $I$  is  $1/2$  for the doublets, allowing for two states with  $I_3 = \pm 1/2$ , while singlets have zero isospin. The resulting electric charge is given by the *Gell-Mann-Nishijima* relation ( $Q = Y/2 + I_3$ , as introduced in equation 1.24). Table 2.1 summarizes the basic quantum numbers for the first generation of leptons and quarks, respectively.

The number of light<sup>3</sup> neutrinos can be determined by examining decays of a real  $Z^0$  boson, produced at  $e^+e^-$  collisions. Such experiments were performed at the *LEP*<sup>4</sup> collider in the beginning of the nineties. Considering the Standard Model prediction for the  $Z^0 \rightarrow \nu\bar{\nu}$  per-flavor decay width ( $\Gamma_{\nu\bar{\nu}} = 166.9 \text{ MeV}$ ), the remaining invisible

<sup>3</sup>Given a  $Z^0$  mass of  $\approx 91 \text{ GeV}/c^2$ , only neutrinos with mass  $\lesssim 45.5 \text{ GeV}/c^2$  can be probed.

<sup>4</sup>Large Electron-Positron collider, precursor to the LHC.

	$\nu_{e,L}$	$e_L$	$e_R$	$u_L$	$d_L$	$u_R$	$d_R$
$I_3$	+1/2	-1/2	0	+1/2	-1/2	0	0
$Y$	-1	-1	-2	+1/3	+1/3	+4/3	-2/3
$Q$	0	-1	-1	+2/3	-1/3	+2/3	-1/3

Table 2.1.: Third isospin component  $I_3$ , weak hypercharge  $Y$  and resulting electric charge  $Q$  for the first generation of left-handed and right-handed leptons and quarks (adapted from [25]).

width can be well accounted for by three neutrino flavors, resulting in an averaged fitted number [58] of

$$N_\nu = 2.984 \pm 0.008 \quad . \quad (2.4)$$

These observations, however, only make a statement about neutrinos that take part in the weak interaction; potential right-handed (sterile) neutrinos are beyond their scope. The number of sterile neutrinos is not required to be the same as the number of charged leptons; for conventional (active) neutrinos this is required in order to make the electroweak interaction anomaly-free. The theoretically rather well motivated right-handed neutrinos will be further discussed in the next section.

Much earlier than accelerator-based experiments, studies of the Big Bang nucleosynthesis were able to put constraints on the number of neutrino species. The amount of helium produced in the Big Bang increases with an increasing number of different types of neutrinos [59]. The larger the amount of relativistic particles in the early universe, the faster it expands and the larger the neutron-proton ratio would be at the time when nuclear reactions start. Most neutrons end up in helium, which is why its abundance is so sensitive on the number of neutrino species. The current bound for established cosmological models ( $N_\nu \lesssim 4.3$ ) is slightly larger than the laboratory bound, being compatible with three neutrino species, but also tolerating a fourth [60].

## 2.2 Neutrino Oscillations

Continuously operating between 1970 and 1994, it was the Homestake experiment that first observed an anomaly in the flux of electron-neutrinos originating from the sun; it was lower than expected by a factor of three [61]. The expectation was based on the *Standard Solar Model*, which was established at that time by John Bahcall [62, 63] and also predicted the amount of neutrinos produced through subsequent decays of solar fusion processes, such as the pp-cycle or the fusion of two helium nuclei to boron-8. The latter process is especially interesting for earth-bound detection of solar neutrinos, because neutrinos originating from the beta decay of  $^8\text{B}$  carry energies up to 15 MeV while the ones produced during proton-proton fusion have maximum energies of 0.5 MeV.

Other detectors could confirm the Homestake deficit, which gave rise to the so-called *solar neutrino problem*. It was only in the late nineties and the beginning of the twenty-first century when this deficit could be definitely attributed to a flavor change by studies of solar and atmospheric neutrinos [64, 65], which were ultimately honored with the 2015 Nobel Prize in Physics. One of the key experiments was the *Sudbury Neutrino Observatory* (SNO), a tank filled with 1000 tons of heavy water and monitored by 9600 photomultipliers. SNO could not only measure the electron-neutrino flux, but was also (due to neutral-current interactions, see section 2.4) sensitive to all neutrino flavors. With distinct signatures in energy and direction, these components could be distinguished from one another and the fluxes for electron-type neutrinos and the other flavors could be determined separately. The total neutrino flux was then consistent with the predicted flux; the prediction, however, only involved electron-neutrinos. These were measured by a factor of three too little (in agreement with the Homestake experiment), while there was a flux of  $\nu_\mu$  and  $\nu_\tau$  coming from the direction of the sun that compensated for the lack in  $\nu_e$  [65].

The observed flavor transformations can be explained by the phenomenon of neutrino oscillations. The physical states of neutrinos are the free-propagation mass eigenstates, which mix into the flavor eigenstates that become manifest during interactions. Since the underlying mass eigenstate is unknown when observing a neutrino of a certain flavor, the system is described by a coherent, linear superposition of all mass eigenstates,  $|\nu_1\rangle$ ,  $|\nu_2\rangle$  and  $|\nu_3\rangle$ . So, quite similar to the treatment of quark mixing, the weak flavor eigenstates are related to the mass eigenstates by a unitary matrix  $U$ , the *Pontecorvo-Maki-Nakagawa-Sakata* (PMNS) matrix (after Pontecorvo who predicted neutrino oscillations [66] and Maki, Nakagawa and Sakata who developed the matrix formalism [67]):

$$\begin{pmatrix} |\nu_e\rangle \\ |\nu_\mu\rangle \\ |\nu_\tau\rangle \end{pmatrix} = \begin{pmatrix} U_{e1} & U_{e2} & U_{e3} \\ U_{\mu1} & U_{\mu2} & U_{\mu3} \\ U_{\tau1} & U_{\tau2} & U_{\tau3} \end{pmatrix} \begin{pmatrix} |\nu_1\rangle \\ |\nu_2\rangle \\ |\nu_3\rangle \end{pmatrix}, \quad (2.5)$$

which can then be parametrized by means of three mixing angles  $\theta_{ij}$  and a phase  $\delta$ , responsible for CP violation:

$$U = \begin{pmatrix} c_{12}c_{13} & s_{12}c_{13} & s_{13}e^{-i\delta} \\ -s_{12}c_{23} - c_{12}s_{23}s_{13}e^{i\delta} & c_{12}c_{23} - s_{12}s_{23}s_{13}e^{i\delta} & s_{23}c_{13} \\ s_{12}s_{23} - c_{12}c_{23}s_{13}e^{i\delta} & -c_{12}s_{23} - s_{12}c_{23}s_{13}e^{i\delta} & c_{23}c_{13} \end{pmatrix}, \quad (2.6)$$

where  $s_{ij} = \sin \theta_{ij}$  and  $c_{ij} = \cos \theta_{ij}$ . Two additional phases would enter if neutrinos were Majorana particles.

As an example, the linear superposition of mass eigenstates for the  $|\nu_\mu\rangle$  state reads:

$$|\nu_\mu\rangle = U_{\mu1} |\nu_1\rangle + U_{\mu2} |\nu_2\rangle + U_{\mu3} |\nu_3\rangle. \quad (2.7)$$

In general, the time evolution of  $|\nu_k\rangle$  ( $k = 1, 2, 3$ ) would be realized by a wave packet. Here we simplify the discussion by limiting ourselves to a plane wave solution:

$$|\nu_k(t)\rangle = e^{-i(E_k t - \vec{p}_k \cdot \vec{x})} |\nu_k(0)\rangle. \quad (2.8)$$

Due to their tiny masses, neutrinos can be treated in the ultra-relativistic limit ( $\vec{p}_k \gg m_k$ ) and the travel time  $t$  can thus be approximated by the travel distance  $L$  by assuming that they essentially travel at the speed of light:

$$|\nu_k(L)\rangle = e^{-im_k^2 L/2E} |\nu_k(0)\rangle \quad . \quad (2.9)$$

Valuable insights concerning oscillation probabilities and lengths can be obtained from a (simplified) two-flavor scenario. In this case, a single mixing angle  $\theta$  suffices to relate mass and flavor eigenstates:

$$\begin{pmatrix} |\nu_e\rangle \\ |\nu_\mu\rangle \end{pmatrix} = \begin{pmatrix} \cos\theta & \sin\theta \\ -\sin\theta & \cos\theta \end{pmatrix} \begin{pmatrix} |\nu_1\rangle \\ |\nu_2\rangle \end{pmatrix} \quad . \quad (2.10)$$

Exploiting equations 2.9 and 2.10 (for a detailed derivation see e.g. [35]), the probability of measuring the  $|\nu_\mu\rangle$  state when the state upon creation was  $|\nu_e\rangle$ , can be written as:

$$P(\nu_e \rightarrow \nu_\mu) = \sin^2(2\theta) \sin^2\left(\frac{\Delta m^2 L}{4E_\nu}\right) \quad , \quad (2.11)$$

where  $\Delta m^2 = m_1^2 - m_2^2$  is the squared-mass difference of the two mass eigenstates. The survival probability then results from the fact that the total probability must be conserved:

$$P(\nu_e \rightarrow \nu_e) = 1 - P(\nu_e \rightarrow \nu_\mu) \quad . \quad (2.12)$$

It is obvious from equation 2.11 that oscillations may only exist if the masses differ – and thus at least one of them has to be different from zero.

While the situation is more complex for the three-flavor scenario, the concept is the same. Due to the fact that one of the (independent) squared-mass differences is small ( $\Delta m_{21}^2$ ) when compared to the other one(s) ( $|\Delta m_{31}^2| \approx |\Delta m_{32}^2|$ ), the survival probability consists of a long-wavelength component which is superimposed with a short-wavelength component (see figure 2.1 for an example) and thus measurements at different distances will be sensitive to different mixing angles and squared-mass differences.

For example, the *Daya Bay* experiment is sensitive to the disappearance of  $\bar{\nu}_e$  stemming from nuclear reactor cores. Employing multiple near and far detectors, the originating  $\bar{\nu}_e$  flux can be measured by a detector near the reactor core and compared to the flux at the far detector, which is about 1 km away.  $\nu_\mu$  and  $\nu_\tau$  cannot undergo charged-current interactions at such low energies (3 MeV) and thus do not induce a signal. For a short-baseline experiment like Daya Bay, the survival probability can be approximated as [68]

$$P(\bar{\nu}_e \rightarrow \bar{\nu}_e) \approx 1 - \sin^2(2\theta_{13}) \sin^2\left(1.267 \cdot \Delta m_{31}^2 L/E_\nu\right) \quad , \quad (2.13)$$

where  $\Delta m^2$ ,  $L$  and  $E_\nu$  are now given in units of eV<sup>2</sup>, km and GeV. In this way (and by including the knowledge on  $\Delta m_{32}^2$  from long-baseline experiments, like e.g. [69]) the mixing angle  $\theta_{13}$  was determined to be [70]

$$\sin^2(2\theta_{13}) \approx 0.090 \pm 0.009 \quad . \quad (2.14)$$

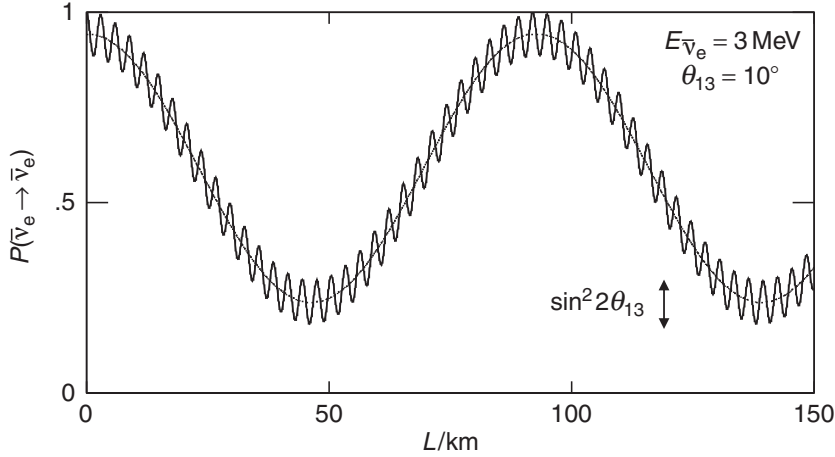


Figure 2.1.: Survival probability for  $\bar{\nu}_e$  as a function of distance, assuming  $\theta_{12} = 0.52$ ,  $\theta_{13} = 0.175$ ,  $\Delta m_{21}^2 = 8 \cdot 10^{-5} \text{ eV}^2$  and  $\Delta m_{32}^2 = 2.5 \cdot 10^{-3} \text{ eV}^2$ . The wavelength of the long-wavelength component is determined by  $\Delta m_{21}^2$  and its amplitude by  $\theta_{12}$ , being maximal for  $\theta_{12} = \frac{2n+1}{4}\pi$ . The amplitude of the superimposed short-wavelength part depends on  $\theta_{13}$ , as labeled inside the figure (from [35]).

The long-wavelength component, and thus  $\theta_{12}$  as well as  $\Delta m_{21}^2$ , can be probed by long-baseline experiments like *KamLAND*: located 1 km underground, it measures the  $\bar{\nu}_e$  flux from reactor cores located at distances between 130 and 240 km. For *KamLAND*, the  $\bar{\nu}_e$  survival probability can be approximated by [71]

$$P(\bar{\nu}_e \rightarrow \bar{\nu}_e) \approx \cos^4 \theta_{13} \left[ 1 - \sin^2 2\theta_{12} \sin^2 \left( \frac{\Delta m_{21}^2 L}{4E_\nu} \right) \right] , \quad (2.15)$$

where  $\cos^4 \theta_{13}$  is  $\approx 0.95$ .

Combining<sup>5</sup> data from solar and atmospheric measurements as well as the various short- and long-baseline experiments which look for (dis)appearances of specific flavors, allows to draw a consistent picture and to determine all mixing angles<sup>6</sup> and mass differences [73]:

$$\begin{aligned} \Delta m_{21}^2 &= (7.37 \pm 0.17) \cdot 10^{-5} \text{ eV}^2 \\ |\Delta m_{32}^2| &= (2.50 \pm 0.04) \cdot 10^{-3} \text{ eV}^2 \\ \sin^2(\theta_{12}) &= 0.297 \pm 0.017 \\ \sin^2(\theta_{23}) &= 0.437_{-0.020}^{+0.033} \\ \sin^2(\theta_{13}) &= 0.0214 \pm 0.0010 \\ \delta &= 1.35_{-0.22}^{+0.29} \cdot \pi , \end{aligned} \quad (2.16)$$

<sup>5</sup>In [72], the contributions are summarized as: “Our knowledge of  $\theta_{12}$  and  $\Delta m_{21}^2$  comes from the *KamLAND* reactor neutrino experiment together with solar neutrino experiments. Our knowledge of  $\theta_{23}$  and  $\Delta m_{32}^2$  comes from atmospheric neutrino experiments and long-baseline accelerator experiments. Results on  $\theta_{13}$  come from reactor antineutrino disappearance experiments”.

<sup>6</sup>In terms of angles, one finds  $\theta_{12} \approx 33.0^\circ$ ,  $\theta_{23} \approx 41.4^\circ$ ,  $\theta_{13} \approx 8.4^\circ$  and  $\delta \approx 243^\circ$ .

where the normal hierarchy (explained below) is assumed and the errors are  $1\sigma$  allowed ranges. Albeit the errors on the CP-violating phase  $\delta$  are fairly large, it seems to be non-zero and CP violation in the neutrino sector is thus favored. The respective confidence level is larger than  $2\sigma$ .

Taking into account the errors on the numbers in equation 2.16, the resulting  $3\sigma$  ranges of the PMNS matrix entries read [74]:

$$|U| = \begin{pmatrix} 0.798 - 0.843 & 0.517 - 0.584 & 0.137 - 0.158 \\ 0.232 - 0.520 & 0.445 - 0.697 & 0.617 - 0.789 \\ 0.249 - 0.529 & 0.462 - 0.708 & 0.597 - 0.773 \end{pmatrix}. \quad (2.17)$$

The fact that so far there are no direct measurements of neutrino masses (only upper limits<sup>7</sup>), leads to the situation that – given the unknown sign of  $\Delta m_{32}^2$  (note the absolute value bars in equation 2.16) – the mass states can be arranged in two possible ways. It is known from solar neutrino measurements that the mass of  $\nu_2$  is larger than the mass of  $\nu_1$  and it is known from measurements of atmospheric neutrinos (and long-baseline experiments) that these masses are much closer to each other than to the mass of  $\nu_3$ . This leaves two possibilities for the arrangement of  $\nu_3$ : being significantly heavier or lighter than  $\nu_1$  and  $\nu_2$  (illustrated in figure 2.2). Quite instructively, the former case is denoted as the *normal hierarchy* whereas the latter is known as the *inverted hierarchy*<sup>8</sup>.

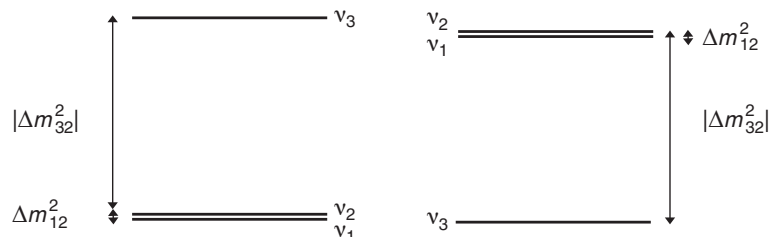


Figure 2.2.: The two possible arrangements of the neutrino mass scale, with normal hierarchy shown on the left and inverted hierarchy on the right (from [35]).

Due to interactions with a medium and themselves, neutrino oscillations in matter look differently when compared to vacuum. Technically, an additional potential is added to the hamiltonian determining the time development of the neutrino states, which accounts for  $\nu_e e^-$  charged-current forward-scattering and thus depends on the matter’s electron density. Since neutral-current interactions are flavor-independent, they do not affect the oscillation behavior (as they result in the same impact on all the hamiltonian’s diagonal elements). Such an alteration of the oscillation by matter has first been described by

<sup>7</sup>It can be deduced from cosmological measurements that the summed mass of all light neutrinos is less than  $0.58\text{ eV}$  [75, 76]. The actual value depends on the datasets that are included in the fits and also on the assumptions on the systematic uncertainties.

<sup>8</sup>According to recent results, the normal hierarchy is slightly favored over the inverted hierarchy, at a significance level of  $1.7\sigma$  [77].

Wolfenstein [78] and was further theorized about by Mikheev and Smirnov [79] – therefore being called the *MSW effect*. Systematic exploitation of this effect will allow long-baseline and atmospheric neutrino experiments to reliably establish the neutrino mass hierarchy within the next years [80]. For this work, matter effects caused by the passage through the earth can be neglected and only the propagation out of the sun (in addition to vacuum oscillations) has to be taken into account [81]. For simulations of the atmospheric neutrino background, earth effects are however considered (see section 5.3).

An interesting approach at embedding neutrino masses into the Standard Model is suggested by the *Seesaw mechanism*: for each left-handed neutrino, a right-handed counterpart is introduced, involving Dirac and Majorana masses, in a way that the small masses of left-handed neutrinos are balanced by (very) large masses for right-handed neutrinos. The latter then can have values that range up to the Planck mass scale – being electroweak singlets the masses of right-handed neutrinos would not take part in electroweak symmetry. The Seesaw mechanism is naturally employed in unified theories (which try to include (super)gravity) or left-right symmetric models. However, it should be noted that in general the number of right-handed neutrinos does not have to coincide with the number of (left-handed) generations: in theory there may as well exist only one or as many as four sterile neutrinos. Observational cosmology, however, constrains the number of different neutrino species, as mentioned at the end of section 2.1.

An explanation of the mechanism, the context of unified theories and an example for the arising Dirac and Majorana masses are given in [82]. An overview of the various ways in which neutrino mass can be introduced to the Standard Model can be found in [83].

## 2.3 Cosmic Messengers

Astrophysical events can be observed by means of various messenger particles, like photons, neutrinos and charged nuclei, where the latter are referred to as *Cosmic Rays*. Each have their distinct properties, as illustrated in figure 2.3. The highly abundant flux of cosmic rays can be deflected by intergalactic magnetic fields and  $\gamma$  rays can get absorbed in dust clouds. Neutrinos on the other hand can traverse large distances without absorption and deflection, but due to their small cross-sections their detection at the earth is challenging.

While neutrinos will be the main focus of this section, charged nuclei and  $\gamma$  rays interacting in the atmosphere produce *secondary*<sup>9</sup> cosmic rays [85, 86], which constitute a dominant background for neutrino detectors and can thus not be neglected in this work’s context.

Highly energetic cosmic rays are believed to originate from the most violent processes in the universe, like Active Galactic Nuclei and Gamma Ray Bursts, and subsequently undergo magnetic field acceleration up to energies of  $10^{20}$  eV – this mechanism is known as

---

<sup>9</sup>For the purpose of distinction parent particles are then called *primary* cosmic rays, in short *primaries*.

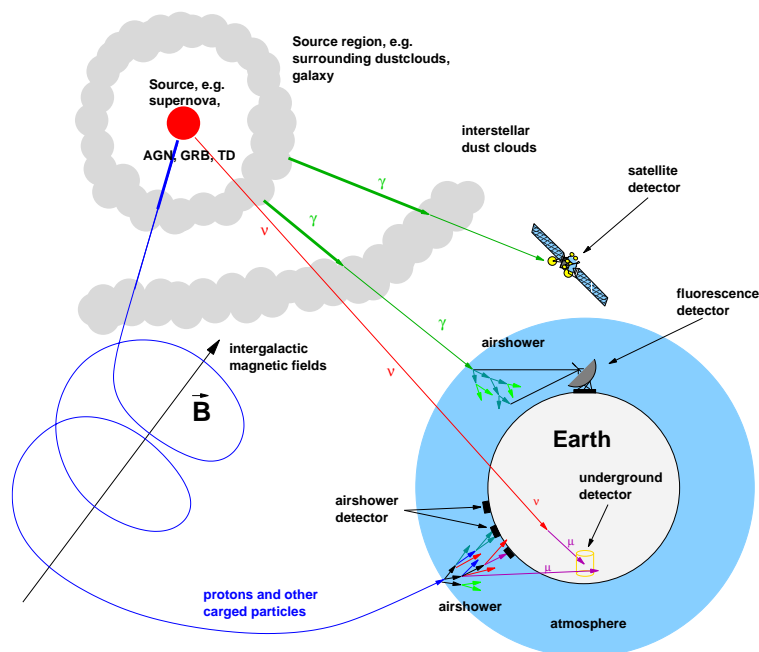


Figure 2.3.: Schematic comparison of the propagation of common cosmic messengers, including their deflection, absorption and typical detector locations at the earth (from [84]).

*Fermi acceleration* [87]. Their energy spectrum can be described by a series of power laws, as shown in figure 2.4. When traversing matter and radiation fields, these high-energy nuclei interact with protons and/or photons and subsequently also produce neutrinos at ultra-high energies [88]. Neutrinos, in contrast to cosmic rays, retain their direction and can in principle help to reveal the sources of highest accelerations, which so far are still subject to speculation. In addition, other point sources that involve the production of neutrinos, can be investigated and conclusions about general properties of neutrino fluxes can be made by means of diffuse studies [89]. The detection at or near the earth, however, is not only impeded by the small neutrino interaction cross-section, but also by the isotropic background flux of cosmic rays, which produce secondary particles in the earth's atmosphere. Despite well-shielded detector locations, these secondary particles pose a dominant background for neutrino detection.

In the GeV to PeV region, before the spectrum steepens at about 4 PeV, the above mentioned power law reads [72]

$$\frac{dN}{dE} \approx 1.8 \cdot 10^4 \left( \frac{E}{1 \text{ GeV}} \right)^{-2.7} \frac{\text{nucleons}}{\text{m}^2 \text{ sr GeV}} . \quad (2.18)$$

A more detailed discussion about the characteristics of the primary energy spectrum, including possible reasons for the change of the spectral index  $\gamma$  (assuming a power law proportional to  $E^{-\gamma}$ ) at the distinct points known as *knee* and *ankle*, can be found in [91].

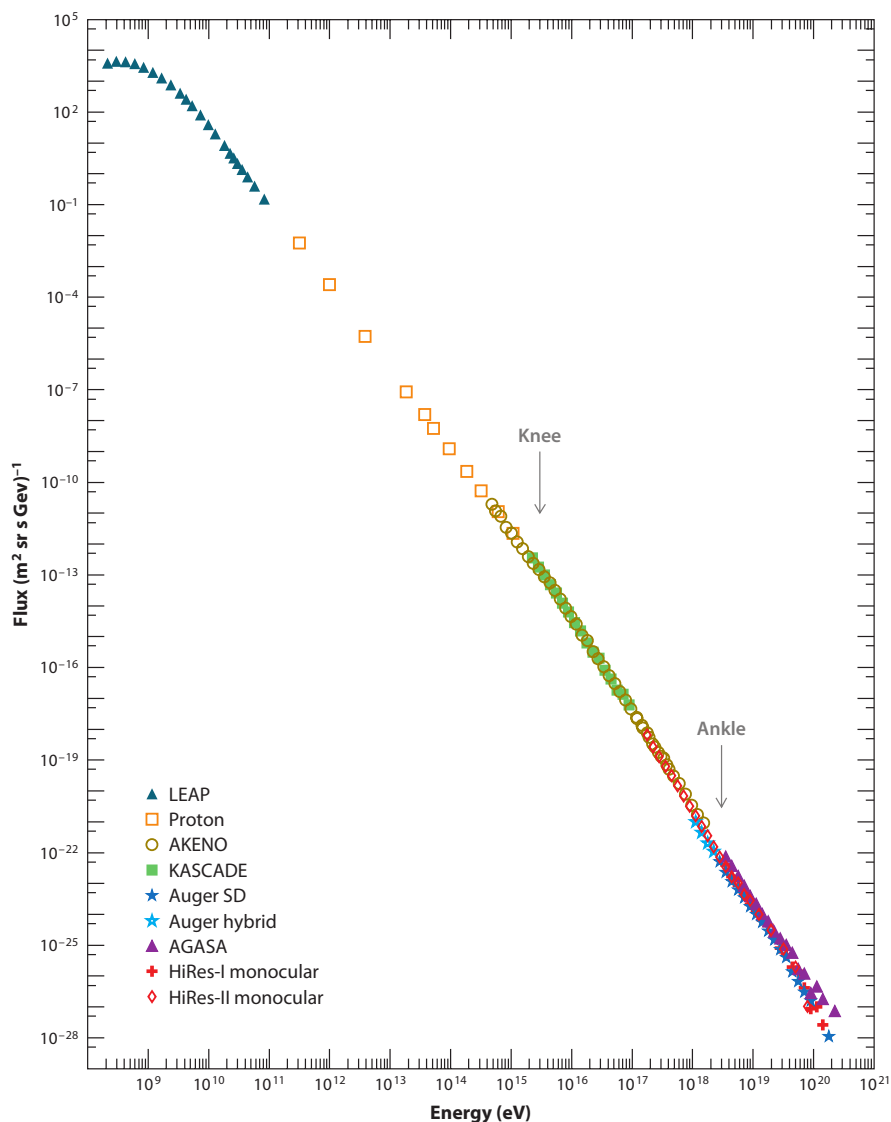


Figure 2.4.: Cosmic ray energy spectrum, as measured by earth-bound experiments. Discontinuities in the power law index, commonly referred to as *knee* and *ankle*, are marked by arrows (from [90]).

These primaries, which constantly bombard the atmosphere, undergo hadronic interactions with air molecules and subsequently produce charged pions and kaons (where production of the latter happens in about 20 % of the cases at TeV energies and increases further for higher energies [92]). Neutral pions undergo a quick electromagnetic decay ( $\pi^0 \rightarrow \gamma\gamma$ ,  $\tau < 10^{-16}$  s) and the produced  $\gamma$  photons cause production of  $e^+e^-$  pairs, due to the presence of matter. These  $e^\pm$  lose energy by bremsstrahlung and ionization processes. After each iteration, the shower particles have less energy until  $\gamma$  energies fall beneath the pair production threshold ( $E_\gamma < 2m_e$ ). Such a shower usually cannot reach the ground, since the atmospheric depth corresponds to about thirty electromag-

netic interaction lengths. The charged pions, on the other hand, decay to muons and muon-neutrinos via the weak interaction, with the dominant decay being:

$$\pi^\pm \rightarrow \mu^\pm + \nu_\mu(\bar{\nu}_\mu) \quad . \quad (2.19)$$

Charged pion and kaon decays to  $e^\pm$  (and associated neutrinos) are helicity-suppressed in this case. Muons can subsequently decay to electrons with associated production of electron- and (anti)muon-neutrinos. However, the decay length of muons in the atmosphere is already larger than its production altitude (about 15 km, depending on primary energy) for energies as low as 2.5 GeV and muons can thus reach the earth's surface and with energies of a few hundred GeV will even penetrate kilometers of material before they decay [86].

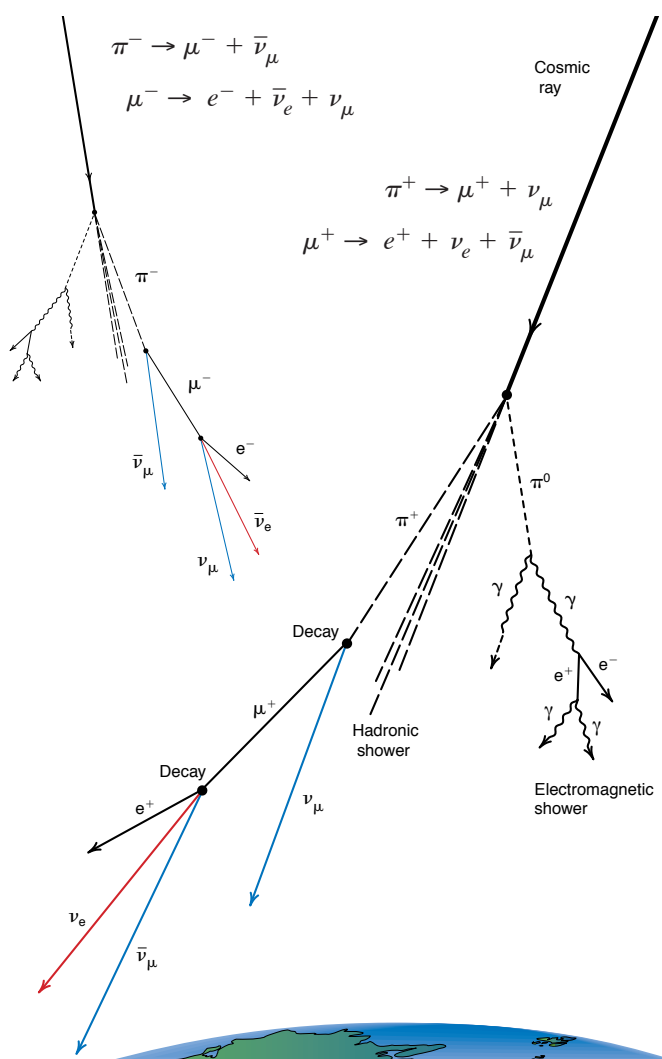


Figure 2.5.: Formation of secondary cosmic ray showers in the atmosphere. The examples show the emergence of electromagnetic, hadronic and muonic components – where the latter does not necessarily decay before reaching the detector (from [93]).

Together with the aforementioned helicity suppression, the fact that high-energy muons do not decay, results in a small electron-neutrino share. However, considering the semi-leptonic kaon decay channels (e.g.  $K^+ \rightarrow \pi^0 e^+ \nu_e$ ) and oscillations of the muon-neutrinos that are created upon leptonic decays of charged pions and kaons, the  $\nu_e$  and  $\bar{\nu}_e$  portion predicted by atmospheric models is around 20% at 100 GeV, with the remainder effectively being  $\nu_\mu$  and  $\bar{\nu}_\mu$  (see sections 5.2 and 5.3, where the more technical aspects, i.e. the correct modeling of this atmospheric background, its simulation and comparisons to experimental data will be discussed). Figure 2.5 illustrates two different kinds of possible interactions and their respective decay products.

## 2.4 Interaction and Detection of Neutrinos

Neutrinos can never be observed directly. They interact weakly and conclusions about the incident neutrino are only possible by examination of reaction products. For example, a neutrino flavor distinction is only possible by identifying its charged lepton counterpart produced in a *charged-current* (CC) interaction, which is mediated by a  $W^\pm$  boson:

$$\nu_l + N \rightarrow l^- + X \quad . \quad (2.20)$$

Here,  $X$  denotes hadronic remnants.  $Z^0$  mediated *neutral-current* (NC) interactions, however, leave the neutrino intact and only the hadronic shower arising from the  $Z^0$ -quark interaction is observed in the detector:

$$\nu_l + N \rightarrow \nu_l + X \quad . \quad (2.21)$$

Therefore, NC interactions are flavor-independent. Figure 2.6 illustrates both charged and neutral-current reactions, where for the former  $\nu_\tau$  are chosen as an example – the process is, however, the same for all flavors.

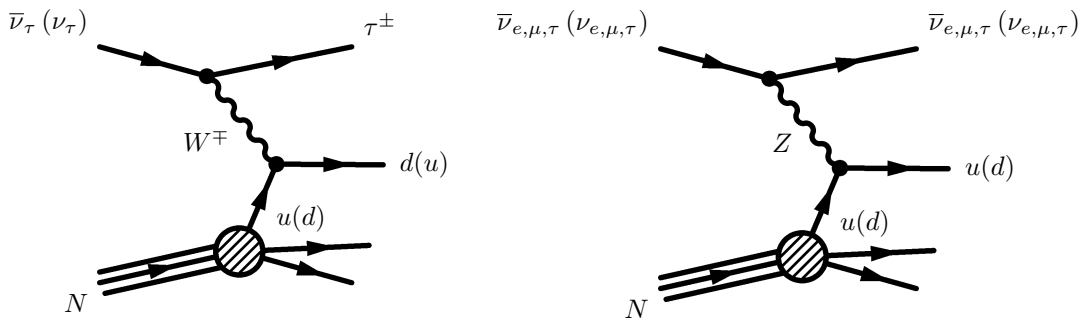


Figure 2.6.: Neutrino charged-current (left) and neutral-current (right) interaction with a nucleus. The momentum transfer can cause the nucleus to break apart. The charged current transforms an up-quark to a down-quark, or vice versa (from [94]).

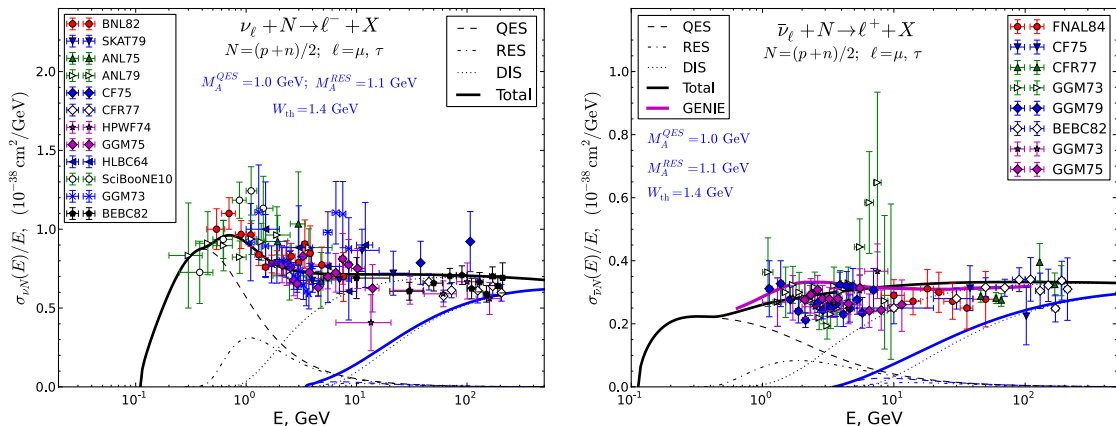


Figure 2.7.: Neutrino (left) and anti-neutrino (right) charged-current scattering cross-sections with nucleons. Dashed and dotted lines show the contributions from the different interaction types. The  $\nu_\tau$  cross-section is depicted as a blue line. For reference, the anti-neutrino cross-sections as implemented in the GENIE Monte-Carlo generator [95] are also shown (figure taken from [80], with data from [96]).

Figure 2.7 shows the various contributions to neutrino-nucleon cross-sections, together with total cross-section measurements. Neutrinos and antineutrinos are plotted separately, since antineutrino interactions are helicity-suppressed (not all scattering directions are allowed due to the right-handed nature of the antineutrino). In the energy regime below 10 GeV, resonant single-pion production (RES) and quasi-elastic scattering (QES)<sup>10</sup> start to dominate [97], while above  $\approx 10$  GeV deep-inelastic scattering (DIS) is the relevant process. For CC interactions, the finite  $\tau^\pm$  mass has to be taken into account [98, 99]; this is why  $\nu_\tau$  cross-sections significantly differ from those of  $\nu_\mu$  in figure 2.7. This effect can also be clearly seen at the low-energy end of the employed signal neutrino spectra<sup>11</sup>, as shown in appendix A. For a DIS process, the center-of-mass energy of the incident tau-neutrino and the interacting quark has to be larger than the  $\tau$  mass, requiring an energy threshold of about 5 GeV for such deeply-inelastic charged-current interactions:

$$E_{\nu_\tau} \geq \frac{m_\tau^2}{2m_q} \cdot c^2 \quad , \quad (2.22)$$

where  $m_\tau \approx 1.77 \text{ GeV}/c^2$  is the mass of the  $\tau^\pm$  lepton and  $m_q$  is the constituent mass of the participating up- or down-type quark ( $m_q \approx 0.3 \text{ GeV}/c^2$ ). Equivalent thresholds can also be calculated for electron and muon flavors, but are only relevant at sub-GeV energies. Aside from this kinematic impact, neutrino-nucleon cross-sections are flavor-independent due to the electroweak universality [81].

<sup>10</sup>In this case the charged-current interaction happens in a quasi-elastic way, where the nucleon itself stays intact, but undergoes transmutation, e.g. from  $n$  to  $p$ .

<sup>11</sup>In the WimpSIM signal simulation (see section 5.1) only deep-inelastic scattering interactions are considered [100] and thus the  $\nu_\tau$  energy spectrum starts at 5 GeV (see [96]).

Figure 2.8 shows inclusive cross-sections for deep-inelastic neutrino scattering off isoscalar nucleons for a broad energy range, which can formally be expressed as [101]:

$$\frac{d^2\sigma}{dx dy} = \frac{2G_F^2 M E_\nu}{\pi} \left( \frac{M_W^2}{Q^2 + M_W^2} \right)^2 \left[ xq(x, Q^2) + x\bar{q}(x, Q^2)(1-y)^2 \right] \quad (2.23)$$

for charged-current reactions. Here  $M = (M_p + M_n)/2$  denotes the neutron-proton averaged nucleon mass,  $G_F = 1.16632 \cdot 10^{-5} \text{ GeV}^{-2}$  is Fermi's constant and  $-Q^2$  is the invariant momentum transfer between incident neutrino and outgoing lepton;  $q$  and  $\bar{q}$  denote the quark distribution functions. The DIS cross-section can as such be obtained through integration over the Bjorken scaling variables  $x = Q^2/2M\nu$  and  $y = \nu/E_\nu$ , where  $\nu = E_\nu - E_l$ . Adjusting  $q$ ,  $\bar{q}$  and replacing the  $W^\pm$  mass by the  $Z^0$  mass, yields the corresponding neutral-current DIS cross-section [101]:

$$\frac{d^2\sigma}{dx dy} = \frac{G_F^2 M E_\nu}{2\pi} \left( \frac{M_Z^2}{Q^2 + M_Z^2} \right)^2 \left[ xq^0(x, Q^2) + x\bar{q}^0(x, Q^2)(1-y)^2 \right] \quad . \quad (2.24)$$

Also shown in figure 2.8 is the  $\bar{\nu}_e$ - $e^-$  scattering cross-section, with a distinct feature in the PeV regime, known as the *Glashow resonance*: in general – due to the small electron mass – an insignificant cross-section contribution is expected from this process. However, the cross-section is considerably increased once the center-of-mass energy becomes sufficient to excite a real<sup>12</sup>  $W^-$  boson:  $\bar{\nu}_e + e^- \rightarrow W^-$  [102]. With a corresponding neutrino energy of  $m_W^2/(2m_e) \cdot c^2 \approx 6.3 \text{ PeV}$ , this process might also play a role in the detection of high-energy astrophysical neutrinos [103, 104], but has not been observed so far.

Among other techniques, the interactions caused by high-energy neutrinos can be detected by means of the *Cherenkov effect* [106]. A charged particle, moving inside a dielectric medium with a speed exceeding the local speed of light, will polarize the matter along its track, which upon returning to its equilibrium state, will emit coherent radiation under a specific angle. This so-called Cherenkov angle can be determined by geometrical considerations (see figure 2.9):

$$\cos(\theta_c) = \frac{ct/n}{\beta ct} = \frac{1}{\beta n} \approx \frac{1}{n} \quad \Rightarrow \quad \theta_c = \arccos(1/n) \approx 40.2^\circ \quad , \quad (2.25)$$

where the refractive index of ice<sup>13</sup> ( $n \approx 1.31$ ) was used and  $\beta \approx 1$  was assumed for the neutrino-induced charged particles.

The corresponding theory, developed by Frank and Tamm [109], predicts the number of produced photons for a certain (angular) frequency  $\omega$  and travel distance  $x$ :

$$\frac{d^2 N}{d\omega dx} = \frac{z^2 \alpha}{c} \sin^2 \theta \quad , \quad (2.26)$$

---

<sup>12</sup>The  $W^-$  subsequently decays hadronically in 2/3 of the cases and to leptons otherwise.

<sup>13</sup>The refractive index is slightly wavelength dependent; for ice see e.g. [107].

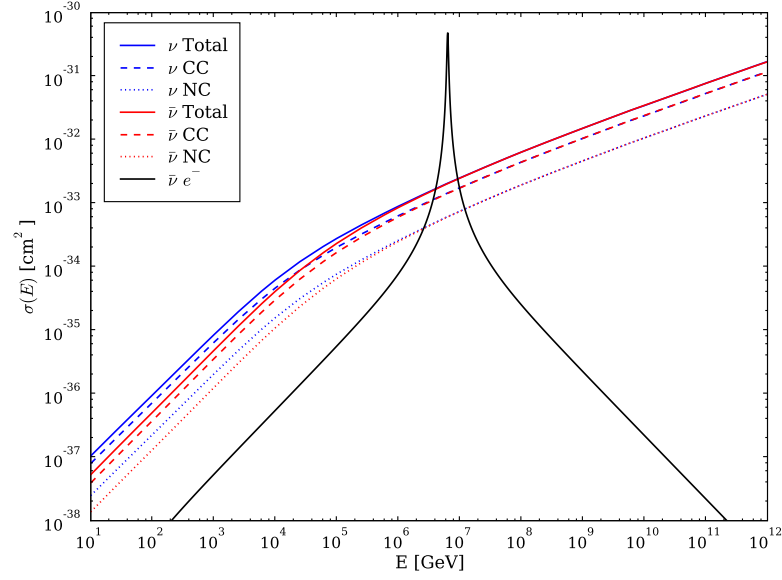


Figure 2.8.: Energy-dependent neutrino-nucleon CC and NC cross-sections for neutrinos and antineutrinos. Shown in black is the  $\bar{\nu}_e e^-$  scattering cross-section which is dominated by the Glashow resonance (from [105]).

where  $z$  is the particle's electric charge and  $\alpha \approx 1/137$  is the fine-structure constant. Equation 2.26 shows that Cherenkov radiation is more intense at higher frequencies (i.e. shorter wavelengths) and thus is blue in the visible spectrum. Hence, for the detection of neutrinos, a large volume of a transparent medium is required, instrumented with photomultipliers which are more sensitive towards the short-wavelength region of the visible spectrum. The next chapter will present a unique example of such a detector; the IceCube Neutrino Observatory, where more than five thousand photomultipliers are instrumented in a cubic kilometer of antarctic ice.

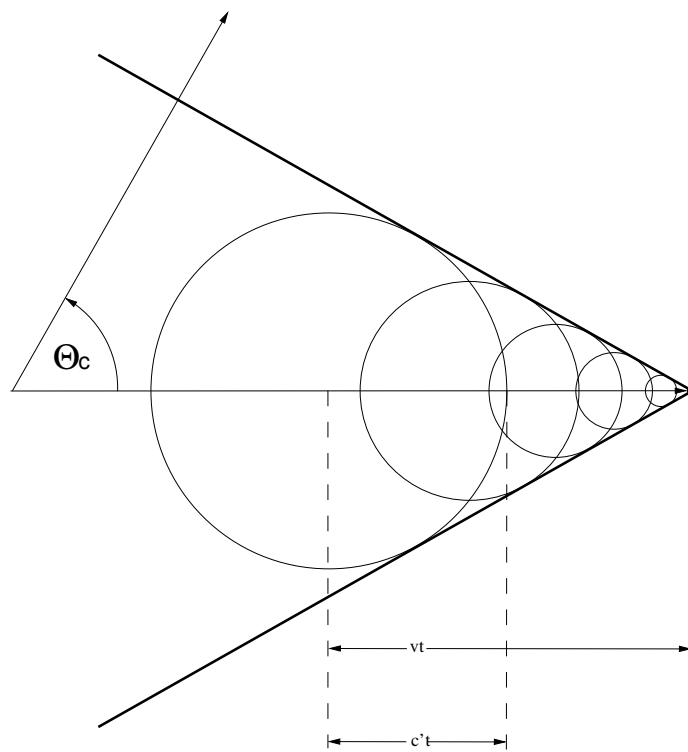


Figure 2.9.: Construction of a Cherenkov radiation wave front by the Huygens principle.  
 $v = \beta c$  and  $c' = c/n$ , where  $c$  is the speed of light in vacuum (adapted from [108]).

# 3

## The IceCube Detector

Wenn man sich die Vorträge hier so anhört,  
dann könnte man wirklich das Gefühl bekommen,  
dass IceCube ein erfolgreiches Experiment ist.

---

Heinz-Georg Sander (2009)

While large-volume Cherenkov based neutrino detectors are usually either located in the depths of seas or in underground caverns, the IceCube experiment is unique in its choice of the transparent medium: the antarctic ice sheet. In the violet and ultra-violet part of the optical spectrum such ice is the most transparent natural solid on earth [110] and combines the advantages of minimal opacity with a low-radiation environment and stationary sensor locations. With a cubic kilometer of instrumented volume and a sophisticated data selection technique, the IceCube experiment was the first detector to prove the existence of a diffuse flux of high-energy extraterrestrial neutrinos [104]. The research mission furthermore extends to cosmic ray physics, the detection of exotic particles, the investigation of neutrino properties and searches for ultra-luminous astrophysical events, like Gamma Ray Bursts or core-collapse supernova explosions [111].

The geometry and components of the IceCube detector are introduced in section 3.1, while section 3.2 discusses data-taking, triggering, online data processing and data transmission to storage in the northern hemisphere. Section 3.3 presents the properties and modeling of the glacial ice. Finally, section 3.4 concludes with the presentation of the different event signatures that arise from charged and neutral-current interactions of the different neutrino flavors.

### 3.1 Detector Layout and Detector Components

A few decades after the discovery of the neutrino it became clear that given its unique properties, the neutrino would be a suitable astronomical messenger. In order to significantly detect high-energy astrophysical neutrinos, which can e.g. be produced by cosmic

ray interactions with the cosmic microwave background, enormous particle detectors are required [112].

Based on the success of the precursor AMANDA<sup>1</sup> detector, a kilometer-scale experiment was suggested; *IceCube* [114]. The construction took place in the austral summer seasons between 2005 and 2011 and data-taking immediately started after each subsequent expansion stage. IceCube's first year performance is summarized in [115].

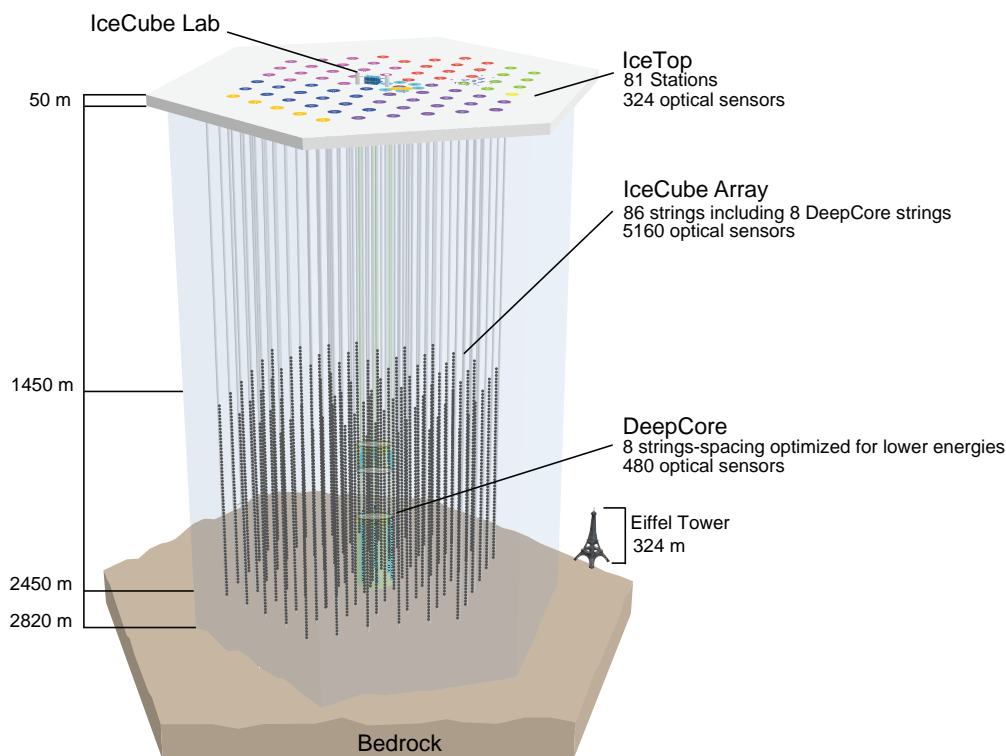


Figure 3.1.: Schematic of the IceCube detector. Points mark string-mounted optical modules, each housing one photomultiplier. The denser *DeepCore* region is depicted in green. The colored circles at the surface correspond to the different instrumentation seasons, the temporal order being: yellow, green, red, magenta, purple, blue, orange. Data from the optical modules are brought together at the *IceCube Laboratory* on the surface, where subsequent data acquisition takes place. The size of the Eiffel tower is shown for reference (from [116]).

The dimensions of the detector are illustrated in figure 3.1, together with the color-coded instrumentation seasons (see figure caption for their time ordering). Photomultipliers (PMTs) are protected against pressure by glass housings, which also enclose electronics for waveform digitization and calibration LEDs. Such a unit is referred to as *Digital Optical Module* (DOM), illustrated in figure 3.2. Technical specifications of the optical

<sup>1</sup>Antarctic Muon And Neutrino Detector Array: technical feasibility study of an antarctic neutrino observatory [113]. Installed beneath the geographical South Pole, the AMANDA detector was operational from 1996 to 2009.

module, including main board design, can be found in [117]. Photomultiplier characteristics are presented in [118]. DOMs are mounted on *Strings* and lowered into water-drilled holes which refreeze afterwards. In total, 5160 optical modules are located on 86 strings, at depths between 1450 and 2450 meters. The regular inter-string spacing is 125 m and the vertical separation is about 17 m. A surface array (*IceTop*), consisting of 324 optical modules extends the capabilities for cosmic ray studies without the restrictive shielding of the ice, that only allows muons (and neutrinos) to penetrate [119]. In order to extend sensitivity to significantly lower energies ( $\gtrsim 10$  GeV), a denser sub-array consisting of eight additional strings, called *DeepCore*, is integrated at the lower central part of the IceCube volume. This extension has 70 m horizontal spacing, 7 m vertical spacing in its lower part and 10 m spacing in the upper part (where the two parts can clearly be distinguished in figure 3.1). This splitting is motivated by the presence of a dust<sup>2</sup> layer, which is mostly abundant at depths of about 2 km and which is responsible for a significant increase in photon scattering and absorption [110]. Measurements of the latter with clearly visible dust impacts are presented in section 3.3. Moreover, PMTs with a quantum efficiency<sup>3</sup> increased by 35 % are deployed on six of these denser-instrumented strings [122]. The fiducial volume of DeepCore comprises 15 strings, including seven conventional IceCube strings with wider module spacing.

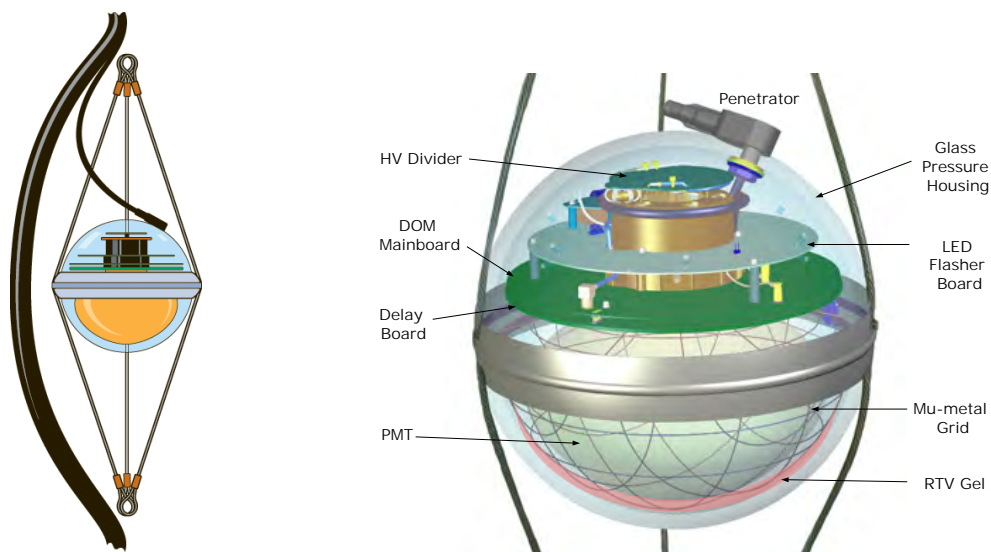


Figure 3.2.: Illustration of a string-mounted DOM and its components (from [123]).

The DeepCore infill array not only allows for a good detector performance at lower energies, but also benefits from background veto capabilities due to the surrounding IceCube instrumentation [124]. This approach permits significant reduction of both

<sup>2</sup>Dust and ash deposits in the ice track climatological changes [120]. The dust concentrations at 2 km depth, for example, correspond to environmental conditions that occurred during the last glacial period, about 65,000 years ago. Since the ice is formed by accumulated and subsequently compressed surface snow, the depth of the ice can be directly related to its age [121].

<sup>3</sup>Effective efficiencies of optical modules are modified once they are deployed in the ice, making in-situ calibrations necessary.

atmospheric muon events as well as atmospheric neutrinos that have been produced in the same shower. Upward directed atmospheric neutrinos, however, cannot be rejected in such way, since no associated muon could reach the detector from below the horizon. In the event selection employed in this work, DeepCore-specific event triggering and filtering are of crucial importance (see sections 3.2 and 5.3).

Once frozen into the glacial ice, optical modules and strings can neither be physically replaced nor maintained. Although each module undergoes thorough testing prior to deployment, in a few cases, modules can stop functioning or do not perform as expected, e.g. by showing an unusual noise behavior. Since they would significantly affect triggers, the data from the  $\sim 130$  *bad*-marked modules (shown in figure 3.3) are usually discarded.

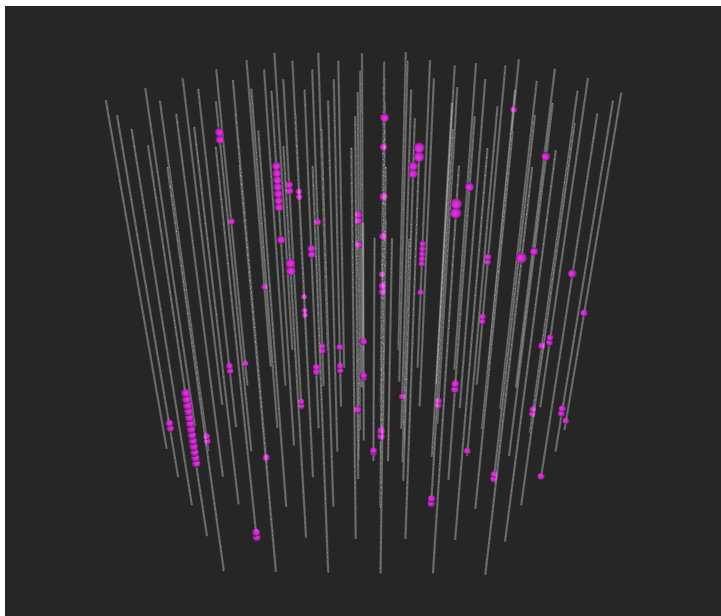


Figure 3.3.: Visualization of *bad*-marked modules in the IceCube detector.

## 3.2 Data Acquisition, Filtering and Transmission

The optical modules are autonomous data acquisition units, housing not only the photomultiplier, but also a suite of electronics to achieve in situ digitization and time-stamping of the waveforms produced by the PMT. Apart from a small boot-up program, the DOM configurations can be altered remotely. In order to reduce noise-related data traffic, a DOM can operate in different coincidence modes, where usually the data-acquisition is

initiated<sup>4</sup> above a  $0.25 \text{ PE}^5$  anode voltage threshold (such an occurrence is referred to as a *hit*) and subsequently neighboring DOMs are consulted. Only if they also observed a pulse in a time interval of  $\pm 1 \mu\text{s}$  [115], the digitized waveforms with local timestamps are sent to the surface. Two coincidence modes are distinguished. The *Hard Local Coincidence* (HLC) requires another hit on one or more of the nearest or next-to-nearest neighboring DOMs; coincidence checks are always performed on the same string. For this purpose, the inter-DOM communication is realized via the connecting copper wires. In pure *Soft Local Coincidence* (SLC) mode, no hit on neighboring modules is required such that rates increase by roughly two orders of magnitude. In order to save transmission bandwidth, only limited waveform information is sent in case of isolated SLC hits, whereas for hits meeting the (hard) local coincidence criterion, the full digitized waveform is transmitted [117]. While accompanying SLC hits are often connected to noise, they can also stem from Cherenkov light and can thus play a crucial role for event reconstruction and vetoing, especially at lower energies.

The data streams of all strings meet at the IceCube lab where hits are discarded or kept depending on software trigger conditions. In the latter case, events are built by merging the hit streams from participating DOMs [125]. All events that meet one or more trigger conditions are recorded on local disks (earlier on tapes) with a total rate of about 2.5 kHz (depending on season [126]), where the vast majority is contributed by atmospheric muons. From the various implemented triggers [125], the one most frequently used (also in this work) is the *Simple Multiplicity Trigger* (SMT), which requires a set number of local coincidence hits to occur in a given time window. For the whole fiducial volume of the in-ice detector, the condition is set to a minimum of eight local coincidences (SMT8) within a time window of  $5 \mu\text{s}$ . If this condition is met, HLC and SLC hits from the whole detector are read out, starting from  $4 \mu\text{s}$  prior to the first HLC hit till  $6 \mu\text{s}$  after the latest HLC hit. In order to lower the energy threshold to less than 10 GeV an independent SMT trigger is added for the DeepCore fiducial volume with a looser condition of three HLC hits (SMT3) [122]. For this trigger, a  $2.5 \mu\text{s}$  time window is set and only DOMs below 2100 m are considered. At such depths, the background from atmospheric muons is significantly reduced, yielding SMT3 trigger rates of about 200 Hz.

Given the remote detector location, not all triggered data can be sent North via geosynchronous satellites; in fact, IceCube's daily quota amounts to merely  $\sim 100 \text{ GB}$ . The necessary reduction is accomplished by software filters, which are motivated by the analyses being performed and are maintained by the individual working groups. Each filter seeks to keep likely signal events and to discard likely background events. If an event fulfills one or more filter conditions, it will be transmitted North within one day. Event filtering happens instantaneously (*online*) at the *Processing and Filtering* (PnF) computing farm located inside the IceCube laboratory. The overall event rate after online filtering is on

<sup>4</sup>In the case of such a trigger, recording of the complete waveform (including the pre-trigger part) is achieved by delaying the signal by 75 ns before it reaches the digitizer.

<sup>5</sup>Anode voltage level corresponding to a single photon-induced electron after being multiplied by all dynodes.

the order of 500 Hz, depending on season. As mentioned before, all triggered data are still recorded to disks and shipped North at the end of each austral season.

The DeepCore filter stream, which acts upon SMT3 triggered DeepCore events, is the relevant stream for this work and shall thus be discussed in more detail. It aims at examining HLC hits in the surrounding fiducial “veto” volume and determining if they are likely to be induced by atmospheric muons. For this purpose, an individual event’s “center of gravity” (COG) is calculated by considering the position and time information of all hits on DeepCore DOMs. This initial COG is then updated by discarding hits with timestamps beyond one standard deviation of the average time. This new subset yields a new average position  $r'$  and a new time  $t'$ , which is the average of individual corrected times. This correction is obtained by individually subtracting the time that unscattered light would travel from  $r'$  to the position of the corresponding DOM. For each HLC hit in the veto region, a particle speed can thus be calculated relative to  $r'$  and  $t'$ . If at least one such hit is attributed a speed that is consistent with the speed of light  $c$ , the event is vetoed. To account for light scattering, the veto region is generously defined to be between 0.25 and 0.4 m/ns. In such a way, 90 % of SMT3-triggered atmospheric muons are discarded, while over 99 % of atmospheric neutrinos can be preserved. This online veto technique is illustrated in figure 3.4. Through further offline processing by means of more CPU-intensive algorithms, a total atmospheric muon rejection by a factor of  $10^5$  is aimed for, while keeping the neutrino efficiency at over 50 % [122].

Once in the North, IceCube events are subjected to more sophisticated, likelihood-based, event reconstructions (more details in section 4.1) as well as *hit cleanings*. The latter shall be briefly discussed at this point, since a few of the variables which are later used for event selection are calculated based on *cleaned* hit series. Hit Cleaning aims at identifying and removing (SLC) hits that are causally disconnected from the actual event and thus are likely to originate from PMT noise. Cleaned hit series are saved as bit masks and can always be applied to the uncleaned series – which are therefore not discarded. While hit cleanings on the basis of the SMT8 trigger are performed in the context of the *offline* processing in the North, cleaned pulse<sup>6</sup> series are re-calculated in the low-energy context by considering the SMT3 trigger. As a first step, hits with timestamps outside a range of  $[-4, +5]$   $\mu\text{s}$  relative to the SMT3 trigger time are removed. Such a process is referred to as *Time Window Cleaning* (TWC). The resulting pulse series serve as the basis for a more sophisticated algorithm: *RT cleaning*. In addition to the time difference  $T$ , also the spatial distance  $R$  is evaluated. In its simple variant, called *classicRT* (cRT), each SLC hit is checked to have any other hit within a radius  $R = 150$  m and a time difference  $T = 1000$  ns. If no other hit can be found, this hit is removed. The choice of parameter values is always a compromise – the employed values retain about 95 % of physics hits, while removing roughly 80 % of noise hits. A more sophisticated approach is pursued

---

<sup>6</sup>A hit comprises the whole waveform information, as recorded over a set time range (e.g. 6.4  $\mu\text{s}$ ) by the digitizers on the DOM, and may consist of many *pulses*. The latter represent the computationally distinguishable arrivals of one or more photons at the PMT. The extraction of pulses from digitized waveforms is performed online.

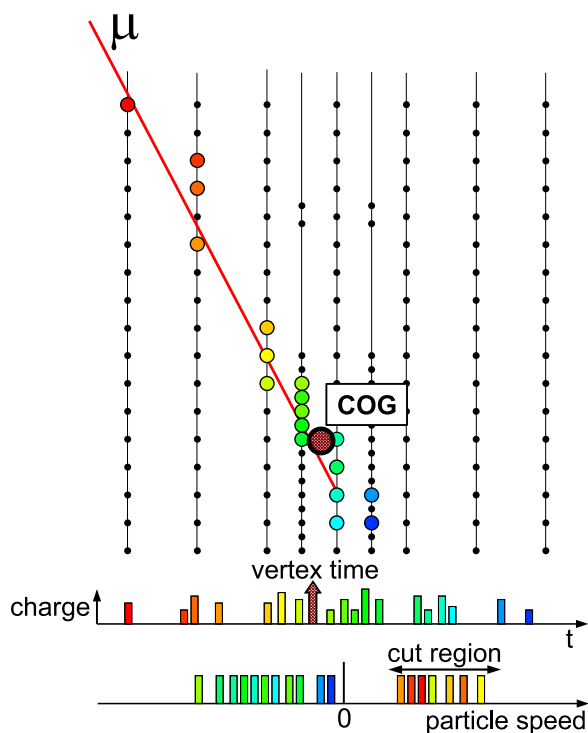


Figure 3.4.: Illustration of the DeepCore filter technique using the example of a simulated downward-going muon. Hit times are continuously color-coded from early (red) to late (deep blue). Particle speeds associated with HLC hits in the veto region have values around the speed of light and therefore cause such an event to be vetoed.

by the *seededRT* (sRT) variant: starting from a “seed” of hits, which fulfill the RT criterion and are believed to be physics hits (e.g. the entirety of HLC hits), nearby hits are added if they also fulfill the RT criterion. This check is iteratively repeated until no further hit can be added (or the maximum number of iterations is reached). With the same parameters for  $R$  and  $T$  as above, 97% of noise can be rejected while 92% of physics hits can be retained [127]. Hit series which have been cleaned by the seededRT algorithm, are commonly used as input for the calculation of discrimination variables and for sophisticated likelihood reconstructions.

The so-obtained data sample is denoted *level 2* and constitutes the basis for most IceCube analyses. Analyses aiming at lower energies are additionally provided with a low-energy focused *level 3* data sample, which marks the entry point for this work – more information about offline event filtering will be presented in section 5.3.

At this point it is worth noting that for simulation (given an event generator), the whole low-level data acquisition process, including photon propagation, PMT response, stochastic noise etc. has to be precisely reproduced, requiring models and various parametrizations. Details about the specific steps and modules are provided in appendix B. The crucial modeling of the South Pole ice will be discussed in the following section.

### 3.3 Ice Properties and Modeling

As introduced in section 3.1, the formation of the glacial ice has a long history with variable dust and ash deposits, resulting in depth-dependent optical scattering and absorption lengths. Air bubbles significantly affect photon propagation in ice, but due to the high pressure, they transform into non-scattering hydrates at depths below  $\sim 1350$  m. Depth and wavelength dependent optical scattering and absorption can be probed by continuous and pulsed LED light sources which are installed on the optical modules [110] and which also serve for geometrical calibration. Results obtained from such measurements are shown in figure 3.5. Furthermore, by means of laser-based dust loggers which are lowered into water-filled boreholes immediately after drilling, dust structures with a resolution of a few mm could be identified [121]. Dust is, however, not the only obstacle impeding photon propagation: after lowering the string-mounted DOMs in the water-filled boreholes, the water slowly refreezes, forming an ice under stress with quite different properties than before. Borehole ice is modeled assuming a dense population of bubbles with corresponding scattering lengths of about 50 cm. These are shorter by about a factor of ten when compared to the ice layer with the highest dust concentration.

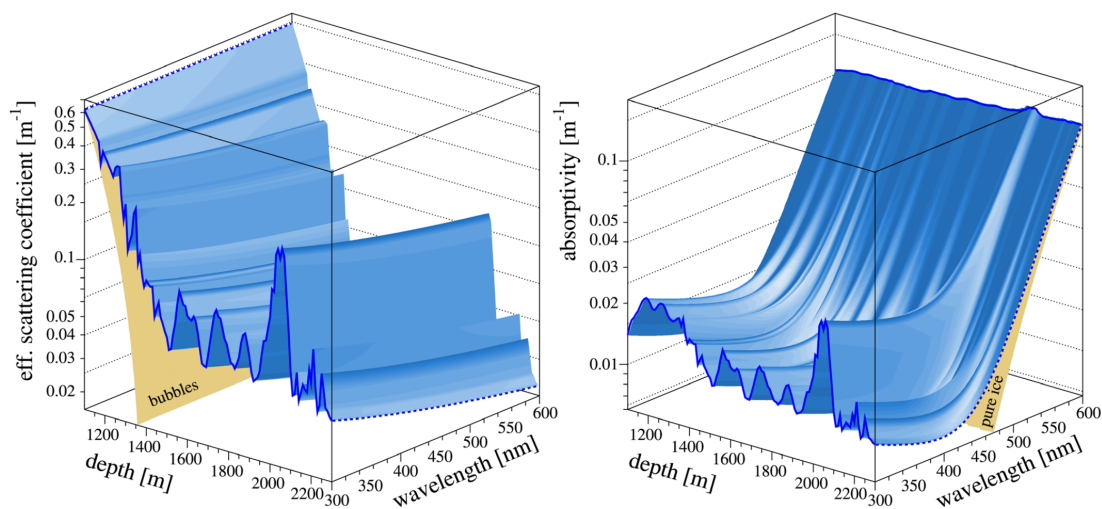


Figure 3.5.: Glacial wavelength and depth dependence of inverse scattering length (left) and inverse absorption length (right), shown as shaded surfaces and superimposed with the bubble contribution to scattering and the pure ice contribution to absorption. Light scattering off bubbles is independent from wavelength, as indicated by the dashed line at 1100 m depth (from [110]).

Data obtained from such measurements serves as phenomenological input for the ice model, which is based on the theory of electromagnetic radiation scattering off small particles, developed by Gustav Mie [128]. Depth and wavelength-dependent effective scattering and absorption coefficients (the reciprocals of the effective light transport

length according to Mie theory and the absorption length<sup>7</sup>, see figure 3.5) are then fitted by matching data obtained from LED flashers and the result of a photon propagation code, which tracks every photon in the ice. Optimized parameters are hence obtained for several fitting points and the whole set of the resulting values is ultimately spline-fitted and tabulated to be used in the simulation and reconstruction of IceCube events. Details about the six-parameter ice model which is employed in this work and is based on the assumption of isotropic dust concentrations, are provided in [129]. A tilt of the dust layers and a slight azimuthal dependence of the ice properties was incorporated in an updated version. For the fiducial volume of DeepCore, however, the effects on scattering and absorption parameters are marginal, as can be seen in [130].

Together with the absolute DOM efficiency, the ice properties pose one of the major sources of systematic uncertainties. This is discussed further in section 5.7.

### 3.4 Event Topologies and Energy Losses

Depending on the type of incident particle as well as its direction, energy and interaction vertex, the resulting light signature can differ significantly. Neutrino-induced charged and neutral-current interactions, including outgoing particles for different flavors, are illustrated in figure 3.6.

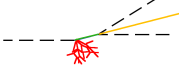
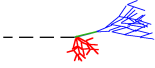
Interaction	Secondary particles	Detector signature
CC $\nu_\mu$		$\mu$ track and hadronic cascade
CC $\nu_\tau$		$\tau$ decays into $\mu$ ( $\sim 17\%$ b.r.)
		$\tau$ decays into $e$ / hadrons
CC $\nu_e$		Hadronic and EM cascades
NC $\nu_\alpha$		Hadronic cascade

Figure 3.6.: Distinction of possible neutrino interactions and related reaction products.

Neutrinos are depicted by dashed lines, muons are shown in orange, electrons and photons in blue and components of hadronic cascades in red (from [131]).

In order to understand the characteristic light topologies that emerge, it is instructive to consider which processes cause muons, electrons and hadrons to lose energy. Aside from

<sup>7</sup>The travel distance at which the photon density is reduced by a factor of  $e$ .

Cherenkov radiation, muons traveling through a medium are subjected to energy losses due to ionization, bremsstrahlung, photo-nuclear interactions and pair production<sup>8</sup>. The average energy loss can be expressed as a sum with energy-dependent weights:

$$-\frac{dE}{dx} = a(E) + b(E) \cdot E \quad , \quad (3.1)$$

where the first term accounts for ionization and the second term includes all radiative contributions.  $a$  and  $b$  are only slightly dependent on energy and can thus be approximated as constant, with  $a \approx 0.259 \text{ GeV m}^{-1}$  and  $b \approx 0.363 \cdot 10^{-3} \text{ m}^{-1}$  for ice [132]. With these values, a critical energy  $E_{\text{crit}}^\mu = a/b \approx 700 \text{ GeV}$  can be calculated for which ionization and radiation losses are equal. Taking into account that typical energies in this work are below  $100 \text{ GeV}$ , the overall energy loss can be well approximated by the value of  $a$ , setting  $b$  to zero.

Due to their small mass, electron and positron energy losses are dominated by bremsstrahlung. They radiate photons, which in turn produce electron-positron pairs when they react in matter, quite similar to an electromagnetic cascade in the atmosphere. The so-produced electrons and positrons are then again subjected to bremsstrahlung losses and the cascade only comes to a stop when ionization becomes the dominant process and all remaining energy is lost immediately. This happens around the critical energy  $E_{\text{crit}}^e$ . The cascade's elongation  $X$  can be related to the initial electron/positron energy  $E$  and the critical energy by:

$$X = X_0 \ln \frac{E}{E_{\text{crit}}^e} \quad , \quad (3.2)$$

where  $X_0$  is the *radiation length*, the distance over which an electron's energy is reduced to  $1/e$ . Typical values for ice are  $X_0 \approx 0.4 \text{ m}$  and  $E_{\text{crit}}^e \approx 80 \text{ MeV}$ . Electromagnetic cascades in IceCube therefore have elongations on the order of 2–5 meters and as such appear almost point-like in the coarse detector.

If neutrinos interact via deep-inelastic scattering, hadrons will be present in the final state. Hadrons also produce cascades, since they react with nuclei in the surrounding matter and subsequently produce more hadrons and leptons – where the latter can arise from charged or neutral pion decays and continue to cool down in the form of electromagnetic cascades. In principle, a hadronic cascade behaves quite similarly to an electromagnetic one. However, it contains heavier particles which have higher Cherenkov thresholds and uncharged particles like neutrons, which do not produce Cherenkov light at all. In addition, hadronic binding processes also contribute to energy loss. Therefore, the light yield from a hadronic cascade is significantly lower than the one from an electromagnetic cascade. Their ratio can be approximately expressed as [133]:

$$F = 1 - (E/E_0)^{-m} \quad , \quad (3.3)$$

where  $E$  is again the initial energy and  $m$  and  $E_0$  are material-dependent parameters. For ice, they have values of  $m \approx 0.16$  and  $E_0 \approx 0.19 \text{ GeV}$  [132], resulting in light yield

---

<sup>8</sup>A virtual photon can be radiated and subsequently converted to a real  $e^+e^-$  pair in the presence of matter.

fractions of about 0.6–0.8 when compared to electromagnetic cascades in IceCube’s low-energy regime.

Light yield parametrizations for electromagnetic and hadronic cascades as well as the one for track-shaped muonic events are given in [129]. Visualizations of selected  $\nu_e$  and  $\nu_\mu$  events at low and intermediate energies are shown in appendix C. Due to the small number of hit modules and the presence of a hadronic cascade, low-energy charged-current events from different neutrino flavors cannot be distinguished on an event by event basis and only marginally in a statistical sense [134].

At energies above one PeV,  $\nu_\tau$  CC interactions can initiate a visible double cascade: upon reaction a hadronic cascade is produced and after traveling about  $50 \text{ m} \cdot E_\tau/\text{PeV}$ , the  $\tau$  decays and produces another cascade in about 83 % of the cases. Such events have never been (undoubtedly) observed in IceCube. The different event signatures are illustrated in figure 3.7 by example of simulated high-energy events.

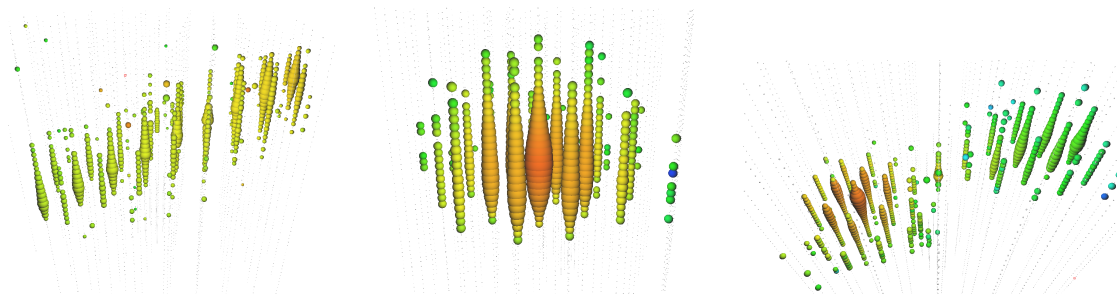


Figure 3.7.: Comparison of high-energy event signatures: a 117 TeV muon track (left), a few-PeV cascade (center) and a  $\nu_\tau$  induced double cascade event with 328 PeV energy (right) [135].

The better event topologies and thus different types of energy losses are understood, the better they can be modeled and simulated. The reverse process, where the incident particle’s energy, direction and interaction point are inferred from light patterns, is known as *reconstruction* and will be treated in the next chapter.



# 4

## A Resolution Estimator for Cascades

As far as the laws of mathematics refer to reality,  
they are not certain; as far as they are certain,  
they do not refer to reality.

---

Albert Einstein

Neutrino-induced charged particles and atmospheric muons passing through the IceCube detector leave a signature of Cherenkov light, which is subsequently detected by photomultiplier tubes. From the amount of light gathered at each optical module and the corresponding time information it is possible to infer the event's interaction vertex, incident direction and energy. For this effort it is essential to understand the ice properties and to be able to precisely simulate the propagation of Cherenkov photons. Given this knowledge, light sources at any position can be simulated and the PMT response at all optical modules can be used for a probability matching of different event hypotheses in reconstruction. For this purpose the simulation results are stored in large multi-dimensional histograms. Section 4.1 will treat likelihood-based event reconstruction by means of such tables, section 4.2 will introduce a method for assessing the uncertainty of individual best-fit reconstructions and sections 4.3 and 4.4 will present the implementation, performance and validation of this newly developed resolution estimator.

### 4.1 Event Reconstruction

As discussed in section 3.4, two main event topologies can occur in the detector: elongated tracks and spherically shaped electromagnetic or hadronic cascades. Assuming one of these as hypothesis, the most likely event parameter values can be calculated by software algorithms on the basis of spatial hit patterns, number of registered photons and their timing. Quick reconstructions are run at the South Pole and serve as input for online filters. Some of them only use the geometrical distribution of hits, while others minimize an analytic likelihood expression in order to find the best fit for the incident

particle [136]. More sophisticated reconstructions can only be performed in the North, with the purpose of being used for a later event selection and characterization. Since this work employs likelihood-based reconstructions and resolution estimation, this approach shall be discussed in more detail.

In general, the process of event reconstruction can be expressed as a problem of determining a set of event parameters  $\vec{\theta}$  from a set of experimentally measured values  $\vec{x}$ , which can be split in independent parts  $x_i$ . In our case the  $i$  typically correspond to different optical modules (or photon hits). The overall likelihood for a signature  $\vec{x}$  being caused by an event with parameters  $\vec{\theta}$  can be written as a product of probability densities [136]. For our purpose, these include the number of registered photons, which are assumed to follow Poisson distributions, with expectation values  $\mu_i(\vec{\theta})$ :

$$L(\vec{\theta}) = \prod_i \frac{\mu_i^{n_i}}{n_i!} e^{-\mu_i} \quad , \quad (4.1)$$

where  $n_i$  are the detected numbers of photons. Maximizing  $L$  by varying  $\vec{\theta}$  implies derivatives and therefore it is sensible to rather work with the likelihood's logarithm, which attains its maximum for the same value as  $L$ :

$$\ln L = \sum_i n_i \ln \mu_i - \mu_i - \ln(n_i!) \quad . \quad (4.2)$$

An expected number of (PMT) noise photons  $\rho_i$  is incorporated into the formalism and absorbed in  $\mu_i$  [137].

The reconstruction result is then obtained by numerically minimizing such (negative) log-likelihoods, employing codes like *SIMPLEX* [138] or gradient-descent algorithms [139]. In order to increase the probability of finding the global minimum, the minimization process can be iteratively repeated with varied input values. The number of performed iterations is typically between 2 and 32.

Photon expectations and their derivatives with respect to  $\theta_i$  (for assumed  $\vec{\theta}$  and event shape) can be obtained from tabulated results of light propagation simulations [140], which are smoothed by multi-dimensional spline-fits [141] to avoid artifacts which can arise from binning. More details about these quantities and their derivatives, as provided by splined tables, are presented in the next section. While impractical, it is also possible to perform the computationally intense photon Monte Carlo on an individual event basis and as such avoid pre-tabulation.

Aside from neutral-current interactions, it is important to understand that Cherenkov light is always produced by charged leptons, not by neutrinos. Therefore, the direction of the *lepton* is reconstructed, which can differ slightly from the neutrino direction due to reaction kinematics. For energies above 1 TeV the mean deviation is less than one degree, while at the lowest event energies in IceCube the kinematic angle can be as large as 10 degrees. An approximation is given by [142]:

$$\Delta\Omega = 0.7^\circ \cdot (E_\nu/\text{TeV})^{-0.7} \quad . \quad (4.3)$$

For cascades with their typical angular resolution of dozens of degrees this effect is sub-dominant, but poses an important statistical uncertainty for the directional determination of low-energy muon-neutrinos.

## 4.2 Likelihood-based Resolution Estimation for Cascades

As illustrated in the last section, a reconstruction result is a best-fit value, corresponding to a maximum in a multi-dimensional likelihood landscape. It is, however, also interesting how sharp the corresponding peak and thus how reliable the best-fit result is. The surrounding shape can be evaluated by resolution estimators and the resulting uncertainty is shown to correlate well with the actual resolution obtained from simulations (details in section 4.4). The so-obtained uncertainty information can be exploited by adjusting event weights in an unbinned likelihood analysis (see section 5.5).

Due to improved reconstruction techniques, cascades recently became more interesting for point-source searches, while traditionally being mostly studied in the context of diffuse fluxes, where pointing is irrelevant. Track-shaped events, however, are traditionally exploited when knowledge of the direction is needed and thus track estimators are established tools within IceCube [143, 144]. For this work, a Cramer-Rao based cascade estimator was developed, which due to its modular design can be employed in any IceCube analysis. This section will treat the underlying formalism.

As motivated in the last section, the likelihood for a set of parameters  $\vec{\theta}$  describing a measured pattern of light deposits under a given event hypothesis, can be written as a product of time-binned likelihoods for all optical modules that registered light, multiplied by a product of the likelihood of optical modules that did not register a (light) hit. The likelihood depends on a set of parameters  $\vec{\theta} = (\theta, \phi, x, y, z, E)$ ; the zenith, azimuth, interaction vertex and energy of the reconstructed event. These parameters are varied in order to find the maximum of the likelihood function.

Equation 4.1 is therefore refined by introducing time bins and furthermore by also including modules which did not register any light ( $n_i=0$ ):

$$L(\vec{\theta}) = \prod_i^h \left[ \prod_j^{b_i} \frac{\mu_{ij}(\vec{\theta})^{n_{ij}}}{n_{ij}!} \cdot e^{-\mu_{ij}(\vec{\theta})} \right] \cdot \prod_k^u e^{-\mu_k(\vec{\theta})} \quad . \quad (4.4)$$

where  $h$  is the number of hit modules,  $b_i$  is the number of time bins<sup>1</sup> for module  $i$  and  $u$  is the number of modules that were not hit. Here,  $n_{ij}$  is the number of measured photons in time bin  $j$ , which ranges from  $t_{\min}^j$  to  $t_{\max}^j$ .  $\mu_{ij}$  is the expectation value of  $n_{ij}$  and can be obtained from splined tables: for a given shape hypothesis and optical module, these tables provide the total (time-integrated) number of expected photons  $\mu_i(\vec{\theta})$ , as

<sup>1</sup>Bins comprise the whole time range of registered photons and do not necessarily have to be equal in size. In the following section the dynamic determination of temporal bins is illustrated.

well as the (normalized) probability density function  $p_i(\vec{\theta}, t)$  and its integrated form, the cumulative density function:

$$c_i(\vec{\theta}, t) = \int_0^t p_i(\vec{\theta}, t') dt' \quad . \quad (4.5)$$

$\mu_{ij}$  can be calculated from  $c_i$  as follows:

$$\begin{aligned} \mu_{ij}(\vec{\theta}) &= \mu_i(\vec{\theta}) \cdot \Delta c_{ij}(\vec{\theta}) \quad , \\ \Delta c_{ij}(\vec{\theta}) &= c_i(\vec{\theta}, t_{\max}^j) - c_i(\vec{\theta}, t_{\min}^j) = \int_{t_{\min}^j}^{t_{\max}^j} p_i(\vec{\theta}, t') dt' \quad . \end{aligned} \quad (4.6)$$

Two examples of the cumulative (photon) density function  $c_i$  at a far and a close optical module are shown in figure 4.1. For the latter, almost all registered photons are expected to arrive within  $\sim 500$  ns, while for distant modules arrival times can be distributed over a few  $\mu$ s due to light scattering.

In order to determine individual-event resolution estimates, one can either numerically evaluate the proximity of the likelihood maximum [143] or exploit the Cramer-Rao bound [145–147]. The latter states that the reciprocal (co)variance cannot exceed the amount of available information

$$(\text{cov}^{-1})_{lm} \leq F_{lm} \quad , \quad (4.7)$$

which is represented by  $F$ , the Fisher information matrix [148]. This information can be related to the likelihood by [149]

$$F_{lm} = \left\langle \frac{\partial \ln L(\vec{\theta})}{\partial \theta_l} \cdot \frac{\partial \ln L(\vec{\theta})}{\partial \theta_m} \right\rangle = - \left\langle \frac{\partial^2 \ln L(\vec{\theta})}{\partial \theta_l \partial \theta_m} \right\rangle \quad , \quad (4.8)$$

where the brackets  $\langle \rangle$  denote expectation values. The second relation strictly only holds if certain regularity conditions, e.g. with respect to the differentiability of the probability density functions, are met [147]. Using this relation,  $F$  is calculated first and inverted later to yield the covariance matrix. After applying the logarithm to the Poisson-based likelihood in equation 4.4 and performing the first partial derivative, the following expression is obtained:

$$\begin{aligned} \frac{\partial \ln L(\vec{\theta})}{\partial \theta_l} &= \frac{\partial \ln L(\vec{\theta})}{\partial \mu_{ij}(\vec{\theta})} \cdot \frac{\partial \mu_{ij}(\vec{\theta})}{\partial \theta_l} + \frac{\partial \ln L(\vec{\theta})}{\partial \mu_k(\vec{\theta})} \cdot \frac{\partial \mu_k(\vec{\theta})}{\partial \theta_l} \\ &= \sum_i^h \left[ \sum_j^{b_i} \left( \frac{n_{ij}}{\mu_{ij}(\vec{\theta})} - 1 \right) \frac{\partial \mu_{ij}(\vec{\theta})}{\partial \theta_l} \right] - \sum_k^u \frac{\partial \mu_k(\vec{\theta})}{\partial \theta_l} \quad . \end{aligned} \quad (4.9)$$

One can then apply the second derivative:

$$\begin{aligned}
 \frac{\partial^2 \ln L(\vec{\theta})}{\partial \theta_l \partial \theta_m} &= \frac{\partial \left( \frac{\partial \ln L(\vec{\theta})}{\partial \theta_l} \right)}{\partial \mu_{ij}(\vec{\theta})} \cdot \frac{\partial \mu_{ij}(\vec{\theta})}{\partial \theta_m} + \frac{\partial \ln L(\vec{\theta})}{\partial \mu_{ij}(\vec{\theta})} \cdot \frac{\partial^2 \mu_{ij}(\vec{\theta})}{\partial \theta_l \partial \theta_m} \\
 &\quad + \frac{\partial \left( \frac{\partial \ln L(\vec{\theta})}{\partial \theta_l} \right)}{\partial \mu_k(\vec{\theta})} \cdot \frac{\partial \mu_k(\vec{\theta})}{\partial \theta_m} + \frac{\partial \ln L(\vec{\theta})}{\partial \mu_k(\vec{\theta})} \cdot \frac{\partial^2 \mu_k(\vec{\theta})}{\partial \theta_l \partial \theta_m} \\
 &= - \sum_i^h \sum_j^{b_i} \left[ \frac{n_{ij}}{\mu_{ij}(\vec{\theta})^2} \frac{\partial \mu_{ij}(\vec{\theta})}{\partial \theta_l} \frac{\partial \mu_{ij}(\vec{\theta})}{\partial \theta_m} + \left( 1 - \frac{n_{ij}}{\mu_{ij}(\vec{\theta})} \right) \frac{\partial^2 \mu_{ij}(\vec{\theta})}{\partial \theta_l \partial \theta_m} \right] \\
 &\quad - \sum_k^u \frac{\partial^2 \mu_k(\vec{\theta})}{\partial \theta_l \partial \theta_m} .
 \end{aligned} \tag{4.10}$$

Forming the expectation value (equation 4.8) makes the Cramer-Rao bound independent on the actually measured  $n_{ij}$ :

$$\langle n_{ij} \rangle = \sum_{n_{ij}=0}^{\infty} n_{ij} \frac{\mu_{ij}(\vec{\theta})^{n_{ij}}}{n_{ij}!} e^{-\mu_{ij}(\vec{\theta})} = \mu_{ij}(\vec{\theta}) . \tag{4.11}$$

The Fisher information therefore assumes the form

$$F_{lm} = - \left\langle \frac{\partial^2 \ln L(\vec{\theta})}{\partial \theta_l \partial \theta_m} \right\rangle = \sum_i^h \sum_j^{b_i} \frac{1}{\mu_{ij}(\vec{\theta})} \frac{\partial \mu_{ij}(\vec{\theta})}{\partial \theta_l} \frac{\partial \mu_{ij}(\vec{\theta})}{\partial \theta_m} + \sum_k^u \frac{\partial^2 \mu_k(\vec{\theta})}{\partial \theta_l \partial \theta_m} . \tag{4.12}$$

The quantity  $\mu_{ij}(\vec{\theta})$  cannot be obtained directly from spline tables and is therefore substituted by  $\mu_i \cdot \Delta c_{ij}$  (compare to equation 4.6). The derivatives of  $\mu_{ij}$  are decomposed according to the product rule. Values for  $\mu_i$  and  $\Delta c_{ij}$  as well as their gradients can be directly obtained from the multi-dimensional spline surface by analytic evaluation. The expression for  $F_{lm}$  is then given by

$$\begin{aligned}
 F_{lm} &= \sum_i^h \sum_j^{b_i} \frac{1}{\mu_i(\vec{\theta}) \cdot \Delta c_{ij}(\vec{\theta})} \left( \frac{\partial \mu_i(\vec{\theta})}{\partial \theta_l} \Delta c_{ij}(\vec{\theta}) + \mu_i(\vec{\theta}) \frac{\partial \Delta c_{ij}(\vec{\theta})}{\partial \theta_l} \right) \\
 &\quad \cdot \left( \frac{\partial \mu_i(\vec{\theta})}{\partial \theta_m} \Delta c_{ij}(\vec{\theta}) + \mu_i(\vec{\theta}) \frac{\partial \Delta c_{ij}(\vec{\theta})}{\partial \theta_m} \right) + \sum_k^u \frac{\partial^2 \mu_k(\vec{\theta})}{\partial \theta_l \partial \theta_m} .
 \end{aligned} \tag{4.13}$$

For computational reasons, a simplified approach is employed, where modules without a hit are not considered for the calculation of the Fisher matrix ( $u=0$ ). Expected noise photons are added to  $\mu_{ij}$  with a rate of  $10^{-8}$  photons per ns, leading to a marginal reduction of the Fisher information.

### 4.3 Implementation of the Resolution Estimator

The Fisher information matrix, as derived in equation 4.13, is implemented using the *Python*<sup>2</sup> interpreted language in the context of IceCube’s C++-based simulation and analysis framework *IceTray* [150]. The module makes extensive use of tabulated and spline-smoothed photon tables (as introduced in section 4.1) and requires input information from a best-fit reconstruction (which corresponds to  $\vec{\theta}$ ) as well as the recorded photon hit series, from which information about the lit modules is extracted.

To ensure a quality result, a light pattern distributed over several modules is required; events need to have light deposits at five modules or more, which have to be located on at least two strings.

The number of time bins as well as their individual sizes can, in principle, be chosen freely. Since photon signals have variable widths and offsets, constant sampling distances would not be optimal to extract information from the relevant part of their shape. Instead, an equally spaced sampling of the  $c_i$  function values is attempted. Because there is no analytical inverse to  $c_i$ , a computationally efficient, iterative algorithm is implemented to determine the corresponding time values, which subsequently define the time bin sizes. The scan granularity (temporal step size), which is used to obtain the equidistant sampling points, is dynamically adjusted depending on the function shape at the current evaluation point. The algorithm starts at -10 ns with a coarse step size of 100 ns until  $c_i$  is above  $1/n_{\text{samples}}$ . In this interesting regime, the step size is reduced to 1 ns. After determination of the first two sampling points, the step size is subsequently adjusted to be a relative fraction of the time bin calculated last. The iteration is concluded, once all sampling points have been determined, i.e. once an ordinate level of  $c_i = 1 - 1/n_{\text{samples}}$  is reached. Time bin edges are subsequently saved in order to be used according to equation 4.13. The resulting sampling points for two examples are shown in figure 4.1. The total number of samples, which corresponds to the number of time bins, can be set by the user, where a standard value of 20 is chosen as a reasonable compromise between speed and precision.

The covariance matrix is obtained from the Fisher matrix by inversion, using the tools provided by the *numpy*<sup>3</sup> package. Before such an attempt is made,  $F_{lm}$  needs to be tested to be positive semidefinite, meaning that none of its eigenvalues is allowed to be negative. In very rare cases negative eigenvalues can occur due to limited computational precision. Such eigenvalues only slightly deviate from zero (the algorithm checks for eigenvalues between 0 and -0.001) and therefore a Tikhonov regularization [151] is carried out, as part of which a small constant  $\lambda$  is added to the diagonal;

$$F'_{lm} = F_{lm} + \lambda \cdot \mathbf{1} \quad , \quad (4.14)$$

---

<sup>2</sup>High-level, interpreted programming language, focusing on code readability and a compact syntax.

<sup>3</sup>A package for scientific computing with Python, which provides efficient data structures as well as e.g. linear algebra, random number and Fourier transform capabilities.

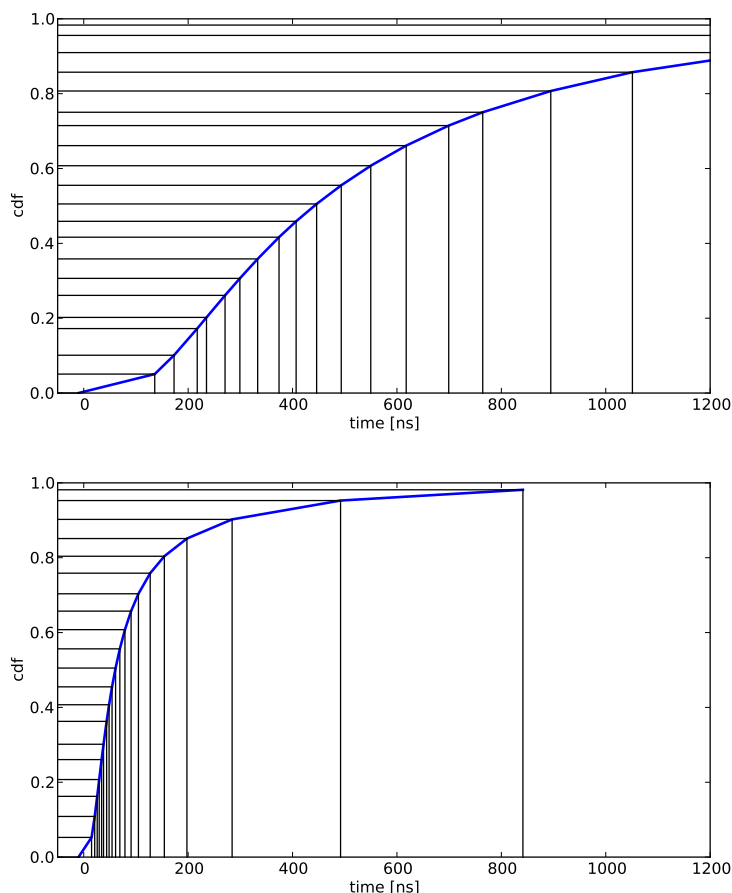


Figure 4.1.: Equidistant ordinate sampling of the cumulative photon density function, shown for modules with long (top) and short (bottom) distance to the event vertex.

just barely enough to make all eigenvalues positive. In the presented scope, the value of  $\lambda$  is simply determined by doubling the magnitude of the most negative eigenvalue.

The covariance matrix is symmetric and its entries are the lower bound covariance for the variables  $\theta_l$  and  $\theta_m$ . Diagonal entries ( $l = m$ ) are the variances of single variables, from which standard deviations  $\sigma_l$  can be obtained by forming the root. Directional uncertainties can thus be calculated for zenith and azimuth angles separately and can subsequently be combined to yield an angular uncertainty – which will be required later for the likelihood analysis (section 5.5). Such a combined opening angle is dependent on the event’s zenith. The resulting uncertainty is approximated by

$$\sigma_\Omega = \sqrt{\sigma_\theta^2 + (\sigma_\varphi \cdot \sin \theta_{\text{reco}})^2} \quad , \quad (4.15)$$

where  $\theta$  and  $\varphi$  are the zenith and azimuth angles in IceCube’s coordinate system<sup>4</sup>, ranging from 0 to  $\pi$  and 0 to  $2\pi$ , respectively. This simplified approach may cause a systematic

<sup>4</sup>By convention, incident particles with a zenith angle of zero come straight down from the atmosphere. The azimuthal origin corresponds to the Greenwich longitude.

over-estimation for larger uncertainty contributions. Such an effect would, however, automatically be straightened out by corrections applied later, as will be presented in the following section. The code is made available for collaboration-wide use [152].

## 4.4 Performance and Validation of the Resolution Estimator

The per-event execution time crucially depends on the number of optical modules (*channels*) that have registered light. Furthermore, execution times can vary depending on combinations of optical module and event hypothesis, due to the dynamic approach in determining temporal bin sizes (as explained in the last section). The algorithm requires about 60 ms per event and channel in a local test environment<sup>5</sup>, as can be seen in figure 4.2. Such a computational cost is justifiable at a sufficiently high level of event filtering (see section 5.3) and is by far less expensive than the employed cascade reconstructions – which are on the order of one minute per event. The rate of failures, which can occur due to a failed matrix inversion or an insufficient number of channels/strings, is typically below 1 %.

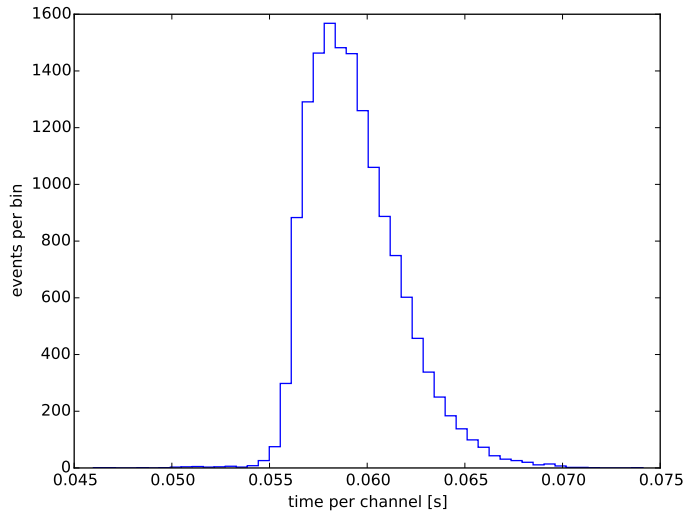


Figure 4.2.: Estimator runtime per event and channel for neutrino events originating from solar WIMP annihilations with candidate mass  $m_\chi = 100 \text{ GeV}/c^2$  and a pure  $W^+W^-$  branching.

For simulations, the estimated angular error can now be compared to the true angular uncertainty, defined as the opening angle between simulated and reconstructed direction. Such a comparison is provided in figure 4.3, for the case of a signal dataset. The estimate and actual resolution correlate well and have a similar spread. For larger uncertainties

<sup>5</sup>Intel Xeon E5530, Nehalem platform [153].

and resolutions, the correlation broadens, however. Owing to the spherical cascade signature, mis-reconstructions occur in some events.

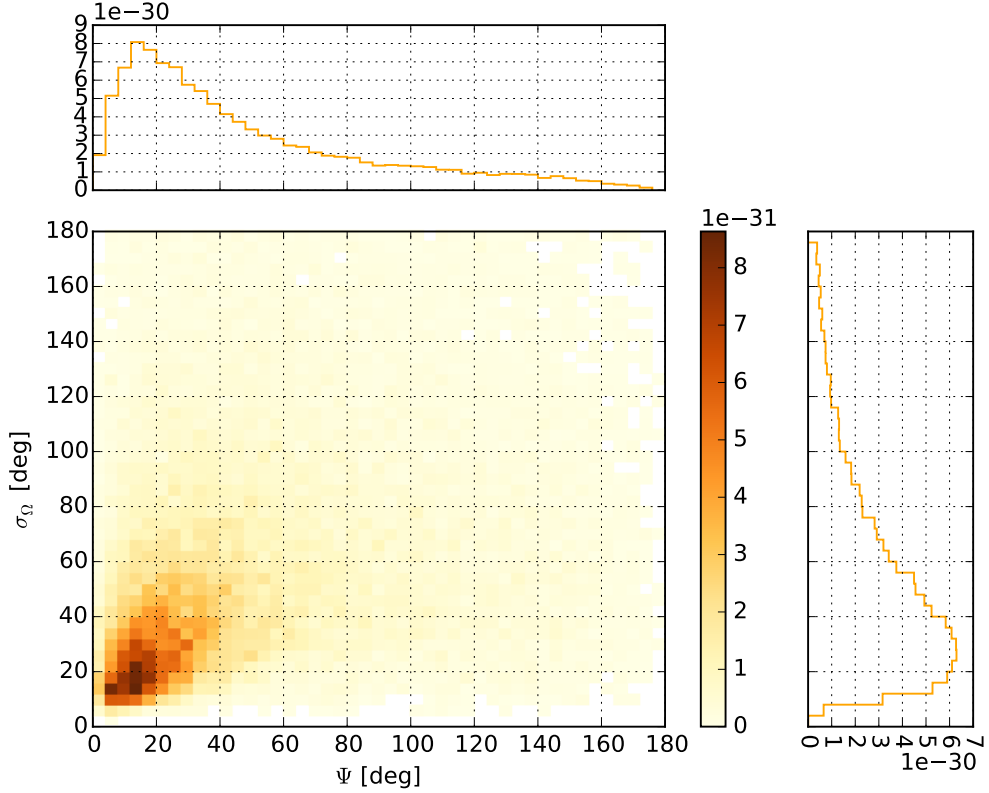


Figure 4.3.: Directional cascade resolution estimate (as defined in equation 4.15) against opening angle between true (simulated) and reconstructed direction. The dataset used consists of neutrinos originating from solar WIMP annihilations; assumed is a candidate mass  $m_\chi = 100 \text{ GeV}/c^2$  and a pure  $\tau^+\tau^-$  branching.

The ratio of the true angular uncertainty  $\Psi$  and the estimated angular error  $\sigma_\Omega$ , is the so-called *pull*, a useful quantity to study over- and under-estimations. A good estimate would yield pull values around one. As can be seen from figure 4.4, the estimate becomes more optimistic with increasing energy. In order to counteract such behavior, an energy-dependent correction is implemented such that the resulting pull median in any energy bin is forced to be 1 (see again figure 4.4). The correction is performed by means of signal simulation, with the motivation that remaining data events on a high filtering level have similar properties as the signal itself. The correction obtained reads as

$$f_{\text{corr}} = (0.430 \pm 0.010) \cdot \log_{10}(E_{\text{reco}}/\text{GeV}) + (0.137 \pm 0.020) \quad . \quad (4.16)$$

Consequently,  $f_{\text{corr}} \cdot \sigma_\Omega$  will be used as angular uncertainty for this analysis (see section 5.5) instead of  $\sigma_\Omega$ . Since the signal signatures (which the event filtering aims at preserving) can fundamentally differ for other studies, such corrections are analysis-dependent.

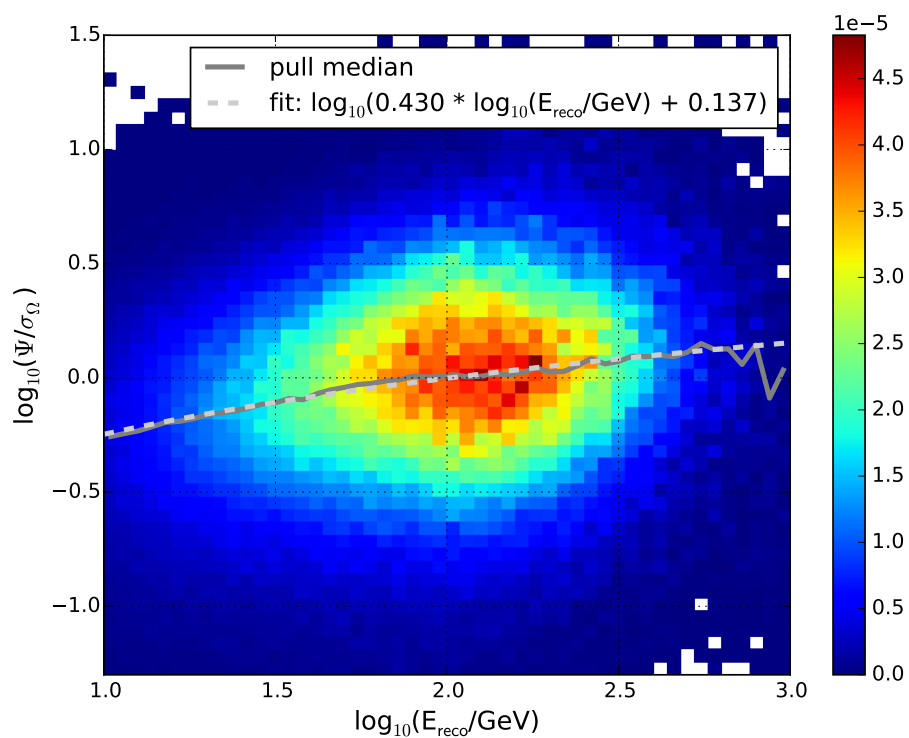


Figure 4.4.: Energy-dependent pull distribution for a neutrino signal induced by solar WIMP annihilations. The solid gray line shows the pull median for each energy bin, while the dashed line is the fit to the median values, which will later be used for correction. In order to determine this energy dependency as precisely as possible, data from all studied signal simulations (on a high selection level) are used as input.

# 5

## All-Flavor Solar Dark Matter Search

Freedom isn't for wimps.

---

Neal Boortz

Self-annihilating WIMP dark matter could accumulate in gravitational wells and produce a signal of detectable Standard Model particles. This analysis probes a neutrino signal originating at the center of the sun by exploiting data collected during one year with the IceCube neutrino observatory. The process of solar dark matter capture, the probability of dark matter annihilation and the magnitude of a resulting neutrino flux are discussed in section 5.1. The characteristics of experimental data, the quality criteria imposed and the Monte Carlo datasets employed are presented in section 5.2. Despite the immense shielding provided by the 1.5 km deep ice overburden, atmospheric muons still pose an overwhelming background which is larger by a factor of one million compared to the flux of neutrinos produced in the atmosphere. Section 5.3 explains the event filtering, which aims at extracting a potential signal including all neutrino flavors among the dominant background through a multi-level processing. Once the data rate is low enough to perform computationally expensive reconstructions, a machine learning algorithm in the form of boosted decision trees is used to reduce background further using carefully picked robust quantities which discriminate against the background (section 5.4). Up to this level, the background Monte Carlo undergoes the same event selection and constantly serves as a comparison. The likelihood analysis, which aims at classifying events according to direction, directional error and energy is presented in section 5.5.

The resulting sensitivity on a number of signal neutrinos can be translated into a sensitivity on the spin-dependent WIMP-proton elastic scattering cross-section by means of the signal simulation. The sensitivities are calculated for a set of candidate masses and annihilation channels and are presented in section 5.6. An interpretation of the results in a chosen supersymmetric framework is provided in chapter 6. A good understanding of the detector behavior is crucial, especially since signal data samples exist only in the form of simulated events. Uncertainties from detector components, cosmology as well as particle physics processes are discussed in section 5.7.

## 5.1 Neutrinos from Dark Matter Annihilation in the Sun

WIMP dark matter particles can accumulate in the sun by capture from the galactic halo and are depleted by self-annihilation or evaporation<sup>1</sup>. The latter effect is only relevant for candidate masses  $m_\chi \lesssim 4 \text{ GeV}/c^2$  [46] and is not treated in this work. As the sun passes through the halo of the Milky Way, dark matter particles may scatter off solar nuclei and lose energy (see section 1.4), subsequently orbiting the sun, and will be bound by its gravitational potential [45]. Subsequent scatterings will cause the WIMP particles to sink closer to the solar core, accumulate and potentially annihilate. The time evolution of the solar WIMP population  $N(t)$  can be expressed in terms of capture and annihilation:

$$\frac{dN}{dt} = C_C - C_A \cdot N^2 \quad , \quad (5.1)$$

where  $C_C = \Gamma_C$  is the capture rate, which is time-independent if the local WIMP halo density  $\rho_0$  remains constant over time.  $C_A N^2$  corresponds to twice the annihilation rate

$$\Gamma_A = \frac{1}{2} C_A \cdot N^2 \quad , \quad (5.2)$$

since the annihilation occurs pair-wise, destroying two WIMPs at one time.  $C_A$  depends on the velocity-averaged dark matter self-annihilation cross-section  $\langle \sigma_A v \rangle$  and furthermore on the density distribution of WIMPs in the sun [154]. The total capture rate  $\Gamma_C$  can be expressed in terms of radii-dependent contributions of solar elements  $i$  [155]:

$$\Gamma_C = \int_0^{R_\odot} 4\pi r^2 dr \sum_i \frac{dC_i(r)}{dV} \quad , \quad (5.3)$$

where  $R_\odot$  is the radius of the sun and

$$\frac{dC_i}{dV} = \int_0^{u_{\max}} du \frac{f(u)}{u} w \cdot \Omega_{v,i}(w) \quad (5.4)$$

is the WIMP capture rate from element  $i$  per solar shell volume [44]. For the element composition, the standard solar model [156] is assumed.  $u$  is the WIMP velocity in the galactic frame and  $u_{\max}$  is the velocity at which the WIMP would reach the escape velocity after scattering. The WIMP velocity at a given interaction point is  $w = \sqrt{u^2 + v^2}$ , where  $v$  is the escape velocity at this point.  $\Omega_{v,i}(w)$  is the capture probability per unit time for element  $i$  (details can be found in [157]) and  $f(u)/u$ , the velocity dependence of the WIMPs, is assumed to follow a Maxwell-Boltzmann distribution with velocity dispersion  $v_d$ :

$$\frac{f(u)}{u} = \sqrt{\frac{3}{2\pi}} \frac{n_\chi}{v_d v_\odot} \left[ \exp\left(-\frac{3(u - v_\odot)^2}{2v_d^2}\right) - \exp\left(-\frac{3(u + v_\odot)^2}{2v_d^2}\right) \right] \quad , \quad (5.5)$$

where  $v_\odot$  is the sun's velocity relative to the halo and  $n_\chi = \rho_0/m_\chi$  is the local WIMP number density. Typical values are  $v_d = 270 \text{ km/s}$  and  $v_\odot = 220 \text{ km/s}$ , assuming

<sup>1</sup>Upon scattering with solar nuclei, escape of already-captured particles can occur once they receive enough energy to reach the solar escape velocity.

a common galactic halo model [158]. For the local dark matter density a value of  $\rho_0 = 0.39 \text{ GeV c}^{-2} \text{ cm}^{-3}$  is assumed [159, 160].

Solving equation 5.1 for  $N$  yields the annihilation rate at a given time  $t$ :

$$\Gamma_A = \frac{1}{2} C_C \tanh^2(t/\tau) \quad , \quad (5.6)$$

where  $\tau = 1/\sqrt{C_C C_A}$  is the time scale at which equilibrium between capture and annihilation is reached. For the age of the sun,  $t_\odot \approx 4.5 \cdot 10^9$  years, equation 5.6 has converged to

$$\Gamma_A = \frac{1}{2} C_C \quad (5.7)$$

and a potential neutrino signal is thus at full strength [21]. The annihilation rates, and as such also the respective neutrino signal, are therefore determined by the elastic scattering cross-section (which determines the capture rate) and *not* by the annihilation cross-section.

The total capture rate is a sum of spin-dependent (SD) and spin-independent (SI) contributions (see section 1.4 for their distinction). Since the sun mostly consists of hydrogen, solar capture is dominated by spin-dependent interactions and therefore the total capture rate is approximated to be exclusively caused by spin-dependent scattering off hydrogen<sup>2</sup> ( $C_C = C_C^{\text{SD}}$ ), neglecting a spin-independent contribution. Such an approach is further supported by supersymmetry, where spin-independent scattering cross-sections are typically smaller by a factor of about 1000 (see section 6.4). Although resonant enhancement of heavier elements can boost SI cross-sections significantly, elements like oxygen or carbon only account for about 1% of the solar mass.

An approximation of the spin-dependent capture rate, which illustrates some of its dependencies and sensitivity to systematic uncertainties, is given by [161]:

$$C_C^{\text{SD}} \approx 3.35 \cdot 10^{20} \text{ s}^{-1} \left( \frac{\rho_0}{0.3 \frac{\text{GeV}}{\text{c}^2 \text{ cm}^3}} \right) \left( \frac{270 \frac{\text{km}}{\text{s}}}{v_d} \right)^3 \left( \frac{100 \frac{\text{GeV}}{\text{c}^2}}{m_\chi} \right)^2 \left( \frac{\sigma_{\text{SD}}^{\chi p}}{10^{-6} \text{ pb}} \right) \quad , \quad (5.8)$$

where  $\sigma_{\text{SD}}^{\chi p}$  is the spin-dependent cross-section for elastic WIMP scattering off protons. Especially for lower WIMP masses, this approximation significantly deviates from the precise results obtained by the numerical integration implemented in [162], which includes integrals over the galactic halo velocity distribution, the radii of the sun taking into account kinematic effects and the momentum transfer of the interaction considering nuclear form factors. The numerical approach is therefore preferred over the approximation when it comes to the calculation of spin-dependent scattering cross-sections from annihilation rate sensitivities – this procedure will be discussed in section 5.6.

WIMP annihilation is possible by means of multiple channels, subsequently producing a variety of Standard Model particles. However, only neutrinos are able to escape the sun.

<sup>2</sup>The quantitative error introduced by such an approximation, however, is small and will be discussed in the context of analysis uncertainties in section 5.7.

In order to obtain their energy spectra for specific annihilation channels, the PYTHIA code is involved [162, 163]. Because of hadronization losses prior to decay, WIMP annihilations to quark pairs ( $\chi\chi \rightarrow q\bar{q}$ ) result in softer<sup>3</sup> neutrino spectra than annihilation to gauge bosons or leptons.

As already motivated in section 1.4, a pure branching into a generic hard ( $\tau^+\tau^-$ ) and soft channel ( $b\bar{b}$ ) is assumed to attain an upper and lower sensitivity limit for models with mixed branching ratios. For comparison with other results, the  $W^+W^-$  channel is also considered. The candidate mass range that was chosen (35 to 1000 GeV/ $c^2$ ) is motivated by the supersymmetric framework (see chapter 6) and also by the use of the DeepCore subdetector, for which the employed all-flavor approach is most beneficial [164].

Neutrinos originating from solar dark matter annihilations are propagated through the sun and through space using a full three-flavor oscillation approach [81]. This code also describes the reaction of neutrinos in the IceCube detector by means of CC and NC interactions and provides them with respective weights. These do not assume a definite annihilation rate and thus are given in units of “number of events per annihilation”. The resulting distributions form the basis for the signal simulation used in this work. Energy histograms for such events are shown in figure 5.1, using the example of a  $m_\chi = 100$  GeV/ $c^2$  WIMP candidate.

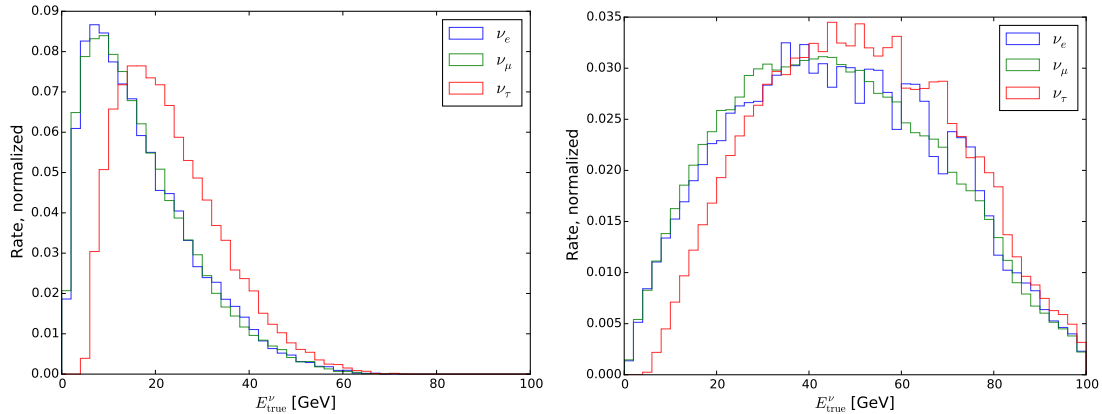


Figure 5.1.: Energy spectra for neutrinos originating from WIMP annihilation, assuming a candidate with a mass  $m_\chi = 100$  GeV/ $c^2$ . The annihilation channels shown are  $b\bar{b}$  (left) and  $\tau^+\tau^-$  (right).

Signal events from neutral-current interactions are not considered in this study. While such interactions would increase signal event rates by one third [46] (see cross-sections in figure 2.8), these events, due to their variable missing energy, would be harder to distinguish from background in the likelihood approach that was chosen (see section 5.5). Furthermore, directional reconstruction and its uncertainty estimation would suffer from the significantly reduced light deposition in the detector.

<sup>3</sup>In this context *hard* and *soft* refer to the energy distribution of the later-produced neutrinos. Softer spectra have lower energies on average.

## 5.2 Experimental and Monte-Carlo Datasets

A neutrino signal from dark matter annihilations in the sun, as introduced in the previous section, is modeled by the *WimpSIM* code [81] and events with their respective parameters are imported in the IceCube analysis framework *IceTray* [150]. The subsequently employed low-level event processing chain (see appendix B) is the same as for atmospheric background datasets. As mentioned before, the Monte-Carlo signal datasets are used as a counterpart for experimental data throughout the event selection, especially for machine learning in the form of *Boosted Decision Trees* (BDTs) (details are provided in section 5.4) and the likelihood minimization procedure (section 5.5), where scrambled<sup>4</sup> experimental data serve as samples of pure background.

Background Monte-Carlo (MC) datasets are used to test the understanding of the detector (ice properties, PMT response, etc.) as well as the models for atmospheric background, i.e. secondary muons and neutrinos, as introduced in section 2.3. In case of a perfect modeling, the summed Monte-Carlo sets should match the data. A good description of experimental data by the simulation furthermore establishes trust in the correct magnitude of the simulated signal, which undergoes the exact same processing chain. Background MC can be employed to optimize the event selection and achieve a good background discrimination.

Background from atmospheric muons is simulated in the energy range from 600 to  $10^{11}$  GeV for primary protons and nuclei, using the CORSIKA code [165], and weighted according to the model presented in [166]. The muons are then propagated through the ice and bedrock considering stochastic and continuous energy losses [167]. Atmospheric neutrinos are simulated with a program called *Neutrino Generator*, an adoption of the ANIS code [168], which considers neutrino-nucleon interaction cross-sections from the CTEQ5 project [169] for neutrino propagation through the earth and the ice. The flux weighting is performed according to the atmospheric model described in [170]. 10% of such an atmospheric neutrino dataset are contaminated with CORSIKA events to account for coincidences<sup>5</sup>. For the low-energy regime ( $\lesssim 200$  GeV), a continuous transition to events generated by the GENIE code [95] is implemented, which offers an improved description of interactions below  $\lesssim 50$  GeV. The background datasets described above are provided in the frame of IceCube’s distributed mass production of Monte Carlo datasets – which takes care of the low-level detector simulations. Implemented light yield parametrizations [129] for hadronic cascades are only correct down to about 30 GeV. Below this threshold, particles are passed to the interfaced GEANT4 code [171] to simulate the indi-

<sup>4</sup>In order to cover a possible signal in experimental data (and subsequently use the latter as a background sample), event azimuth information is replaced by random values, distributed uniformly across the whole azimuth range. This process is referred to as *scrambling*. Due to the unique detector location, the background has a uniform azimuth distribution in the first place and thus no data characteristics are affected by scrambling.

<sup>5</sup>Coincident events can significantly disturb reconstructions; an algorithm aiming at detecting and removing coincident events is described in the scope of selection level 5.

vidual propagation. This approach is also followed for the simulation of signal datasets (see appendix B).

Experimental data, on the other hand, have to be purged from anomalies, like erroneous runs and misbehaving optical modules, which are not accounted for in the simulation. A first level of quality is established by close monitoring of the detector data and further quality criteria are imposed at a later point. In addition to runs which failed the monitoring criteria and thus were marked as *bad*, short runs (less than 8 hours) are excluded, since an unplanned interruption usually is related to unexpected detector behavior. Furthermore, all strings are required to be functional for the most part, meaning that their fraction of idle DOMs has to be less than 25%. In a few cases, one or more strings are offline due to failure, which can crucially affect veto algorithms, reconstruction and the code: runs with such string inactivity are therefore excluded<sup>6</sup> for this analysis. The resulting data sample has a live time of about 304 days. This work is an exploratory analysis and therefore uses only one year of detector data. Run-based data rates for selection levels 3–6 are shown in figure 5.2. The noticeable rate increase and short-term spike are caused by a DOM software change on July 26<sup>th</sup> 2011. For higher selection levels, however, these effects – as well as the seasonal variation impact – become irrelevant due to statistical fluctuations.

### 5.3 Event Selection

The computationally expensive event reconstruction and likelihood analysis, which are essential to this study, can only be performed on a strongly reduced data sample. Therefore, a multi-step event filtering is implemented which achieves a significant background reduction and thus allows for the time-consuming calculation of more advanced variables. After each such step, the remaining data sample is saved and labeled with *level* numbers in an ascending order. Experimental data and Monte Carlo datasets are equally subjected to this event selection. For the former, a set of quality criteria is additionally imposed (see previous section), which accounts for unusual detector behavior that is not represented in simulated samples. Monte-Carlo starts with individual events on *generator* level, where merely the event parameters and the type of particle(s) is known. These events, as well as the Cherenkov photons they induce, have to be propagated through the ice and the resulting PMT response as well as noise have to be simulated. Subsequently, as introduced in section 3.2, the resulting hits have to be checked for coincidences and trigger/filter conditions. This whole simulation chain is referred to as *low-level* processing and presented in appendix B for the example of signal Monte-Carlo.

The following paragraphs will treat each selection level by presenting the nature of the cut variables employed, their background discrimination power and the cut values subsequently applied. The first levels, up to level 5, aim at drastically reducing background

---

<sup>6</sup>The following data-taking runs are otherwise okay, but fail to meet the criterion for zero bad strings and thus are consequently excluded for the analysis: 119034, 119036, 119581, 119588, 119627, 119628, 119634, 120131.

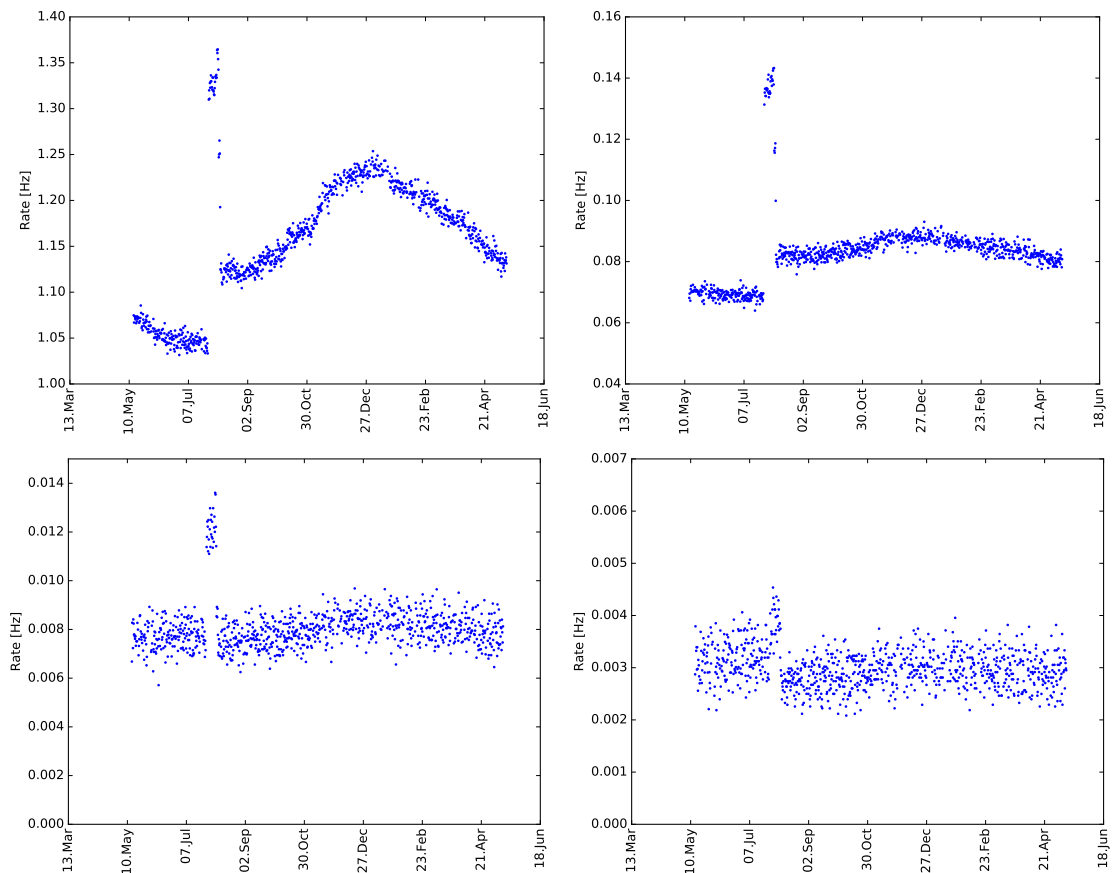


Figure 5.2.: Run-based rates for experimental data with quality criteria being fulfilled.

Shown from top left to bottom right are rates on selection levels 3–6. See text for remarks on the distinct rate characteristics. Level 6 rates are shown for the example of a  $100 \text{ GeV}/c^2$  candidate (the event selection is split into multiple streams at selection level 6, as will be explained shortly).

from atmospheric muon events. Therefore, a generic spectrum of atmospheric neutrinos can as well be used as a “signal counterpart” for background discrimination. Signal distributions for a chosen channel/mass combination are shown for reference. As such, parts of the event selection are shared with a different low-energy focused analysis [172], especially on level 4 and 5. After level 5, the rate of atmospheric muons is roughly reduced to the rate of atmospheric neutrinos and a WimpSIM-based signal Monte-Carlo for six different candidate masses is employed in a machine learning algorithm, resulting in multiple event selection streams. On level 7, in preparation for the likelihood analysis, the event samples are further split depending on the annihilation channel.

The discussion of the selection levels is organized as follows: cuts are applied based on existing variables. Before level  $n$  is written out, the (potential) cut variables for level  $n + 1$  are calculated and included in the output. In this way, their distributions can be studied in order to find the optimal cut value. In the following paragraphs the cut

variables with their respective cut values are presented. For a given level, these cuts were applied beforehand. The included figures, however, show distributions at the *previous* level so that the portions which were cut away can also be viewed.

The WIMP signal MC and thus the differences between the various candidate masses will only be relevant from level 6 onward. Therefore, the presented figures (5.3 et seq.) show signal rates only for reference. A candidate mass of  $100 \text{ GeV}/c^2$  and an annihilation rate of  $10^{25}$  annihilations per second are assumed. Since distributions are shown for previous cut levels, the redundancy or complementarity of the various cut variables are not obvious from the plots. At selection level 6, a machine-learning algorithm is employed, which considers inter-variable dependencies.

In order to study the agreement between experimental data and simulation, it is instructive to compare the black (data) and blue (dominant muon background) lines. Only at higher selection levels the contributions from atmospheric neutrinos also become relevant. Discrepancies are symptoms of imperfect simulation. Their origin and relevance will be discussed in the event selection summary.

## Level 1

Data events that have passed one or more online filters, are transmitted to storage in the North by satellite and not subjected to further filtering before being stored.

## Level 2

Events undergo likelihood-based reconstructions and hit cleaning; for a discussion of the latter see section 3.2. No cuts are applied at this level, exact PMT waveforms are however purged from the data in order to save storage space. Level 2 marks the starting point for most IceCube analyses.

## Level 3

This selection level is provided by IceCube's low-energy working group as a basis for DeepCore-focused analyses and is adopted for this work. Background from atmospheric muons is reduced by a factor of roughly 500, while about one third of atmospheric and signal neutrinos can be retained. For this analysis, data samples on this level are loaded from the common IceCube storage and were subsequently processed on local resources. The variables exploited and the respective cut values are listed below.

- **C2QR6 > 0.4**

This variable holds the fraction of charge, deposited within the first 600 ns, relative to the total charge in the given sRT-cleaned pulse series (with the first two hits removed). This cut aims at removing atmospheric muon background, since muons

deposit light over long distances and times and thus produce rather small charge ratios.

- **CausalVetoPE < 7 PE**

The DeepCore filter, as described in section 3.2, is rerun on the basis of pulses which contain detailed information on the arrival times of individual photons in contrast to the inclusive hits. The charge deposition in the veto region [124] is required to be less than 7 photo electrons in order to veto against atmospheric muons.

- **ChargeRatio < 1.5**

ChargeRatio is the ratio of charges deposited in the veto and non-veto region of the detector. The latter corresponds to the fiducial volume of DeepCore. This variable is calculated on the basis of the sRT pulse series. A cut threshold of 1.5 is imposed in order to achieve further discrimination against muon background.

- **MicroCountHits > 2**

A dynamic time window with a size of 300 ns is established across a statically cleaned pulse series in a way that the contained amount of hits is maximized. In order to discriminate against noise, a minimum of 3 hits within this time window is required.

- **MicroCountPE > 2 PE**

For additional noise discrimination a minimum charge of 2 PE is required in the aforementioned dynamic time window.

- **NAbove200 < 12 PE**

The total charge in the detector part above -200 m <sup>7</sup> on the basis of an uncleaned pulse series is required to be below 12 PE to further reduce background from atmospheric muons.

- **NoiseEngine criterion**

This algorithm targets noise reduction. Based on an uncleaned pulse series, all possible links between participating DOMs are constructed and checked for directional correlation in a binned approach, employing a spherical pixelization routine. At least one bin is required to have three or more entries in order to characterize an event as physical so that it passes the NoiseEngine cut.

- **RTVeto250PE criteria**

On the basis of a cRT-cleaned pulse series with settings  $R = 250$  m and  $T = 1000$  ns, the largest cluster in the veto region is identified and its total charge deposit is compared to the one of the DeepCore fiducial volume. If the latter is below 100 PE, the charge deposit in the veto region is required to be lower than 4 PE. Between 100 and 150 PE, the maximal veto region charge is 6 PE and 10 PE is the threshold

---

<sup>7</sup>In the IceCube coordinate system the  $z$  axis is directed towards the surface with its origin at the geometrical center of the IceCube volume.

for veto region charge deposits in the range of 150 to 200 PE. Above 200 PE, no cut is applied.

- **VertexGuessZ < -120 m**

An approximate  $z$  coordinate estimate of the interaction vertex is provided by the  $z$  position of the first-lit module in a sRT-cleaned pulse series. The vertex thereby obtained is required to be located in the bottom part of the detector in order to discriminate against down-going muons.

## Level 4

This cut level is designed to achieve a significant reduction of atmospheric muon background. Figures 5.3–5.5 show the cut variable distributions on the previous selection level, with marked cut values. Once applied, the passing events constitute level 4.

- **nCh<sup>sRT</sup> ≥ 6**

In order to achieve quality reconstructions for the variables below, a minimal set of geometry information in the form of six lit DOMs or more is required. The distribution of this variable on selection level 3 and the corresponding cut value are shown in figure 5.3. The obvious discrepancy at low numbers of channels originates from imperfect noise simulation – this issue is discussed in the event selection summary.

- **cos( $\theta_{\text{reco}}^{\text{LineFitDC}}$ ) < 0.2**

The *LineFit* algorithm [173] is a simple analytical method for reconstructing muon tracks. The muon is assumed to move along a straight line  $\vec{r}(t) = \vec{r}_0 + \vec{v} \cdot t$  with a velocity  $\vec{v}$ . The fact that light is emitted under the Cherenkov angle is ignored and so are the ice properties. The agreement of this hypothesis with the measurement is quantified by a  $\chi^2$  value, which considers the track distance from the hit modules  $\vec{r}_i$ , at a given time  $t_i$ :

$$\chi^2 = \sum_{i=1}^{N_{\text{hit}}} (\vec{r}_i - \vec{r}_0 - \vec{v} \cdot t_i)^2 \quad . \quad (5.9)$$

The  $\chi^2$  minimum can be determined analytically, which results in a runtime benefit of a factor larger than  $10^3$  compared to likelihood-based reconstructions where the fit result has to be obtained by means of a numerical minimization. This fit is therefore calculated online and often serves as a background discrimination tool at low selection levels and furthermore as a first-guess seed for more sophisticated reconstruction algorithms. For the cut applied, the algorithm is rerun for a DeepCore subset of pulses and a subsequent cut value of 0.2 is chosen, which discards the major part of downward-directed atmospheric muons (see figure 5.4).

- **cos( $\theta_{\text{reco}}^{\text{SPE2DC}}$ ) < 0.2**

During an event, every lit module may register one or more photons. The likelihood-based *SPE* (“single photo electron”) reconstruction only considers the first reg-

istered photon, with the motivation that it is the least scattered one and thus contains most of the information. To obtain improved directional information, a double-iterative SPE reconstruction is performed using a DeepCore subset of the pulse series and a cut value of 0.2 is imposed (see figure 5.5). This cut has a significant overlap with the previously described LineFit cut, but is able to reconstruct tracks more precisely and thus discard a larger portion of the downward oriented atmospheric muons. The extension of the SPE algorithm, which considers all registered photons, is called *MPE* (“multi photo electron”). Exploiting the additional information, a better reconstruction can be achieved, however, usually only for event energies above several TeV [144].

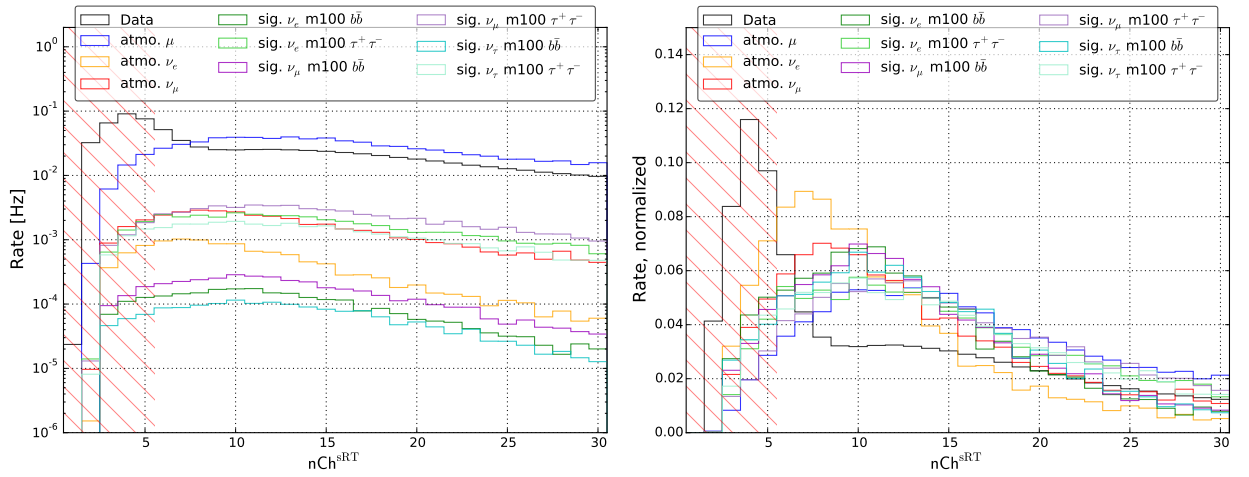


Figure 5.3.: Distribution of the  $nCh^{sRT}$  variable on selection level 3 and region rejected by the cut (dashed red).

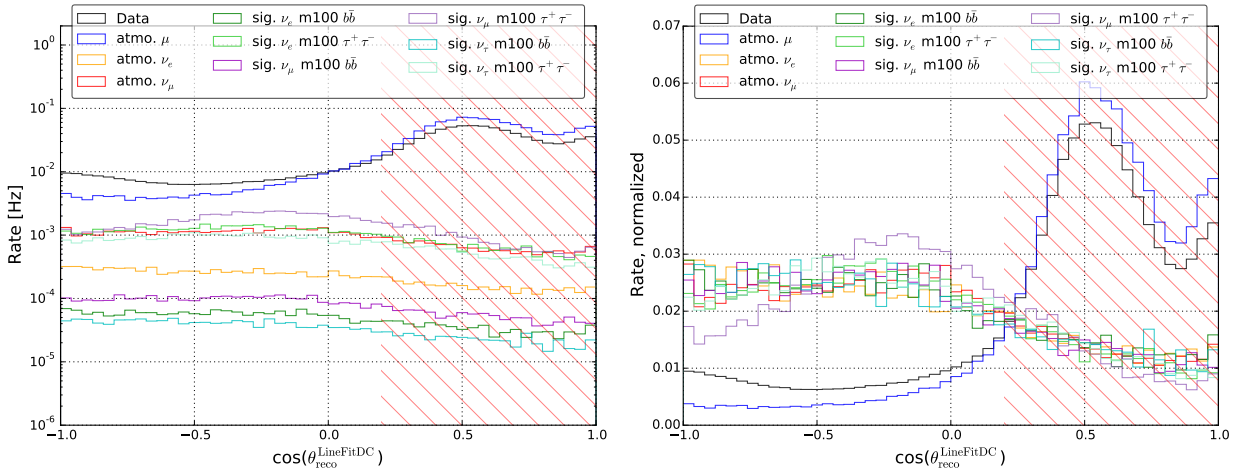


Figure 5.4.: Distribution of  $\cos(\theta_{\text{reco}}^{\text{LineFitDC}})$  on selection level 3 and region rejected by the cut (dashed red). The spike in the right-most bin is caused by failed reconstructions. The zenith angle is attributed a value of zero in such cases.

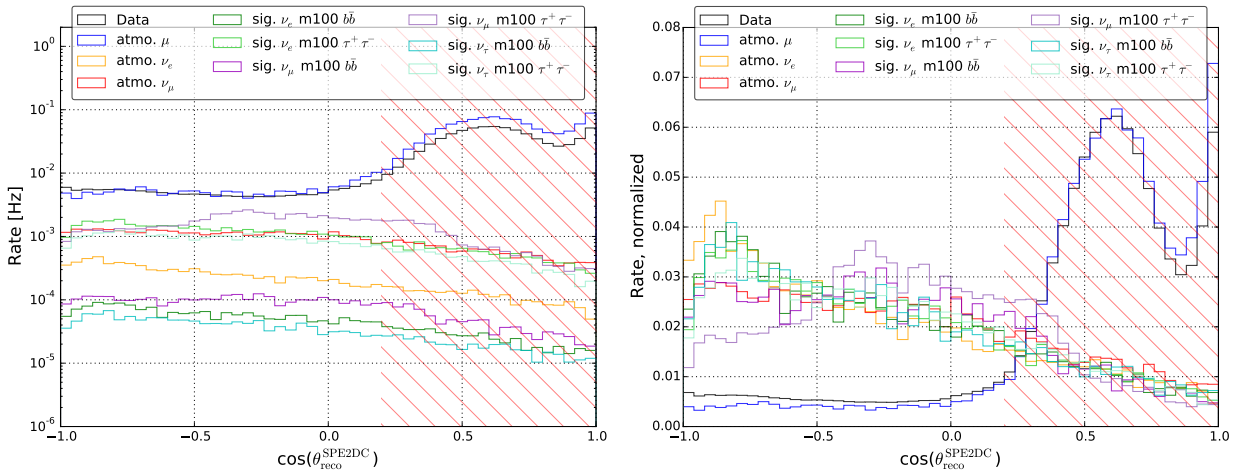


Figure 5.5.: Distribution of  $\cos(\theta_{\text{reco}}^{\text{SPE2DC}})$  on selection level 3 and region rejected by the cut (dashed red). The spike in the right-most bin is caused by failed reconstructions. The zenith angle is attributed a value of zero in such cases. The distribution of atmospheric  $\nu_{\mu}$  illustrates nicely that upward-directed track events are clearly favored in low-energy analyses, since a significant amount of downgoing  $\nu_{\mu}$  are rejected together with atmospheric muons.

## Level 5

This selection level aims at a further rejection of background from noise and atmospheric muons. In addition, a topological algorithm tries to identify disjoint clusters in the light patterns and as such tries to identify and discard coincident events. The cut variables with their corresponding cut values are listed below.

- $n\text{Ch}_{\text{veto}}^{\text{cRT}} \leq 1$

This variable holds the number of lit modules in the veto region (defined as the whole detector except the fiducial volume of DeepCore), as found in a cRT-cleaned pulse series, is required to be one or zero. While this cut rejects a significant amount of remaining atmospheric muons, it also cuts away a severe portion of the signal. The distribution of this variable, as well as the cut applied, are illustrated in figure 5.7.

- $n\text{Ch}_{\text{DC}}^{\text{cRT}} \geq 6$

In order to ensure that quality event reconstructions on the basis of light deposits in the fiducial volume of DeepCore are possible, each event is required to have at least six lit modules within this volume. The distribution of this variable, as well as the applied cut, are illustrated in figure 5.8.

- **TT criterion**

Multiple atmospheric muons can pass the detector simultaneously and thus significantly impact reconstructions, since the latter assume exactly one incident particle (illustrated in figure 5.6). The *Topological Trigger* algorithm aims at identifying such disjoint clusters. Hits that are attributed to the same cluster have to meet the following separation criteria: if on the same string, they must not be separated by more than 15 modules. The allowed vertical spacing is 150 m or less. Furthermore, hits belonging to the same cluster have to be causally connected by fulfilling the condition  $\Delta t - \Delta r/c < 450$  ns (where  $\Delta t$  is their time difference and  $\Delta r$  is their spatial distance). The cut requires that there is exactly one identified cluster. Zero identified clusters are attributed to pure-noise events.

- $v_{12}/v_{13} > 0.5$

This variable targets noise, but is also suited for muon discrimination. Considering the spatial and temporal distances between the first and second as well as the first and the third HLC hit (on different channels), one can define a velocity ratio:

$$\frac{v_{12}}{v_{13}} = \frac{d(\text{HLC}_1, \text{HLC}_2)/\Delta t(\text{HLC}_1, \text{HLC}_2)}{d(\text{HLC}_1, \text{HLC}_3)/\Delta t(\text{HLC}_1, \text{HLC}_3)} \quad , \quad (5.10)$$

where  $d$  is the distance of modules that recorded the specified HLC hits and  $\Delta t$  is the hits' time difference. Ratios significantly smaller than one can be caused by noise or very elongated tracks, while ratios around one are caused by spherical light patterns induced by cascades and low-energy events in general, since the corresponding lit DOMs are usually close to each other and therefore only little

scattering of Cherenkov photons is expected. The distribution of this variable, as well as the applied cut, is illustrated in figure 5.9.

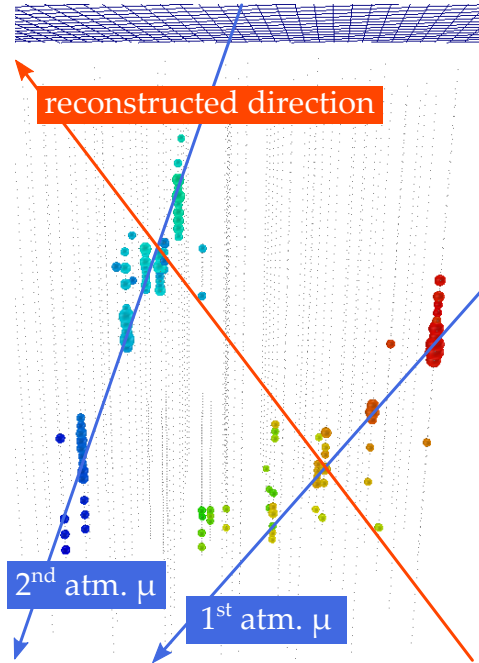


Figure 5.6.: Illustration of a coincident muon event with corresponding incident angles. Since event reconstruction is always based on a single-event hypothesis, the marginal temporal separation of the two events causes the reconstruction to fit a perpendicular direction (from [172]).

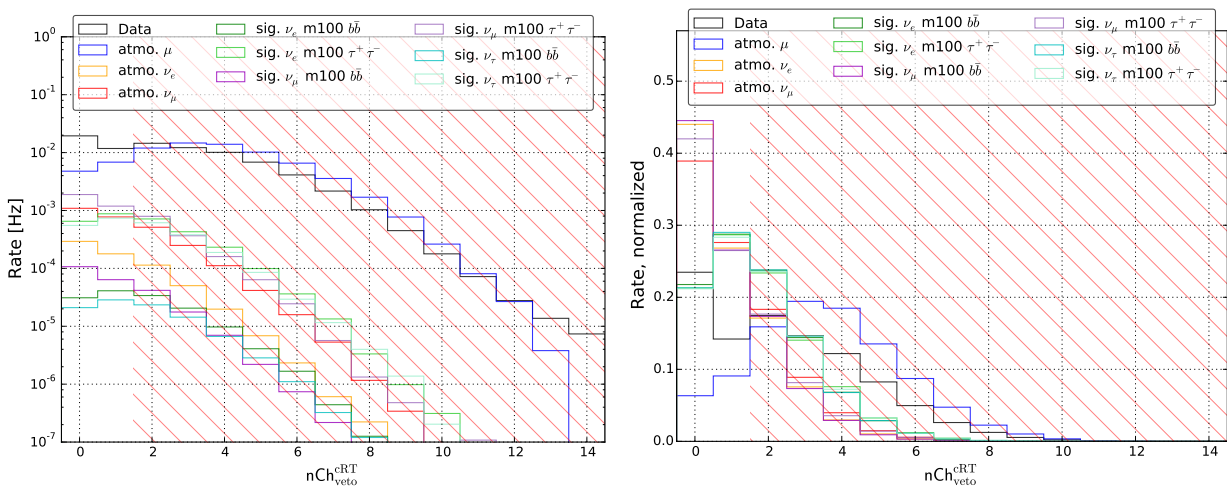


Figure 5.7.: Distribution of the  $n\text{Ch}_{\text{veto}}^{\text{CRT}}$  variable on selection level 4 and region rejected by the cut (dashed red).

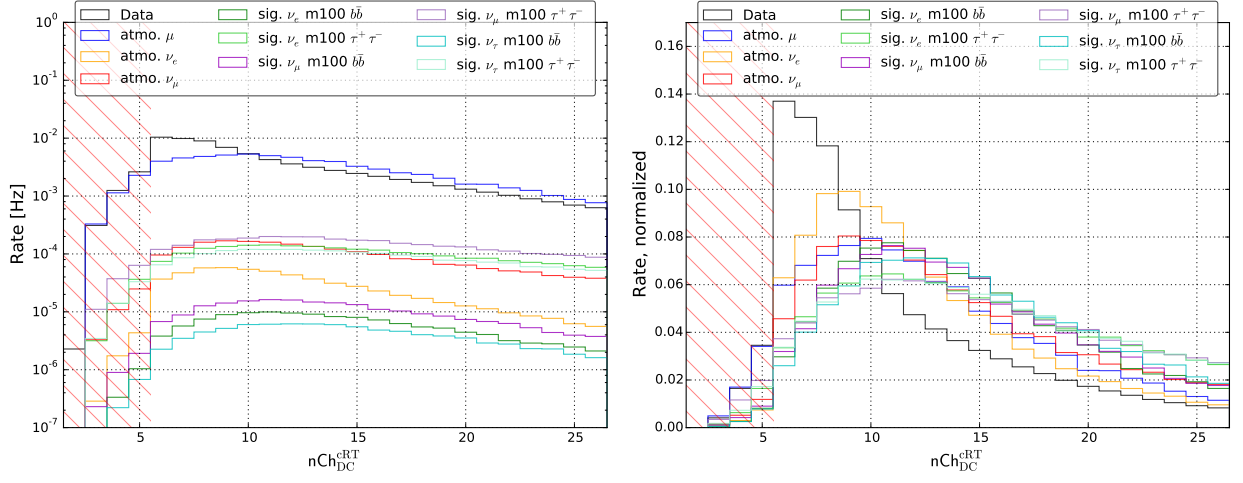


Figure 5.8.: Distribution of the  $n\text{Ch}_{\text{DC}}^{\text{CRT}}$  variable on selection level 4 and region rejected by the cut (dashed red).

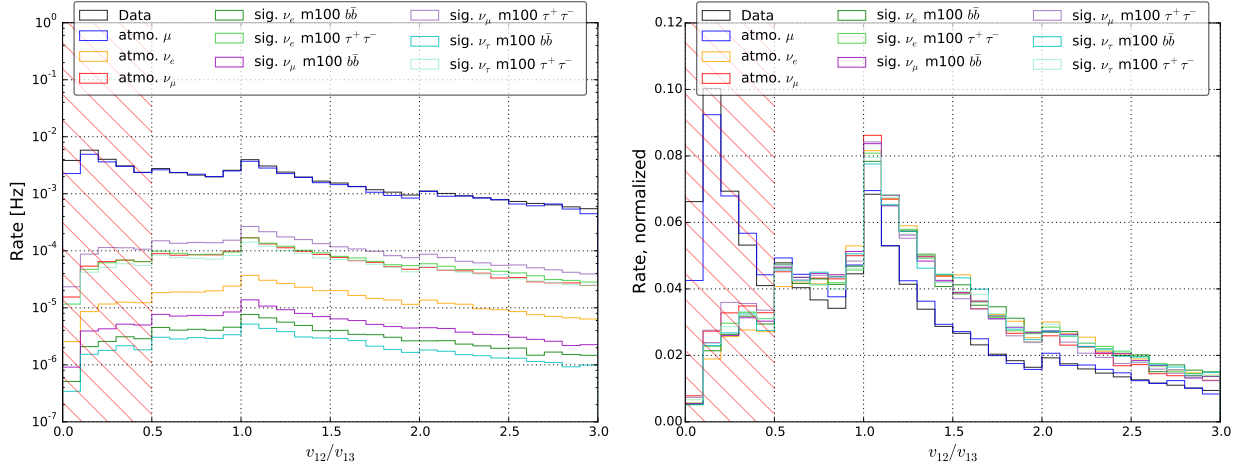


Figure 5.9.: Distribution of the  $v_{12}/v_{13}$  ratio on selection level 4 and region rejected by the cut (dashed red).

## Level 6

After level 5 the data rate is reduced by a factor of about  $10^5$  with respect to selection level 1. This allows one to run sophisticated event reconstructions and variable calculations. Listed below are the variables that are exploited and that comprise selection level 6. Their distributions, including the signals from a  $m_\chi = 100 \text{ GeV}/c^2$  candidate as examples, can be found in appendix D. Unlike the procedure on previous selection levels, the variables are passed to a machine learning code (described in section 5.4) prior to cut execution. Therefore, no fixed cut values are set for these variables. Cuts are performed on the basis of an *overall* score, which is determined on the basis of the best-possible final sensitivity result (see section 5.5). Therefore, a soft cut on this score (-0.1) is chosen prior to writing out the level 6 samples, which only removes the most obvious atmospheric background (see section 5.4 and appendix E).

- $\sigma_z^{\text{resca}}$

The cascade resolution estimator described in chapter 4 is referred to as *resca* (“resolution estimator for cascades”). The  $z$  uncertainty for the reconstruction of tracks under cascade hypothesis should be larger than the one of cascades assuming the same event hypothesis. This variable has some potential for discrimination of atmospheric muons.

- $\text{rLogL}^{\text{SPE32}}$

An SPE reconstruction with 32 iterations yields a (log-)likelihood value which gives a measure of the probability of the best-fit result matching the hypothesis and therefore should be different for tracks compared to cascades. The “r” denotes that the given log-likelihood value is *reduced*, meaning that it has been rescaled by taking into account the number of lit modules  $N$ , from which a correctional factor of 2.5 is subtracted [144]:  $\text{rlogL} = \log\text{L}/(N - 2.5)$ .

- $\text{nVetoHits}$

This is a more sophisticated veto variable that aims at discarding muon events. The third HLC hit in DeepCore is chosen as reference point in space and time. Temporal and spatial differences are calculated for all other modules which also registered light. By convention, positive time differences are attributed to earlier light hits, and negative time differences correspond to later hits. Figure 5.10 illustrates the possible signature types that occur in the so-chosen space and time plane. A muon that enters the detector far outside the fiducial DeepCore volume, starts with considerably positive time differences, moves with roughly the speed of light towards the origin of this system (upper half of the figures) and leaves the DeepCore region again by increasing the distances to the reference point (lower half of the figures). Hits found along the upper line are interpreted as indication for an incoming muon and this region is consequently defined as veto region (figure 5.10, right). The number of modules located in this region is the value of the  $\text{nVetoHits}$  variable. The four lines, which confine this veto region, are motivated

by the physical arguments above, but have been optimized to provide a maximal background rejection capability. Their linear equations read as [172]:

$$\begin{aligned}\Delta t &= \frac{\Delta r}{0.3 \text{ m/ns}} + 150 \text{ ns} \\ \Delta t &= -\frac{\Delta r}{0.2 \text{ m/ns}} + 500 \text{ ns} \\ \Delta t &= \frac{\Delta r}{0.3 \text{ m/ns}} - 1850 \text{ ns} \\ \Delta r &= 750 \text{ m} \quad .\end{aligned}\tag{5.11}$$

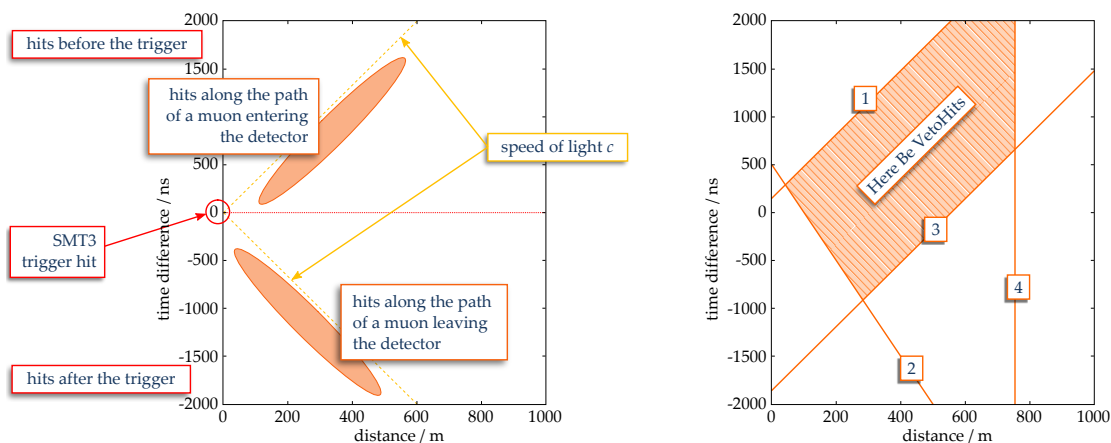


Figure 5.10.: Underlying concept of the `nVetoHits` variable (left) and location of the veto region (right), from [172].

- $\cos(\theta_{\text{reco}}^{\text{monopod}})$

If reconstructed correctly, the event's zenith angle can be used to reject down-going muons. The computationally expensive 32-iterative `monopod` reconstruction is supposed to reconstruct events even more precisely and hence identify additional background events. This likelihood-based reconstruction assumes an (almost-)spherical light topology [137].

- $z_{\text{reco}}^{\text{monopod}}$

As could already be seen on cut level 3, the reconstructed  $z$  coordinate incorporates powerful discrimination potential against muon background.

- $E_{\text{reco}}^{\text{monopod}}$

The neutrino signal from WIMP annihilations has a constrained energy range – especially for low candidate masses. Atmospheric muons, on the other hand, typically will have larger energies if they reach the detector. At the low-energy end, atmospheric neutrinos may be discarded, due to the fact that their flux drops like  $E^{-3.7}$ . The reconstructed energy thus helps in the background discrimination.

- $\cos(\theta_{\text{reco}}^{\text{millipede}})$

`millipede`, a generalization of the `monopod` algorithm is able to seed many cascades

with different energies along a hypothetical track. While being a computationally expensive track reconstruction, its zenith angle has a strong rejection potential, even at such a high selection level (see figure D.7).

- **Ndir**

For a given track reconstruction, the number of direct hits is determined. An MPE fit is used in this case, seeded with the result of a SPE32 reconstruction. Direct hits are hits with residual times between -15 and 75 ns. The residual is the difference of measured arrival time and the time that an unscattered Cherenkov photon would require to travel from the track origin to the optical module. A larger number of direct hits establishes more trust in the reconstruction result, but of course depends on the chosen reconstruction and event hypothesis.

- **NAbove200**

Total charge in the upper detector part. Same definition as on selection level 3.

- **Ldir**

Related to the number of direct hits, the direct length is defined as the projection of the outermost direct hits on the reconstructed track. Since this quantity defines the lever arm that enables a good (track) reconstruction, larger values are associated with potentially better reconstructions.

- **FRLength**

Track reconstructions usually assume an infinite muon track. A neutrino-induced track can, however, start or end inside the detector, depending on the energy and the interaction point. The *FiniteReco* algorithm aims at reconstructing the starting point as well as the length of a muon track. The latter can serve as an energy proxy and should be significantly smaller for cascades compared to tracks. Starting with a track seed, the algorithm first tries to roughly determine the track's start and stop point. It considers all hit modules within a distance of 200 m from the track. For each module, the track's light ejection point is calculated, by taking into account the Cherenkov angle. The outermost points define the track's starting and stopping point. This procedure is illustrated in figure 5.11. The so-determined points are further refined by employing a likelihood optimization, which evaluates the probability of non-lit modules along the track to have registered light [174].

- **C2QR6**

Charge ratio, as described in the context of the level 3 cuts. This variable is also offered to the BDT training (see following section).

Distributions of the `nVetoHits` variable are shown in figure 5.12 as an example. The complete set of level 6 cut variables can be found in appendix D.

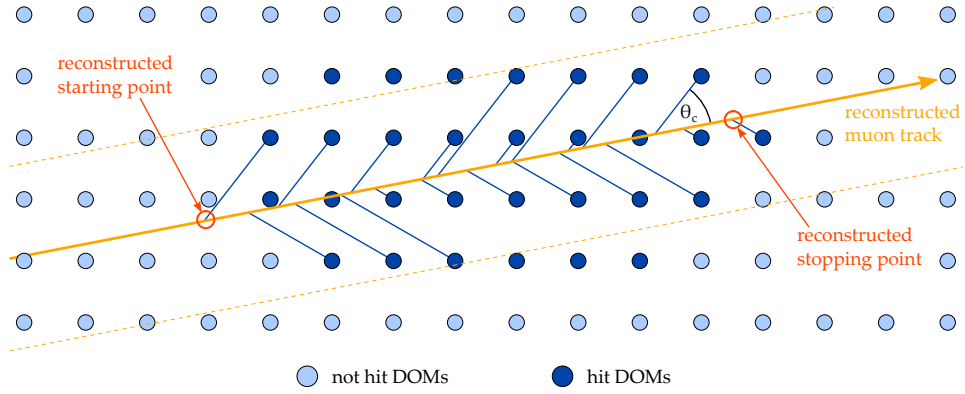


Figure 5.11.: Illustration of FiniteReco's first-guess determination of the track's starting and stopping point (from [172]).

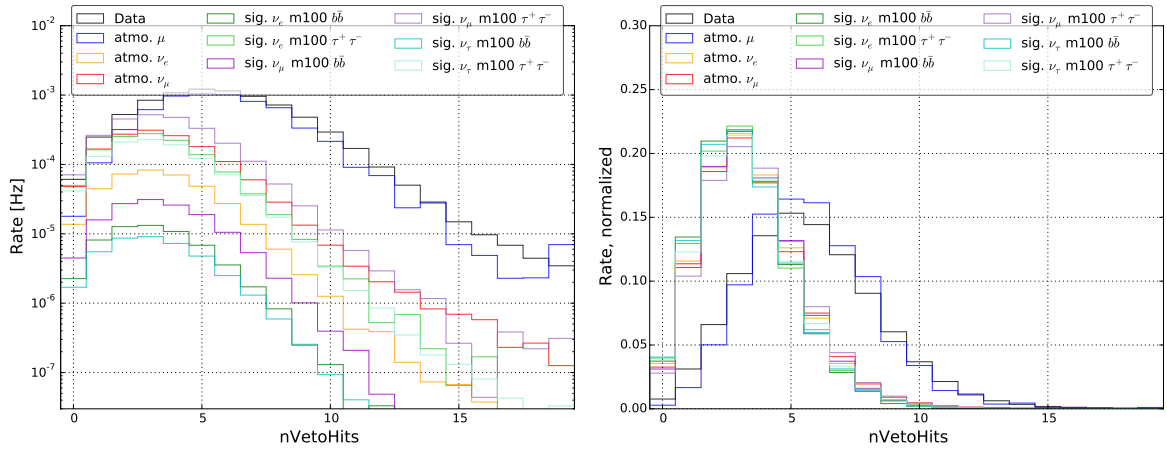


Figure 5.12.: Distribution of the nVetoHits variable at selection level 5.

## Level 7

As will be presented in section 5.5, the likelihood analysis relies on two-dimensional spline-smoothed surfaces of probability density functions (PDFs) for the background and energy terms. Especially at the margins of these PDFs, low statistics can introduce artifacts, which can be amplified further by the spline fits. Therefore, permitted ranges are imposed on the reconstructed energy of the events,  $\log_{10}(E_{\text{reco}}^{\text{monopod}}/\text{GeV})$ , and on the angular uncertainty estimate<sup>8</sup>  $\sigma$ . These ranges depend on the mass of the annihilating WIMPs,  $m_\chi$ , and in the case of the energy also on the annihilation channel. Furthermore, a cut on the BDT score is applied, with the value being optimized on the best sensitivity result from the likelihood fit.

<sup>8</sup>Since from this point forward only the directional uncertainty estimate will be employed, the suffix specifying the opening angle will be omitted:  $\sigma = \sigma_\Omega$ .

- **Angular Uncertainty Estimate**

The uncertainty spread is energy-dependent<sup>9</sup> and hence differs for the WIMP masses studied. The ranges are constrained to:

$$[\sigma_{\min}, \sigma_{\max}] = \begin{cases} [0.1, 1.7]; & \text{for } m_\chi = 35 \text{ GeV}/c^2. \\ [0.1, 1.6]; & \text{for } m_\chi = 50 \text{ GeV}/c^2. \\ [0.1, 1.4]; & \text{for } m_\chi = 100 \text{ GeV}/c^2 \text{ and } m_\chi = 250 \text{ GeV}/c^2. \\ [0.1, 1.3]; & \text{for } m_\chi = 500 \text{ GeV}/c^2 \text{ and } m_\chi = 1000 \text{ GeV}/c^2. \end{cases} \quad (5.12)$$

The lower bound is introduced in order to prevent the exponent in equation 5.18 from becoming too large.

- **Reconstructed Energy**

Signal enters the construction of the energy PDF. The signal energy range depends on the chosen candidate mass as well as the annihilation channel. Therefore, the logarithm of the energy  $\log_{10}(E_{\text{reco}}^{\text{monopod}}/\text{GeV})$  is required to fall within

$$\left[ \log_{10} \left( m_\chi / (\text{GeV}c^{-2}) \right) - 1, \log_{10} \left( m_\chi / (\text{GeV}c^{-2}) \right) + 0.2 \right]$$

for hard channels ( $W^+W^-$ ,  $\tau^+\tau^-$ ), while for the soft ( $b\bar{b}$ ) channel a range of

$$\left[ \log_{10} \left( m_\chi / (\text{GeV}c^{-2}) \right) - 1.5, \log_{10} \left( m_\chi / (\text{GeV}c^{-2}) \right) - 0.1 \right]$$

is imposed. In the latter case, however, logarithms of the energy are not allowed to go below 0.2 and to not exceed 2.8. The resulting cut values can clearly be seen on the probability density function distributions (see figure 5.25).

- **BDT Score**

The cut on the BDT score is chosen depending on the best sensitivity that can be achieved by the likelihood fit (see section 5.5). The optimization range is constrained to the region between -0.04 and 0.02. Too soft cuts would take insufficient advantage of the BDT discrimination power, while hard cuts would result in an unacceptable loss of (background) statistics, which are crucially required for the construction of the two-dimensional PDFs. Sensitivities<sup>10</sup> for the considered BDT score range are shown in appendix F. Obviously, in the limited range studied, the results are almost independent of the exact BDT score cut value.

Table 5.1 summarizes the resulting cut values on the BDT score for all considered masses and channels. It can be seen that softer cuts are preferred sometimes. The additional amount of background is tolerated, since most of it enters from a different direction than the signal. The reconstructed angular distance to the signal source is not used as a discrimination variable yet, because direction based decisions are reserved for the likelihood analysis (section 5.5) in order to keep enough statistics for the PDF constructions.

---

<sup>9</sup>Typically, larger uncertainties are expected for lower energies.

<sup>10</sup>The procedure of calculating these sensitivities will be explained in section 5.6.

$m_\chi$ [GeV/c <sup>2</sup> ]	$\chi\chi$ annihilation channel		
	$b\bar{b}$	$\tau^+\tau^-$	$W^+W^-$
35	-0.04	-0.04	–
50	0.0	-0.04	–
100	-0.02	0.02	-0.04
250	-0.02	0.02	0.0
500	-0.04	0.02	0.02
1000	0.02	-0.02	-0.04

Table 5.1.: Optimized cut values on BDT scores.

### Event selection summary

The event rates for experimental data, as well as simulated signal and background, are summarized in table 5.2 for all WIMP masses and annihilation channels studied. A more complete set of rates, including all selection levels and the respective cut efficiencies, can be found in appendix G. At the final selection level, muon background is reduced by a factor of about a million, while signal is retained with a 1–15 % efficiency (depending on the mass and channel chosen), when compared to selection level 2. Final level signal efficiencies will also be shown at a later point (see table 5.3).

Statistical uncertainties<sup>11</sup> on Monte-Carlo rates at selection level 6 are around 4 % for atmospheric muons and smaller than 1 % for signal and atmospheric neutrinos. On preceding levels, corresponding errors are substantially lower. The rate development and agreement between experimental data and simulation throughout the selection levels are illustrated in figure 5.13, including all-flavor rates for the example of a WIMP candidate with a mass of 100 GeV/c<sup>2</sup>.

It can be seen that data and MC do not agree perfectly. The main reason is an insufficient simulation of correlated noise hits in the optical modules. Low-energy analyses crucially rely on a good noise description since the SMT3 trigger condition introduced with the DeepCore sub-detector can be fulfilled by the aid of noise hits and occasionally even causes in events to be triggered by pure noise. Dark noise rates depend on the ambient temperature and also on the quantum efficiency of the deployed PMTs [118] – DeepCore PMTs have a 35 % higher quantum efficiency which corresponds to a noise rate increase by 25 %. Furthermore, various processes can contribute to the total noise rate. Uncorrelated noise hits do occur due to cathode thermionic electron emission and can be modeled by means of Poisson statistics. This process has a strong temperature dependence [175] and should effectively be zero for the glacial temperatures of the instrumented IceCube volume (about -40 °C to -20 °C) [176]. Due to defects and impurities in the PMT cathode

<sup>11</sup>The uncertainties are calculated as  $\sqrt{\sum_i w_i^2}$ , where  $w_i$  are the individual event weights.

WIMP mass [GeV/c <sup>2</sup> ]	Annihilation Channel	L2			L6		
		Data	BG-MC	Signal	Data	BG-MC	Signal
35	$b\bar{b}$	663	655	$3.35 \cdot 10^{-4}$	$2.75 \cdot 10^{-3}$	$2.11 \cdot 10^{-3}$	$5.66 \cdot 10^{-5}$
	$\tau^+ \tau^-$			$6.58 \cdot 10^{-3}$			$8.64 \cdot 10^{-4}$
50	$b\bar{b}$			$5.92 \cdot 10^{-4}$	$2.93 \cdot 10^{-3}$	$3.44 \cdot 10^{-3}$	$9.13 \cdot 10^{-5}$
	$\tau^+ \tau^-$			$1.46 \cdot 10^{-2}$			$1.54 \cdot 10^{-3}$
100	$b\bar{b}$			$1.96 \cdot 10^{-3}$	$3.04 \cdot 10^{-3}$	$3.64 \cdot 10^{-3}$	$2.24 \cdot 10^{-4}$
	$\tau^+ \tau^-$			$7.01 \cdot 10^{-2}$			$4.45 \cdot 10^{-3}$
	$W^+ W^-$			$3.11 \cdot 10^{-2}$			$1.97 \cdot 10^{-3}$
250	$b\bar{b}$			$9.36 \cdot 10^{-3}$	$3.16 \cdot 10^{-3}$	$3.89 \cdot 10^{-3}$	$6.26 \cdot 10^{-4}$
	$\tau^+ \tau^-$			$3.78 \cdot 10^{-1}$			$1.33 \cdot 10^{-2}$
	$W^+ W^-$			$1.69 \cdot 10^{-1}$			$5.32 \cdot 10^{-3}$
500	$b\bar{b}$			$2.38 \cdot 10^{-2}$	$2.87 \cdot 10^{-3}$	$3.54 \cdot 10^{-3}$	$1.18 \cdot 10^{-3}$
	$\tau^+ \tau^-$			$8.42 \cdot 10^{-1}$			$2.12 \cdot 10^{-2}$
	$W^+ W^-$	$3.09 \cdot 10^{-1}$	$7.22 \cdot 10^{-3}$				
1000	$b\bar{b}$	$4.55 \cdot 10^{-2}$	$2.63 \cdot 10^{-3}$	$3.20 \cdot 10^{-3}$	$1.71 \cdot 10^{-3}$		
	$\tau^+ \tau^-$	1.28			$2.71 \cdot 10^{-2}$		
	$W^+ W^-$	$3.81 \cdot 10^{-1}$			$7.66 \cdot 10^{-3}$		

Table 5.2.: All-flavor rates for experimental data, sum of background Monte-Carlo and signal, shown for selection levels 2 and 6. Rates are given in units of events per  $10^{25}$  annihilations per second for the WIMP-induced neutrino signal and in Hz for the background MC and for the data. Background MC datasets are not required at the final selection level and therefore are only processed until level 6.

this effect may, however, still be relevant for IceCube DOMs. Temperature-independent noise signals can arise from radioactivity in the glass (e.g. from potassium-40 [177]), spontaneous electron emissions in the PMT high-voltage field or leak currents. The studies performed in [118, 176, 178] show that there is an additional noise contribution at sub-zero temperatures which grows for decreasing temperatures. While the process causing these noise signals is yet unknown, it is clear that the hits arrive in (correlated) bursts [176, 179]. The authors of [179] trace this effect back to scintillation and Cherenkov light in the glass of the PMTs and the pressure spheres, since measurements with removed pressure spheres have shown a significant decrease of the dark noise rate [180, 181].

Since some of the noise components are temperature-dependent, the total noise expectation depends on the instrumented depth of the optical modules. Furthermore, high quantum efficiency modules show a different noise behavior. This situation necessitates an individual model fit for each of the 5160 DOMs. Efforts in the collaboration are ongoing to implement improved noise descriptions [180] which will result in a better agreement of data and MC for low-energy focused analyses.

The effects of improper noise modeling are very hard to quantify, since events may not

get vetoed due to the fact that noise hits would be less present in the veto region. For example, the exaggerated rate of atmospheric muons in figure 5.3 (and as such the non-perfect agreement of data and simulation at selection level 3) is attributed to improper simulation of noise. On the low-energy end, however, missing noise simulation causes less (pure) noise events to trigger. The employed datasets for signal and (atmospheric) neutrino background use a refined noise model [180] with a substantially improved simulation compared to code that was used for atmospheric muons – the latter account for a significant part of the events, even at the final selection level. With the improved simulations, the agreement with experimental data is still imperfect (which e.g. can later be seen in the right part of figure 5.17) and therefore the noise model is still subject to further improvements.

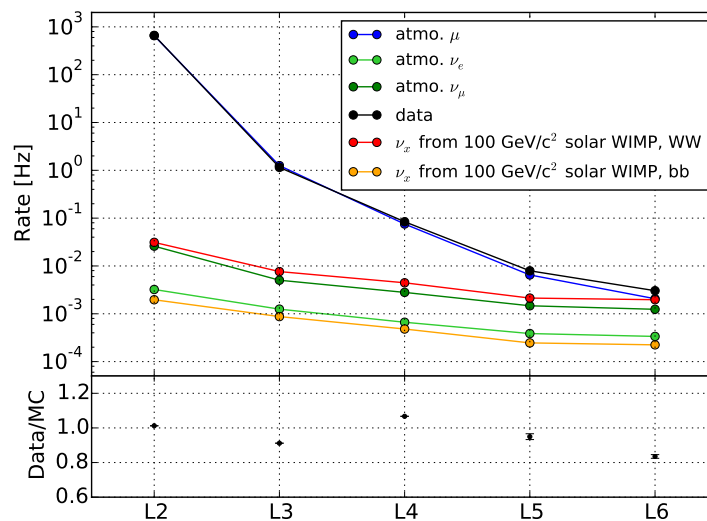


Figure 5.13.: Rates and data-MC ratio at the individual selection levels, including signal rates for the example of a  $100 \text{ GeV}/c^2$  WIMP candidate. Signal rates are for combined flavors and assume an annihilation rate of  $10^{25} \text{ s}^{-1}$ .

The final level signal efficiencies can be presented in the form of effective volumes. This quantity corresponds to a volume of lossless detection of the CC events injected at generation level and – at final selection level – is defined as:

$$V_{\text{eff}} = V_{\text{inj}} \frac{\sum_i^{N_{\text{final}}} w_i}{\sum_i^{N_{\text{gen}}} w_i}, \quad (5.13)$$

where  $w_i$  are the weights of the individual signal events and  $V_{\text{inj}}$  is their injection volume, as discussed in appendix B. The effective volumes for the candidate masses studied are shown in figure 5.14. Note that the  $\nu_\tau$  lines have a different low-energy trend, which follows from the fact that  $\nu_\tau$  undergoing deep-inelastic CC interactions have an energy threshold around 5 GeV (see section 2.4). This affects effective volumes especially at lower energies, because a higher fraction of events can trigger and be conserved when compared to the other flavors. The effective volume drops for the highest candidate

mass ( $m_\chi = 1000 \text{ GeV}/c^2$ ) due to the low-energy focused DeepCore filter. This trend is particularly distinct for the muon flavor, since muon neutrinos at higher energies have very similar event signatures when compared to atmospheric muon background and are consequently more likely to be rejected by cuts and vetoes as opposed to electron and tau neutrinos.

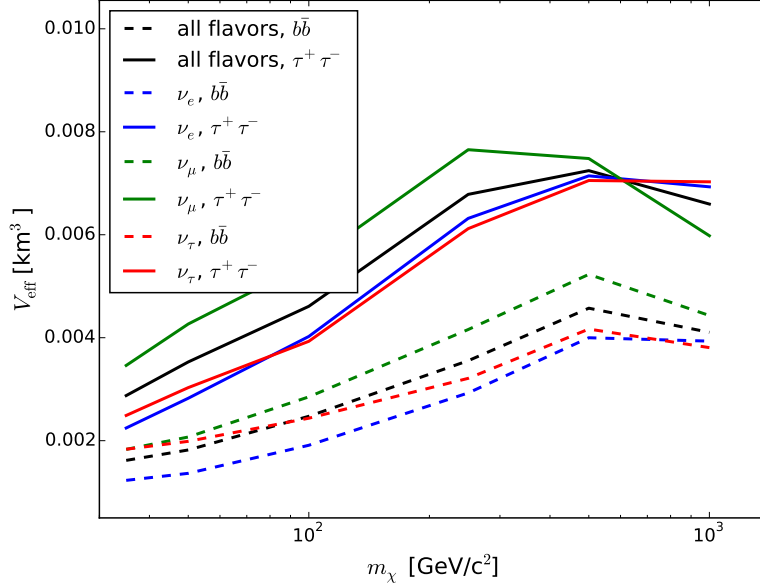


Figure 5.14.: Final-level effective all-flavor detector volume as a function of candidate mass, for soft ( $b\bar{b}$ ) and hard ( $\tau^+\tau^-$ ) annihilation channels. The contributions from individual neutrino flavors are also shown.

A quantity that makes a statement about how well a flux of signal neutrinos can trigger and subsequently survive up to the final event selection level, is the *Effective Area*<sup>12</sup> [182]:

$$A_{\text{eff}} = n_{\text{ice}} \cdot V_{\text{inj}} \frac{\sum_i^{N_{\text{final}}} w_i}{\sum_i^{N_{\text{gen}}} w_i / \sigma_{\nu \rightarrow l}(E_i)}, \quad (5.14)$$

with  $\sigma_{\nu \rightarrow l}$  being the total neutrino-nucleon charged-current cross-section, as discussed in section 2.4.  $n_{\text{ice}}$  is the number density in ice (number of nucleons per volume). The parametrizations<sup>13</sup> from [81, 100] were used in the cross-section determination, which employ the data provided in [72]. Neutrino-nucleon scattering cross-sections are usually given as an *isoscalar* proton-neutron average (e.g. see equation 2.23). For our  $\text{H}_2\text{O}$  detector, however, the different number of protons and neutrons has to be taken into account,

<sup>12</sup>This is a convenient quantity for theorists, as the number of events  $N$  seen in the detector as a result of a flux  $\Phi$  can be calculated as  $N = A_{\text{eff}} \cdot \Phi$ .

<sup>13</sup>The approximated  $\nu_e$  and  $\nu_\mu$  cross-section parametrizations for CC interactions with protons and neutrons read [100]:

$$\begin{aligned} \sigma_{\text{CC}}^{\nu p} &= 5.43 \cdot 10^{-39} \cdot E_\nu^{0.965}, & \sigma_{\text{CC}}^{\nu n} &= 1.23 \cdot 10^{-38} \cdot E_\nu^{0.929} \\ \sigma_{\text{CC}}^{\bar{\nu} p} &= 4.59 \cdot 10^{-39} \cdot E_{\bar{\nu}}^{0.978}, & \sigma_{\text{CC}}^{\bar{\nu} n} &= 2.19 \cdot 10^{-39} \cdot E_{\bar{\nu}}^{1.022}. \end{aligned}$$

as well as the significant effect of the finite  $\tau^\pm$  mass for  $\nu_\tau$  interactions. Metaphorically speaking, the effective area is the detector section at which a through-going neutrino flux could be detected at the final event selection level with an efficiency of 100 %. Given the small neutrino-nucleon cross-sections,  $A_{\text{eff}}$  is of the order of less than a square centimeter (see figure 5.15).

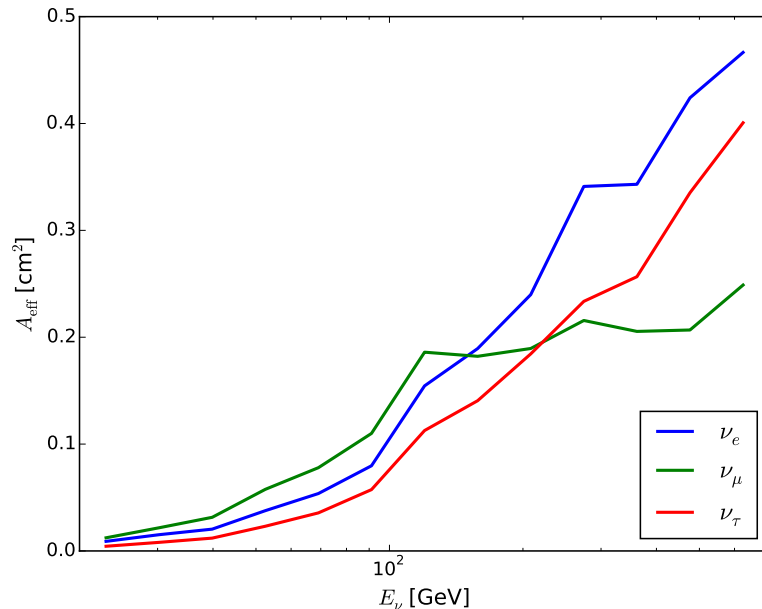


Figure 5.15.: Effective areas at final selection level for an assumed neutrino flux originating from WIMP annihilations. The effective area primarily depends on energy and merely depends on the slightly different event selections. Fluctuations are due to the limited statistics.

Since each mass in the selection of candidate masses studied undergoes individual cut optimizations, the corresponding effective areas can differ slightly. However, the overall trend is governed by the cross-section dependence on the energy of the incident neutrino. The plotted energy range ends at about 600 GeV due to insufficient statistics above. As discussed in section 1.4, neutrinos with energies significantly larger than 200 GeV are hardly able to escape the sun (see also figure A.6).

At this point, it is worth noting that neither the background reduction, nor the refined likelihood technique and the therein exploited variables are considered for the effective volume and the effective area. Therefore, these quantities alone do not serve as a good basis for a comparison to final sensitivities of other analyses.

## 5.4 BDT Training

Following selection level 5, two event samples, signal and background, are passed to a machine learning algorithm, in order to computationally develop a model that achieves the best-possible sample separation, based on a collection of twelve discrimination variables<sup>14</sup>. The chosen algorithm for establishing such a statistical model involves a *Boosted Decision Tree Forest* (BDT) [183]. The advantages of boosted decision trees in a particle physics context are discussed in [184].

For background, experimental data are used from this point forward. This has two advantages: statistics are substantially higher compared to the simulated atmospheric muon dataset and no model uncertainties (which arise from imperfect understanding of noise or PMT efficiencies) are present in the background sample. To avoid signal bias, an *off-source* region is defined and subsequently events with an angular distance of less than 40 degrees to the source (the sun) are excluded from the training.

For signal samples, the datasets introduced in section 5.2 are used. The signal shape differs depending on the WIMP candidate mass. Therefore, separate trainings are performed for each of the six candidate masses studied. Events from all flavors and all annihilation channels are combined for each candidate mass chosen. Event weights are adopted from the WimpSIM Monte-Carlo generator and scaled assuming  $10^{25}$  annihilations per second.

Half of the events (for background and signal each) are retained for over-training checks. These are performed in order to reliably test whether the trained model was trained specifically on the characteristics of the events in the training sample or if it can distinguish the generic properties of signal and background. In the latter case, the resulting distributions for training and testing samples should be the same, meaning that no over-training has occurred.

Sequentially, a user-defined number of trees is trained. Each tree starts with a root node and the sum of all events (signal and background) normalized to 1. Binned distributions of the discrimination variables are calculated and cuts on the variables which separate signal and background best<sup>15</sup>, are taken as the basis to form two child nodes – one for each class of events. This procedure is repeated for the emerging nodes until the content of a node consists of pure signal or background, or until a user-defined maximum depth is reached. The basic tree concept is illustrated in figure 5.16.

The final nodes, the so-called “leaves”, are checked for incorrectly classified events, whose weights are increased before they enter the next classification tree, in order to focus on the events that are more difficult to classify. This process, referred to as *boosting*, is carried out according to the *AdaBoost* algorithm [183]. The boost strength  $\beta$  can be set by the user. Due to their larger specialization, the overall contribution weight of the

---

<sup>14</sup>These were presented in the scope of event selection level 6.

<sup>15</sup>The Gini criterion [185] is chosen as the metric for the “best” separation.

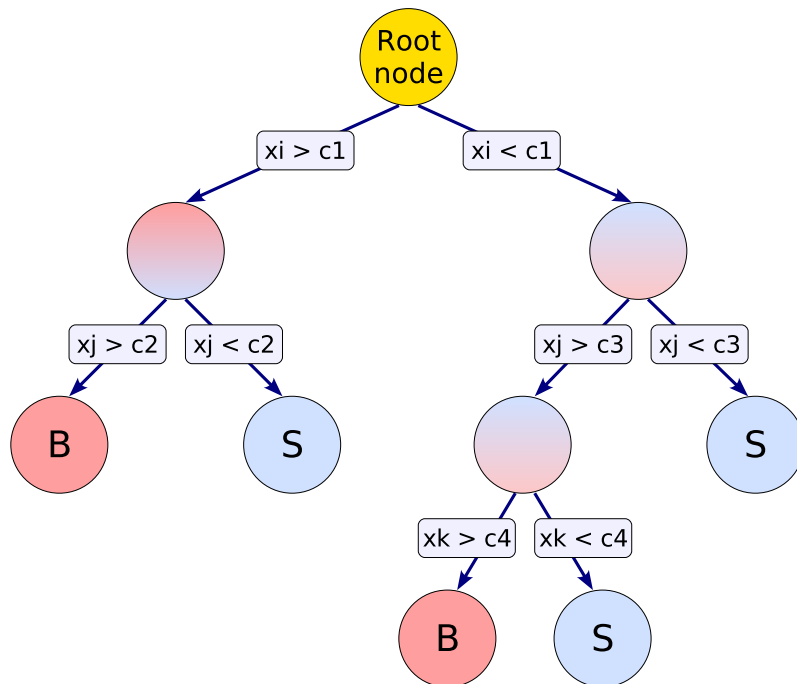


Figure 5.16.: Schematic illustration of the basic BDT structure. Events are classified as signal ( $S$ ) or background ( $B$ ) based on cuts on the variables  $x_i$ ,  $x_j$  and  $x_k$  (from [186]).

following trees is reduced in correlation with the boosting. An individual event's final BDT score is the weighted average of its scores in each tree, the weights being the boost factors, which depend on the boost strength and the fraction of incorrectly classified events. Higher scores correspond to more signal-like events. After a user-defined number of trees, the forest is completed.

In order to reach the best possible classification, while avoiding over-training, the number of trees was set to 320, the maximum tree depth was defined to be 3 and the boost strength was set to 0.7.

The algorithm is implemented in the form of Python code [187] and is commonly used within the IceCube collaboration. Meanwhile, general-purpose tools within the *scipy*<sup>16</sup> collection have also reached a very sophisticated functionality level [189].

The resulting BDT score distribution is shown in figure 5.17 for the example of a WIMP candidate with mass  $m_\chi = 100 \text{ GeV}/c^2$ . Plots for all candidate masses can be found in appendix E. Rates for background simulations are shown for comparison. For BDT scores above 0.2, figure 5.17 shows that the remaining data are almost exclusively comprised by atmospheric neutrinos. The ratio of experimental data (black dots) and total background simulation (green line) is presented in the lower part of the figure. The reason for the

<sup>16</sup>A “python-based ecosystem of open-source software for mathematics, science, and engineering” [188].

slight disagreement is discussed in the event selection summary (see section 5.3). A hypothetical score cut at 0.0 is illustrated by a dashed line.

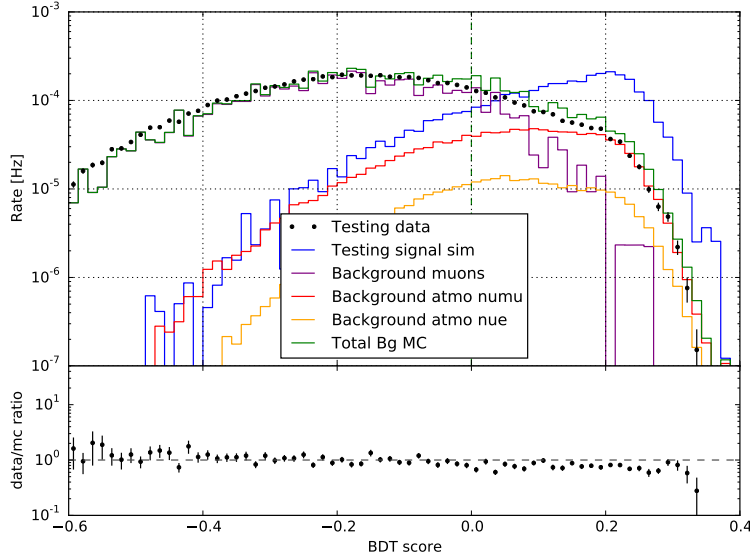


Figure 5.17.: BDT score distribution, for the signal from a WIMP candidate with a mass  $m_\chi = 100 \text{ GeV}/c^2$ .

Score-dependent cut efficiencies are shown in figure 5.18. Atmospheric neutrinos practically cannot be distinguished from signal neutrinos and thus have only slightly reduced cut efficiencies – although not being included in the training sample. As can be seen in figure 5.19, training and testing samples yield the same score distributions (within error bars), meaning that no over-training has occurred. The disparity between training and testing sample can be quantified by performing a *Kolmogorov-Smirnov* (KS) test [190]. This test calculates the probability of the two samples being drawn from the same distribution; its result is also included in figure 5.19. While perfect agreement between training and testing samples would yield KS values close to 1, a significant difference would result in KS values far less than 0.1%. Finally, figure 5.20 shows the cut correlations for all possible variable pairs. It can be seen that for both signal and background none of the chosen variables is overly redundant.

The relevance of individual variables can be extracted from the model. Such numbers, however, only quantify the technical importance of the variables for decision-making. This importance differs substantially for events which can easily be separated and are thus treated in early trees and events which are hard to separate and as such are treated in later trees, where a more refined separation is attempted. Since such quantities do not necessarily correlate with the distinction power for physical events [191], they are not listed. The number of variables is not limited by runtime and (weak) variables cannot have a negative impact on the separation power of the model.

The selection methods discussed above were published in a conference proceeding [192].

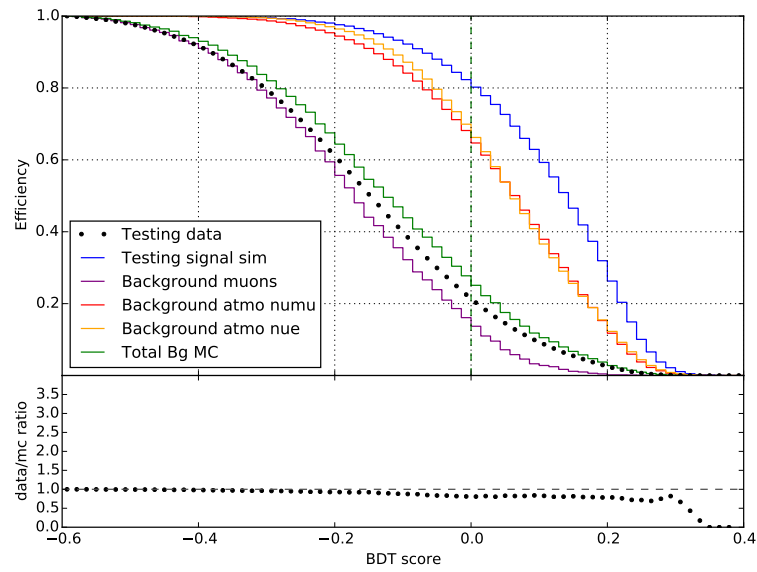


Figure 5.18.: Post-cut efficiencies as a function of the BDT score cut value, shown for signal from a WIMP candidate with a mass  $m_\chi = 100 \text{ GeV}/c^2$ .

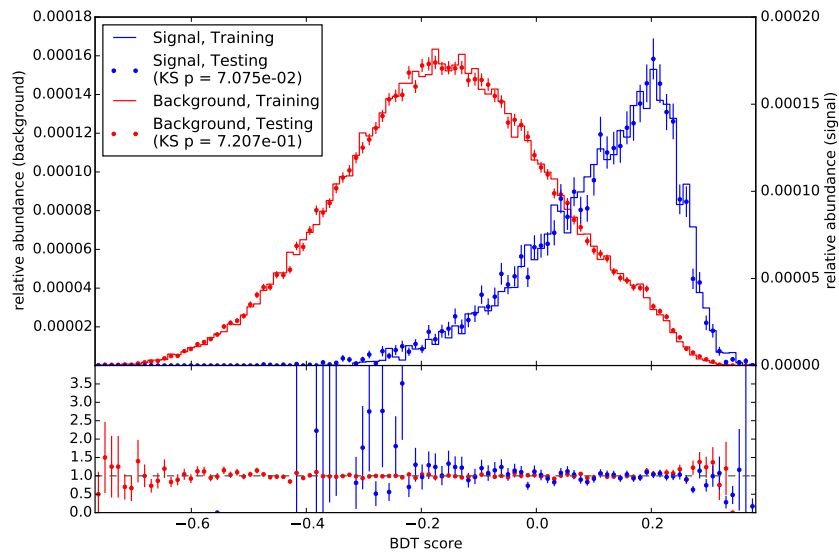


Figure 5.19.: Over-training check, shown for signal from a WIMP candidate with a mass  $m_\chi = 100 \text{ GeV}/c^2$ .

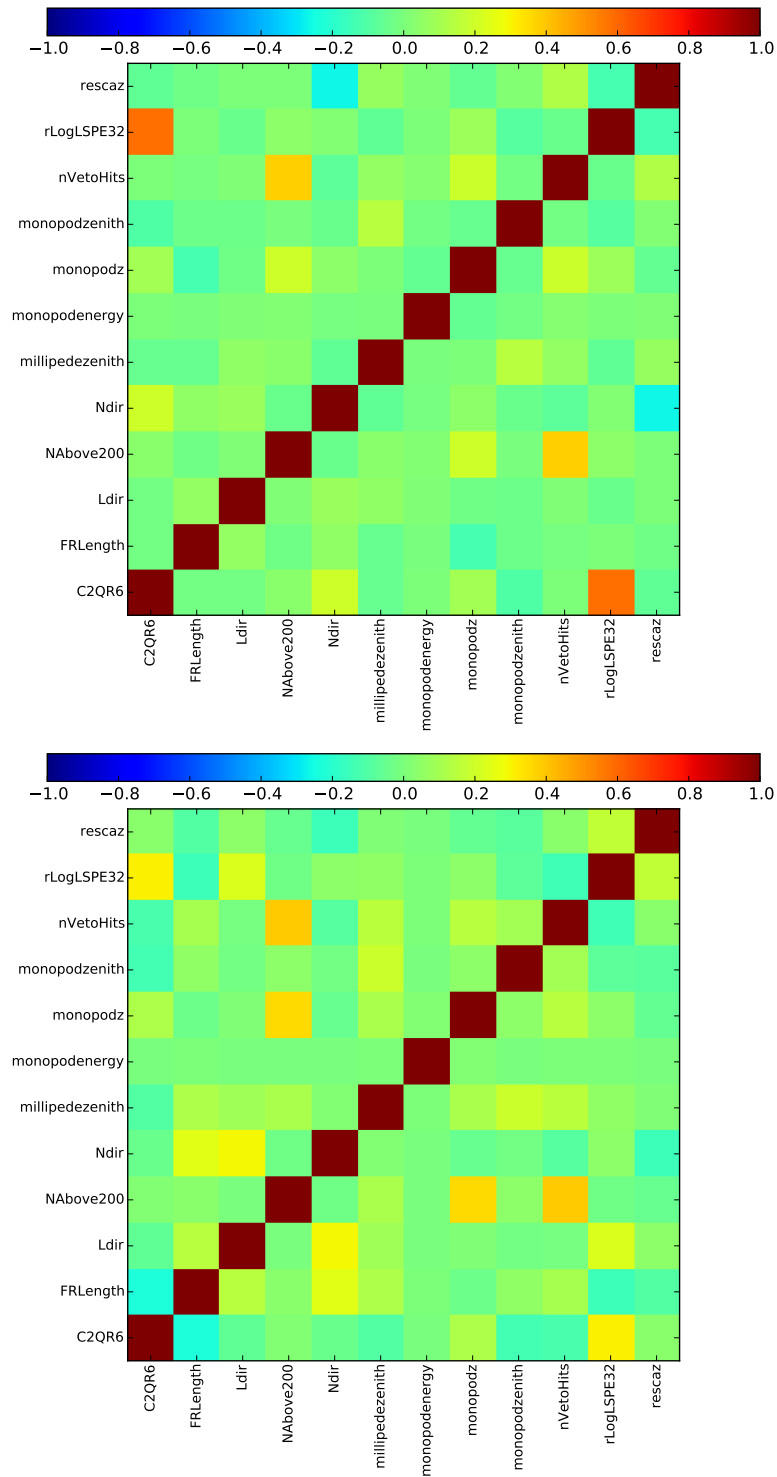


Figure 5.20.: Correlation matrix for pairs of discrimination variables for signal (top) and background (bottom), shown for the signal from a WIMP candidate with a mass  $m_\chi = 100 \text{ GeV}/c^2$ .

## 5.5 Likelihood Analysis

At the final selection level, the quantity that is most obviously able to discriminate signal from background is the reconstructed angular distance to the signal source. However, with cascade resolutions of 30 degrees and more (see figure 5.21), signal events themselves are reconstructed with substantially divergent directions. Since no reliable flavor identification is possible on an event by event basis, all events are reconstructed assuming the cascade hypothesis. For a better signal/background distinction of data events, it is therefore reasonable to additionally include event-based energy and angular uncertainty information – the calculation of the latter is described in chapter 4. While inclusion of energy information can result in a sensitivity increase by a factor of two [193], low-energy analyses only gain about 20% due to less separation of signal and background. The code that was adapted for this analysis is commonly employed in IceCube point source searches (e.g. [194]). It was altered substantially to work for cascade-shaped events which are associated with larger angular uncertainties due to their spherical event topology.

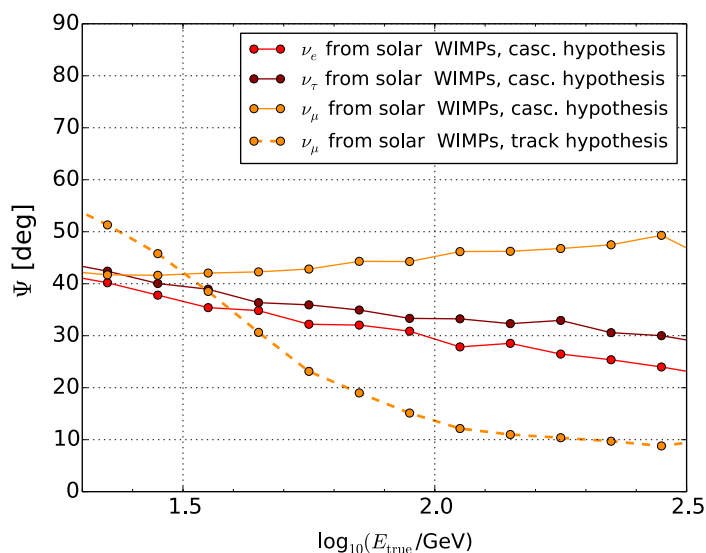


Figure 5.21.: Angular distance between true (simulated) and reconstructed direction at final selection level for a neutrino signal originating from solar WIMP annihilation. Solid lines show median resolutions obtained by assuming a spherical event signature, while the dashed line shows resolutions for track-shaped events being reconstructed assuming a track hypothesis (from [192]).

In order to extract signal-like events from the abundant background and calculate sensitivities on signal event numbers, an unbinned likelihood maximization approach is employed. Again, experimental data are used as the background sample for the same reasons as in the previous section. Here, no off-source region is defined since the azimuth angle is randomly scrambled, as will be explained later. Event clustering at a specified

source location is identified by maximizing the likelihood  $\mathcal{L}$  by variation of the associated signal events  $n_s$ :

$$\mathcal{L} = \prod_i \left[ \frac{n_s}{N} \mathcal{S}_i(|\vec{x} - \vec{x}_S|; \sigma, E, \delta) + \left(1 - \frac{n_s}{N}\right) \mathcal{B}_i(\delta; E, \sigma) \right] \quad , \quad (5.15)$$

where  $N$  is the sum of background and signal events,  $n_s/N$  is the signal fraction and  $(1 - n_s/N)$  is the background fraction.  $\mathcal{S}_i$  and  $\mathcal{B}_i$  are normalized probability density functions (PDFs) for signal and background and associate every event with a probability of being signal or background-like, based on their angular distance to the source  $|\vec{x} - \vec{x}_S|$ , estimated angular uncertainty  $\sigma$ , reconstructed energy  $E$  and the declination relative to the solar position  $\delta$ .

In order to obtain the relative declination  $\delta$ , the zenith angle in the local IceCube system  $\theta$  as well as the current position of the sun  $|\vec{x}_S|$  enter the likelihood, where  $|\vec{x}_S|$  is time-dependent. To eliminate this dependency, each background and signal event is rotated by  $\Delta\theta$  and  $\Delta\phi$ , the zenith and azimuth angle deviations from the solar position in the local coordinate system. In this way, a sun-centered coordinate system is introduced in which the solar position is always  $(0,0)$ . The new coordinates are denoted as the *relative declination* and the *relative right ascension*, following the usual designation of the equatorial coordinates in point source studies. From this point forward, these relative quantities will be simply referred to as *declination* and *right ascension*. The resulting angular distributions for signal and background are shown in figure 5.22, using the signal example of electron-neutrinos originating from self-annihilations of WIMPs with a mass of  $100 \text{ GeV}/c^2$ .

As expected, the signal clusters around the location of the sun, while the background is uniform in azimuth – and thus also in the relative right ascension. The non-uniform distribution of background in  $\delta$  is a symptom of the event selection which concentrates on preserving the nearly horizontal signal events<sup>17</sup>. In principle, the background probability is better characterized by the local zenith  $\theta$ , but given the relatively large angular uncertainties in cascade event reconstruction, the distribution of the declination assumes a very similar shape with the important advantage of introducing less variables (and thus less interdependence) to the likelihood formalism. As another consequence of the poor angular resolution, the shape of the distribution of  $\delta$  is practically independent of the data-taking season.

In order to test whether a null hypothesis (i.e. no signal) can be confirmed or rejected, the test statistic  $TS$  is introduced:

$$TS = \text{sgn}(n_s) \ln \Lambda \quad , \quad (5.16)$$

where the sign of the fitted number of signal events accounts for the separation of over- and under-fluctuations and  $\Lambda$  is the likelihood ratio w.r.t. the null hypothesis ( $n_s = 0$ ):

$$\ln \Lambda = \ln \left( \frac{\mathcal{L}(n_s)}{\mathcal{L}(n_s = 0)} \right) = \sum_i \ln \left[ 1 + \frac{n_s}{N} \left( \frac{\mathcal{S}_i(|\vec{x} - \vec{x}_S|; \sigma)}{\mathcal{B}_i(\delta; \sigma)} \mathcal{W}_i(E; \sigma) - 1 \right) \right] \quad . \quad (5.17)$$

---

<sup>17</sup>At the South Pole, the sun is at most 22 degrees above (or below) the horizon.

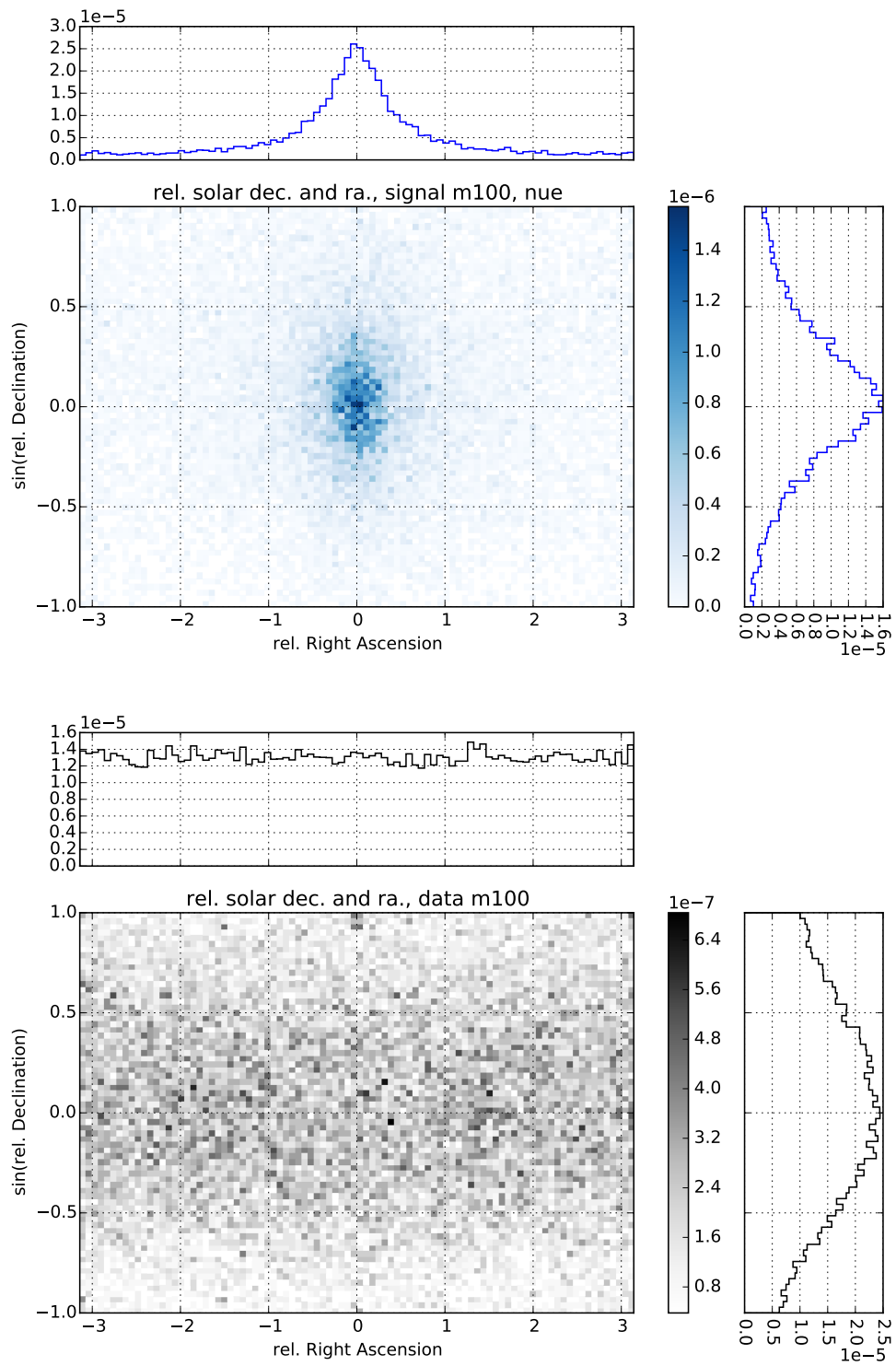


Figure 5.22.: Spherical angles in the used coordinate system for an example  $\nu_e$  signal from a WIMP candidate with a mass of  $100 \text{ GeV}/c^2$  (top) and background (bottom).

Here the energy dependence of the signal and background PDFs have been transferred to  $\mathcal{W}_i$ , so that  $\mathcal{S}_i$  and  $\mathcal{B}_i$  would consequently only depend on spatial quantities. The signal PDF is expressed analytically by means of the *von Mises–Fisher distribution*, which is the first-order non-elliptical term of the five-parameter Kent distribution [195]. For a two-dimensional sphere this distribution assumes the form

$$\mathcal{S}_i(|\vec{x} - \vec{x}_S|; \sigma) = \frac{\kappa}{4\pi \sinh \kappa} e^{\kappa \cos(|\vec{x} - \vec{x}_S|)} \quad , \quad (5.18)$$

where  $\kappa = \sigma^{-2}$  is the so-called concentration parameter. Examples for three different angular uncertainties  $\sigma$  are shown in figure 5.23.

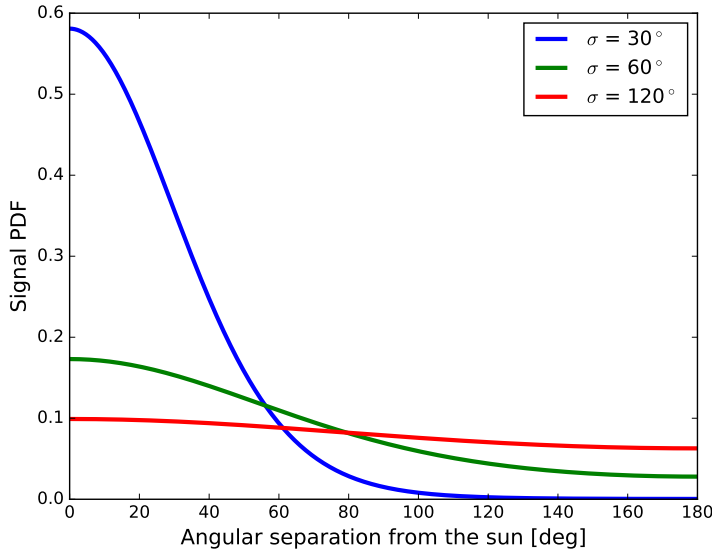


Figure 5.23.: Signal PDF for three example values of the angular uncertainty.

The background PDF  $\mathcal{B}_i$  is a function of the event’s declination. However, the dependence on the uncertainty  $\sigma$  requires a conditional formulation, as is instructively illustrated by [196]. Technically, this dependence is implemented as a spline-smoothed two-dimensional histogram (for an example see figure 5.24), where the one-dimensional declination distribution is normalized for any given value of  $\sigma$ . Events that can potentially be better reconstructed, and therefore have smaller angular uncertainties  $\sigma$ , have a larger concentration around the horizon. As can also be seen from the figure, the sine of  $\delta$  is employed instead of the declination itself. The choice histogram binning will be discussed below.

For the energy PDF  $\mathcal{W}_i$ , a two-dimensional  $\sigma$  against  $\log_{10}(E_{\text{reco}})$  histogram is created, one for the signal and one for the background. The conditional energy PDF (see figure 5.25 for an example) is obtained by calculating signal/background ratios for each bin and subsequently smoothing the whole histogram by means of a spline fit. In this way, there is only one energy term in equation 5.17 which combines the uncertainty dependent signal and background spectra. The PDF assumes values around one in regions

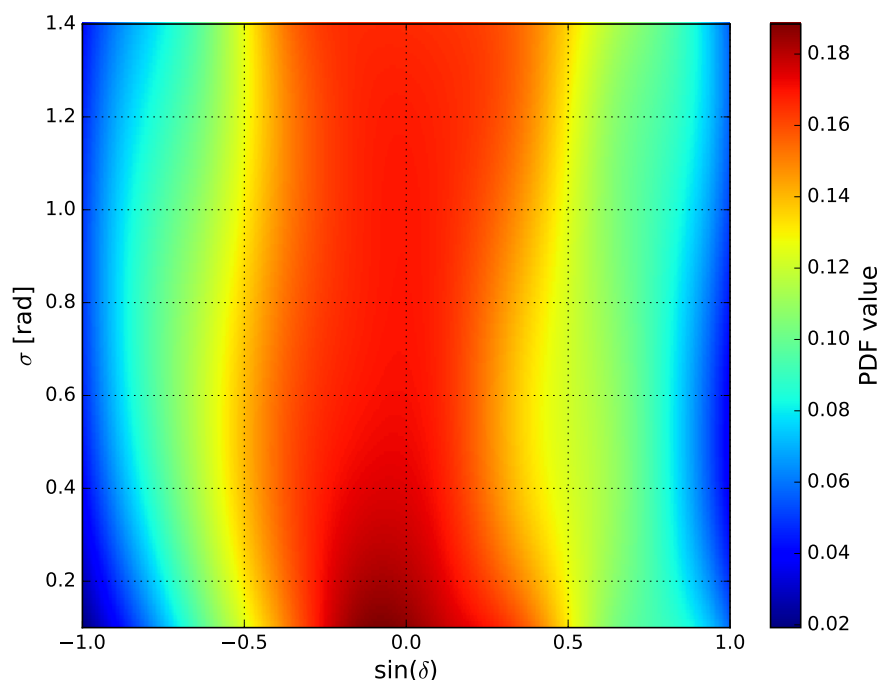


Figure 5.24.: Background PDF for the example of a  $100 \text{ GeV}/c^2$  WIMP annihilating to a  $b\bar{b}$  pair. The color-coded probability density corresponds to the smoothed bin entries which were normalized to 1 for all  $\sigma$  bins.

where signal is not separable from background. Deviations from one characterize events as rather signal or background-like.

Correct spline distributions are crucial for a correct evaluation of the signal and the background in the likelihood procedure. However, the number of bins is limited by the data statistics. Therefore, to ensure the functionality of the fit procedure, the number of bins for the two-dimensional background and energy histograms were optimized automatically for each potential BDT score cut value in the range from -0.04 to 0.02. A very fine binning causes fluctuation artifacts in the spline fits, while a coarse binning introduces the risk of hiding the characteristics of the distribution. As a quality criterion, the fit needs to reproduce the number of injected signal events; the resulting  $TS$  distribution is thus required to peak at zero for pure-background runs. For soft channels, the sum of x and y bins is limited to 13 for the energy PDF and to 15 for the background PDF. As stated in section 5.3, the final cut value for the BDT score is determined by the best resulting sensitivity on the spin-dependent WIMP-proton scattering cross-section.

By variation of the number of signal events  $n_s$ , the negative logarithm of the likelihood expression in equation 5.15 is minimized by an implementation of the *Broyden-Fletcher-Goldfarb-Shanno* algorithm [197]. Starting with a pure background sample, each event's azimuth angle is randomly drawn from a uniform distribution (*scrambled*) to ensure that no potential signal is present in the background sample. The fol-

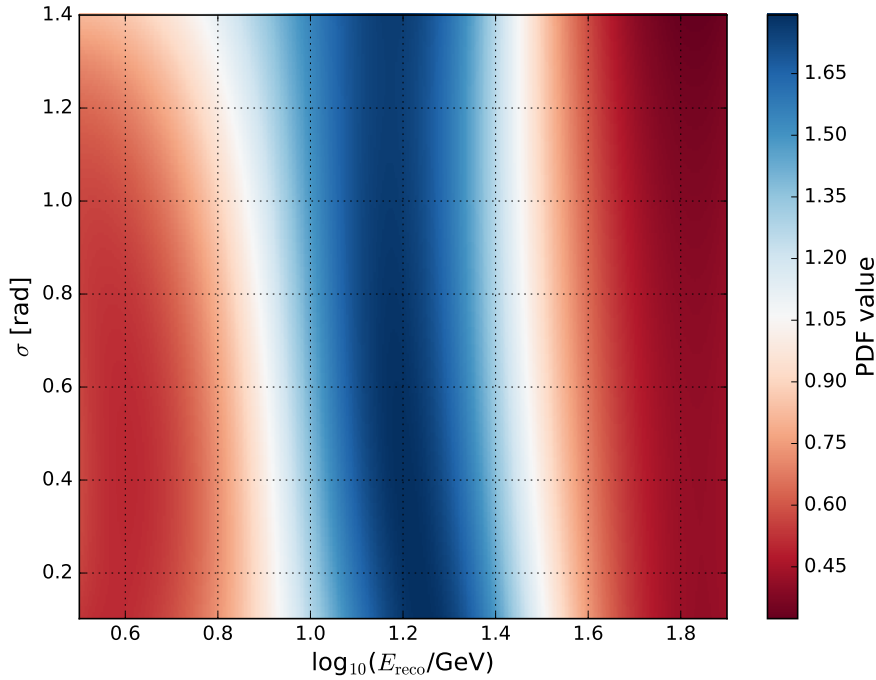


Figure 5.25.: Energy PDF for the example of a  $100 \text{ GeV}/c^2$  WIMP annihilating to a  $b\bar{b}$  pair. The color-coded probability density corresponds to the magnitude of the bin-wise signal/background ratio, which is subsequently smoothed by a spline fit. Prior to the division, signal and background histograms are both normalized to 1 for all  $\sigma$  bins.

lowing minimization of the (negative) likelihood yields a result for  $n_s$  and  $TS$  – which is expected to be close to zero for both quantities. Subsequent iterations of the resampled background sample will cause these results to fluctuate statistically and yield distributions around zero (see the left curves in figures 5.26 and 5.27 for two examples).

As the next step, individual signal events are randomly drawn according to a Poisson distribution and added to the background sample. For a quantification of the signal sensitivity, the *90 % confidence level* is commonly employed. This number is defined as the Poisson expectation value that causes 90 % of the signal-contaminated trials to have  $TS$  values larger than the median (50 % quantile) of the background-only trials. Such a separation is achieved through a successive increase of the expectation value  $\mu$  and a repeated realization of new signal-contaminated trial runs. The statistical uncertainty on  $\mu$  is set to 0.2 %, requiring randomized iterations to be performed for as long as the statistical error remains above this threshold. The expectation value which achieves the required separation (examples are shown in figures 5.26 and 5.27) is then defined as the sensitivity on a number of signal events,  $\mu_{\text{fit}}^{90\%}$ . The signal and background samples differ depending on WIMP candidate mass and annihilation channel – the described fitting procedure is therefore performed independently for each mass-channel combination.

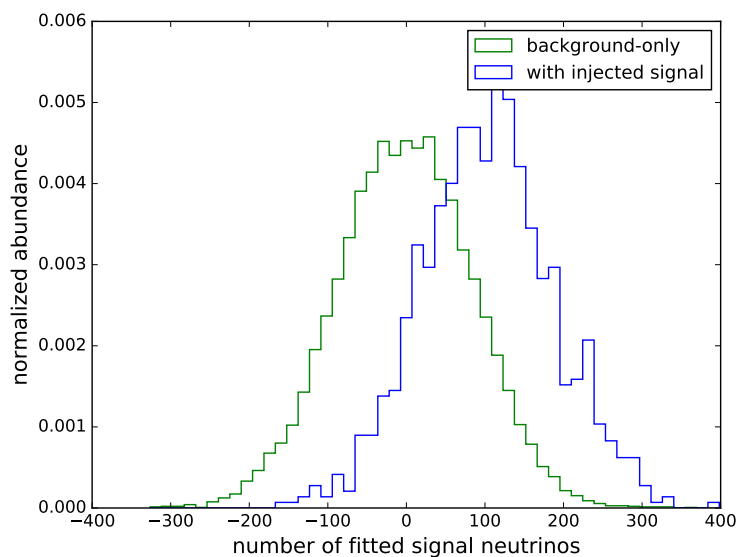


Figure 5.26.: Number of fitted signal events for pure-background and signal-contaminated runs (for the example of a  $100 \text{ GeV}/c^2$  WIMP annihilating to a  $b\bar{b}$  pair). The shown separation corresponds to the 90% confidence level, i.e. the number of injected signal events are drawn from a Poisson distribution with the expectation value set to  $\mu_{\text{fit}}^{90\%}$ .

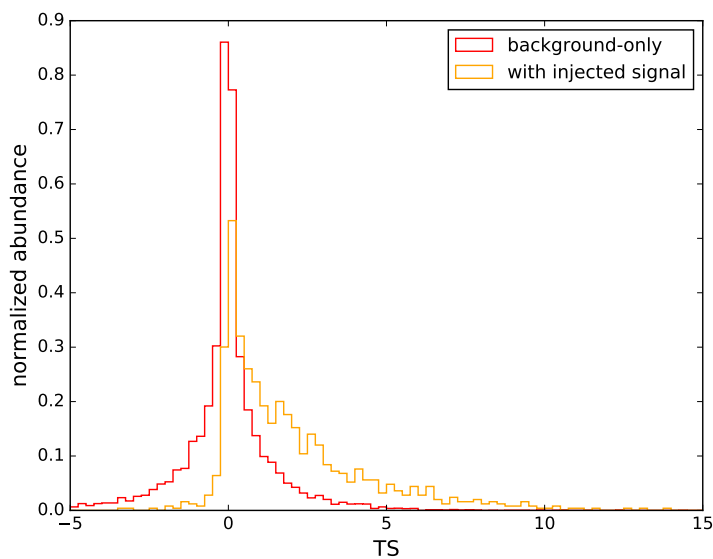


Figure 5.27.:  $TS$  values for pure-background and signal-contaminated runs (for the example of a  $100 \text{ GeV}/c^2$  WIMP annihilating to a  $b\bar{b}$  pair). The shown separation corresponds to the 90% confidence level, i.e. the number of injected signal events are drawn from a Poisson distribution with the expectation value set to  $\mu_{\text{fit}}^{90\%}$ .

In order to test the quality of signal-contaminated fit results, it is instructive to compare the number of injected signal events to the corresponding number of fitted signal events  $n_s$ . Figure 5.28 shows that, while the  $n_s$  have a larger spread than the Poisson-drawn number of injected events, the peaks roughly match.

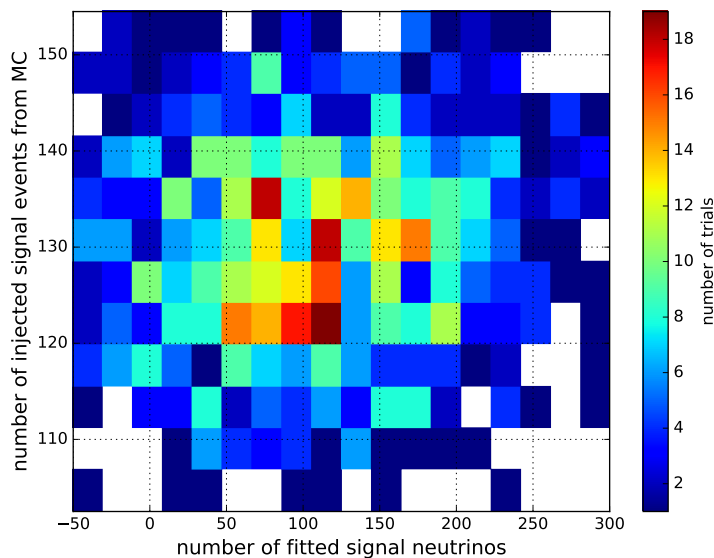


Figure 5.28.: Number of injected signal events against the number of fitted signal events for signal-contaminated trial runs (for the example of a  $100 \text{ GeV}/c^2$  WIMP annihilating to  $b\bar{b}$  pairs).

The obtained  $\mu_{\text{fit}}^{90\%}$  and the formalism which allows for the calculation of cross-section sensitivities from the best-fit results will be presented in the following section.

## 5.6 Sensitivities on the Spin-Dependent WIMP-Proton Scattering Cross-Section

In order to not bias the analysis results towards a positive or negative outcome, the development of the analysis technique and event selection were performed in a *blind* way [198]. For blind analyses, usually only a fraction of detector data is used during the development of the cuts and the likelihood code. An *unblinding* is then granted after careful review of the analysis procedure under the condition that all cut values and other tuning possibilities are frozen. Consequently, observational limits can be calculated.

Since this work requires a high-statistics background sample (see previous section), the complete set of experimental data was used, while omitting a crucial quantity – the azimuth angle. Consequently, this angle is uniformly scrambled for all background events and a signal discovery (or a null result) can thus not be artificially attained. However, a sensitivity can be calculated given the assumption that all data are background events – which practically can also be assumed for an unblinded data sample, since data on the final selection level are still dominated by background (see section 5.3).

The purpose of this work is a feasibility study of the all-flavor approach, which trades the better pointing resolution of tracks for a stronger signal and a better energy reconstruction. In addition, a novel resolution estimator and a state-of-the-art likelihood procedure were employed. The numbers presented in this section will make clear that this approach is especially beneficial for low-mass WIMP candidates which are associated with low-energy signal neutrinos.

The fit procedure described in the previous section yields a sensitivity on a number of signal events ( $\mu_{\text{fit}}^{90\%}$ ) from which a sensitivity on the WIMP annihilation rate  $\Gamma_A$  at the solar core can be calculated:

$$\mu_{\text{fit}}^{90\%} = \Gamma_A \cdot W_{\text{tot}} \cdot t_{\text{live}} \quad \Leftrightarrow \quad \Gamma_A = \frac{\mu_{\text{fit}}^{90\%}}{W_{\text{tot}} \cdot t_{\text{live}}} \quad , \quad (5.19)$$

where

$$W_{\text{tot}} = \sum_i W_i \quad (5.20)$$

is the sum of the respective signal event weights  $W_i$  and

$$t_{\text{live}} = 2.6312452 \cdot 10^7 \text{ s} \approx 304.5 \text{ d} \quad (5.21)$$

is the total duration of the data-taking period (*livetime*), considering the exclusions discussed in section 5.2. Keeping in mind that the event weights are given in units of signal events per annihilation, the annihilation rate can be regarded as a scaling factor which (together with the livetime) adjusts the signal to the magnitude determined by the likelihood fit.

In order to convert the obtained self-annihilation rate to a WIMP scattering cross-section, knowledge of the local dark matter density, the sun's velocity relative to the halo and the

local dark matter dispersion velocity is required. While an analytic approximation can be found (see equation 5.8), this work uses the approach of numerical evaluation [162, 199] of the integrals which were introduced in section 5.1. As also mentioned in section 5.1, the astrophysical values from [81, 162] are adopted, with the exception of the local dark matter density, which is set to  $\rho_0 = 0.39 \text{ GeV c}^{-2}/\text{cm}^3$ , as motivated in [159, 160]. The so-obtained cross-section sensitivities are summarized in table 5.3, together with the respective likelihood best-fit values and sensitivities on the WIMP annihilation rate. Smaller values correspond to better sensitivities. At this point, it is worth noting that the numbers in table 5.3 do not include systematic uncertainties yet – these will be discussed in the following section.

WIMP mass [GeV/c <sup>2</sup> ]	Annihilation Channel	Signal Eff. [%]	$\mu_{\text{fit}}^{90\%}$ [events]	$\Gamma_A$ [1/s]	$\sigma_{\text{SD}}^{\chi:P}$ [cm <sup>2</sup> ]
35	$b\bar{b}$	12.0	156.6	$1.48 \cdot 10^{24}$	$1.42 \cdot 10^{-39}$
	$\tau^+\tau^-$	10.2	144.9	$8.21 \cdot 10^{22}$	$7.90 \cdot 10^{-41}$
50	$b\bar{b}$	10.6	140.6	$8.51 \cdot 10^{23}$	$1.50 \cdot 10^{-39}$
	$\tau^+\tau^-$	8.1	137.4	$4.38 \cdot 10^{22}$	$7.71 \cdot 10^{-41}$
100	$b\bar{b}$	7.9	138.9	$3.42 \cdot 10^{23}$	$2.12 \cdot 10^{-39}$
	$\tau^+\tau^-$	4.3	102.9	$1.29 \cdot 10^{22}$	$8.02 \cdot 10^{-41}$
	$W^+W^-$	4.7	106.2	$2.74 \cdot 10^{22}$	$1.70 \cdot 10^{-40}$
250	$b\bar{b}$	4.5	119.0	$1.06 \cdot 10^{23}$	$3.85 \cdot 10^{-39}$
	$\tau^+\tau^-$	2.3	71.8	$3.08 \cdot 10^{21}$	$1.11 \cdot 10^{-40}$
	$W^+W^-$	2.2	69.1	$7.08 \cdot 10^{21}$	$2.56 \cdot 10^{-40}$
500	$b\bar{b}$	3.3	112.9	$5.40 \cdot 10^{22}$	$7.65 \cdot 10^{-39}$
	$\tau^+\tau^-$	1.6	53.7	$1.52 \cdot 10^{21}$	$2.15 \cdot 10^{-40}$
	$W^+W^-$	1.5	47.4	$3.91 \cdot 10^{21}$	$5.53 \cdot 10^{-40}$
1000	$b\bar{b}$	2.0	76.4	$3.13 \cdot 10^{22}$	$1.76 \cdot 10^{-38}$
	$\tau^+\tau^-$	1.2	39.9	$1.03 \cdot 10^{21}$	$5.75 \cdot 10^{-40}$
	$W^+W^-$	1.1	39.1	$3.49 \cdot 10^{21}$	$1.96 \cdot 10^{-39}$

Table 5.3.: Final level efficiencies (with respect to level 2), the best-fit sensitivity on the number of signal events as well as the respective annihilation rate and WIMP-proton scattering cross-section sensitivities for all WIMP masses and annihilation channels studied.

The sensitivities on the WIMP-proton elastic scattering cross-sections are shown in figure 5.29. The likelihood analyses were performed at discrete intervals of the mass range; for sample points at 35, 50, 100, 250, 500 and 1000 GeV/c<sup>2</sup>. The resulting sensitivity points were connected to guide the eye. While the effective volume, as expected, falls for lower candidate masses (figure 5.14), the sensitivity in the low-energy regime stays fairly constant. This is due to a  $m_\chi^{-2}$  dependence of the signal expectation [161] and a much better signal efficiency at lower energies. Also, since reconstruction and resolution estimation are performed based on a cascade hypothesis, the significant muonic component

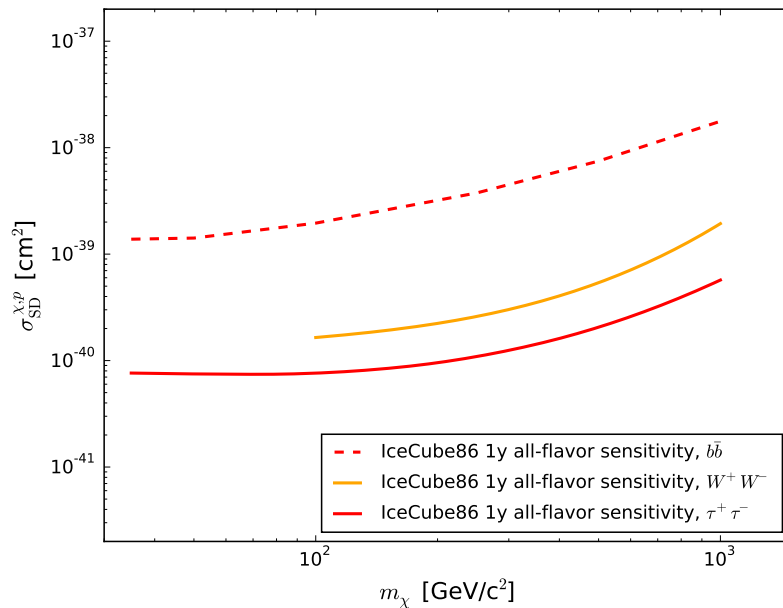


Figure 5.29.: Spin-dependent scattering cross-section sensitivities for three neutralino branching channels ( $b\bar{b}$ ,  $W^+W^-$  and  $\tau^+\tau^-$ ), obtained with one year of data from the IceCube detector in its full 86-string instrumentation.

(which has a larger hadronic portion at lower energies) can be exploited better in the spatial part of the likelihood formalism (see section 5.5). Furthermore, the background discrimination benefits from a much more restricted energy range and a better spatial containment. For larger candidate masses, the sensitivities are inferior when compared to track-based analyses which exploit the full IceCube detector [200], as will be seen in the following section. The parallel development of an independent high-energy event selection is required in order to obtain optimal sensitivities for larger candidate masses, since the effective area of the densely instrumented DeepCore region only dominates for energies below  $\sim 100$  GeV [122].

## 5.7 Systematic Uncertainties

The likelihood analysis (see section 5.5) uses scrambled experimental data for an estimation of the background levels. Therefore the background trials are not subject to uncertainties from atmospheric flux models, neutrino cross-sections or the detector modeling. The obtained signal sensitivities, however, are calculated by injection of simulated signal events and as such depend on the correct modeling of the detector response and the detector medium as well as particle physics uncertainties, such as interaction cross-sections and neutrino flavor oscillation parameters. Astrophysical uncertainties, like the local dark matter density, are another significant contribution which will be briefly discussed at the end of this section.

In an earlier solar WIMP study [201], which used the same signal simulation code as this analysis, the efficiency of the optical modules and the light absorption and scattering in the glacial ice were found to be the primary sources of detector related uncertainties. Other sources, e.g. from time and position calibration, play a minor role. The dominant uncertainty contribution, especially at lower energies, is the absolute light detection efficiency of the DOMs which is therefore concentrated on for the quantitative study of systematics in this work. The DOM efficiency is a linear scaling parameter which quantifies how well the detected light can be transformed to an electrical signal. Considering the quantum efficiency of the PMT, the opacity of the optical gel and the glass housing (see figure 3.2) as well as the contribution from the re-frozen hole ice, a conservative estimate of  $\pm 10\%$  was chosen which approximately corresponds to laboratory measurements of this quantity's deviation [118].

The effects of a varied efficiency are assessed by the production of signal datasets for which the efficiency of the DOMs was artificially lowered or increased by 10%. These systematic datasets are processed through the whole simulation and event selection chain while all cut parameters are left unchanged with respect to the baseline datasets. The systematically adjusted signal is subsequently used for the likelihood fit procedure which is also conducted with the same settings. In this way, the systematic effect on the final sensitivities can be directly determined.

The sensitivity ranges which arise from the DOM efficiency uncertainty are shown in figure 5.30. Since the optimizations on the PDF binning and the BDT cut value are adapted without change from the baseline runs, in a few cases the resulting sensitivities for an increased DOM efficiency are about equal or even slightly worse when compared to the baseline results. The uncertainty for a given combination of the WIMP mass and the annihilation channel is taken as the half width of the error bands presented in figure 5.30.

The effect from photon scattering and absorptivity uncertainties in the ice model is considered with an approximate magnitude of 10% [182, 201] for the energy regime studied in this work.

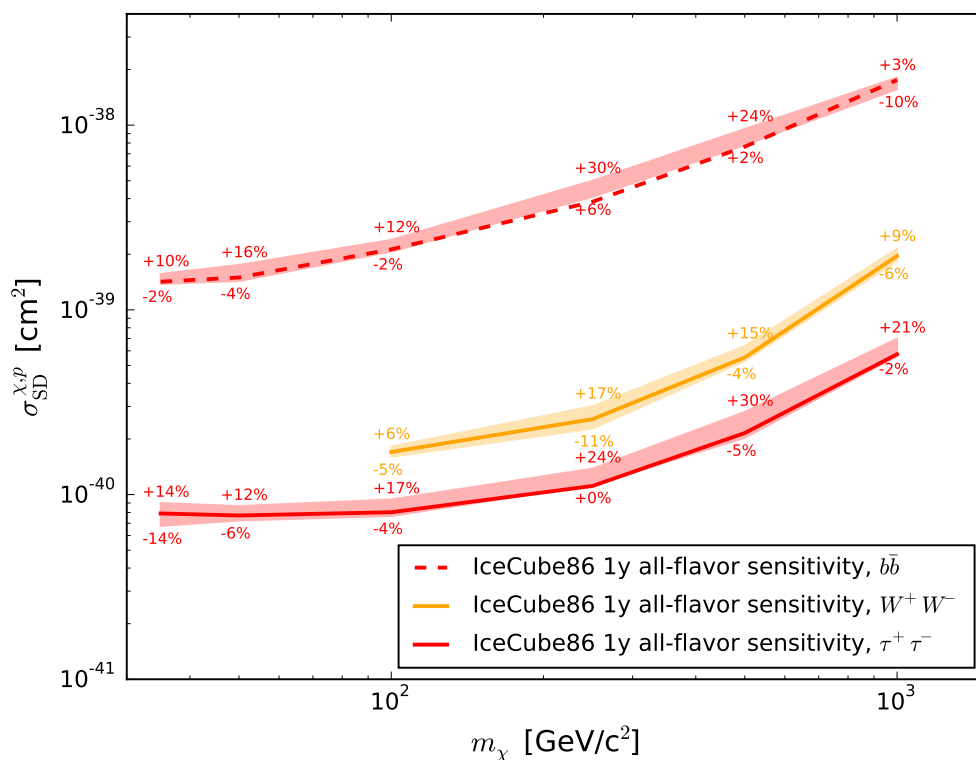


Figure 5.30.: All-flavor based spin-dependent scattering cross-section sensitivity band for DOM efficiencies varied by  $\pm 10\%$ , together with the corresponding relative deviation from the baseline sensitivities. The latter are shown for reference.

Coincident events from atmospheric showers are not included in the signal simulation, but would rather matter at higher candidate masses. Experimental data naturally includes coincident events, they are, however, mostly removed by a topological splitting algorithm, which is part of the event filtering (see section 5.3) and is thus applied to both data and simulations. This algorithm, however, does not work at 100% efficiency. The error introduced by missing coincident events in the simulated signal is estimated to be about 1% [182].

A second class of uncertainties is associated with the imprecise measurements of neutrino oscillation and interaction magnitudes as well as the errors introduced by the approximation and the simplification of the employed signal model.

The neutrino oscillation parameters introduce significant uncertainties (see equation 2.17) and so do the used DIS neutrino-nucleon interaction cross-sections (see figure 2.7) which are parametrized using the fits described in [100]. The uncertainty contribution from neutrino cross-section approximations is estimated to 10%, while the effect of the neutrino flavor oscillation parameter errors is adapted from [182] with a magnitude of 6%.

Non-DIS CC interactions are ignored by the codes used [81, 100]. In figure 2.7, it can,

however, be seen that for neutrino energies below  $\approx 30$  GeV the quasi-elastic scattering and resonant pion production have to be taken into account for a precise description. This effect therefore dominates for the lightest WIMP candidates. Ignoring the part of the potential signal which would arise from QES and RES interactions will yield conservative results. A quantitative contribution to the total uncertainty will therefore not be considered for this error.

For solar dark matter capture by spin-dependent elastic scattering, the code used [162] ignores elements other than hydrogen. The relative effect on the capture rate is at a few percent for lower dark matter masses [202], however increases to about 20% at  $m_\chi = 1$  TeV/ $c^2$ . The sole consideration of hydrogen results in a conservative signal assumption and is therefore not considered as a (two-sided) uncertainty.

Finally, the total uncertainty is the root of the discussed contributions added in quadrature.

WIMP mass [GeV/ $c^2$ ]	Annihilation Channel	DOM Eff. [%]	Ice Model [%]	Coincident Events [%]	$\nu$ $\sigma^{\text{CC}}$ [%]	$\nu$ Osc. [%]	Total [%]
35	$b\bar{b}$	6.3	10	1	10	6	16.6
	$\tau^+\tau^-$	14.2					21.0
50	$b\bar{b}$	10.0					18.4
	$\tau^+\tau^-$	9.0					17.8
100	$b\bar{b}$	6.3					16.6
	$\tau^+\tau^-$	14.2					21.0
	$W^+W^-$	6.4					16.7
250	$b\bar{b}$	10.0					18.4
	$\tau^+\tau^-$	9.0					17.8
	$W^+W^-$	13.9					20.7
500	$b\bar{b}$	7.3					17.0
	$\tau^+\tau^-$	10.3					18.5
	$W^+W^-$	9.4	18.0				
1000	$b\bar{b}$	10.1	18.4				
	$\tau^+\tau^-$	10.3	18.5				
	$W^+W^-$	7.7	17.2				

Table 5.4.: Individual and total relative uncertainties from various error sources, shown for each combination of the WIMP candidate mass and the annihilation channel.

The third uncertainty class is given by astrophysical quantities such as the local density and the velocity distribution of dark matter which both affect the magnitude of the solar dark matter capture and thus enter the numerical calculation of scattering cross-sections from solar self-annihilation rate sensitivities. These quantities are subject to significant uncertainties and further depend on the method by which they were determined.

For this work, a local dark matter density value of  $\rho_0 = 0.39 \text{ GeV c}^{-2}/\text{cm}^3$  [159, 160] is adapted. A recent study of giant star kinematics suggests even larger values for  $\rho_0$  [203]. Some indirect searches, however, tend to present their limits based on the formerly established value of  $0.30 \text{ GeV c}^{-2}/\text{cm}^3$ . Limits or sensitivities can be easily adjusted to a different dark matter density since they scale proportionally (larger densities yield smaller sensitivity values, i.e. sensitivities to smaller WIMP scattering cross-sections).

A detailed discussion of the impact of the local dark matter velocity distribution and a potential dark disk on solar dark matter capture can be found in [204]. The authors conclude that the effects of the former are not very significant. For the spin-dependent scattering scenario, the estimated uncertainty effect for  $20 \text{ GeV}/c^2$  WIMPs is less than 24 %, taking into account the local circular speed, a high-velocity cutoff and a deviation of the velocity distribution function (VDF) from a Maxwellian approximation. The impact of the latter on the capture rate is suppressed since its magnitude is obtained through an integration over a broad velocity range. Simplifications introduced by high-velocity cutoffs are not very significant, because solar capture cannot occur efficiently for high relative velocities. For larger candidate masses the total (velocity-related) uncertainty increases, but does not exceed 50 %.

An additional accretion of dark matter near the spiral structure of the Milky Way would result in an increase of the local dark matter density and as such would boost solar capture significantly [204], because this dark matter would rotate with a similar velocity as the solar system and capture in the sun would thus be very efficient due to the low relative velocity. Direct searches, however, would not benefit significantly, since they depend on WIMPs being fast in order to produce detectable nuclear recoils. The existence of such a co-rotating dark disk is usually not considered in the community of indirect searches and is consequently also neglected in this work, resulting in conservative values for the obtained sensitivities.

The elemental composition of the sun and nuclear form factors are another source of uncertainty associated with dark matter scattering and energy loss in the sun. This effect is however only significant for the spin-independent interaction scenario and would result in an uncertainty level of around 15 %. The spin-dependent scattering, which is considered for this work, neglects all solar elements other than hydrogen. If the elemental composition were to be considered, the quantitative uncertainty effect would only be about 2 %, since the solar hydrogen abundance is well-known, in contrast to heavier elements [205].

The results of this work are based on astrophysical assumptions that are broadly used in the community and thus uncertainties which are associated with the respective astrophysical quantities are not included, in consistency with previous studies [200, 201, 206].

Figure 5.31 finally shows the resulting sensitivities including the uncertainties discussed above – their deviations are summarized in table 5.4. Figures 5.32 and 5.33 show comparisons to a track-based analysis of IceCube data [207] and to recent results published by the SUPER-K [208] and PICO-2L [209] collaborations, respectively. Comparing to

one-year sensitivities of track-based IceCube searches, the all-flavor approach is beneficial for WIMP masses below  $\sim 70 \text{ GeV}/c^2$  for the hard  $\tau^+\tau^-$  channel and below  $\sim 200 \text{ GeV}/c^2$  for the soft  $b\bar{b}$  channel.

In the following chapter, the obtained sensitivities (from this point forward including systematic uncertainties) will be interpreted in a supersymmetric framework.

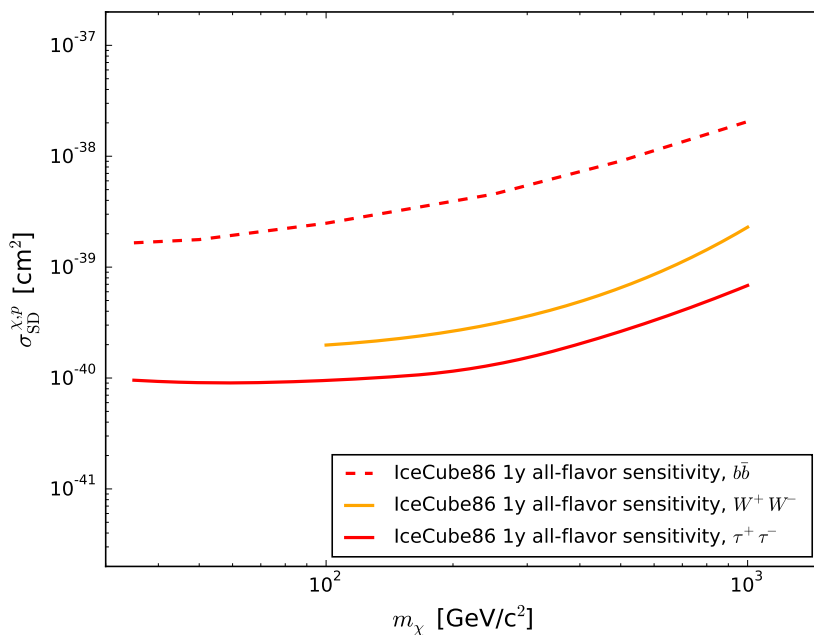


Figure 5.31.: Spin-dependent scattering cross-section sensitivities including systematic uncertainties, shown for the three neutralino branching channels studied ( $b\bar{b}$ ,  $W^+W^-$  and  $\tau^+\tau^-$ ). The sensitivities were obtained by an analysis of one year of data collected with the IceCube detector in its full 86-string instrumentation.

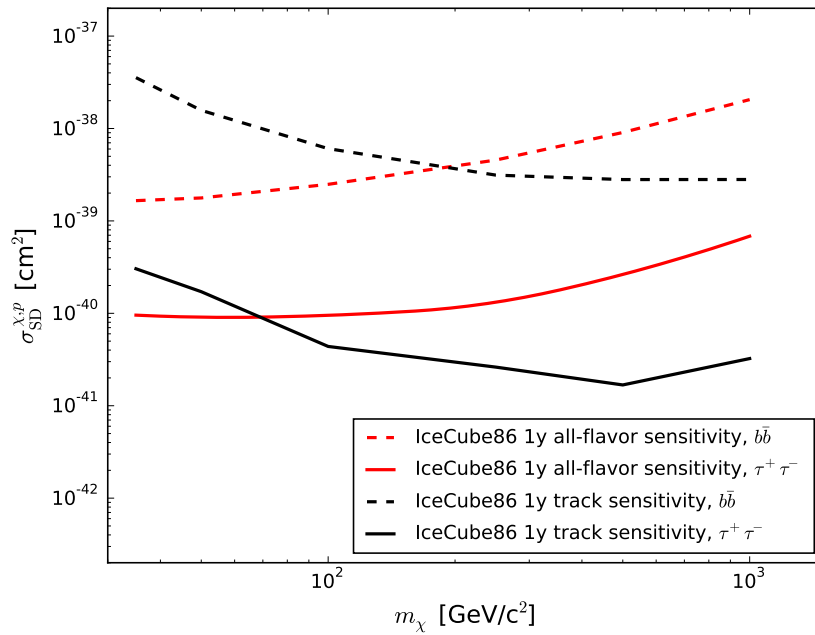


Figure 5.32.: Comparison of the all-flavor based spin-dependent scattering cross-section sensitivities (including systematic uncertainties) to those obtained by a track-focused analysis of IceCube data [207]. Note that the track-based sensitivities have been scaled to a local dark matter density of  $\rho_0 = 0.39 \text{ GeV c}^{-2}/\text{cm}^3$  and one year of data-taking to facilitate the comparison.

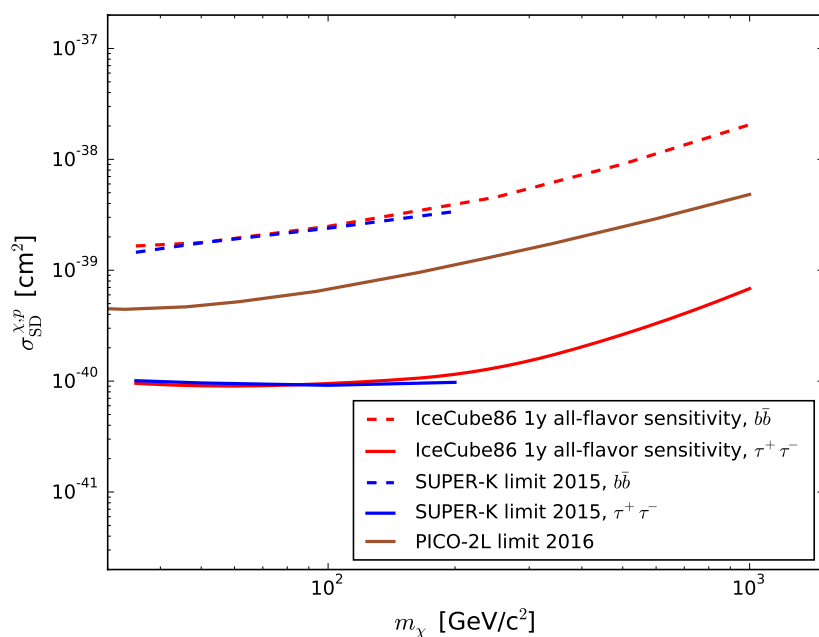


Figure 5.33.: Comparison of the all-flavor based spin-dependent scattering cross-section sensitivities (including systematic uncertainties) to limits from SUPER-K [208] and the direct-detection limit from the PICO-2L experiment [209]. The latter is independent of annihilation channels. Note that these limits have been scaled to a local dark matter density of  $\rho_0 = 0.39 \text{ GeV c}^{-2}/\text{cm}^3$  to facilitate the comparison.

# 6

## Supersymmetric Model Scans

You know you have a distributed system when the crash of a computer you've never heard of stops you from getting any work done.

---

Leslie Lamport

The results discussed in the last chapter provide sensitivity limits on a generic dark matter property, the spin-dependent WIMP-proton elastic scattering cross-section. They can, in principle, be interpreted in any theoretical framework that offers a stable and neutral Majorana particle with weak scale interactions and a sufficiently high mass (about 10–1000 GeV/c<sup>2</sup>). The supersymmetric neutralino, as motivated in section 1.3, is a popular particle candidate for dark matter. Therefore it is intriguing to interpret our results in a detailed manner within the supersymmetric paradigm.

Taking into account current cosmological and Standard Model measurements, a large number of models were calculated in the framework of the so-called phenomenological MSSM which is characterized by 19 independent model parameters. Initially, about 100 billion independent models were computed, of which about 100 thousand complied with recent accelerator and cosmological measurements. Scattering and annihilation cross-sections as well as neutralino annihilation branching ratios are available for each individual model and can be used to study the complementarity between direct searches and IceCube's indirect exclusion capabilities. Since IceCube exclusions are not presented on an individual model basis, but rather as (sensitivity) limits on generic hard and soft annihilation channels, it is instructive to consider how hard the energy spectrum of the neutrinos produced from neutralino self-annihilations is for each model.

Section 6.1 will discuss the motivation for performing new model scans taking into account the relevant Standard Model parameters which were obtained or refined in recent years. The ranges of the assumed prior parameters and their distribution within these ranges will be presented in section 6.2. The resulting quantities will be shown in section 6.3, together with a discussion of posterior constraints. Finally, the remaining

models are put in context of the sensitivity limits discussed in the last chapter and the sensitivities are compared to limits from direct searches (section 6.4).

## 6.1 Motivation

The 19-parameter phenomenological MSSM (pMSSM), as motivated in section 1.3, is a popular compromise between phenomenological flexibility and computational accessibility. Assuming the phenomenological constraints discussed in [32, 38] (see section 1.3 for a short list), the pMSSM is characterized by 19 real and independent input parameters in the supersymmetric Lagrangian: five first/second generation sfermion masses ( $m_{\tilde{q}}, m_{\tilde{u}_R}, m_{\tilde{d}_R}, m_{\tilde{l}}, m_{\tilde{e}_R}$ ), five third generation sfermion masses ( $m_{\tilde{Q}}, m_{\tilde{t}_R}, m_{\tilde{b}_R}, m_{\tilde{L}}, m_{\tilde{\tau}_R}$ ), three gaugino (bino, wino, gluino) masses ( $m_{\tilde{B}}, m_{\tilde{W}}, m_{\tilde{g}}$ ), the Higgsino mixing parameter ( $\mu$ ), the pseudoscalar Higgs boson mass ( $m_A$ ), the ratio of the vacuum expectation values of the two Higgs doublets ( $\tan\beta$ ) and the third generation trilinear<sup>1</sup> coupling mass parameters ( $A_t, A_b, A_\tau$ ). In order to perform a scan of this multi-dimensional space, the `micrOMEGAs` code [212] is employed which internally uses further modules, such as the `CalcHEP` [213] and the `SuSpect` [214] packages.

The introduction of superpartner fermions and bosons can have a significant impact on the magnitude of Standard Model processes. One example is the helicity suppressed decay of the  $B_s$  meson to muons,  $B_s \rightarrow \mu^+ \mu^-$ . This is a purely leptonic decay which involves a flavor changing neutral current (FCNC). In supersymmetric extensions, such currents can be mediated by the exchange of neutral Higgs bosons which would not be subject to helicity suppression, resulting in a significant increase of the branching fraction for this process [215]. Although the effect is not severe in the scope of the pMSSM [216, 217], the  $B_s \rightarrow \mu^+ \mu^-$  branching fraction is included for the scans and required to be between  $2.2 \cdot 10^{-9}$  and  $3.5 \cdot 10^{-9}$ , in agreement with the results published in [218, 219].

Furthermore, a novel measurement of the CKM<sup>2</sup> matrix element  $|V_{ub}|$  [222] is included for the model calculations. The `micrOMEGAs` code uses the phase space ratio  $C$ , a quantity which absorbs  $|V_{ub}|$ ,  $|V_{cb}|$  and two radiative decay widths of the  $B$  meson [223]. The default values for the calculation of the phase space ratio are originally adapted from [224], but for this work were replaced by more recent results from [222, 225].

The impact of the Higgs mass measurement will be subject to a separate consideration by imposing a-posteriori constraints on non-excluded pMSSM models (see section 6.3).

<sup>1</sup>Supersymmetric squarks and sleptons have interactions similar to the trilinear self-couplings of gauge bosons in the Standard Model, e.g. the coupling of two oppositely charged  $W$  bosons to a  $Z^0$  or  $\gamma$  boson [210]. Since the associated first and second generation Yukawa couplings are small, only third generation trilinear couplings are being considered. Further details on trilinear couplings in the supersymmetric context can e.g. be found in [211].

<sup>2</sup>The Cabibbo–Kobayashi–Maskawa matrix is a unitary matrix that describes the mixing of the weak quark eigenstates [220, 221], quite similar to the leptonic PMNS matrix which was introduced in equation 2.5.

## 6.2 Prior Ranges and Distribution

The prior ranges chosen follow earlier scans described in [38, 226], with minor modifications that were coordinated with the authors of the `micrOMEGAs` code. In order to map both the low and high neutralino mass regions, prior values are drawn according to a logarithmic as well as a uniform distribution. The two independent model sets are later combined for a maximal model space coverage. The parameter ranges differ for these two cases: priors that follow the logarithmic distribution allow for more extended parameter ranges compared to uniformly drawn (*flat*) priors. The input parameters and the allowed ranges for both prior distributions are provided in table 6.1.

prior	$\log_{10}$ distribution	flat distribution
$ \mu $	50–2000	50–2000
$m_A$	50–10000	50–4000
$\tan \beta$		1–60
$ m_{\tilde{B}} $	50–10000	50–4000
$ m_{\tilde{W}} $	50–10000	50–4000
$m_{\tilde{g}}$	300–10000	300–4000
$ A_t ,  A_b ,  A_\tau $	0.01–10000	0.01–4000
$m_{\tilde{u}_R}, m_{\tilde{d}_R}, m_{\tilde{t}}, m_{\tilde{e}_R}$	100–10000	500–4000
$m_{\tilde{q}}$	1000–10000	1000–4000
$m_{\tilde{t}_R}, m_{\tilde{b}_R}, m_{\tilde{L}}, m_{\tilde{\tau}_R}$	100–10000	500–4000
$m_{\tilde{Q}}$	1000–10000	1000–4000

Table 6.1.: Ranges for logarithmic and uniform distributions of input parameters in units of  $\text{GeV}/c^2$  (except for  $\tan \beta$ ). While some quantities share the same range and are thus grouped in the same row for a better readability, their values are still drawn independently. Values for  $\tan \beta$  are always taken from a uniform distribution.

## 6.3 Model Characteristics and posterior Constraints

The individual models are fixed by the choice of input priors and the updated Standard Model properties discussed in section 6.1. In order to be considered as *valid* and subsequently be written out, models are required to yield a suitable dark matter particle candidate in the form of the lightest neutralino which is furthermore required to be compatible with an upper bound relic density as measured by the PLANCK satellite (see equation 1.15).

Being considered as valid, a number of neutralino properties (scattering and annihilation cross-sections, mass, self-annihilation branching fractions) are extracted and written out for each model, in addition to the Higgs mass and the relic dark matter density under

the assumptions that it would be made up by exactly one particle type; the lightest neutralino  $\chi_1^0$  (also denoted as “ $\chi$ ” for simplification).

In the assumed supersymmetric framework, the boson which was discovered a few years ago [29] is interpreted as the light Higgs boson  $h$  (see table 1.1). Considering the uncertainty associated with the mass measurement [30], valid models are required to yield a Higgs mass between 124 and 126  $\text{GeV}/c^2$ . From the distribution of the Higgs mass  $m_h$  (see figure 6.1), it can be easily seen that most models resulting from logarithmic priors produce Higgs masses below this range. This is also true for flat prior models. In this case, however, a larger model fraction can be retained after the cut on the Higgs mass. The impact of the cut on the quantity which is most relevant for this work, the spin-dependent neutralino-proton cross-section, is shown in figure 6.2.

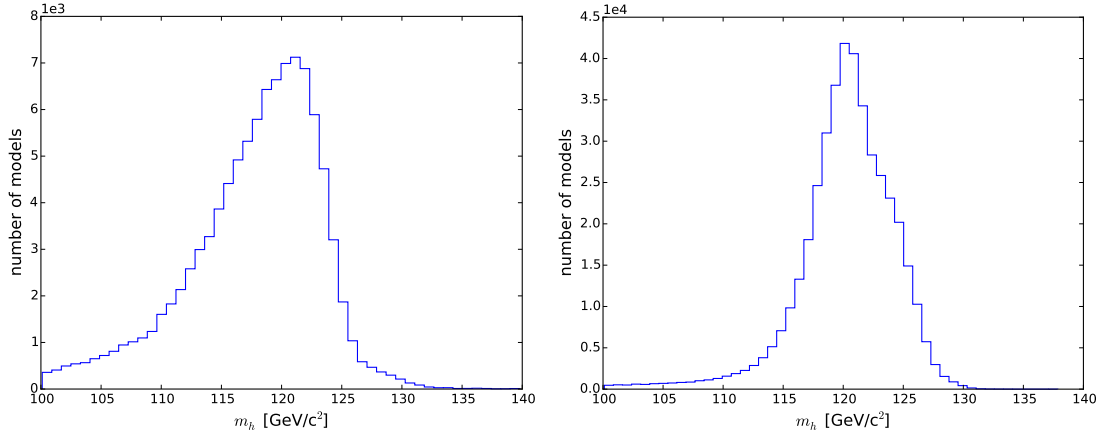


Figure 6.1.: Distribution of  $m_h$  in valid supersymmetric models, for (left) logarithmic and (right) uniform priors. Statistics were reduced for these plots.

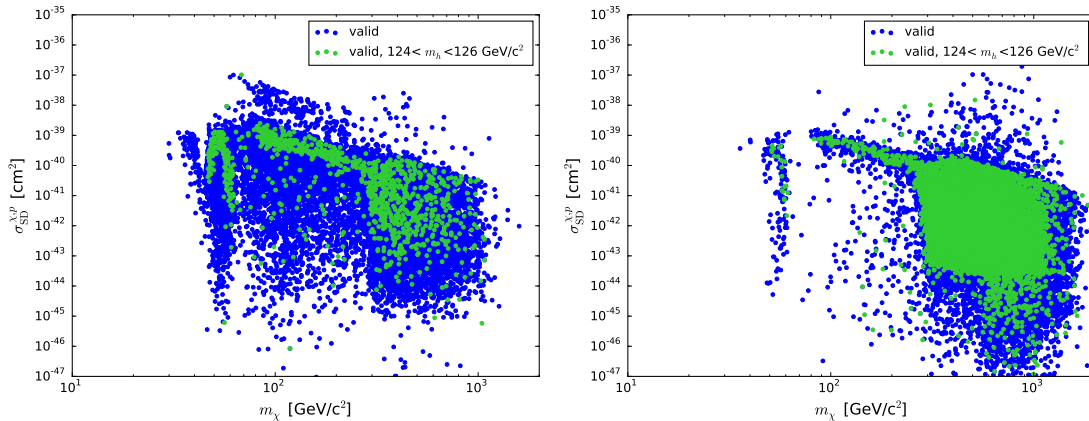


Figure 6.2.: Impact of the Higgs mass cut on the spin-dependent neutralino-proton scattering cross-section as function of the neutralino mass, for (left) logarithmic and (right) uniform priors. Statistics were reduced in these plots to help distinguish the distributions.

At this point, it is important to note that the density of model points is strongly prior dependent and thus does not hint toward “likely” regions of supersymmetry. Parameter regions containing (even few) models could be arbitrarily filled by customized scans.

Next, the relic density  $\Omega_C h^2$  is constrained, in compliance with cosmological measurements [3]. Here,  $h$  denotes the dimensionless Hubble parameter. With the Higgs mass constrained to the range discussed above, the distributions of the relic density are shown in figure 6.3. The model sets based on both logarithmic and flat priors produce many models with relic densities well below the measured value of  $\sim 0.12$ . Considering the uncertainties of equation 1.15, the relic density is required to lie between 0.115 and 0.125. With the possibility of a multi-component dark matter, the supersymmetric neutralino could have any relic density as long as it does not exceed the measured value. However, the employed signal model [81] assumes the WIMP dark matter to consist of only *one* particle type, as do most direct dark matter searches.

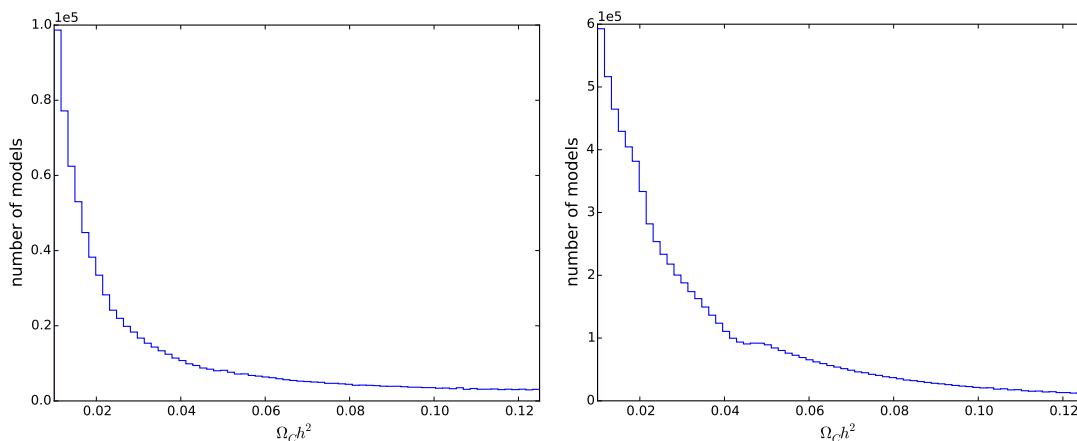


Figure 6.3.: Distribution of the dark matter relic density in valid supersymmetric models with the Higgs mass constrained, for (left) logarithmic and (right) uniform priors. Statistics were reduced for these plots.

As the model calculations are time-consuming, they were distributed among many CPU cores. With an average model execution time of about 0.1s on AMD Opteron 6272 units, about 100 billion models were calculated, corresponding to a total (single-CPU) runtime of about 300 years. Due to the generously chosen parameter ranges (table 6.1), only 0.1% of all probed models pass as “valid”. The number of models is subsequently strongly reduced by cuts on the Higgs mass and the relic density of the neutralino (as described above). Absolute numbers for each stage are provided in table 6.2.

The following section will discuss the complementarity between direct and indirect searches. From this point forward, the model sets produced with logarithmic and flat priors are combined.

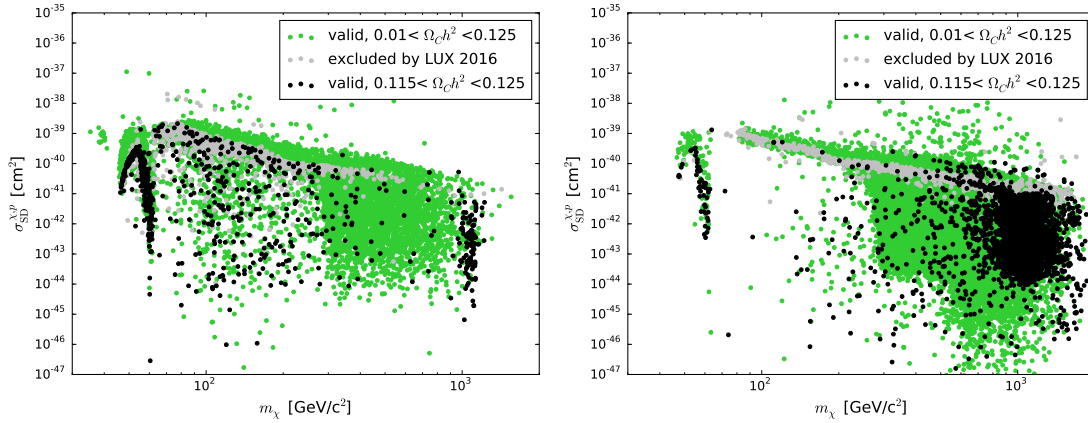


Figure 6.4.: Impact of the dark matter relic density cut on the spin-dependent neutralino-proton scattering cross-section as function of the neutralino mass, for (left) logarithmic and (right) uniform priors. Models excluded by the LUX experiment [227] are shown in gray. Statistics were reduced in these plots for a better visibility.

	log <sub>10</sub> priors	flat priors	total
scanned			95·10 <sup>9</sup>
“valid” (see text)	16·10 <sup>6</sup>	71·10 <sup>6</sup>	87·10 <sup>6</sup>
after $m_h$ cut	0.9·10 <sup>6</sup>	7.5·10 <sup>6</sup>	8.4·10 <sup>6</sup>
after $\Omega_C h^2$ cut	8·10 <sup>3</sup>	71·10 <sup>3</sup>	79·10 <sup>3</sup>

Table 6.2.: Number of models scanned at generation and at the subsequent filter stages.

## 6.4 Cross-Section Exclusion Complementarity between Direct and Indirect Measurements

The sensitivities obtained in section 5.6 constrain the spin-dependent neutralino-proton cross-section. This cross-section is available for each individual supersymmetric model, and so is the spin-independent cross-section which is usually constrained by direct-detection experiments. Figure 6.5 shows the spin-dependent cross-section of the models together with the sensitivities obtained by the analysis of IceCube data (see previous section). Distinct features and shapes can be spotted in the model distribution. They are symptoms of disallowed regions and/or parameter combinations and will not be discussed in further detail. Individual models which are excluded by direct searches [227] are marked in gray. Model points which are not excluded by direct searches are presented by means of a continuous color scale which is associated with the hardness of the neutrino spectrum produced after neutralino self-annihilations. Sensitivities related to a rather hard spectrum ( $\tau^+\tau^-$ ,  $W^+W^-$ ) can therefore only exclude models marked as “hard” while the sensitivity lines for the soft benchmark annihilation channel ( $b\bar{b}$ )

exclude all models with larger cross-sections. The value for the model hardness was approximated by adding the branching fractions of the two hard annihilation channels which were considered and subtracting the branching fraction of the benchmark soft annihilation channel:

$$\text{hardness} = \mathcal{B}(\chi_1^0 \chi_1^0 \rightarrow \tau^+ \tau^-) + \mathcal{B}(\chi_1^0 \chi_1^0 \rightarrow W^+ W^-) - \mathcal{B}(\chi_1^0 \chi_1^0 \rightarrow b \bar{b}) \quad . \quad (6.1)$$

A difference of branching fractions was preferred over a ratio since other annihilation channels which produce neutrino spectra with intermediate energies also exist. The actual neutrino spectra, which result from mixed-channel models, could not be assessed since the employed signal simulation only produces data samples for the pure branching of a specific annihilation channel.

While IceCube can definitely cut some areas of parameter space, this is not very severe in the scope of the pMSSM. However, the presented exclusion lines are shown for an analysis of only one year of data-taking. With e.g. ten years of experimental data the sensitivities are expected to improve by more than a factor of three. Progress in analysis and data selection techniques as well as event reconstructions may result in additional improvements as well.

The spin-independent cross-section is shown in figure 6.6, where models excluded by limits presented in [227] are shown in gray. The same excluded models were previously shown in figure 6.5, allowing for a comparison of LUX and IceCube. It should be noted that limits calculated in [227] constrain the (proton-neutron averaged) neutralino-nucleon cross-section, whereas the quantity available from the scans performed in this work (and constrained by IceCube analyses) is the neutralino-proton cross-section – which is typically 10–20% smaller than the neutralino-neutron cross-section. The error introduced by this approximation is thus less than 10% and is varying between individual models.

The relation of spin-dependent and spin-independent scattering cross-sections is shown in figure 6.7. Leaving aside the neutralino mass dependence on the sensitivities obtained, direct and indirect searches typically constrain from two different sides (from the right and from the top) and thus naturally provide complementarity. For reference, the (velocity-averaged) annihilation cross-section is shown in figure 6.8 including recent limits from a joint analysis of data from the Fermi-LAT and MAGIC experiments. Their exclusion potential in the scope of the pMSSM is only marginal. The natural scale (equation 1.19) is also shown, including the slight dependence on the WIMP mass [228].

Limits from accelerator studies were not included in this work, since they have been studied extensively in literature. The complementarity of accelerator measurements for a similar model space is shown in [229]; it can be seen that the strength of the LHC experiments lies in probing lower-mass WIMP candidates with scattering cross-sections that are inaccessible to direct searches. While exclusion capabilities obtained with the LHC data from the first run are very limited in the scope of the pMSSM, a significant portion of the parameter space will be probed after the analysis of data from the second LHC run [230].

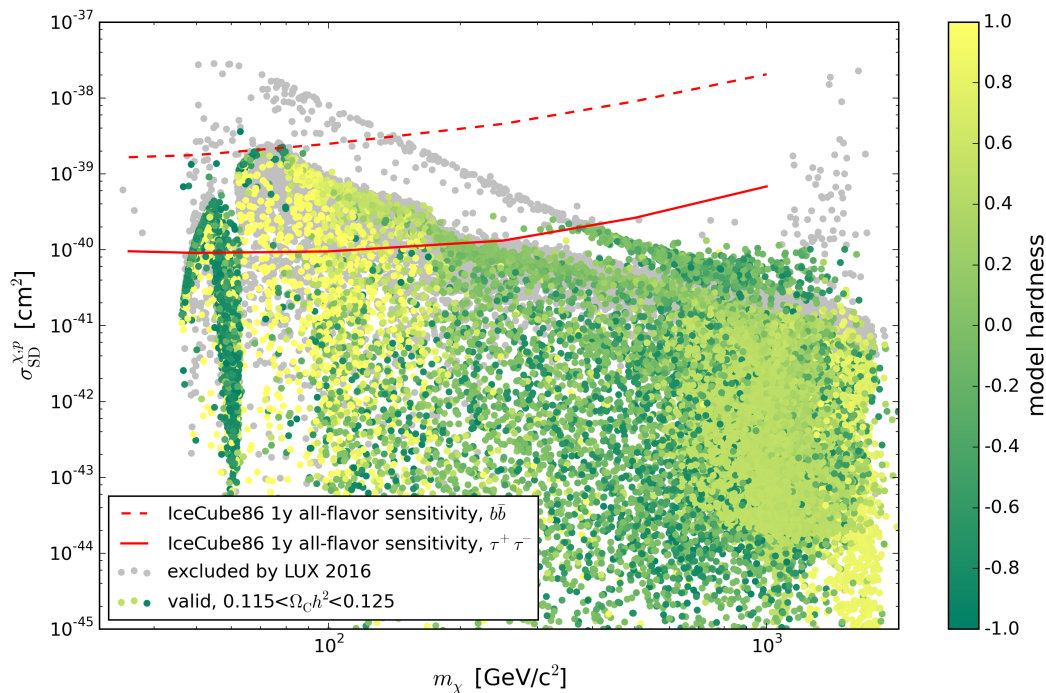


Figure 6.5.: Spin-dependent neutralino-proton scattering cross-section of scanned models as a function of neutralino mass. Each point marks a valid pMSSM model, with its lightest neutralino being a valid WIMP candidate which saturates the required relic density for cold dark matter. Models are continuously color-coded depending on how hard the neutrino spectrum is they produce after neutralino self-annihilations. Models excluded by the LUX experiment [227] are shown in gray and 1-year all-flavor sensitivities from the IceCube experiment, as calculated in chapter 5, are shown in solid (dashed) red for hard (soft) benchmark channels.

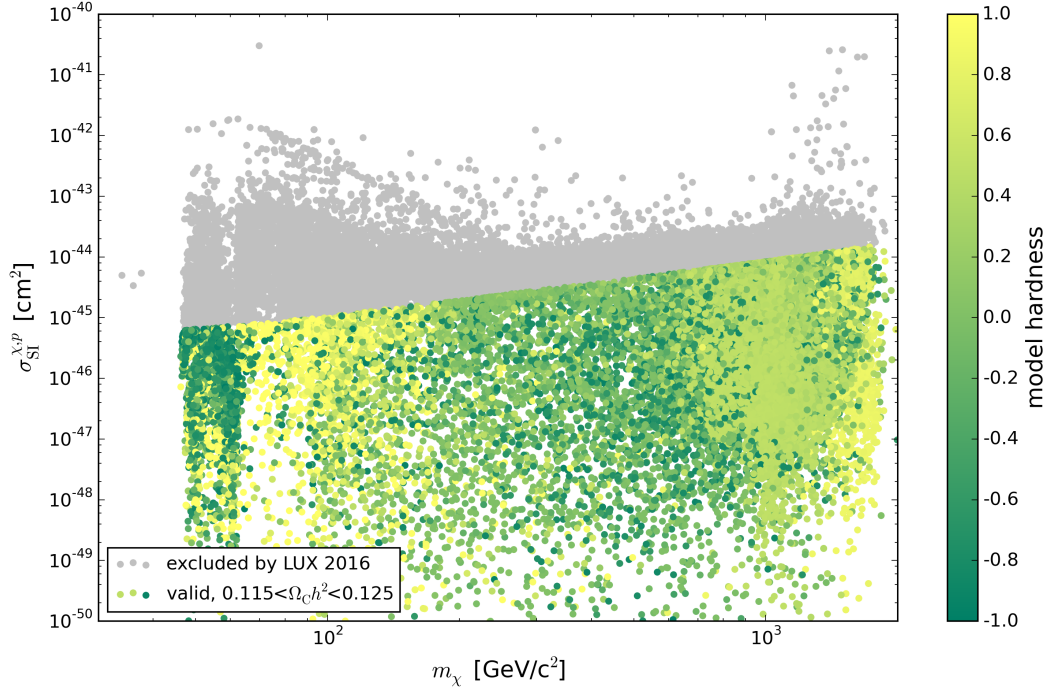


Figure 6.6.: Spin-independent neutralino-proton scattering cross-section. Individual models excluded by limits obtained by the LUX experiment [227] are shown in gray.

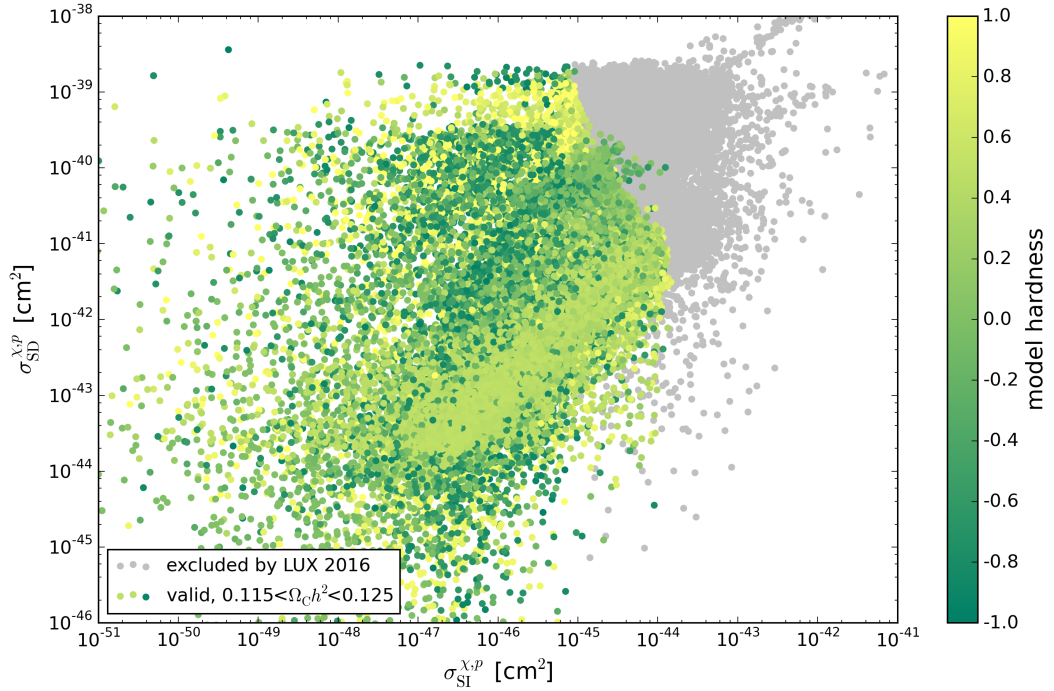


Figure 6.7.: Spin-dependent against spin-independent neutralino-proton scattering cross-section. Individual models excluded by limits obtained by the LUX experiment [227] are shown in gray.

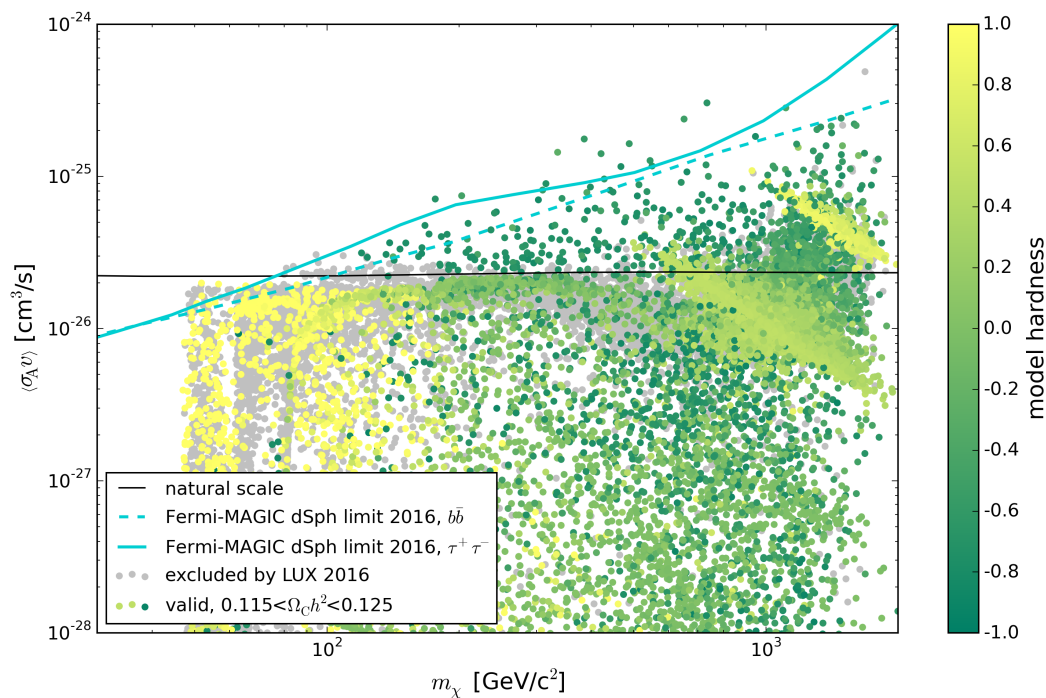


Figure 6.8.: Velocity-averaged neutralino self-annihilation cross-section of scanned models as a function of neutralino mass. Limits obtained by a joint MAGIC and Fermi-LAT analysis of dwarf spheroidal galaxies [53] are shown in turquoise. The slight mass dependence of the natural scale is included [228].

## Summary and Outlook

The detection of particle dark matter is one of the main challenges of present-day astroparticle physics. Over the last few years, complementary measurements of elementary particle properties and detection experiments were able to significantly constrain attributes of popular dark matter candidates. This work attempts to indirectly detect dark matter annihilation products by searching for a neutrino signal of solar origin with the IceCube Neutrino Observatory, located in the clear ice beneath the geographical South Pole. The sun serves as a gravitational well for dark matter particles to get trapped and subsequently undergo self-annihilation, creating Standard Model particles. Previous searches in the IceCube data produced the world's best sensitivities on the spin-dependent neutrino-proton scattering cross-section and this work was able to further improve on the sensitivity for lower-mass candidates by including neutrinos of all flavors. Modern techniques were employed for event filtering, exploiting multi-variate machine learning for efficient background discrimination and a likelihood minimization approach for the determination of the sensitivity to a specific signal. As input for the latter, a novel resolution estimator algorithm for cascade-shaped events was developed, making it possible to weight individual events based on their angular resolution. Furthermore, last years' advances in the field of high-performance computing allowed for expensive event reconstructions to mitigate the worse pointing reconstruction of cascade-shaped events, when compared to the track-like topologies of high-energy muon-neutrino induced events. Since the sun is a point source, the reconstructed direction crucially enters the likelihood procedure, as does the event energy which, due to containment, can be reconstructed more precisely for cascade-shaped events specifically and lower energies in general.

In this way, a range of possible dark matter candidate masses was probed, from 35 to 1000  $\text{GeV}/c^2$ , for benchmark annihilation channels producing an extremely soft and hard neutrino spectrum. Sensitivity to any model with an individual branching mixture would hence be enclosed by these two extreme sensitivities – results for a third annihilation channel,  $W^+W^-$ , were calculated for reference. The so-obtained sensitivities for one year of IceCube data in its full 86-string configuration are superior to track-only analyses below  $\sim 200 \text{ GeV}/c^2$  for the soft  $b\bar{b}$  channel and below  $\sim 70 \text{ GeV}/c^2$  for the hard  $\tau^+\tau^-$  channel. The spin-dependent elastic neutralino-proton scattering cross-section sensitivities for the soft channel reach below  $2 \cdot 10^{-39} \text{ cm}^2$  and for the hard channel below  $10^{-40} \text{ cm}^2$ .

These calculated sensitivities are interpreted in the supersymmetric framework of the phenomenological MSSM, a computationally more accessible subset of the unconstrained Minimal Supersymmetric extension of the Standard Model (MSSM). More than 100 billion individual models were assessed and filtered in compliance with laboratory and observational constraints. The remaining  $\sim 100,000$  models were put in context of exclusion capabilities by the currently strongest direct detection experiment and indirect

detection efforts by means of  $\gamma$  rays and neutrinos. In the context of this model space, limits from  $\gamma$  ray searches have insignificant exclusion power, while limits obtained from direct and indirect detection offer some complementarity. Laboratory constraints, e.g. from LHC measurements, offer yet another complementary approach to the exclusion of supersymmetric dark matter candidates and have been included.

There is, however, substantial room for possible refinements, which could not be accommodated in the presented work. Meanwhile four years of IceCube data in the full 86-string configuration are available – corresponding to a sensitivity increase by a factor of two. In this work, only the fiducial volume of the deep infill array DeepCore was considered. Inclusion of the whole IceCube volume may render all-flavor sensitivities competitive over the whole mass range. Furthermore, reconstruction and analysis techniques have evolved, for example a hybrid reconstruction became available, which accounts for the initial hadronic cascade and the subsequent leptonic signature, making it especially valuable for low-energy events. The understanding of the detector behavior has improved recently, resulting in a better noise description and a refined ice model. Together with advanced models for atmospheric neutrinos, a more precise Monte Carlo description of data and a reduction of systematic errors can be achieved. The signal models can be improved by including non-DIS neutrino interactions and furthermore by avoiding approximations concerning the elemental composition of the sun.

The planned successor of the IceCube neutrino observatory, called IceCube-Gen2, will both implement a coarse high-energy extension as well as a more densely instrumented low-energy infill inside the fiducial volume of DeepCore. The low-energy extension will allow for precise measurements of fundamental neutrino properties and will as well provide a significant improvement on the sensitivities for low-mass dark matter.

Finally, a variety of cosmological and particle physics measurements will produce further advances in the field and together with direct and indirect searches will help to carve out the nature of dark matter.

# A

## Signal Energy Spectra

The figures A.1–A.6 show the WIMP-induced signal neutrino energy spectra at the detector. Individual event weights are included. The WIMP annihilation, its decay products and the subsequent neutrino propagation to the earth, including neutrino oscillations both in vacuum and matter, are taken care of by the WIMPSim code [81], which internally employs the DarkSUSY package [162]. The plots show events at generation level, i.e. these events are injected in and around the detector volume, before triggers and filters are applied. Furthermore, the distributions are normalized to illustrate the spectral difference of the different neutrino flavors.  $\nu_\tau$  rates are usually significantly smaller when compared to the other flavors, due to the reduced  $\nu_\tau$  cross-section (see figure 2.7). Absolute rates and thus the flavor ratios, as well as the rate evolution and relative efficiencies throughout the event selection, can be read off from the tables G.1–G.6.

A distinct feature of the  $\nu_\tau$  spectra is the threshold energy of approximately 5 GeV, which is caused by the need for  $\tau^\pm$  production in charged-current interactions (for a more detailed discussion see section 2.4, especially equation 2.22).

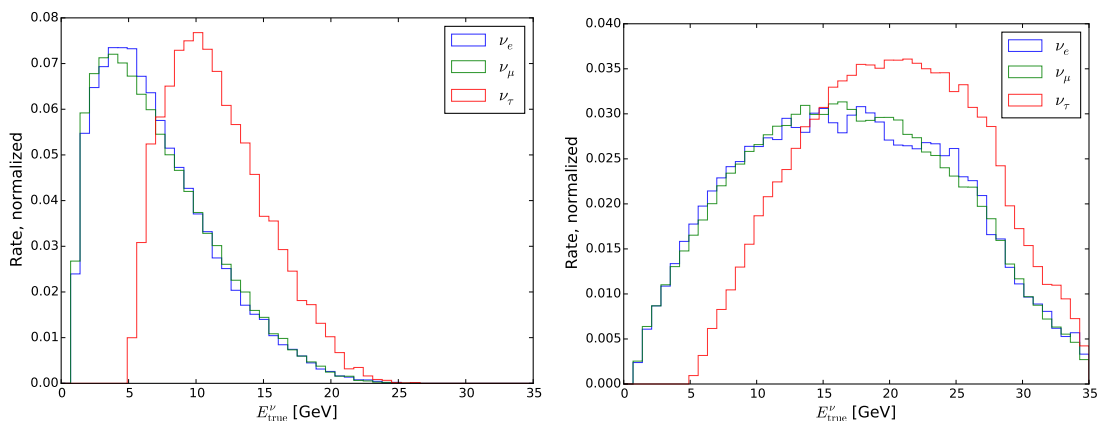


Figure A.1.: Neutrino energy spectra at generation level for a WIMP candidate with mass  $m_\chi = 35 \text{ GeV}/c^2$ . The annihilation channels shown are  $b\bar{b}$  (left) and  $\tau^+\tau^-$  (right).

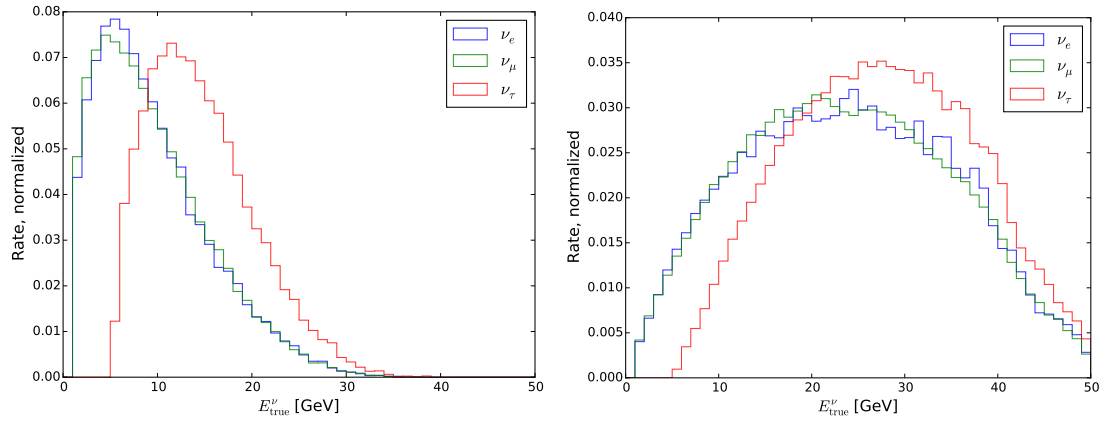


Figure A.2.: Neutrino energy spectra at generation level for a WIMP candidate with mass  $m_\chi = 50 \text{ GeV}/c^2$ . The annihilation channels shown are  $b\bar{b}$  (left) and  $\tau^+\tau^-$  (right).

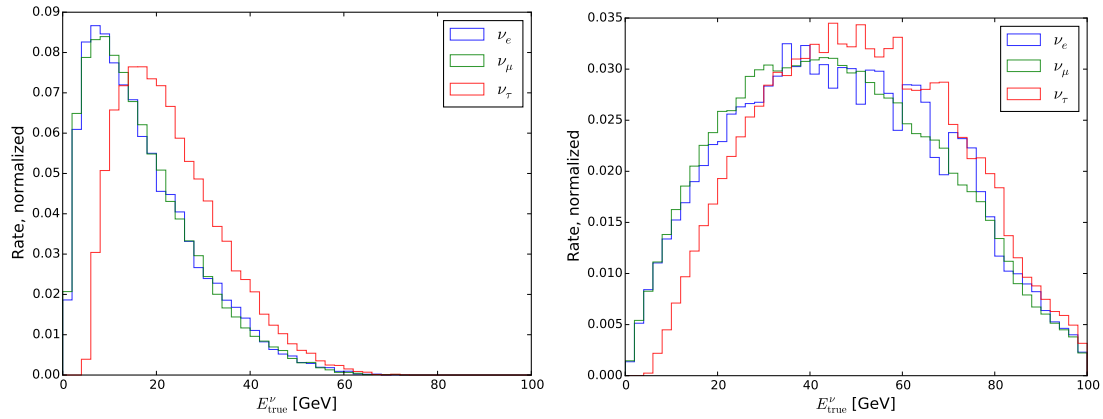


Figure A.3.: Neutrino energy spectra at generation level for a WIMP candidate with mass  $m_\chi = 100 \text{ GeV}/c^2$ . The annihilation channels shown are  $b\bar{b}$  (left) and  $\tau^+\tau^-$  (right).

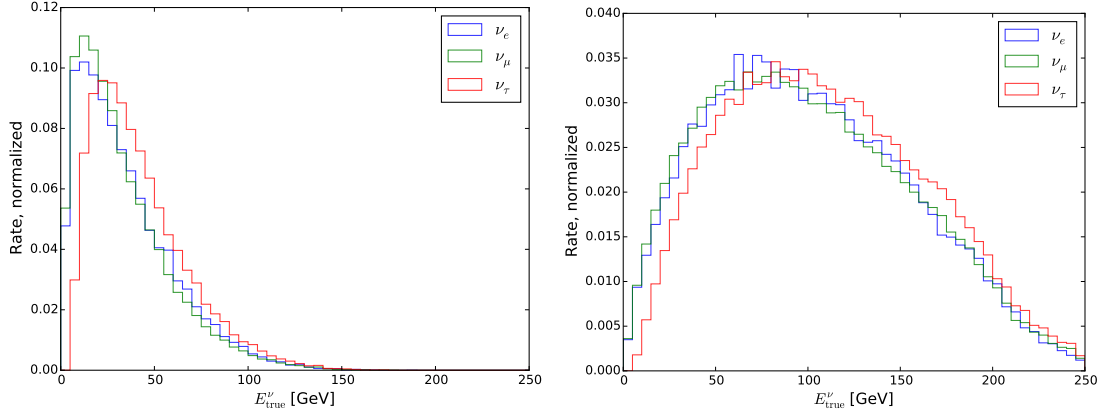


Figure A.4.: Neutrino energy spectra at generation level for a WIMP candidate with mass  $m_\chi = 250 \text{ GeV}/c^2$ . The annihilation channels shown are  $b\bar{b}$  (left) and  $\tau^+\tau^-$  (right).

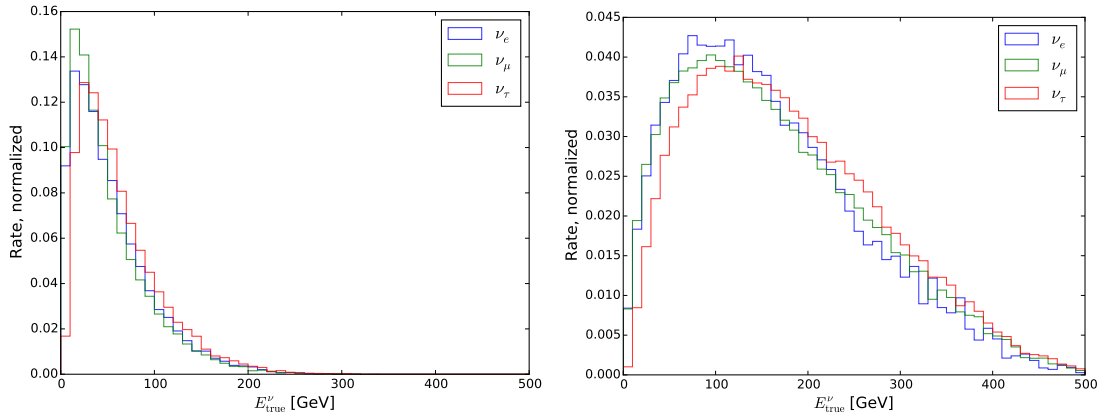


Figure A.5.: Neutrino energy spectra at generation level for a WIMP candidate with mass  $m_\chi = 500 \text{ GeV}/c^2$ . The annihilation channels shown are  $b\bar{b}$  (left) and  $\tau^+\tau^-$  (right).

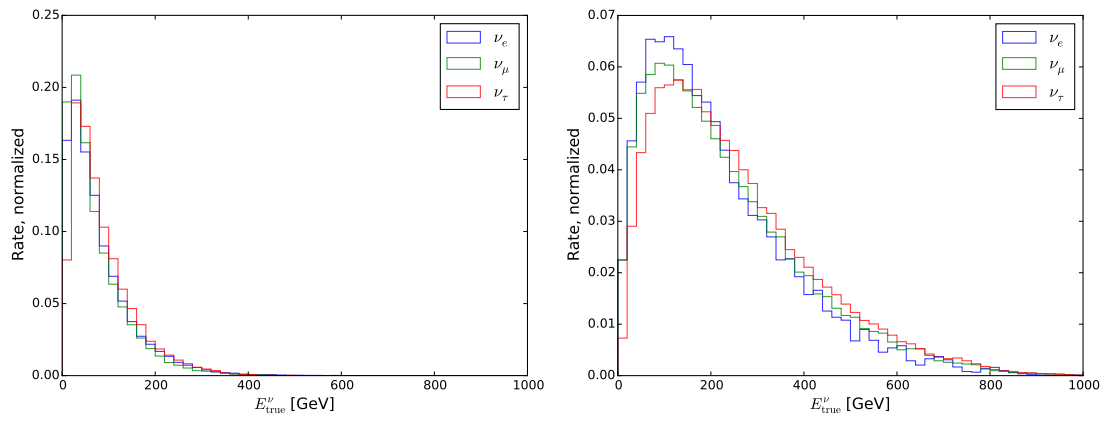


Figure A.6.: Neutrino energy spectra at generation level for a WIMP candidate with mass  $m_\chi = 1000 \text{ GeV}/c^2$ . The annihilation channels shown are  $b\bar{b}$  (left) and  $\tau^+\tau^-$  (right).

# B

## Low-level Production of Signal Simulation

Various IceCube data analyses usually rely on the same background simulations to develop their event filtering. Therefore the collaboration takes care of the central Monte-Carlo production and data storage. These simulation datasets are then made available for the individual filtering of the high-level analyses. Processing is distributed among collaborating computing sites in the United States, Germany, Canada, Japan and Belgium by exploiting existing grid infrastructures. Central bookkeeping and control over the remote instances is maintained by the lightweight *IceProd* code [231].

As introduced in section 5.2, simulations start off with an event generator, which inserts muon or neutrino events into the detector according to an assumed signal [81] or background [166, 170] model.

Signal simulations which are used by one or just a few collaborators are not produced in the framework of the distributed mass production, but instead have to be processed independently.

This work employs neutrino events from the WimpSIM code [81] as signal simulation. While  $\nu_\mu$  datasets were shared with the track-based study presented in [182], datasets for the electron and  $\tau$  flavors had to be produced at the local *high-performance computing* (HPC) cluster starting at generation level.

ASCII-encoded WimpSIM events are imported in IceCube's analysis framework *IceTray* [150] by the aid of the `wimpsim-reader` interface [232]. Events are injected at random positions into a cubic volume which is centered at the origin of the detector coordinate system. The edge lengths are generously set to 1.4 km to cover the whole sensitive<sup>1</sup> region, resulting in an injection volume of 2.744 km<sup>3</sup>. For muon neutrinos, with their extended light deposits, a cylindrical volume approach is implemented [182]. Signal event rates at generation level (and beyond) can be found in appendix G.

---

<sup>1</sup>Light from events with a vertex outside the detector volume may still reach optical modules and hence cause the event to trigger.

After event generation and injection into the detector volume, the particles are propagated<sup>2</sup> according to the energy losses discussed in section 3.4. As motivated in section 5.2, hadronic particles below 30 GeV and electromagnetic particles below 0.1 GeV are precisely propagated by means of the GEANT4 code [171] instead of using parametrizations. Subsequently, Cherenkov light is propagated through the detector on a photon by photon basis by means of GPU-enabled massive parallelizations. Tabulated ice properties (see section 3.3) serve as the basis for this light propagation. Next, the response of the detector electronics and noise are simulated, yielding timed signal pulses which allow for subsequent local coincidence and trigger checks (see section 3.2). The low-level simulation steps are summarized in figure B.1.

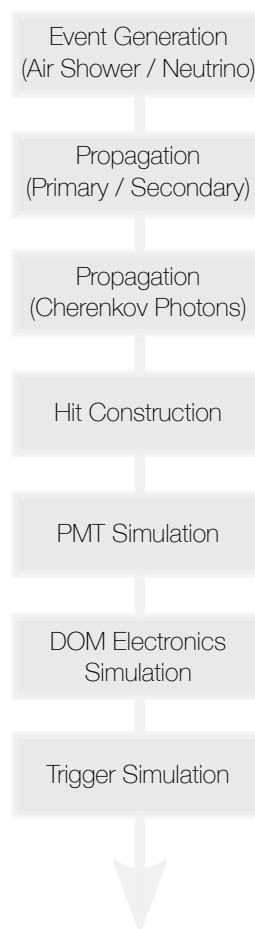


Figure B.1.: IceCube low-level simulation chain.

---

<sup>2</sup>The Java-based `Muon Monte Carlo` code [167] used to be employed for muon energy loss simulations. Meanwhile, it has been replaced by a C++ based approach, the `PROPOSAL` code [233].

# C

## Cascade and Track Signatures

Signatures of different neutrino flavors can differ substantially.  $\nu_\mu$  undergoing a charged-current interaction produce an initial hadronic cascade together with a muon, which leaves a track-like signature in the detector. The other flavors and neutral-current reactions all produce almost spherical light signatures. The event reconstruction can account for these different types by assuming the appropriate event hypothesis (see section 4.1 for a discussion of the event reconstruction). For data however, the flavor is generally unknown and a particle identification at low energies is quite challenging [134].

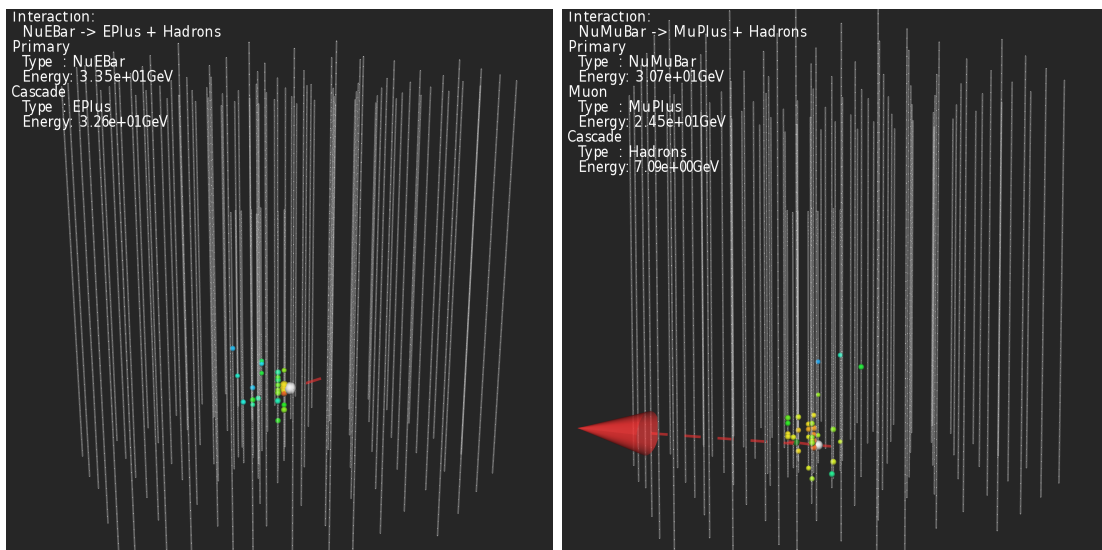


Figure C.1.: Signature of lit optical modules for incident neutrinos with  $E_\nu \approx 30$  GeV undergoing a charged-current reaction inside the detector volume. The direction of the incident neutrino (and in the case of the muon also the direction of the outgoing charged lepton) are shown as dashed red lines. Timing information is color coded, ranging from red (early hits) to blue (late hits). From the hit pattern and timing information, there is no distinction of the electromagnetic cascade (left) and the continuous energy loss along a muon track (right).

Figure C.1 shows a simulated muon- and electron-neutrino, both with an energy of about 30 GeV, undergoing a deep-inelastic scattering interaction in IceCube. They both originate from WIMPs with  $50 \text{ GeV}/c^2$  mass, annihilating to a  $\tau^+\tau^-$  pair.

At energies of a few hundred GeV or more, outgoing muons leave tracks which extend over hundreds of meters and cascades with such energies produce huge blobs of light that range over many strings. In this case, an automated track-cascade distinction is possible by evaluating the likelihood of a fit with the respective topological hypothesis. Selected examples are shown in figure C.2 for a 400 GeV neutrino.

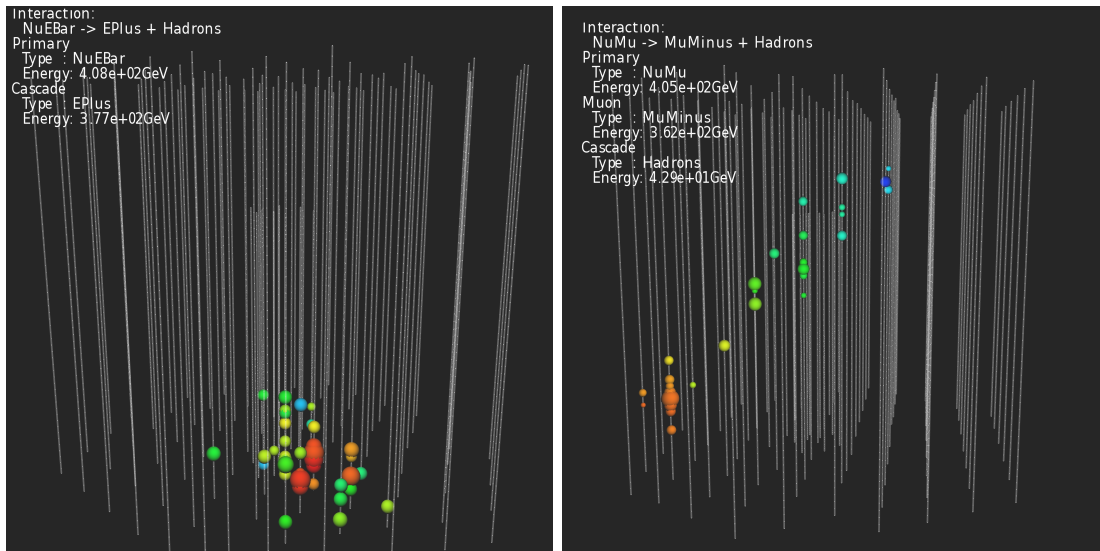


Figure C.2.: Signature of lit optical modules for incident atmospheric neutrinos with  $E_\nu \approx 400 \text{ GeV}$  undergoing a charged-current reaction inside the detector volume. The  $\nu_e$  producing an electromagnetic cascade of spherical shape (left) is clearly distinguishable from the  $\nu_\mu$  that produces an up-going track of deposited light (right). Timing information is color coded, ranging from red (early hits) to blue (late hits). In this illustration, the size of the lit modules scales with the amount of deposited light (which induces a proportional amount of charge in the photomultiplier).

## BDT Input Variables Distribution

The figures below show variables with background discrimination potential after the level 5 selection.

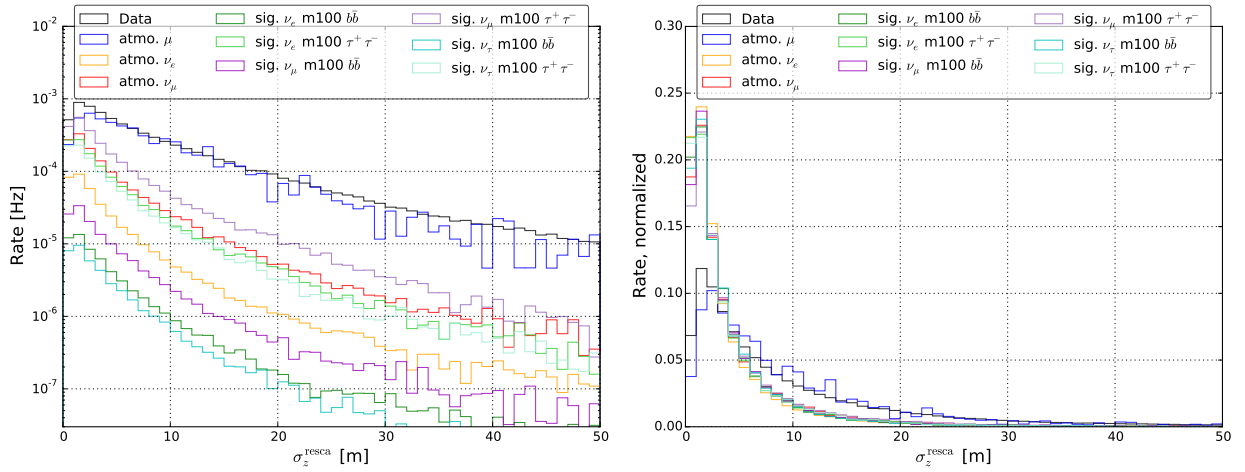


Figure D.1.: Distribution of  $\sigma_z^{\text{resca}}$  at selection level 5. Left in logarithmic scale and right in linear scale normalized to 1.

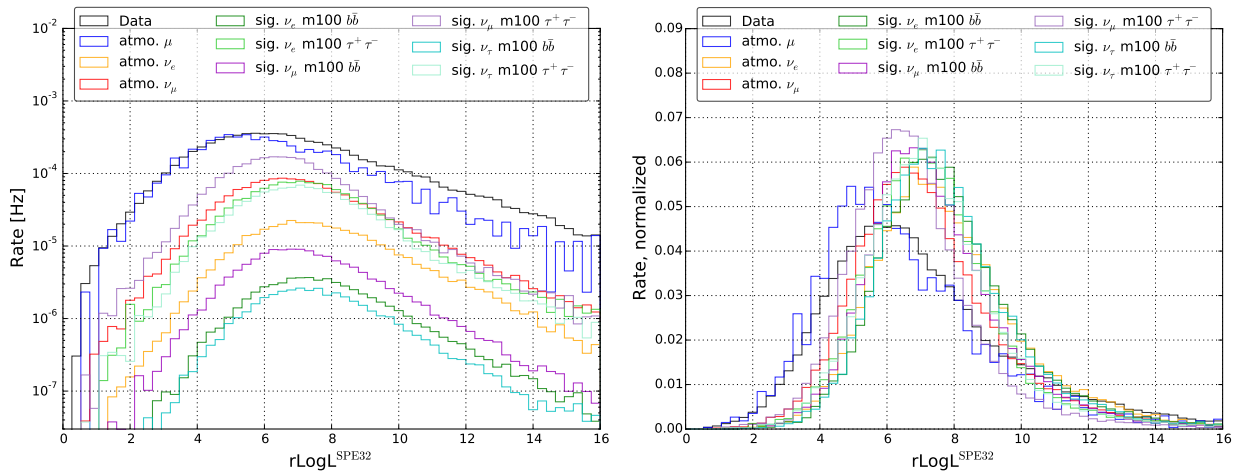


Figure D.2.: Distribution of the  $r\text{LogL}^{\text{SPE32}}$  variable at selection level 5. Left in logarithmic scale and right in linear scale normalized to 1.

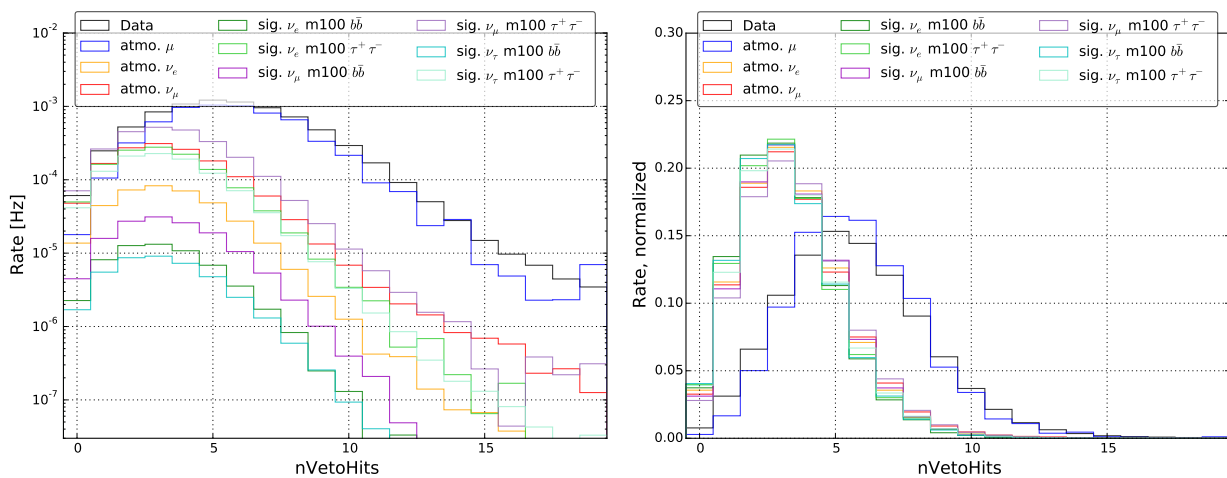


Figure D.3.: Distribution of the  $nVetoHits$  variable at selection level 5. Left in logarithmic scale and right in linear scale normalized to 1.

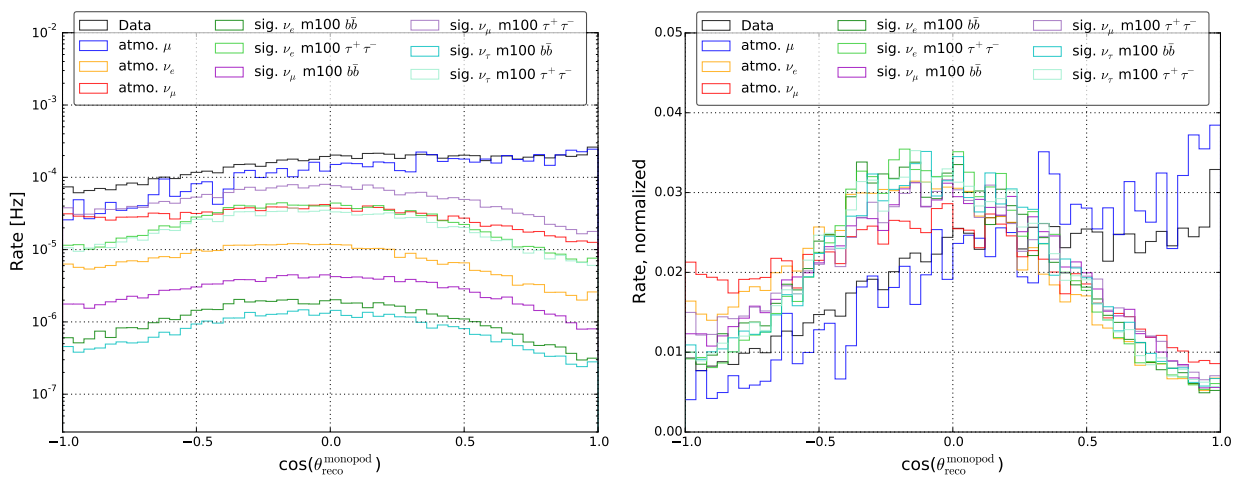


Figure D.4.: Distribution of  $\cos(\theta_{reco}^{monopod})$  at selection level 5. Left in logarithmic scale and right in linear scale normalized to 1.

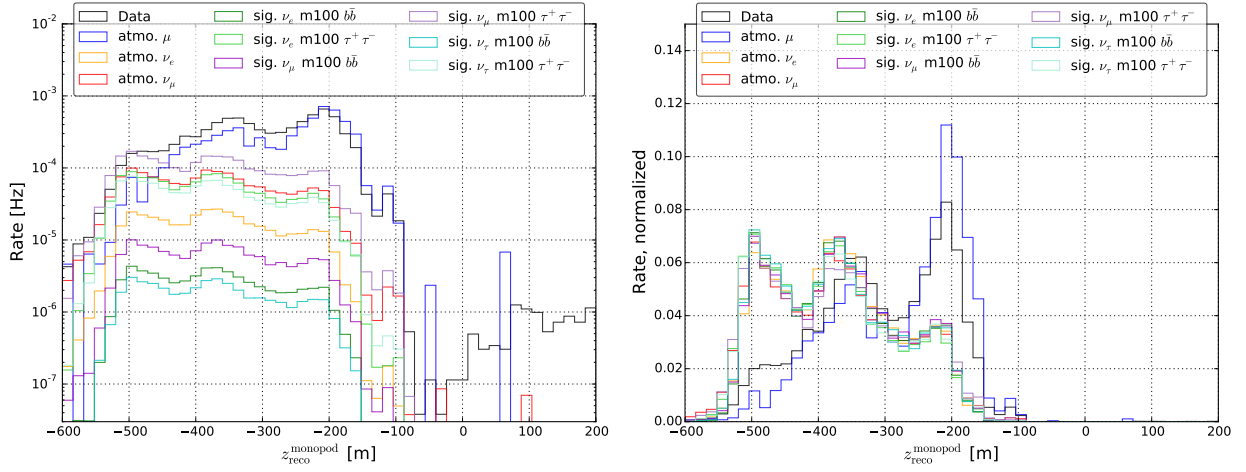


Figure D.5.: Distribution of  $z_{\text{reco}}^{\text{monopod}}$  at selection level 5. Left in logarithmic scale and right in linear scale normalized to 1.

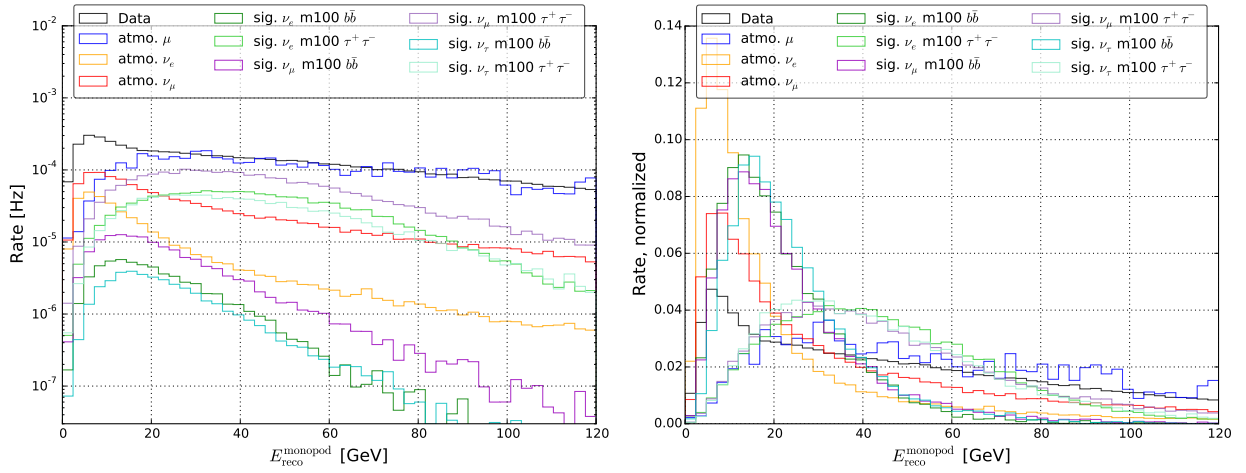


Figure D.6.: Distribution of  $E_{\text{reco}}^{\text{monopod}}$  at selection level 5. Left in logarithmic scale and right in linear scale normalized to 1.

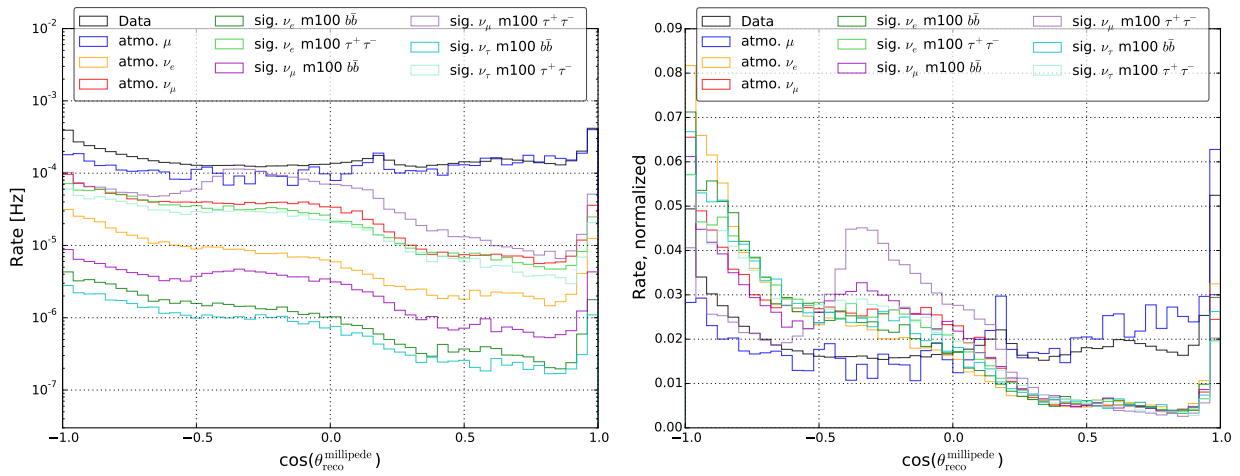


Figure D.7.: Distribution of  $\cos(\theta_{\text{millipede}}^{\text{reco}})$  at selection level 5. Left in logarithmic scale and right in linear scale normalized to 1.

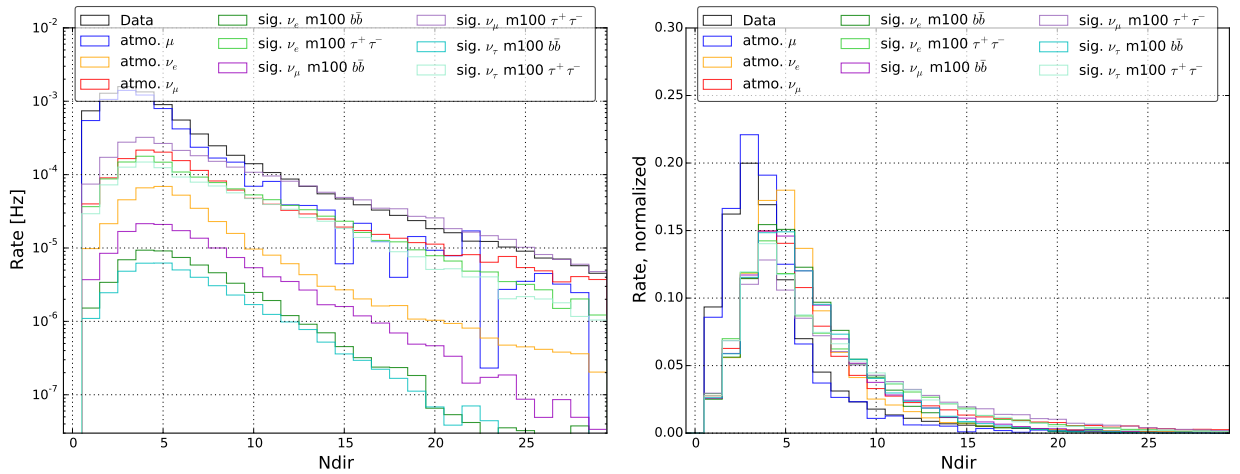


Figure D.8.: Distribution of the Ndir variable at selection level 5. Left in logarithmic scale and right in linear scale normalized to 1.

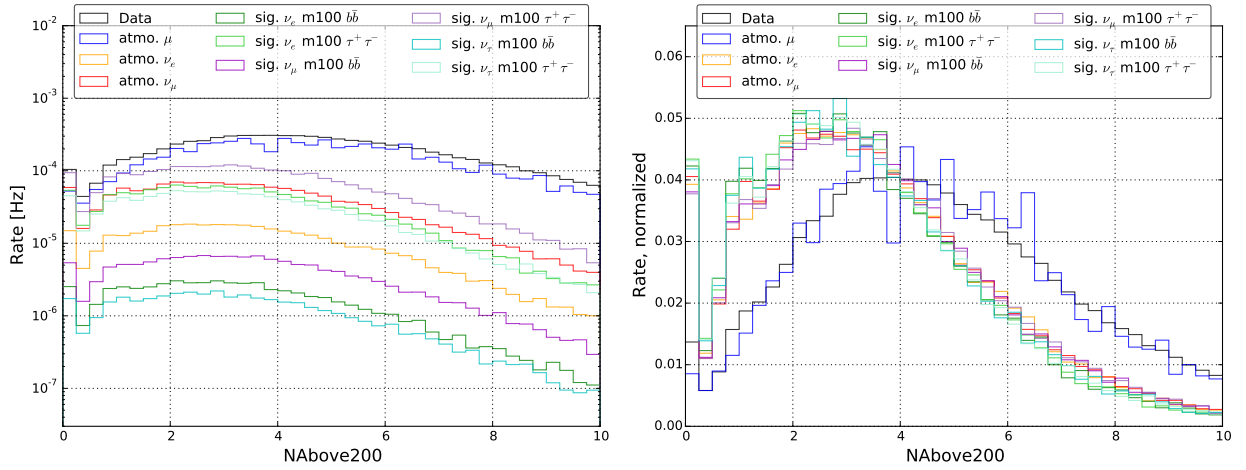


Figure D.9.: Distribution of the  $N_{\text{Above200}}$  variable at selection level 5. Left in logarithmic scale and right in linear scale normalized to 1.

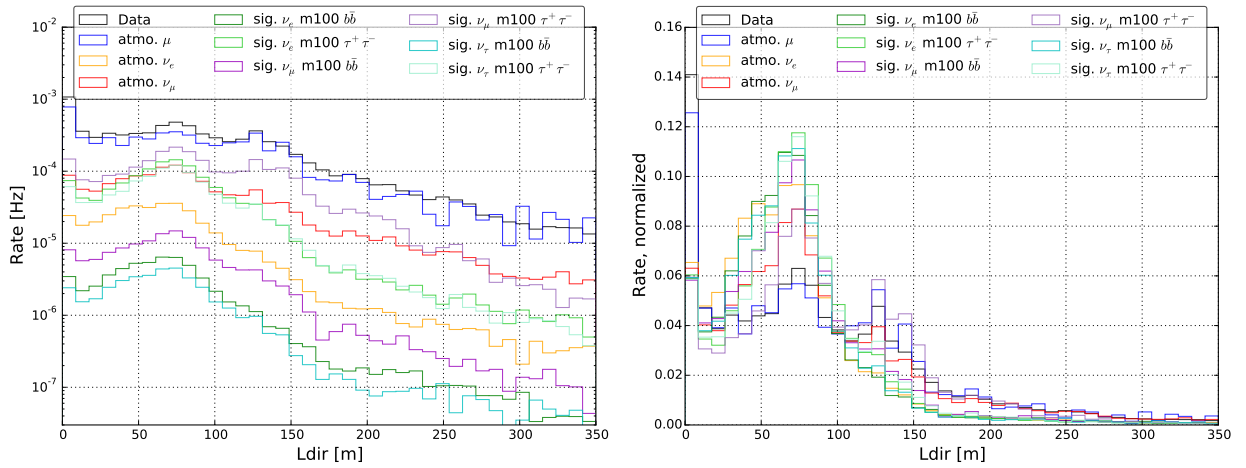


Figure D.10.: Distribution of the  $L_{\text{dir}}$  variable at selection level 5. Left in logarithmic scale and right in linear scale normalized to 1.

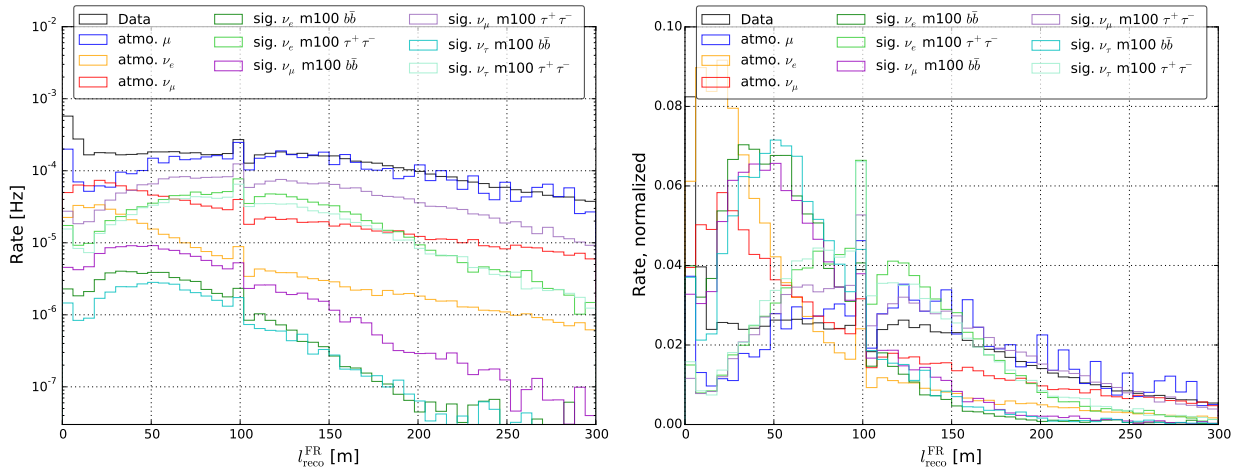


Figure D.11.: Distribution of the `FRLength` variable at selection level 5. Left in logarithmic scale and right in linear scale normalized to 1.

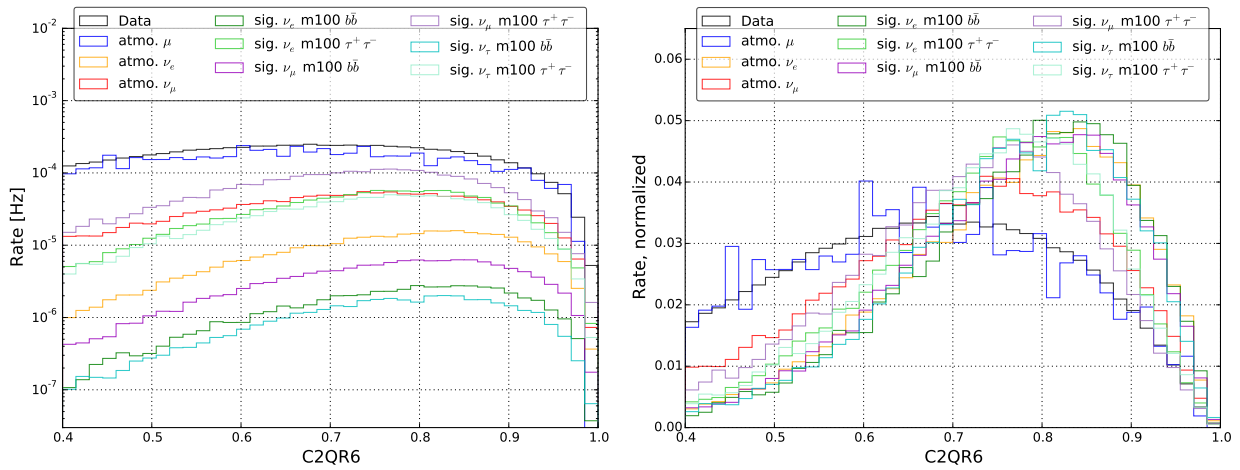


Figure D.12.: Distribution of the `C2QR6` variable at selection level 5. Left in logarithmic scale and right in linear scale normalized to 1.

# E

## BDT Results

The figures E.1–E.18 show post-BDT training distributions and discrimination variable correlations for all studied WIMP masses, ranging from 35 to 1000 GeV/ $c^2$ .

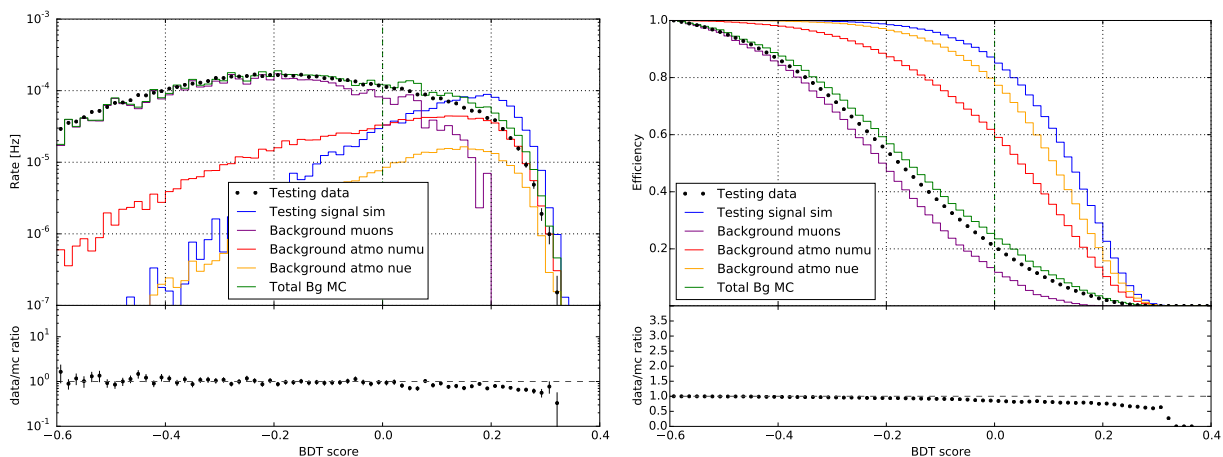


Figure E.1.: BDT score (left) and score cut efficiency (right) for  $m_\chi = 35 \text{ GeV}/c^2$ .

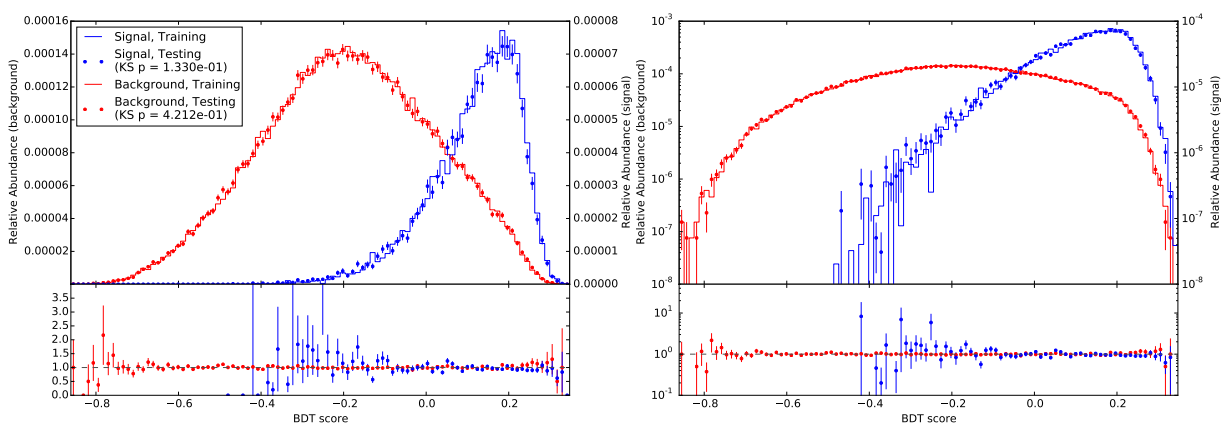


Figure E.2.: BDT over-training check for  $m_\chi = 35 \text{ GeV}/c^2$ .

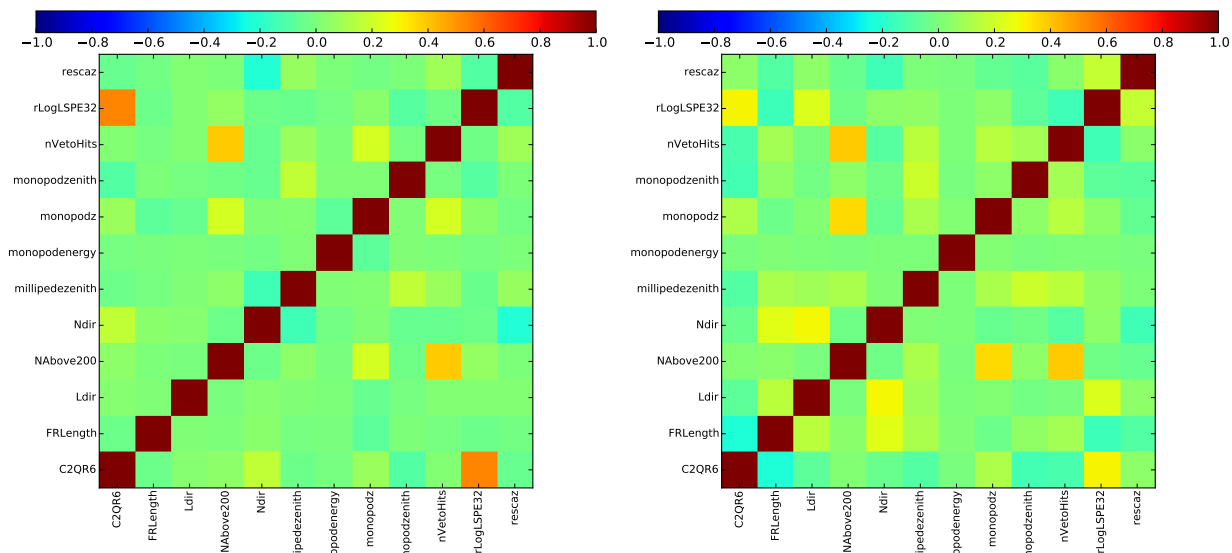


Figure E.3.: Discrimination variables correlation matrix for signal (left) and background (right), for  $m_\chi = 35 \text{ GeV}/c^2$ .

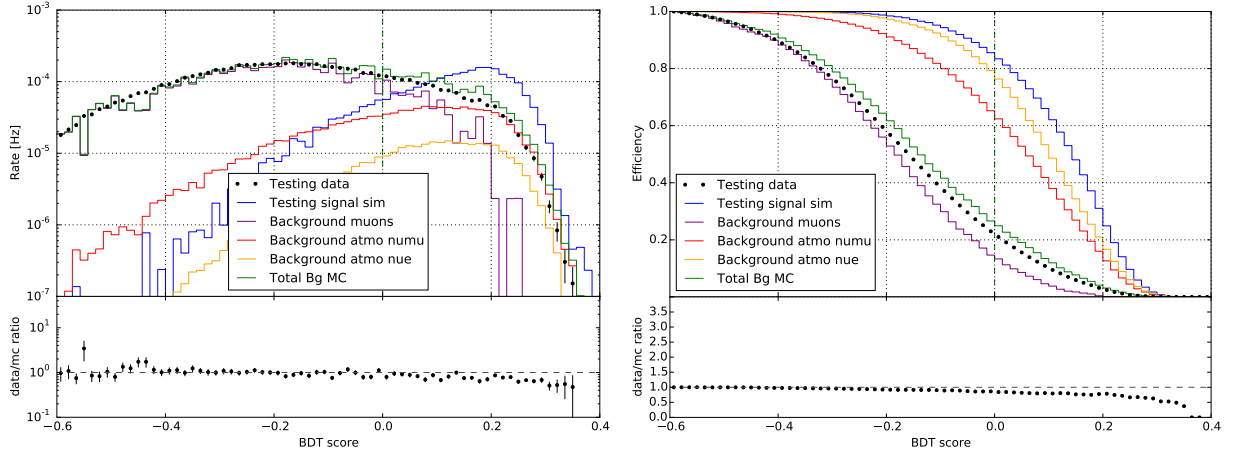


Figure E.4.: BDT score (left) and score cut efficiency (right) for  $m_\chi = 50 \text{ GeV}/c^2$ .

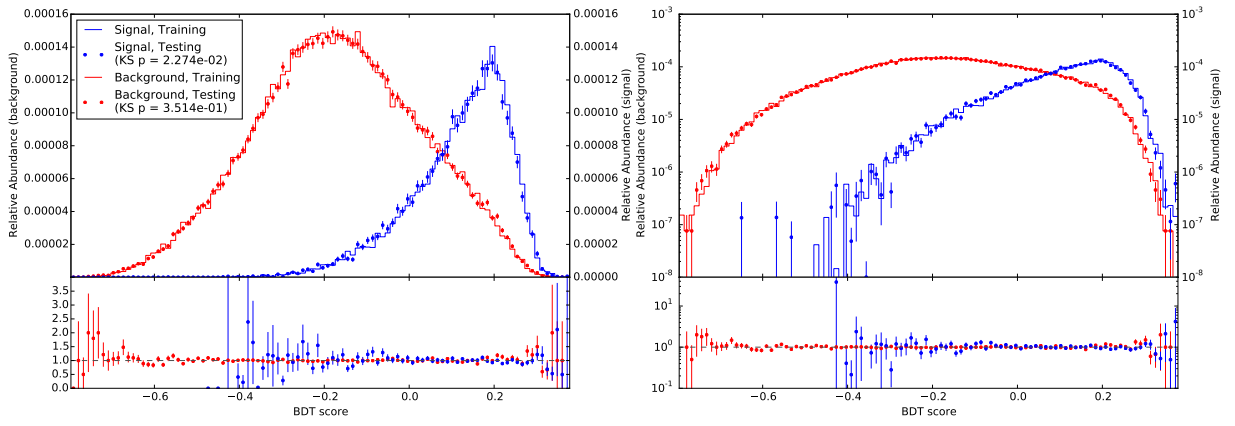


Figure E.5.: BDT over-training check for  $m_\chi = 50 \text{ GeV}/c^2$ .

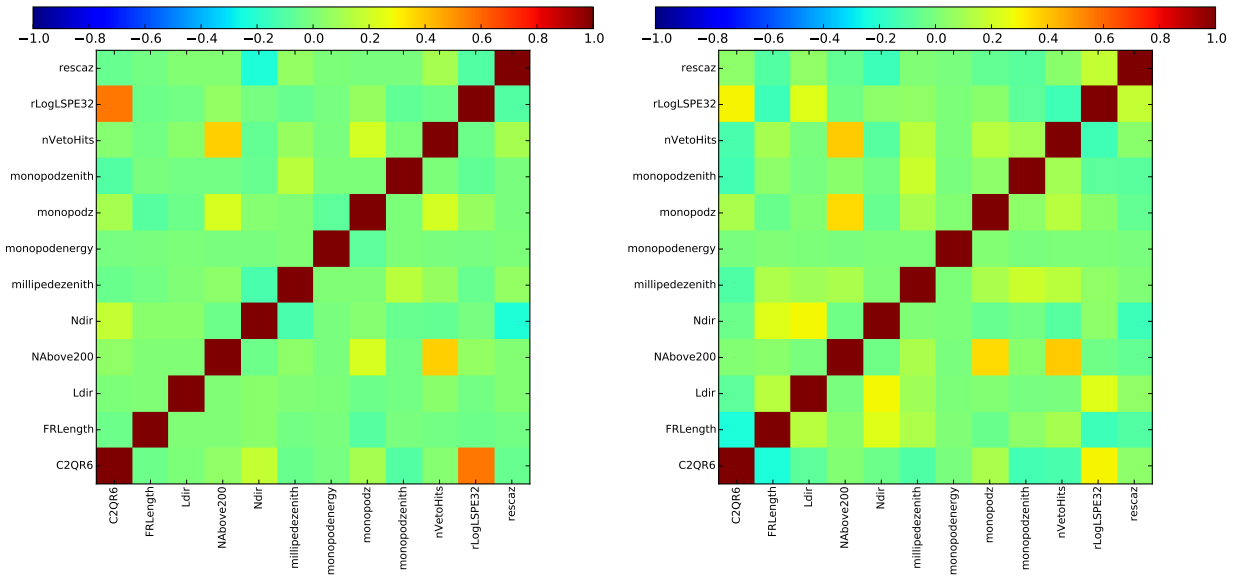


Figure E.6.: Discrimination variables correlation matrix for signal (left) and background (right), for  $m_\chi = 50 \text{ GeV}/c^2$ .

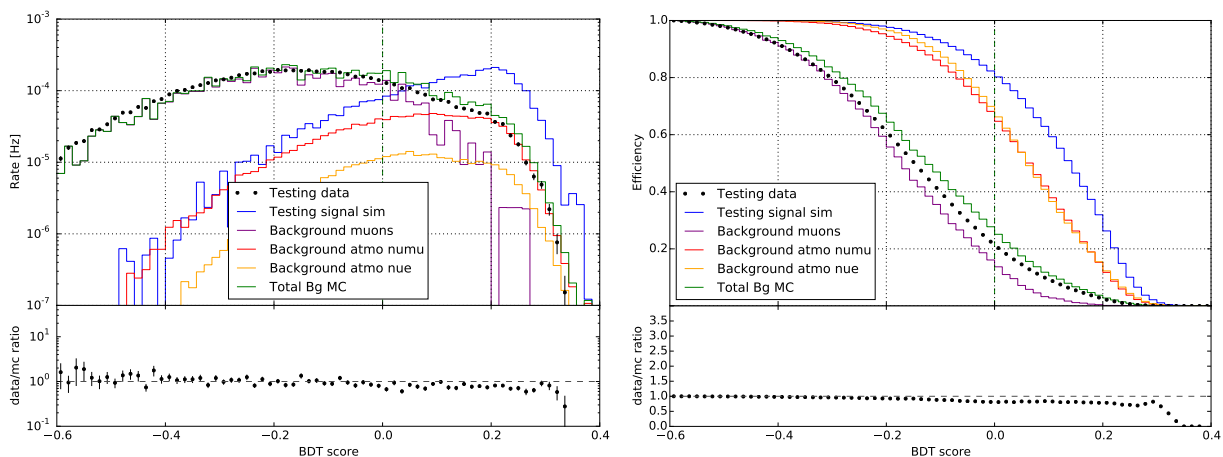


Figure E.7.: BDT score (left) and score cut efficiency (right) for  $m_\chi = 100 \text{ GeV}/c^2$ .

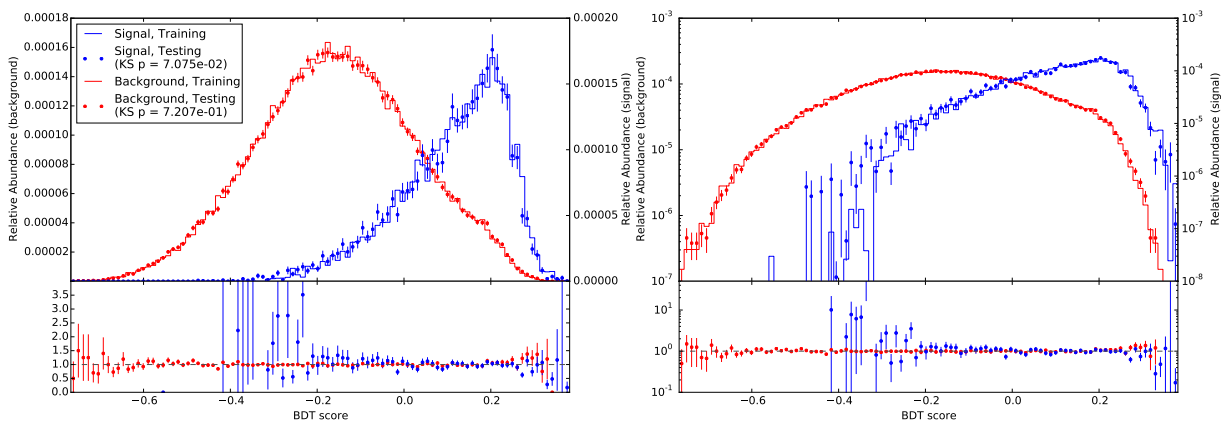


Figure E.8.: BDT over-training check for  $m_\chi = 100 \text{ GeV}/c^2$ .

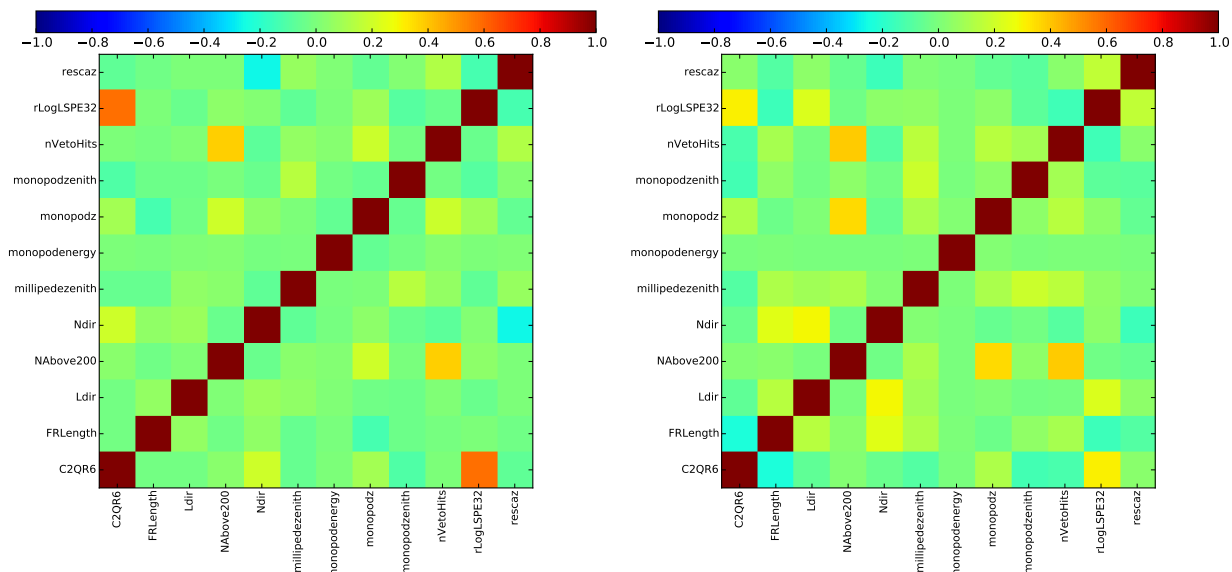


Figure E.9.: Discrimination variables correlation matrix for signal (left) and background (right), for  $m_\chi = 100 \text{ GeV}/c^2$ .

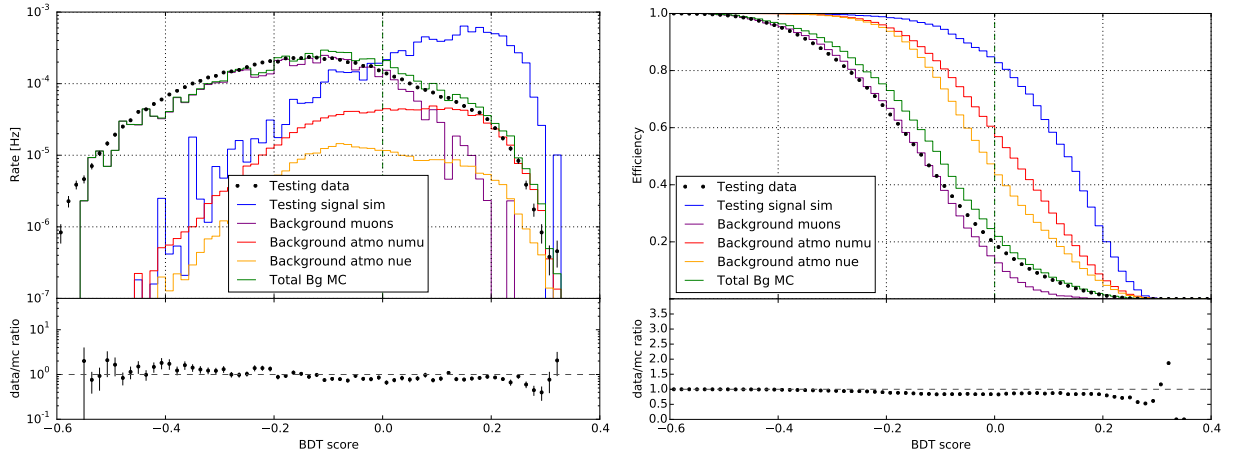


Figure E.10.: BDT score (left) and score cut efficiency (right) for  $m_\chi = 250 \text{ GeV}/c^2$ .

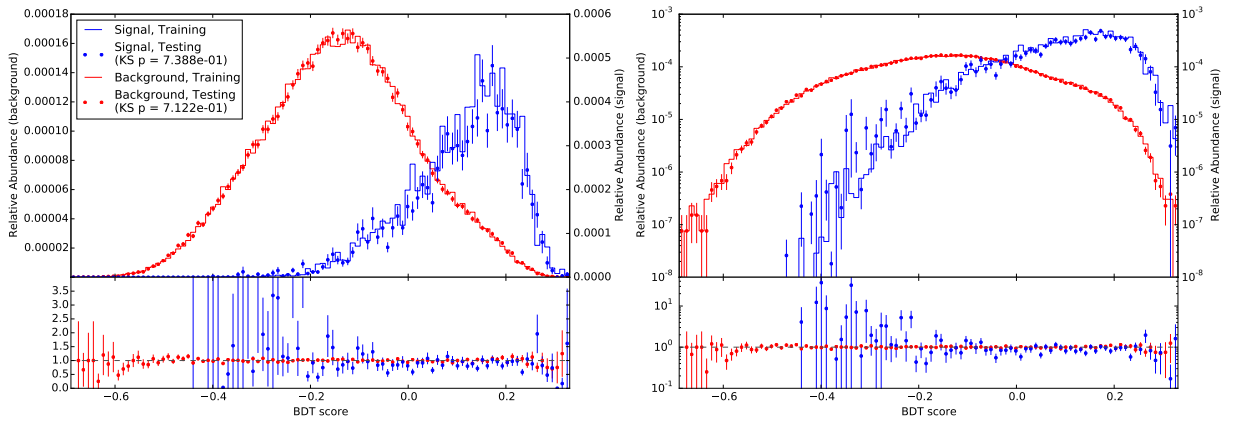


Figure E.11.: BDT over-training check for  $m_\chi = 250 \text{ GeV}/c^2$ .

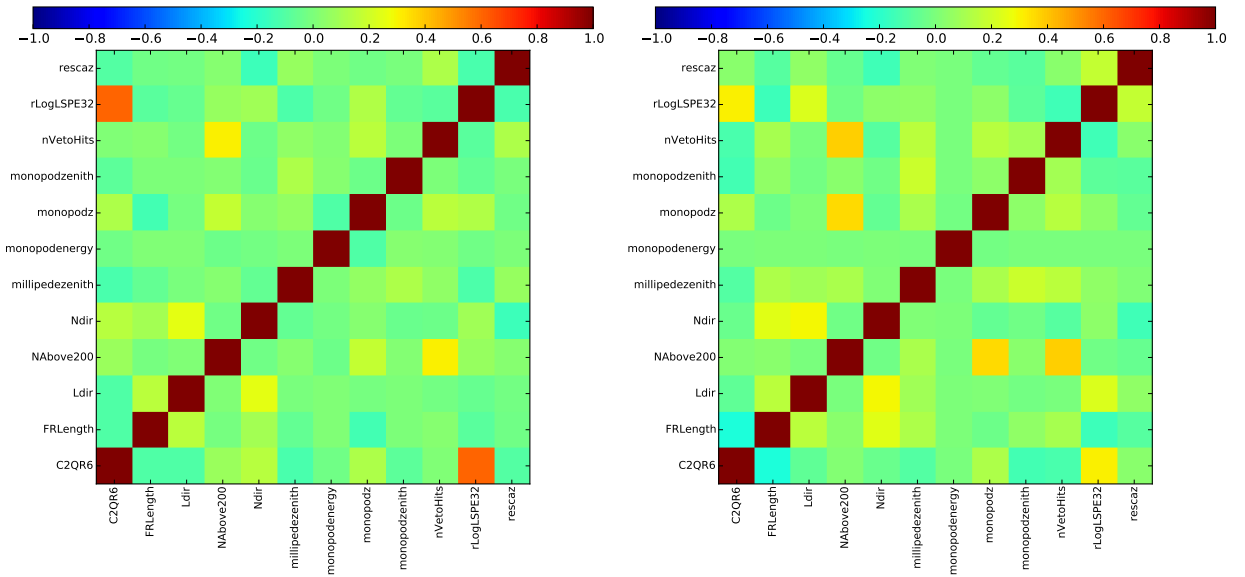


Figure E.12.: Discrimination variables correlation matrix for signal (left) and background (right), for  $m_\chi = 250 \text{ GeV}/c^2$ .

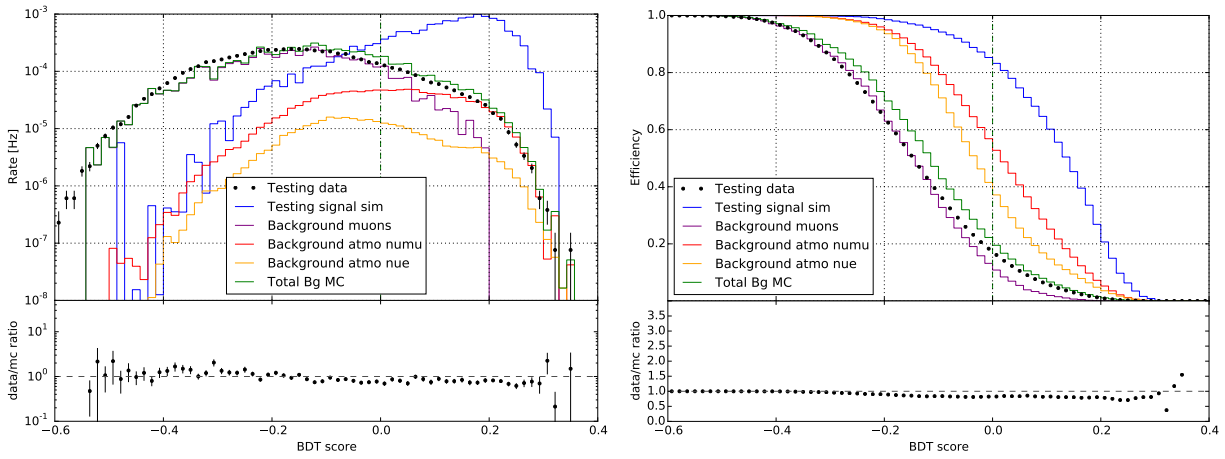


Figure E.13.: BDT score (left) and score cut efficiency (right) for  $m_\chi = 500 \text{ GeV}/c^2$ .

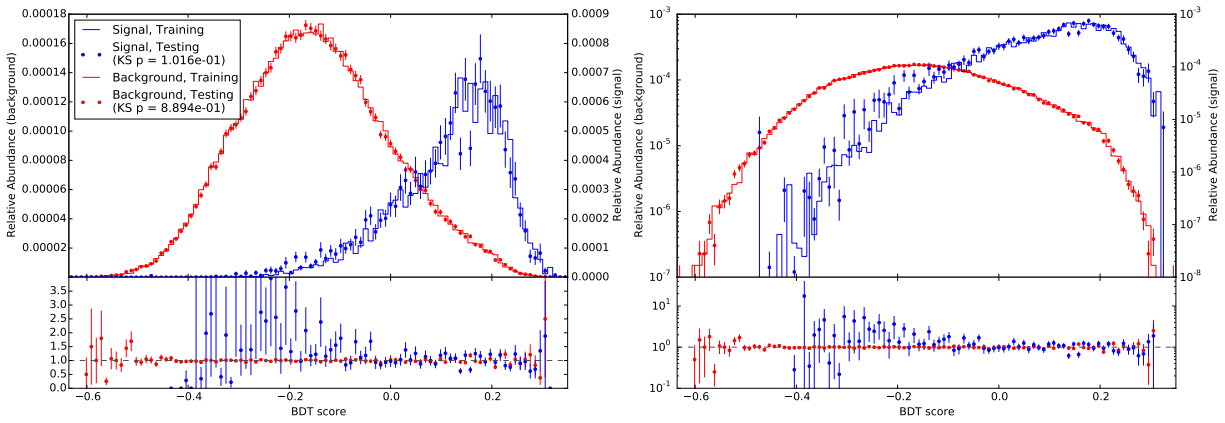


Figure E.14.: BDT over-training check for  $m_\chi = 500 \text{ GeV}/c^2$ .

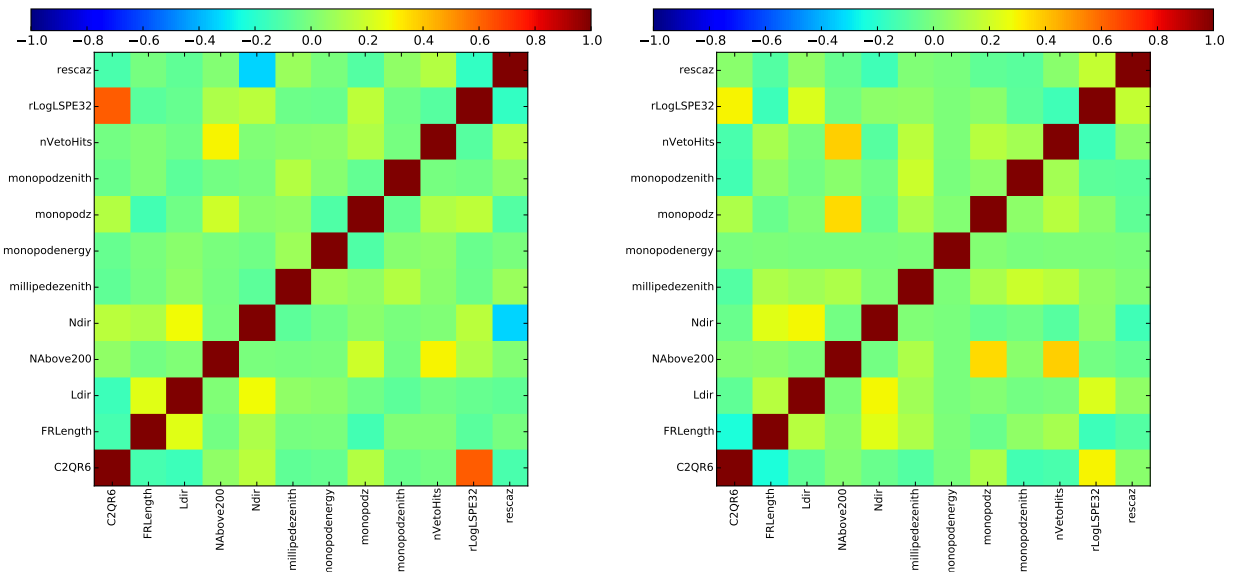


Figure E.15.: Discrimination variables correlation matrix for signal (left) and background (right), for  $m_\chi = 500 \text{ GeV}/c^2$ .

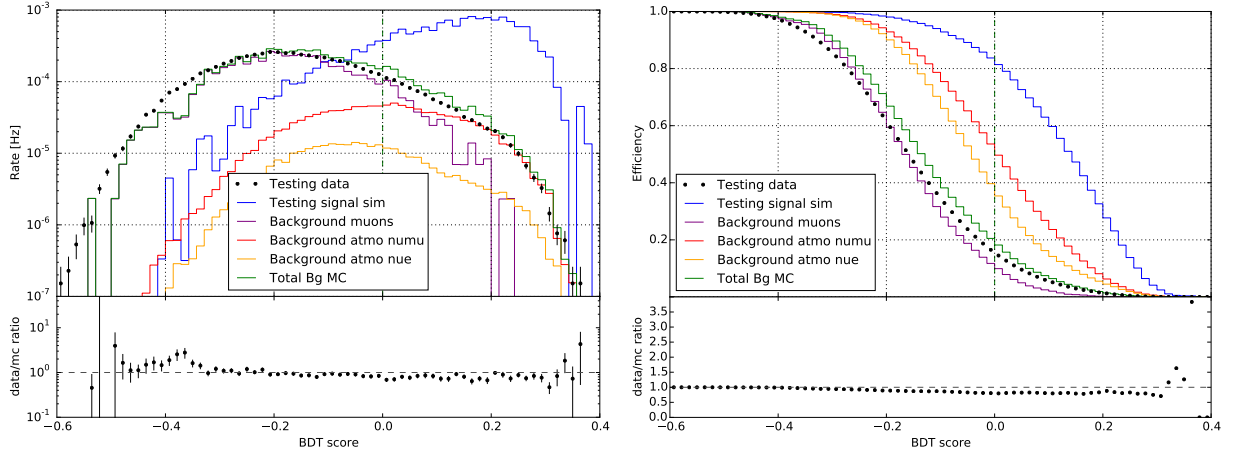


Figure E.16.: BDT score (left) and score cut efficiency (right) for  $m_\chi = 1000 \text{ GeV}/c^2$ .

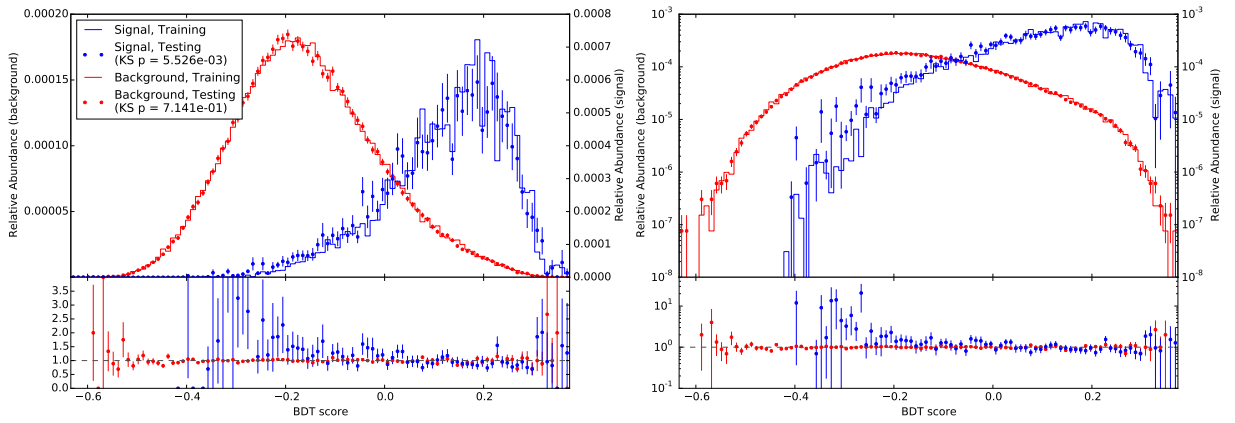


Figure E.17.: BDT over-training check for  $m_\chi = 1000 \text{ GeV}/c^2$ .

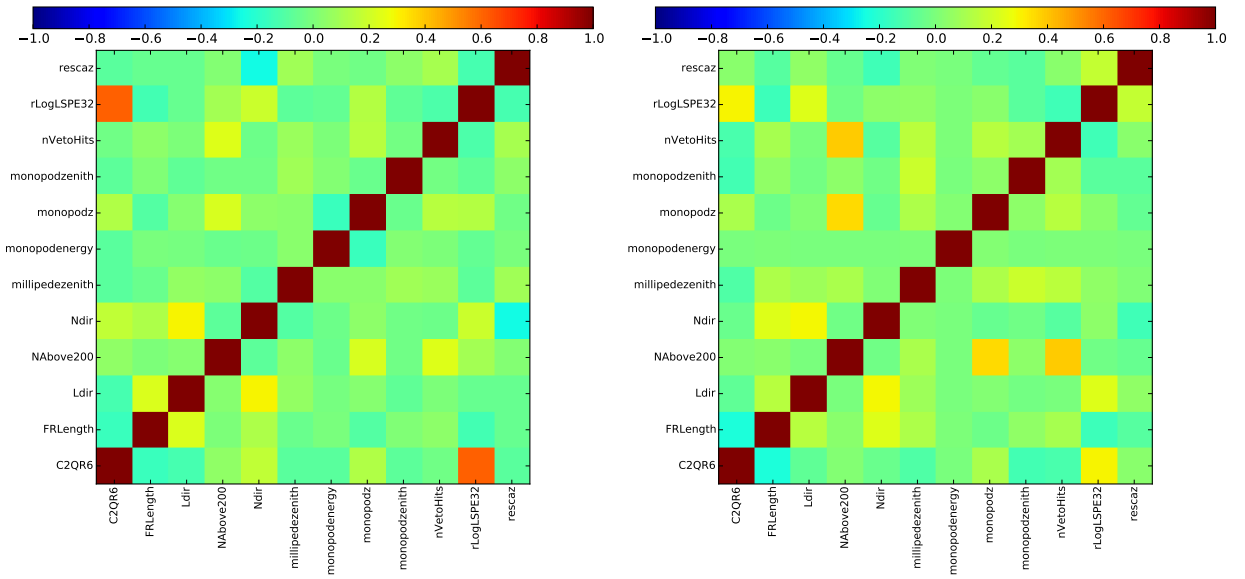


Figure E.18.: Discrimination variables correlation matrix for signal (left) and background (right), for  $m_\chi = 1000 \text{ GeV}/c^2$ .



# F

## BDT Cut Score Optimization

The exact cut values on the BDT score are determined depending on the best resulting final sensitivities. Probing different cut values requires full runs of the likelihood fit (section 5.5) and the subsequent calculation of sensitivity results. This is a time-consuming process, especially since it needs to be performed independently for each combination of candidate mass and annihilation channel. Therefore only a constrained region (-0.04–0.02) is studied, with the intervals chosen to be rather coarse. Figure F.1 shows sensitivity results for the example of a WIMP with a mass of  $100 \text{ GeV}/c^2$ . The gain achieved by this optimization is marginal (1–10%).

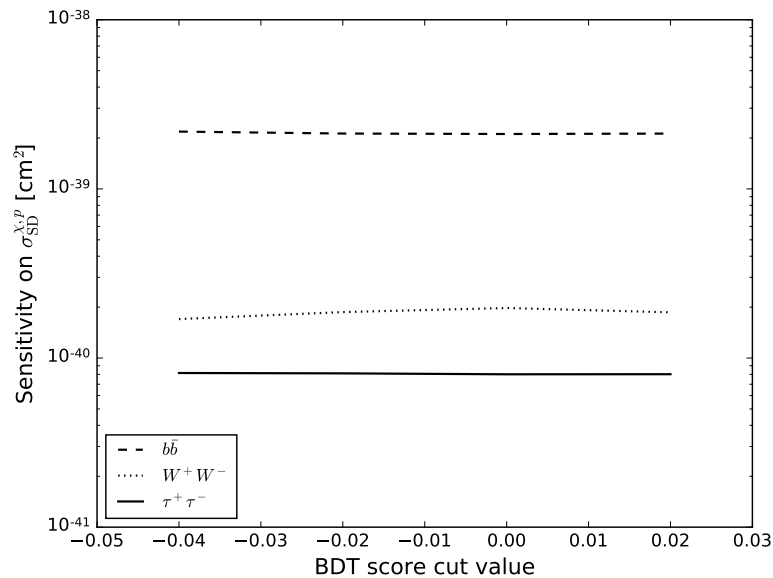


Figure F.1.: Spin-dependent scattering cross-section against BDT score cut value, shown for a WIMP with a mass of  $100 \text{ GeV}/c^2$ .



# G

## Event Rates at the various Selection Levels

The tables G.1–G.6 show the development of data and MC event rates throughout the event selection (the latter is described in section 5.3).

		$m_\chi = 35 \text{ GeV}/c^2$									
type	channel	flavor	event rate at level:								
			generation	L2	L3	L4	L5	L6	L7		
data	-	-	-	6.63e+02 {1.0}	1.15e+00 {1.74e-03}	8.29e-02 {1.25e-04}	8.10e-03 {1.22e-05}	2.75e-03 {4.15e-06}	7.72e-04 {1.16e-06}	1.11e-03 {1.68e-06}	$\tau^+\tau^-$ $b\bar{b}$
atmo. $\mu$ (MC)	-	-	-	6.55e+02 {1.0}	1.26e+00 {1.92e-03}	7.53e-02 {1.15e-04}	6.49e-03 {9.91e-06}	1.65e-03 {2.53e-06}	-	-	-
atmo. $\nu$ (MC)	-	e	-	3.22e-03 {1.0}	1.25e-03 {3.88e-01}	6.65e-04 {2.06e-01}	3.86e-04 {1.20e-01}	3.49e-04 {1.08e-01}	3.49e-04 {1.08e-01}	1.11e-03 {4.26e-02}	-
		$\mu$	-	2.60e-02 {1.0}	5.03e-03 {1.94e-01}	2.80e-03 {1.08e-01}	1.47e-03 {5.68e-02}	1.11e-03 {4.26e-02}	1.09e-05 {1.39e-01}	1.09e-05 {1.39e-01}	-
		e	-	1.09e-04 {1.0}	6.82e-05 {6.27e-01}	3.67e-05 {3.38e-01}	1.57e-05 {1.44e-01}	1.51e-05 {1.39e-01}	1.09e-05 {1.39e-01}	1.09e-05 {1.39e-01}	-
		$\mu$	-	1.88e-04 {4.47e-03}	1.15e-04 {2.80e-03}	6.19e-05 {1.51e-03}	3.80e-05 {6.44e-04}	3.65e-05 {6.22e-04}	2.59e-05 {4.48e-04}	2.59e-05 {4.48e-04}	-
	$b\bar{b}$	all	-	6.84e-02 {1.0}	3.35e-04 {1.0}	2.05e-04 {6.12e-01}	1.11e-04 {3.30e-01}	5.88e-05 {1.75e-01}	5.66e-05 {1.69e-01}	5.66e-05 {1.69e-01}	4.03e-05 {1.20e-01}
		$\tau$	-	5.30e-03 {1.0}	3.87e-05 {1.0}	2.20e-05 {5.69e-01}	1.19e-05 {3.07e-01}	5.14e-06 {1.33e-01}	4.96e-06 {1.28e-01}	3.54e-06 {9.16e-02}	3.54e-06 {9.16e-02}
		e	-	2.14e-01 {1.0}	2.02e-03 {1.0}	1.01e-03 {5.02e-01}	5.52e-04 {2.74e-01}	2.36e-04 {1.17e-01}	2.26e-04 {1.12e-01}	1.75e-04 {8.67e-02}	1.75e-04 {8.67e-02}
		$\mu$	-	3.08e-01 {1.0}	3.29e-03 {1.0}	1.60e-03 {4.86e-01}	8.80e-04 {2.68e-01}	5.32e-04 {1.62e-01}	5.02e-04 {1.53e-01}	3.88e-04 {1.18e-01}	3.88e-04 {1.18e-01}
		all	-	6.40e-01 {1.0}	6.58e-03 {1.0}	3.23e-03 {4.90e-01}	1.77e-03 {2.68e-01}	9.13e-04 {1.39e-01}	8.64e-04 {1.31e-01}	6.71e-04 {1.02e-01}	6.71e-04 {1.02e-01}
	$\tau^+\tau^-$	$\tau$	-	1.18e-01 {1.0}	1.28e-03 {1.08e-02}	6.16e-04 {4.81e-01}	3.35e-04 {2.61e-01}	1.45e-04 {1.13e-01}	1.37e-04 {1.07e-01}	1.07e-04 {8.37e-02}	1.07e-04 {8.37e-02}

Table G.1.: Rates and efficiencies for  $m_\chi = 35 \text{ GeV}/c^2$ . Rates are given in events per  $10^{25}$  annihilations per second for the WIMP-induced neutrino signal and in Hz for background MC and data. Selection efficiencies relative to L2 are presented in square brackets and efficiencies relative to generation level (for signal) in curly brackets. Dashed fields state that the value is not available – typically because the respective low-level processing was performed in a collaboration-wide framework.

type		channel	flavor	event rate at level:								
				generation	L2	L3	L4	L5	L6	L7		
data	-	-	-		6.63e+02 [1.0]	1.15e+00 [1.74e-03]	8.29e-02 [1.25e-04]	8.10e-03 [1.22e-05]	2.93e-03 [4.43e-06]	8.11e-04 [1.22e-06] 1.21e-03 [1.83e-06]	$b\bar{b}$ $\tau^+\tau^-$	
atmo. $\mu$ (MC)	-	-	-		6.55e+02 [1.0]	1.26e+00 [1.92e-03]	7.53e-02 [1.15e-04]	6.49e-03 [9.91e-06]	1.91e-03 [2.91e-06]	-	-	
atmo. $\nu$ (MC)	-	-	e		3.22e-03 [1.0]	1.25e-03 [3.88e-01]	6.65e-04 [2.06e-01]	3.86e-04 [1.20e-01]	3.51e-04 [1.09e-01]	-	-	
	-	-	$\mu$		2.60e-02 [1.0]	5.03e-03 [1.94e-01]	2.80e-03 [1.08e-01]	1.47e-03 [5.68e-02]	1.18e-03 [4.53e-02]	-	-	
WIMP- induced $\nu$ (MC)	e	e	3.25e-02 {1.0}	1.81e-04 [1.0] {5.58e-03}	1.06e-04 [5.87e-01] {3.27e-03}	5.70e-05 [3.14e-01] {1.76e-03}	2.49e-05 [1.37e-01] {7.66e-04}	2.36e-05 [1.30e-01] {7.26e-04}	1.62e-05 [8.92e-02] {4.98e-04}			
			5.15e-02 {1.0}	3.18e-04 [1.0] {6.18e-03}	1.82e-04 [5.70e-01] {3.53e-03}	9.88e-05 [3.10e-01] {1.92e-03}	1.82e-04 [3.08e-01] {1.92e-03}	6.01e-05 [1.89e-01] {1.17e-03}	9.64e-05 [1.63e-01] {1.02e-03}	9.13e-05 [1.54e-01] {9.64e-04}	3.89e-05 [1.22e-01] {7.55e-04}	6.28e-05 [1.06e-01] {6.63e-04}
	$\mu$	$\mu$	1.08e-02 {1.0}	9.18e-05 [1.0] {8.53e-03}	4.94e-05 [5.38e-01] {4.59e-03}	2.64e-05 [2.88e-01] {2.46e-03}	1.14e-05 [1.24e-01] {1.06e-03}	1.09e-05 [1.18e-01] {1.01e-03}	1.62e-05 [8.49e-02] {7.24e-04}			
			2.99e-01 {1.0}	4.39e-03 [1.0] {1.47e-02}	1.81e-03 [4.13e-01] {6.06e-03}	9.94e-04 [2.26e-01] {3.32e-03}	4.18e-04 [9.52e-02] {1.40e-03}	3.96e-04 [9.01e-02] {1.32e-03}	3.08e-04 [7.01e-02] {1.03e-03}			
	$\tau$	$\tau$	4.24e-01 {1.0}	7.09e-03 [1.0] {1.67e-02}	2.81e-03 [3.97e-01] {6.63e-03}	5.93e-03 [4.05e-01] {6.39e-03}	3.28e-03 [2.24e-01] {3.71e-03}	1.65e-03 [1.31e-01] {2.19e-03}	1.54e-03 [1.21e-01] {1.66e-03}	1.54e-03 [1.05e-01] {1.66e-03}	6.59e-04 [9.30e-02] {1.55e-03}	1.19e-03 [8.14e-02] {1.29e-03}
			2.04e-01 {1.0}	3.17e-03 [1.0] {1.55e-02}	1.30e-03 [4.11e-01] {6.39e-03}	7.18e-04 [2.27e-01] {3.52e-03}	3.03e-04 [9.58e-02] {1.49e-03}	2.86e-04 [9.04e-02] {1.41e-03}	2.25e-04 [7.11e-02] {1.10e-03}			

Table G.2.: Rates and efficiencies for  $m_\chi = 50 \text{ GeV}/c^2$ . Rates are given in events per  $10^{25}$  annihilations per second for the WIMP-induced neutrino signal and in Hz for background MC and data. Selection efficiencies relative to L2 are presented in square brackets and efficiencies relative to generation level (for signal) in curly brackets. Dashed fields state that the value is not available – typically because the respective low-level processing was performed in a collaboration-wide framework.

Appendix G. Event Rates at the various Selection Levels

		$m_\chi = 100 \text{ GeV}/c^2$															
type	channel	flavor	event rate at level:														
			generation	L2	L3	L4	L5	L6	L7								
data	-	-	-	6.63e+02 {1.0}	1.15e+00 {1.74e-03}	8.29e-02 {1.25e-04}	8.10e-03 {1.22e-05}	3.04e-03 {4.59e-06}	8.18e-04 {1.23e-06}	$\tau^+ \tau^-$ $W^+ W^-$							
											1.11e-03 {1.68e-06}						
atmo. $\mu$ (MC)	-	-	-	6.55e+02 {1.0}	1.26e+00 {1.92e-03}	7.53e-02 {1.15e-04}	6.49e-03 {9.91e-06}	2.06e-03 {3.15e-06}	-	-							
atmo. $\nu$ (MC)	-	e	-	3.22e-03 {1.0}	1.25e-03 {3.88e-01}	6.65e-04 {2.06e-01}	3.86e-04 {1.20e-01}	3.36e-04 {1.04e-01}	-	-							
											2.60e-02 {1.0}	5.03e-03 {1.94e-01}	2.80e-03 {1.08e-01}	1.47e-03 {5.68e-02}	1.24e-03 {4.76e-02}	-	
WIMP induced $\nu$ (MC)	$b\bar{b}$	e	all	5.50e-02 {1.0}	5.73e-04 {1.0}	2.61e-04 {4.57e-01}	1.43e-04 {2.49e-01}	6.06e-05 {1.06e-01}	5.52e-05 {9.65e-02}	3.83e-05 {6.69e-02}	$b\bar{b}$						
				8.52e-02 {1.0}	9.81e-04 {1.0}	4.33e-04 {4.42e-01}	2.40e-04 {4.45e-01}	1.44e-04 {1.47e-01}	2.46e-04 {1.26e-01}	1.30e-04 {1.33e-01}		2.24e-04 {1.14e-01}	8.85e-05 {9.03e-02}	1.54e-04 {7.86e-02}			
		$\mu$	all	3.09e-02 {1.0}	4.09e-04 {1.0}	1.79e-04 {4.39e-01}	9.85e-05 {2.41e-01}	4.19e-05 {1.69e-03}	3.84e-05 {9.39e-02}	2.74e-05 {6.70e-02}	2.74e-05 {8.88e-04}	2.74e-05 {9.02e-04}	$\tau^+ \tau^-$				
				5.55e-01 {1.0}	2.09e-02 {1.33e-02}	5.30e-03 {2.54e-01}	3.06e-03 {1.47e-01}	1.26e-03 {6.03e-02}	1.17e-03 {5.61e-02}	8.14e-04 {3.90e-02}	8.14e-04 {3.90e-02}	8.14e-04 {3.90e-02}		3.03e-03 {4.32e-02}			
		$\tau$	all	7.68e-01 {1.0}	3.17e-02 {1.0}	7.01e-02 {1.0}	7.65e-03 {2.41e-01}	1.75e-02 {2.50e-01}	4.49e-03 {5.84e-03}	1.01e-02 {1.45e-01}	2.54e-03 {8.00e-02}	4.86e-03 {6.94e-02}	2.30e-03 {7.24e-02}	4.45e-03 {6.36e-02}	1.53e-03 {4.82e-02}	3.03e-03 {4.32e-02}	
				4.78e-01 {1.0}	1.75e-02 {3.66e-02}	4.54e-03 {2.59e-01}	2.60e-03 {1.49e-01}	6.07e-03 {6.08e-02}	1.07e-03 {5.64e-02}	9.87e-04 {5.64e-02}	6.85e-04 {3.91e-02}						
		e	all	2.28e-01 {1.0}	9.19e-03 {4.03e-02}	2.28e-03 {2.48e-01}	1.31e-03 {1.00e-02}	5.44e-04 {5.92e-02}	5.07e-04 {5.51e-02}	5.07e-04 {5.51e-02}	5.07e-04 {5.51e-02}	5.07e-04 {5.51e-02}	5.07e-04 {5.51e-02}	5.07e-04 {5.51e-02}	5.07e-04 {5.51e-02}	5.07e-04 {5.51e-02}	5.07e-04 {5.51e-02}
				3.10e-01 {1.0}	1.41e-02 {4.55e-02}	3.11e-02 {4.16e-02}	3.35e-03 {2.38e-01}	7.67e-03 {2.46e-01}	1.99e-03 {1.43e-01}	4.46e-03 {1.43e-01}	1.12e-03 {6.85e-02}	2.13e-03 {6.85e-02}	1.02e-03 {7.26e-02}	1.97e-03 {6.33e-02}	7.59e-04 {5.39e-02}	7.59e-04 {5.39e-02}	1.47e-03 {4.73e-02}
		$\mu$	all	2.11e-01 {1.0}	7.88e-03 {3.74e-02}	2.04e-03 {1.08e-02}	1.16e-03 {2.58e-01}	4.74e-04 {1.47e-01}	4.74e-04 {1.47e-01}	4.74e-04 {1.47e-01}	4.74e-04 {1.47e-01}	4.74e-04 {1.47e-01}	4.74e-04 {1.47e-01}	4.74e-04 {1.47e-01}	4.74e-04 {1.47e-01}	4.74e-04 {1.47e-01}	4.74e-04 {1.47e-01}
				2.11e-01 {1.0}	7.88e-03 {3.74e-02}	2.04e-03 {1.08e-02}	1.16e-03 {2.58e-01}	4.74e-04 {1.47e-01}	4.74e-04 {1.47e-01}	4.74e-04 {1.47e-01}	4.74e-04 {1.47e-01}	4.74e-04 {1.47e-01}	4.74e-04 {1.47e-01}	4.74e-04 {1.47e-01}	4.74e-04 {1.47e-01}	4.74e-04 {1.47e-01}	4.74e-04 {1.47e-01}
$\tau$																	

Table G.3.: Rates and efficiencies for  $m_\chi = 100 \text{ GeV}/c^2$ . Rates are given in events per  $10^{25}$  annihilations per second for the WIMP-induced neutrino signal and in Hz for background MC and data. Selection efficiencies relative to L2 are presented in square brackets and efficiencies relative to generation level (for signal) in curly brackets. Dashed fields state that the value is not available – typically because the respective low-level processing was performed in a collaboration-wide framework.

$m_\chi = 250 \text{ GeV}/c^2$

type	channel	flavor	event rate at level:						
			generation	L2	L3	L4	L5	L6	L7
data	-	-	-	6.63e+02	1.15e+00	8.29e-02	8.10e-03	3.16e-03	9.86e-04
				{1.0}	{1.74e-03}	{1.25e-04}	{1.22e-05}	{4.77e-06}	{1.49e-06}
atmo. $\mu$ (MC)	-	-	-	6.55e+02	1.26e+00	7.53e-02	6.49e-03	2.43e-03	9.86e-04
				{1.0}	{1.92e-03}	{1.15e-04}	{9.91e-06}	{3.72e-06}	{1.49e-06}
atmo. $\nu$ (MC)	-	e	-	3.22e-03	1.25e-03	6.65e-04	3.86e-04	2.83e-04	6.73e-04
				{1.0}	{3.88e-01}	{2.06e-01}	{1.20e-01}	{8.79e-02}	{1.02e-06}
	-	$\mu$	-	2.60e-02	5.03e-03	2.80e-03	1.47e-03	1.18e-03	7.65e-04
				{1.0}	{1.94e-01}	{1.08e-01}	{5.68e-02}	{4.56e-02}	{1.15e-06}
	-	e	-	2.74e-03	7.70e-04	4.38e-04	1.81e-04	1.59e-04	1.08e-04
				{1.0}	{2.80e-01}	{1.59e-01}	{6.58e-02}	{5.79e-02}	{3.93e-02}
	-	$\mu$	all	4.30e-03	1.17e-03	6.75e-04	3.86e-04	3.35e-04	2.26e-04
				{1.0}	{2.72e-01}	{1.57e-01}	{8.98e-02}	{7.64e-02}	{6.68e-02}
	-	$\tau$	-	2.89e-02	7.85e-03	4.54e-03	2.59e-03	2.25e-03	1.52e-03
				{1.0}	{7.85e-03}	{4.54e-03}	{2.59e-03}	{2.25e-03}	{1.52e-03}
	-	e	-	2.32e-03	6.44e-04	3.66e-04	1.49e-04	1.32e-04	9.15e-05
				{1.0}	{2.77e-01}	{1.57e-01}	{6.42e-02}	{5.69e-02}	{3.94e-02}
	-	$\mu$	all	2.97e-02	8.23e-03	4.67e-03	1.91e-03	1.69e-03	1.17e-03
				{1.0}	{8.23e-03}	{4.67e-03}	{1.91e-03}	{1.69e-03}	{1.17e-03}
WIMP induced $\nu$ (MC)	$\tau^+ \tau^-$	e	-	1.07e-01	1.56e-02	9.57e-03	3.81e-03	3.56e-03	2.45e-03
				{1.0}	{1.46e-01}	{8.95e-02}	{3.56e-02}	{2.29e-02}	{2.30e-03}
	-	$\mu$	all	1.42e+00	2.01e-02	3.22e-02	1.43e-02	1.33e-02	8.87e-03
				{1.0}	{1.25e-01}	{7.96e-02}	{4.10e-02}	{3.77e-02}	{3.52e-02}
	-	$\tau$	-	1.10e+00	1.61e-02	9.87e-03	3.87e-03	3.60e-03	2.46e-03
				{1.0}	{1.46e-01}	{8.95e-02}	{3.51e-02}	{2.24e-02}	{2.23e-03}
	-	e	-	4.83e-02	6.30e-03	3.89e-03	1.51e-03	1.43e-03	1.03e-03
				{1.0}	{1.30e-01}	{8.04e-02}	{3.12e-02}	{2.95e-02}	{2.12e-02}
	-	$\mu$	all	1.34e+00	7.65e-03	4.93e-03	2.55e-03	2.38e-03	1.59e-03
				{1.0}	{1.09e-01}	{6.99e-02}	{3.61e-02}	{3.36e-02}	{3.15e-02}
	-	$\tau$	-	4.98e-02	6.51e-03	4.03e-03	1.60e-03	1.51e-03	1.09e-03
				{1.0}	{1.31e-01}	{8.08e-02}	{3.22e-02}	{3.04e-02}	{2.18e-02}
	-	e	-	1.18e-01	1.54e-02	9.54e-03	3.80e-03	3.59e-03	2.57e-03
				{1.0}	{1.54e-02}	{9.54e-03}	{3.80e-03}	{3.59e-03}	{2.57e-03}

Table G.4.: Rates and efficiencies for  $m_\chi = 250 \text{ GeV}/c^2$ . Rates are given in events per  $10^{25}$  annihilations per second for the WIMP-induced neutrino signal and in Hz for background MC and data. Selection efficiencies relative to L2 are presented in square brackets and efficiencies relative to generation level (for signal) in curly brackets. Dashed fields state that the value is not available – typically because the respective low-level processing was performed in a collaboration-wide framework.

## Appendix G. Event Rates at the various Selection Levels

		$m_\chi = 500 \text{ GeV}/c^2$										
type	channel	flavor	event rate at level:									
			generation	L2	L3	L4	L5	L6	L7			
data	-	-	-	6.63e+02 {1.0}	1.15e+00 {1.74e-03}	8.29e-02 {1.25e-04}	8.10e-03 {1.22e-05}	2.87e-03 {4.33e-06}	9.82e-04 {1.48e-06}	4.53e-04 {6.84e-07}	$\tau^+\tau^-$ $W^+W^-$	
atmo. $\nu$ (MC)	-	-	-	6.55e+02 {1.0}	1.26e+00 {1.92e-03}	7.53e-02 {1.15e-04}	6.49e-03 {9.91e-06}	2.11e-03 {3.23e-06}	2.74e-04 {8.49e-02}	-	-	
atmo. $\nu$ (MC)	-	e	-	3.22e-03 {1.0}	1.25e-03 {3.88e-01}	6.65e-04 {2.06e-01}	3.86e-04 {1.20e-01}	2.74e-04 {8.49e-02}	1.16e-03 {4.48e-02}	-	-	
		$\mu$	-	2.60e-02 {1.0}	5.03e-03 {1.94e-01}	2.80e-03 {1.08e-01}	1.47e-03 {5.68e-02}	1.16e-03 {4.48e-02}	-	-	-	
		e	1.45e-01 {1.0}	6.98e-03 {4.81e-02}	1.43e-03 {2.05e-01}	8.36e-04 {1.20e-01}	3.44e-04 {4.93e-02}	3.09e-04 {4.42e-02}	2.11e-04 {3.03e-02}	2.11e-04 {3.03e-02}		
		$\mu$	2.05e-01 {1.0}	1.05e-02 {1.0}	2.02e-03 {1.92e-01}	1.22e-03 {1.16e-01}	6.64e-04 {6.33e-02}	1.32e-03 {5.55e-02}	5.87e-04 {5.60e-02}	1.8e-03 {4.94e-02}	3.91e-04 {3.73e-02}	7.94e-04 {3.33e-02}
	$b\bar{b}$	all	1.27e-01 {1.0}	6.36e-03 {5.03e-02}	1.31e-03 {2.06e-01}	7.70e-04 {1.21e-01}	3.14e-04 {4.94e-02}	2.81e-04 {2.22e-03}	2.81e-04 {2.22e-03}	1.92e-04 {3.02e-02}	1.92e-04 {3.02e-02}	1.67e-03 {1.67e-03}
		$\tau$	1.43e+00 {1.0}	2.16e-01 {1.0}	2.45e-02 {1.13e-01}	1.53e-02 {7.11e-02}	5.99e-03 {2.78e-02}	5.61e-03 {2.60e-02}	3.73e-03 {1.73e-02}	3.73e-03 {1.73e-02}	3.73e-03 {1.73e-02}	
		e	1.98e+00 {1.0}	3.65e-01 {1.0}	3.04e-02 {8.32e-02}	2.01e-02 {5.49e-02}	9.77e-03 {2.67e-02}	9.15e-03 {2.50e-02}	3.92e-03 {4.63e-03}	5.59e-03 {2.73e-03}	5.59e-03 {2.73e-03}	1.34e-02 {1.59e-02}
		$\mu$	1.67e+00 {1.0}	2.61e-01 {1.0}	2.85e-02 {1.54e-02}	1.81e-02 {1.01e-02}	6.92e-03 {4.94e-03}	6.50e-03 {4.63e-03}	6.50e-03 {4.63e-03}	4.28e-03 {2.73e-03}	4.28e-03 {2.73e-03}	4.28e-03 {2.73e-03}
		$\tau$	4.95e-01 {1.0}	8.43e-02 {1.56e-01}	8.68e-03 {1.71e-02}	5.54e-03 {1.09e-02}	2.14e-03 {4.15e-03}	2.04e-03 {3.90e-03}	1.41e-03 {2.57e-03}	1.41e-03 {2.57e-03}	1.41e-03 {2.57e-03}	
		e	6.35e-01 {1.0}	1.31e-01 {1.0}	9.84e-03 {7.54e-02}	6.53e-03 {5.00e-02}	1.82e-02 {5.89e-02}	3.19e-03 {2.45e-02}	3.01e-03 {2.31e-02}	7.22e-03 {2.34e-02}	1.73e-03 {1.33e-02}	4.61e-03 {1.49e-02}
		$\mu$	5.51e-01 {1.0}	9.40e-02 {1.0}	9.55e-03 {1.02e-01}	6.10e-03 {6.49e-02}	2.28e-03 {2.43e-02}	2.17e-03 {2.31e-02}	1.47e-03 {1.57e-02}	1.47e-03 {1.57e-02}	1.47e-03 {1.57e-02}	2.74e-03 {2.74e-03}
		$\tau$	5.51e-01 {1.0}	9.40e-02 {1.0}	9.55e-03 {1.02e-01}	6.10e-03 {6.49e-02}	2.28e-03 {2.43e-02}	2.17e-03 {2.31e-02}	1.47e-03 {1.57e-02}	1.47e-03 {1.57e-02}	1.47e-03 {1.57e-02}	2.74e-03 {2.74e-03}

Table G.5.: Rates and efficiencies for  $m_\chi = 500 \text{ GeV}/c^2$ . Rates are given in events per  $10^{25}$  annihilations per second for the WIMP-induced neutrino signal and in Hz for background MC and data. Selection efficiencies relative to L2 are presented in square brackets and efficiencies relative to generation level (for signal) in curly brackets. Dashed fields state that the value is not available – typically because the respective low-level processing was performed in a collaboration-wide framework.

		event rate at level:							
type	channel	flavor	generation	L2	L3	L4	L5	L6	L7
data	-	-	-	6.63e+02	1.15e+00	8.29e-02	8.10e-03	2.63e-03	5.35e-04
				{1.0}	{1.74e-03}	{1.25e-04}	{1.22e-05}	{3.97e-06}	{8.07e-07}
atmo. $\nu$ (MC)	-	-	-	6.55e+02	1.26e+00	7.53e-02	6.49e-03	1.84e-03	2.92e-04
				{1.0}	{1.92e-03}	{1.15e-04}	{9.91e-06}	{2.80e-06}	{4.41e-07}
atmo. $\nu$ (MC)	-	e	-	3.22e-03	1.25e-03	6.65e-04	3.86e-04	2.54e-04	3.16e-04
				{1.0}	{3.88e-01}	{2.06e-01}	{1.20e-01}	{7.89e-02}	{4.77e-07}
	-	$\mu$	-	2.60e-02	5.03e-03	2.80e-03	1.47e-03	1.11e-03	W+W-
				{1.0}	{1.94e-01}	{1.08e-01}	{5.68e-02}	{4.26e-02}	
	$b\bar{b}$	e	-	1.33e-02	2.18e-03	1.31e-03	5.25e-04	4.68e-04	2.69e-04
				{1.0}	{1.63e-01}	{9.79e-02}	{3.94e-02}	{2.02e-02}	
	$b\bar{b}$	$\mu$	all	6.19e-01	2.86e-03	1.76e-03	9.42e-04	8.13e-04	4.15e-04
				{1.0}	{1.16e-02}	{6.95e-03}	{2.80e-03}	{1.43e-03}	
	$b\bar{b}$	$\tau$	-	4.55e-02	7.12e-03	4.31e-03	1.96e-03	1.71e-03	9.26e-04
				{1.0}	{1.47e-01}	{9.07e-02}	{4.85e-02}	{4.30e-02}	
	$b\bar{b}$	$\tau$	-	{7.55e-02}	{1.11e-02}	{6.84e-03}	{3.66e-03}	{3.16e-03}	{2.04e-02}
				{1.0}	{1.15e-02}	{6.96e-03}	{3.16e-03}	{2.77e-03}	
	$b\bar{b}$	$\tau$	-	1.27e-02	2.08e-03	1.24e-03	4.90e-04	4.34e-04	2.42e-04
				{1.0}	{1.64e-01}	{9.76e-02}	{3.85e-02}	{1.90e-02}	
	$b\bar{b}$	$\tau$	-	{7.31e-02}	{1.20e-01}	{7.14e-03}	{2.82e-03}	{2.49e-03}	{1.39e-03}
				{1.0}	{3.03e-02}	{1.94e-02}	{7.37e-03}	{4.25e-03}	
WIMP induced $\nu$ (MC)	$\tau^+\tau^-$	e	-	3.04e-01	3.03e-02	1.94e-02	7.37e-03	6.93e-03	4.25e-03
				{1.0}	{1.80e-02}	{9.97e-02}	{6.38e-02}	{2.28e-02}	
	$\tau^+\tau^-$	$\mu$	all	5.79e-01	3.80e-02	2.59e-02	1.24e-02	1.15e-02	5.19e-03
				{1.0}	{1.06e-01}	{6.97e-02}	{2.14e-02}	{2.25e-02}	
	$\tau^+\tau^-$	$\tau$	-	{2.43e-01}	{8.23e-02}	{4.48e-02}	{2.14e-02}	{1.99e-02}	{8.97e-03}
				{1.0}	{2.09e-01}	{1.13e-02}	{5.21e-03}	{4.70e-03}	
	$\tau^+\tau^-$	$\tau$	-	4.02e-01	3.75e-02	2.43e-02	9.11e-03	8.59e-03	5.34e-03
				{1.0}	{1.80e-02}	{9.32e-02}	{6.05e-02}	{4.37e-03}	
	$\tau^+\tau^-$	e	-	{1.93e-01}	9.13e-03	5.93e-03	2.25e-03	2.11e-03	1.37e-03
				{1.0}	{9.35e-02}	{6.07e-02}	{2.31e-02}	{1.41e-02}	
	$\tau^+\tau^-$	$\mu$	all	{1.92e-01}	{1.79e-02}	{1.16e-02}	{4.42e-03}	{4.14e-03}	{2.70e-03}
				{1.0}	3.81e-01	3.03e-02	8.18e-03	7.66e-03	
	$\tau^+\tau^-$	$\mu$	all	1.66e-01	1.07e-02	7.36e-03	2.00e-02	3.21e-03	1.42e-03
				{1.0}	{6.46e-02}	{4.42e-02}	{5.26e-02}	{2.01e-02}	
	$\tau^+\tau^-$	$\tau$	-	{2.53e-01}	{1.63e-02}	{1.12e-02}	{5.23e-03}	{4.86e-03}	{2.15e-03}
				{1.0}	1.04e-02	6.74e-03	2.48e-03	2.34e-03	
	$\tau^+\tau^-$	$\tau$	-	1.17e-01	1.04e-02	6.74e-03	2.48e-03	2.34e-03	1.47e-03
				{1.0}	{8.95e-02}	{5.79e-02}	{4.17e-03}	{2.01e-02}	
	$\tau^+\tau^-$	$\tau$	-	{1.96e-01}	{1.75e-02}	{1.13e-02}	{4.17e-03}	{3.94e-03}	{2.47e-03}
				{1.0}					

Table G.6.: Rates and efficiencies for  $m_\chi = 1000 \text{ GeV}/c^2$ . Rates are given in events per  $10^{25}$  annihilations per second for the WIMP-induced neutrino signal and in Hz for background MC and data. Selection efficiencies relative to L2 are presented in square brackets and efficiencies relative to generation level (for signal) in curly brackets. Dashed fields state that the value is not available – typically because the respective low-level processing was performed in a collaboration-wide framework.



# List of Figures

1.1.	Temperature fluctuation dependence on multipole moment as measured by the PLANCK satellite . . . . .	17
1.2.	Matter distribution in the Bullet Cluster . . . . .	18
1.3.	Comoving WIMP number density in the early universe . . . . .	20
1.4.	Proton decay to $\pi^0$ and $e^+$ . . . . .	24
1.5.	Neutralino-quark spin-dependent elastic scattering processes . . . . .	30
1.6.	Possible neutralino self-annihilations into fermions . . . . .	31
2.1.	Survival probability for $\bar{\nu}_e$ as a function of distance . . . . .	38
2.2.	The two possible arrangements of the neutrino mass scale . . . . .	39
2.3.	Schematic comparison of the propagation of common cosmic messengers .	41
2.4.	Cosmic ray energy spectrum, as measured by earth-bound experiments . .	42
2.5.	Formation of secondary cosmic ray showers in the atmosphere . . . . .	43
2.6.	Neutrino charged-current and neutral-current interaction with a nucleus .	44
2.7.	Neutrino and anti-neutrino charged-current scattering cross-sections with nucleons . . . . .	45
2.8.	Energy-dependent neutrino-nucleon CC and NC cross-sections for neutrinos and antineutrinos . . . . .	47
2.9.	Construction of a Cherenkov radiation wave front by the Huygens principle	48
3.1.	Schematic of the IceCube detector . . . . .	50
3.3.	Visualization of <i>bad</i> -marked modules in the IceCube detector . . . . .	52
3.4.	Illustration of the DeepCore filter technique using the example of a simulated downward-going muon . . . . .	55
3.5.	Glacial wavelength and depth dependence of inverse scattering length and inverse absorption length . . . . .	56
3.6.	Distinction of possible neutrino interactions and related reaction products	57
3.7.	Comparison of high-energy event signatures . . . . .	59
4.1.	Equidistant ordinate sampling of the cumulative photon density function .	67
4.2.	Estimator runtime per event and channel . . . . .	68
4.3.	Directional cascade resolution estimate against opening angle between true and reconstructed direction . . . . .	69
4.4.	Energy-dependent pull distribution for a neutrino signal induced by solar WIMP annihilations . . . . .	70
5.1.	Energy spectra for neutrinos originating from WIMP annihilation, assuming a candidate with a mass $m_\chi = 100 \text{ GeV}/c^2$ . . . . .	74
5.2.	Run-based rates for experimental data with satisfied quality criteria . . .	77
5.3.	Distribution of the $n\text{Ch}^{\text{sRT}}$ variable on selection level 3 . . . . .	81

5.4. Distribution of $\cos(\theta_{\text{reco}}^{\text{LineFitDC}})$ on selection level 3 . . . . .	82
5.5. Distribution of $\cos(\theta_{\text{reco}}^{\text{SPE2DC}})$ on selection level 3 . . . . .	82
5.6. Illustration of a coincident muon event with corresponding incident angles	84
5.7. Distribution of the $n\text{Ch}_{\text{veto}}^{\text{CRT}}$ variable on selection level 4 . . . . .	84
5.8. Distribution of the $n\text{Ch}_{\text{DC}}^{\text{CRT}}$ variable on selection level 4 . . . . .	85
5.9. Distribution of the $v_{12}/v_{13}$ ratio on selection level 4 . . . . .	85
5.10. Underlying concept of the $n\text{VetoHits}$ variable . . . . .	87
5.11. Illustration of FiniteReco's first-guess determination of the track's starting and stopping point . . . . .	89
5.12. Distribution of the $n\text{VetoHits}$ variable at selection level 5 . . . . .	89
5.13. Rates and data-MC ratio at the individual selection levels . . . . .	93
5.14. Final-level effective all-flavor detector volume as a function of candidate mass . . . . .	94
5.15. Effective areas at final selection level . . . . .	95
5.16. Schematic illustration of the basic BDT structure . . . . .	97
5.17. BDT score distribution . . . . .	98
5.18. Post-cut efficiencies as a function of the BDT score cut value . . . . .	99
5.19. Over-training check . . . . .	99
5.20. Correlation matrix for pairs of discrimination variables for signal and back- ground . . . . .	100
5.21. Angular distance between true (simulated) and reconstructed direction . .	101
5.22. Spherical angles in the used coordinate system for an example $\nu_e$ signal .	103
5.23. Signal PDF for three example values of the angular uncertainty. . . . .	104
5.24. Background PDF for the example of a 100 GeV/c <sup>2</sup> WIMP annihilating to a $b\bar{b}$ pair . . . . .	105
5.25. Energy PDF for the example of a 100 GeV/c <sup>2</sup> WIMP annihilating to a $b\bar{b}$ pair . . . . .	106
5.26. Number of fitted signal events for pure-background and signal-contaminated runs (for the example of a 100 GeV/c <sup>2</sup> WIMP annihilating to a $b\bar{b}$ pair) .	107
5.27. $TS$ values for pure-background and signal-contaminated runs (for the ex- ample of a 100 GeV/c <sup>2</sup> WIMP annihilating to a $b\bar{b}$ pair) . . . . .	107
5.28. Number of injected signal events against the number of fitted signal events for signal-contaminated trial runs . . . . .	108
5.29. Spin-dependent scattering cross-section sensitivities . . . . .	111
5.30. All-flavor based spin-dependent scattering cross-section sensitivity band for DOM efficiencies varied by $\pm 10\%$ . . . . .	113
5.31. Spin-dependent scattering cross-section sensitivities including systematic uncertainties . . . . .	116
5.32. Comparison of the all-flavor based spin-dependent scattering cross-section sensitivities to those obtained by a track-focused IceCube analysis . . . .	117
5.33. Comparison of the all-flavor based spin-dependent scattering cross-section sensitivities to limits from SUPER-K and the direct-detection limits from the PICO-2L experiment . . . . .	118

---

6.1.	Distribution of $m_h$ in valid supersymmetric models . . . . .	122
6.2.	Impact of the Higgs mass cut on the spin-dependent neutralino-proton scattering cross-section . . . . .	122
6.3.	Distribution of the dark matter relic density in valid supersymmetric models with the Higgs mass constrained . . . . .	123
6.4.	Impact of the dark matter relic density cut on the spin-dependent neutralino-proton scattering cross-section . . . . .	124
6.5.	Spin-dependent neutralino-proton scattering cross-section as a function of neutralino mass . . . . .	126
6.6.	Spin-independent neutralino-proton scattering cross-section . . . . .	127
6.7.	Spin-dependent against spin-independent neutralino-proton scattering cross-section . . . . .	127
6.8.	Velocity-averaged neutralino self-annihilation cross-section as a function of neutralino mass . . . . .	128
A.1.	Neutrino energy spectra at generation level for a WIMP candidate with mass $m_\chi = 35 \text{ GeV}/c^2$ . . . . .	131
A.2.	Neutrino energy spectra at generation level for a WIMP candidate with mass $m_\chi = 50 \text{ GeV}/c^2$ . . . . .	132
A.3.	Neutrino energy spectra at generation level for a WIMP candidate with mass $m_\chi = 100 \text{ GeV}/c^2$ . . . . .	132
A.4.	Neutrino energy spectra at generation level for a WIMP candidate with mass $m_\chi = 250 \text{ GeV}/c^2$ . . . . .	133
A.5.	Neutrino energy spectra at generation level for a WIMP candidate with mass $m_\chi = 500 \text{ GeV}/c^2$ . . . . .	133
A.6.	Neutrino energy spectra at generation level for a WIMP candidate with mass $m_\chi = 1000 \text{ GeV}/c^2$ . . . . .	134
B.1.	IceCube low-level simulation chain . . . . .	136
C.1.	Signature of lit optical modules for incident signal neutrinos with $E_\nu \approx 30 \text{ GeV}$ undergoing a charged-current reaction . . . . .	137
C.2.	Signature of lit optical modules for incident atmospheric neutrinos with $E_\nu \approx 400 \text{ GeV}$ undergoing a charged-current reaction . . . . .	138
D.1.	Distribution of $\sigma_z^{\text{resca}}$ at selection level 5 . . . . .	139
D.2.	Distribution of the $\mathbf{rlogL}^{\text{SPE32}}$ variable at selection level 5 . . . . .	139
D.3.	Distribution of the $\mathbf{nVetoHits}$ variable at selection level 5 . . . . .	140
D.4.	Distribution of $\cos(\theta_{\text{reco}}^{\text{monopod}})$ at selection level 5 . . . . .	140
D.5.	Distribution of $z_{\text{reco}}^{\text{monopod}}$ at selection level 5 . . . . .	141
D.6.	Distribution of $E_{\text{reco}}^{\text{monopod}}$ at selection level 5 . . . . .	141
D.7.	Distribution of $\cos(\theta_{\text{reco}}^{\text{millipede}})$ at selection level 5 . . . . .	142
D.8.	Distribution of the $\mathbf{Ndir}$ variable at selection level 5 . . . . .	142
D.9.	Distribution of the $\mathbf{NAbove200}$ variable at selection level 5 . . . . .	143
D.10.	Distribution of the $\mathbf{Ldir}$ variable at selection level 5 . . . . .	143

---

D.11. Distribution of the <b>FRLength</b> variable at selection level 5 . . . . .	144
D.12. Distribution of the <b>C2QR6</b> variable at selection level 5 . . . . .	144
E.1. BDT score (left) and score cut efficiency (right) for $m_\chi = 35 \text{ GeV}/c^2$ . . . . .	146
E.2. BDT over-training check for $m_\chi = 35 \text{ GeV}/c^2$ . . . . .	146
E.3. Discrimination variables correlation matrix for $m_\chi = 35 \text{ GeV}/c^2$ . . . . .	146
E.4. BDT score (left) and score cut efficiency (right) for $m_\chi = 50 \text{ GeV}/c^2$ . . . . .	147
E.5. BDT over-training check for $m_\chi = 50 \text{ GeV}/c^2$ . . . . .	147
E.6. Discrimination variables correlation matrix for $m_\chi = 50 \text{ GeV}/c^2$ . . . . .	147
E.7. BDT score (left) and score cut efficiency (right) for $m_\chi = 100 \text{ GeV}/c^2$ . . . . .	148
E.8. BDT over-training check for $m_\chi = 100 \text{ GeV}/c^2$ . . . . .	148
E.9. Discrimination variables correlation matrix for $m_\chi = 100 \text{ GeV}/c^2$ . . . . .	148
E.10. BDT score (left) and score cut efficiency (right) for $m_\chi = 250 \text{ GeV}/c^2$ . . . . .	149
E.11. BDT over-training check for $m_\chi = 250 \text{ GeV}/c^2$ . . . . .	149
E.12. Discrimination variables correlation matrix for $m_\chi = 250 \text{ GeV}/c^2$ . . . . .	149
E.13. BDT score (left) and score cut efficiency (right) for $m_\chi = 500 \text{ GeV}/c^2$ . . . . .	150
E.14. BDT over-training check for $m_\chi = 500 \text{ GeV}/c^2$ . . . . .	150
E.15. Discrimination variables correlation matrix for $m_\chi = 500 \text{ GeV}/c^2$ . . . . .	150
E.16. BDT score (left) and score cut efficiency (right) for $m_\chi = 1000 \text{ GeV}/c^2$ . . . . .	151
E.17. BDT over-training check for $m_\chi = 1000 \text{ GeV}/c^2$ . . . . .	151
E.18. Discrimination variables correlation matrix for $m_\chi = 1000 \text{ GeV}/c^2$ . . . . .	151
F.1. Spin-dependent scattering cross-section against BDT score cut value, shown for a WIMP with a mass of $100 \text{ GeV}/c^2$ . . . . .	153

# List of Tables

1.1. Standard Model particles and their MSSM superpartners . . . . .	24
2.1. Third isospin component $I_3$ , weak hypercharge $Y$ and resulting electric charge $Q$ for the first generation of leptons and quarks . . . . .	35
5.1. Optimized cut values on BDT scores . . . . .	91
5.2. All-flavor rates for experimental data, sum of background Monte-Carlo and signal, shown for selection levels 2 and 6 . . . . .	92
5.3. Final level efficiencies, the best-fit sensitivity on the number of signal events as well as the respective annihilation rate and WIMP-proton scattering cross-section sensitivities . . . . .	110
5.4. Individual and total relative uncertainties from various error sources . . .	114
6.1. Ranges for logarithmic and uniform distributions of input parameters . .	121
6.2. Number of models scanned at generation and at the subsequent filter stages	124
G.1. Rates and efficiencies for $m_\chi = 35 \text{ GeV}/c^2$ . . . . .	156
G.2. Rates and efficiencies for $m_\chi = 50 \text{ GeV}/c^2$ . . . . .	157
G.3. Rates and efficiencies for $m_\chi = 100 \text{ GeV}/c^2$ . . . . .	158
G.4. Rates and efficiencies for $m_\chi = 250 \text{ GeV}/c^2$ . . . . .	159
G.5. Rates and efficiencies for $m_\chi = 500 \text{ GeV}/c^2$ . . . . .	160
G.6. Rates and efficiencies for $m_\chi = 1000 \text{ GeV}/c^2$ . . . . .	161



# Bibliography

- [1] H. P. Robertson, *Kinematics and World-Structure*, *Astrophys. J.* 82, 284 (1935).
- [2] A. G. Walker, *On Milne's Theory of World-Structure*, *Proc. London Math. Soc.* s2-42, 90 (1937).
- [3] P. A. R. Ade, et al., *Planck 2015 results. XIII. Cosmological parameters*, submitted to *Astron. Astrophys.* (2015).
- [4] A. R. Liddle, *An introduction to modern cosmology* (2003).
- [5] F. Zwicky, *Die Rotverschiebung von extragalaktischen Nebeln*, *Helv. Phys. Acta* 6, 110 (1933).
- [6] D. R. Law, S. R. Majewski, K. V. Johnston, *Evidence for a Triaxial Milky Way Dark Matter Halo from the Sagittarius Stellar Tidal Stream*, *Astrophys. J.* 703, L67 (2009).
- [7] V. C. Rubin, W. K. Ford, Jr., *Rotation of the Andromeda Nebula from a Spectroscopic Survey of Emission Regions*, *Astrophys. J.* 159, 379 (1970).
- [8] V. C. Rubin, N. Thonnard, W. K. Ford, Jr., *Rotational properties of 21 SC galaxies with a large range of luminosities and radii, from NGC 4605 ( $R = 4$  kpc) to UGC 2885 ( $R = 122$  kpc)*, *Astrophys. J.* 238, 471 (1980).
- [9] S. van den Bergh, *The Early history of dark matter*, *Publ. Astron. Soc. Pac.* 111, 657 (1999).
- [10] Y. Sofue, V. Rubin, *Rotation curves of spiral galaxies*, *Ann. Rev. Astron. Astrophys.* 39, 137 (2001).
- [11] W. Hu, M. J. White, *Acoustic signatures in the cosmic microwave background*, *Astrophys. J.* 471, 30 (1996).
- [12] S. Perlmutter, et al., *Measurements of  $\Omega$  and  $\Lambda$  from 42 High-Redshift Supernovae*, *Astrophys. J.* 517, 565 (1999).
- [13] A. G. Riess, et al., *Observational evidence from supernovae for an accelerating universe and a cosmological constant*, *Astron. J.* 116, 1009 (1998).
- [14] V. Springel, et al., *Simulating the joint evolution of quasars, galaxies and their large-scale distribution*, *Nature* 435, 629 (2005).
- [15] R. E. Angulo, et al., *Scaling relations for galaxy clusters in the Millennium-XXL simulation*, *Mon. Not. Roy. Astron. Soc.* 426, 2046 (2012).
- [16] *Composite image of the galaxy cluster 1E 0657-56*, <http://chandra.harvard.edu/photo/2006/1e0657> (2006).
- [17] D. Clowe, A. Gonzalez, M. Markevitch, *Weak lensing mass reconstruction of the interacting cluster 1E0657-558: Direct evidence for the existence of dark matter*, *Astrophys. J.* 604, 596 (2004).

- [18] M. Bradac, et al., *Revealing the properties of dark matter in the merging cluster MACSJ0025.4-1222*, *Astrophys. J.* 687, 959 (2008).
- [19] E. W. Kolb, M. S. Turner, *The Early Universe*, *Front. Phys.* 69, 1 (1990).
- [20] R. J. Scherrer, M. S. Turner, *On the Relic, Cosmic Abundance of Stable Weakly Interacting Massive Particles*, *Phys. Rev. D*33, 1585 (1986), [Erratum: *Phys. Rev. D*34,3263(1986)].
- [21] G. Jungman, M. Kamionkowski, K. Griest, *Supersymmetric dark matter*, *Phys. Rept.* 267, 195 (1996).
- [22] G. Steigman, M. S. Turner, *Cosmological Constraints on the Properties of Weakly Interacting Massive Particles*, *Nucl. Phys. B*253, 375 (1985).
- [23] G. Bertone, D. Hooper, J. Silk, *Particle dark matter: Evidence, candidates and constraints*, *Phys. Rept.* 405, 279 (2005).
- [24] M. E. Peskin, D. V. Schroeder, *An Introduction to quantum field theory* (1995).
- [25] W. Hollik, *Quantum field theory and the Standard Model*, in *High-energy physics. Proceedings, 17th European School, ESHEP 2009, Bautzen, Germany, June 14-27, 2009* (2010).
- [26] S. L. Glashow, *Partial Symmetries of Weak Interactions*, *Nucl. Phys.* 22, 579 (1961).
- [27] S. Weinberg, *A Model of Leptons*, *Phys. Rev. Lett.* 19, 1264 (1967).
- [28] W. Hollik, *Electroweak theory*, *J. Phys. Conf. Ser.* 53, 7 (2006).
- [29] G. Aad, et al., *Observation of a new particle in the search for the Standard Model Higgs boson with the ATLAS detector at the LHC*, *Phys. Lett. B*716, 1 (2012).
- [30] G. Aad, et al., *Combined Measurement of the Higgs Boson Mass in  $pp$  Collisions at  $\sqrt{s} = 7$  and 8 TeV with the ATLAS and CMS Experiments*, *Phys. Rev. Lett.* 114, 191803 (2015).
- [31] S. P. Martin, *A Supersymmetry primer*, *Adv. Ser. Direct. High Energy Phys.* 18, 1 (1998).
- [32] A. Djouadi, et al., *The Minimal supersymmetric standard model: Group summary report*, in *GDR (Groupement De Recherche) - Supersymetrie Montpellier, France, April 15-17, 1998* (1998).
- [33] J. Edsjö, *Aspects of neutrino detection of neutralino dark matter*, Ph.D. thesis, Uppsala U. (1997).
- [34] S. Dimopoulos, D. W. Sutter, *The Supersymmetric flavor problem*, *Nucl. Phys. B*452, 496 (1995).
- [35] M. Thomson, *Modern particle physics*. Cambridge University Press, New York (2013).
- [36] G. L. Kane, et al., *Study of constrained minimal supersymmetry*, *Phys. Rev. D*49, 6173 (1994).
- [37] H. Baer, V. Barger, A. Mustafayev, *Neutralino dark matter in  $mSUGRA/CMSSM$  with a 125 GeV light Higgs scalar*, *JHEP* 05, 091 (2012).
- [38] C. F. Berger, et al., *Supersymmetry Without Prejudice*, *JHEP* 02, 023 (2009).
- [39] G. Duda, et al., *Indirect detection of a subdominant density component of cold dark matter*, *Phys. Rev. D*67, 023505 (2003).

- 
- [40] V. Khachatryan, et al., *Searches for electroweak neutralino and chargino production in channels with Higgs, Z, and W bosons in pp collisions at 8 TeV*, Phys. Rev. D90(9), 092007 (2014).
- [41] G. Bélanger, et al., *LHC constraints on light neutralino dark matter in the MSSM*, Phys. Lett. B726, 773 (2013).
- [42] L. Baudis, *A review of direct WIMP search experiments*, Nucl. Phys. Proc. Suppl. 235-236, 405 (2013).
- [43] C. Rott, *Review of Indirect WIMP Search Experiments*, Nucl. Phys. Proc. Suppl. 235-236, 413 (2012).
- [44] A. Gould, *Resonant Enhancements in WIMP Capture by the Earth*, Astrophys. J. 321, 571 (1987).
- [45] W. H. Press, D. N. Spergel, *Capture by the sun of a galactic population of weakly interacting massive particles*, Astrophys. J. 296, 679 (1985).
- [46] T. K. Gaisser, G. Steigman, S. Tilav, *Limits on Cold Dark Matter Candidates from Deep Underground Detectors*, Phys. Rev. D34, 2206 (1986).
- [47] M. Ackermann, et al., *Constraints on the Galactic Halo Dark Matter from Fermi-LAT Diffuse Measurements*, Astrophys. J. 761, 91 (2012).
- [48] M. G. Aartsen, et al., *Multipole analysis of IceCube data to search for dark matter accumulated in the Galactic halo*, Eur. Phys. J. C75(99), 20 (2015).
- [49] E. Aprile, et al., *The XENON100 Dark Matter Experiment*, Astropart. Phys. 35, 573 (2012).
- [50] D. S. Akerib, et al., *The LUX Experiment*, Phys. Procedia 61, 74 (2015).
- [51] J. Engel, S. Pittel, P. Vogel, *Nuclear physics of dark matter detection*, Int. J. Mod. Phys. E1, 1 (1992).
- [52] S. P. Ahlen, et al., *Limits on Cold Dark Matter Candidates from an Ultralow Background Germanium Spectrometer*, Phys. Lett. B195, 603 (1987).
- [53] M. L. Ahnen, et al., *Limits to dark matter annihilation cross-section from a combined analysis of MAGIC and Fermi-LAT observations of dwarf satellite galaxies*, JCAP 1602(02), 039 (2016).
- [54] F. Hoyle, *Concluding remarks*, in *Proceedings of the Royal Society of London A: Mathematical, Physical and Engineering Sciences*, vol. 301, pp. 171–171 (1967).
- [55] C. L. Cowan, et al., *Detection of the free neutrino: A Confirmation*, Science 124, 103 (1956).
- [56] C. Weinheimer, et al., *High precision measurement of the tritium beta spectrum near its endpoint and upper limit on the neutrino mass*, Phys. Lett. B460, 219 (1999).
- [57] S. R. Elliott, P. Vogel, *Double beta decay*, Ann. Rev. Nucl. Part. Sci. 52, 115 (2002).
- [58] S. Schael, et al., *Precision electroweak measurements on the Z resonance*, Phys. Rept. 427, 257 (2006).

- [59] D. N. Schramm, G. Steigman, *On the Relation of the Cosmological Constraints on Neutrino Flavors to the Width of the  $Z^0$* , Phys. Lett. B141, 337 (1984).
- [60] G. Mangano, P. D. Serpico, *A robust upper limit on  $N_{eff}$  from BBN, circa 2011*, Phys. Lett. B701, 296 (2011).
- [61] B. T. Cleveland, et al., *Measurement of the solar electron neutrino flux with the Homestake chlorine detector*, Astrophys. J. 496, 505 (1998).
- [62] J. N. Bahcall, *Solar neutrinos. I: Theoretical*, Phys. Rev. Lett. 12, 300 (1964).
- [63] J. N. Bahcall, et al., *Standard Solar Models and the Uncertainties in Predicted Capture Rates of Solar Neutrinos*, Rev. Mod. Phys. 54, 767 (1982).
- [64] Y. Fukuda, et al., *Evidence for oscillation of atmospheric neutrinos*, Phys. Rev. Lett. 81, 1562 (1998).
- [65] Q. R. Ahmad, et al., *Measurement of the rate of  $\nu_e + d \rightarrow p + p + e^-$  interactions produced by  $^8B$  solar neutrinos at the Sudbury Neutrino Observatory*, Phys. Rev. Lett. 87, 071301 (2001).
- [66] B. Pontecorvo, *Inverse beta processes and nonconservation of lepton charge*, Sov. Phys. JETP 7, 172 (1958).
- [67] Z. Maki, M. Nakagawa, S. Sakata, *Remarks on the unified model of elementary particles*, Prog. Theor. Phys. 28, 870 (1962).
- [68] F. P. An, et al., *Observation of electron-antineutrino disappearance at Daya Bay*, Phys. Rev. Lett. 108, 171803 (2012).
- [69] P. Adamson, et al., *Measurement of the neutrino mass splitting and flavor mixing by MINOS*, Phys. Rev. Lett. 106, 181801 (2011).
- [70] F. P. An, et al., *Spectral measurement of electron antineutrino oscillation amplitude and frequency at Daya Bay*, Phys. Rev. Lett. 112, 061801 (2014).
- [71] K. Eguchi, et al., *First results from KamLAND: Evidence for reactor anti-neutrino disappearance*, Phys. Rev. Lett. 90, 021802 (2003).
- [72] K. A. Olive, et al., *Review of Particle Physics*, Chin. Phys. C38, 090001 (2014).
- [73] F. Capozzi, et al., *Neutrino masses and mixings: Status of known and unknown  $3\nu$  parameters*, Nucl. Phys. B908, 218 (2016).
- [74] NuFIT, *Leptonic mixing matrix*, <http://www.nu-fit.org/?q=node/115#label115> (2016).
- [75] E. Komatsu, et al., *Seven-Year Wilkinson Microwave Anisotropy Probe (WMAP) Observations: Cosmological Interpretation*, Astrophys. J. Suppl. 192, 18 (2011).
- [76] J. Lesgourgues, S. Pastor, *Neutrino mass from Cosmology*, Adv. High Energy Phys. 2012, 608515 (2012).
- [77] A. Marrone, *Status and prospects of global analyses of neutrino mass-mixing parameters*, [http://neutrino2016.iopconfs.org/IOP/media/uploaded/EVIOP/event\\_948/16.00\\_\\_5\\_\\_Marrone.pdf](http://neutrino2016.iopconfs.org/IOP/media/uploaded/EVIOP/event_948/16.00__5__Marrone.pdf) (2016).
- [78] L. Wolfenstein, *Neutrino Oscillations in Matter*, Phys. Rev. D17, 2369 (1978).

- 
- [79] S. P. Mikheev, A. Yu. Smirnov, *Resonant amplification of neutrino oscillations in matter and solar neutrino spectroscopy*, Nuovo Cim. C9, 17 (1986).
- [80] M. G. Aartsen, et al., *Letter of Intent: The Precision IceCube Next Generation Upgrade (PINGU)* (2014).
- [81] M. Blennow, J. Edsjö, T. Ohlsson, *Neutrinos from WIMP annihilations using a full three-flavor Monte Carlo*, JCAP 0801, 021 (2008).
- [82] M. Gell-Mann, P. Ramond, R. Slansky, *Complex Spinors and Unified Theories*, Conf. Proc. C790927, 315 (1979).
- [83] E. K. Akhmedov, *Neutrino physics*, in *Proceedings, Summer School in Particle Physics*, pp. 103–164 (1999).
- [84] W. Wagner, *Design and realisation of a new AMANDA data acquisition system with transient waveform recorders*, Ph.D. thesis, Universität Dortmund (2005).
- [85] V. F. Hess, *Über Beobachtungen der durchdringenden Strahlung bei sieben Freiballonfahrten*, Physikalische Zeitschrift 13, 1084 (1912).
- [86] T. K. Gaisser, R. Engel, E. Resconi, *Cosmic Rays and Particle Physics*. Cambridge University Press.
- [87] E. Fermi, *On the Origin of the Cosmic Radiation*, Phys. Rev. 75, 1169 (1949).
- [88] I. F. M. Albuquerque, J. Lamoureux, G. F. Smoot, *Astrophysical neutrino event rates and sensitivity for neutrino telescopes*, Astrophys. J. Suppl. 141, 195 (2002).
- [89] M. G. Aartsen, et al., *Search for a diffuse flux of astrophysical muon neutrinos with the IceCube 59-string configuration*, Phys. Rev. D89(6), 062007 (2014).
- [90] J. J. Beatty, S. Westerhoff, *The Highest-Energy Cosmic Rays*, Ann. Rev. Nucl. Part. Sci. 59, 319 (2009).
- [91] P. L. Biermann, G. A. Medina-Tanco, *Ultrahigh-energy cosmic ray sources and experimental results*, Nucl. Phys. Proc. Suppl. 122, 86 (2003).
- [92] A. Fedynitch, J. Becker Tjus, P. Desiati, *Influence of hadronic interaction models and the cosmic ray spectrum on the high energy atmospheric muon and neutrino flux*, Phys. Rev. D86, 114024 (2012).
- [93] B. Louis, et al., *The evidence for oscillations*, Los Alamos Sci. 25, 116 (1997).
- [94] J. van Santen, *Neutrino Interactions in IceCube above 1 TeV: Constraints on Atmospheric Charmed-Meson Production and Investigation of the Astrophysical Neutrino Flux with 2 Years of IceCube Data taken 2010–2012*, Ph.D. thesis, U. Wisconsin, Madison (2014).
- [95] C. Andreopoulos, et al., *The GENIE Neutrino Monte Carlo Generator*, Nucl. Instrum. Meth. A614, 87 (2010).
- [96] A. Gazizov, et al., *Neutrino-nucleon cross sections at energies of Megaton-scale detectors*, EPJ Web Conf. 116, 08003 (2016).
- [97] J. A. Formaggio, G. P. Zeller, *From eV to EeV: Neutrino Cross Sections Across Energy Scales*, Rev. Mod. Phys. 84, 1307 (2012).

- [98] J.-M. Levy, *Cross-section and polarization of neutrino-produced tau's made simple*, J. Phys. G36, 055002 (2009).
- [99] S. Kretzer, M. H. Reno, *Tau neutrino deep inelastic charged current interactions*, Phys. Rev. D66, 113007 (2002).
- [100] J. Edsjö, *Calculation of neutrino cross sections and the nusigma neutrino-nucleon scattering Monte Carlo* (2007).
- [101] R. Gandhi, et al., *Neutrino interactions at ultrahigh-energies*, Phys. Rev. D58, 093009 (1998).
- [102] S. L. Glashow, *Resonant Scattering of Antineutrinos*, Phys. Rev. 118, 316 (1960).
- [103] R. Gandhi, et al., *Ultrahigh-energy neutrino interactions*, Astropart. Phys. 5, 81 (1996).
- [104] M. G. Aartsen, et al., *Evidence for High-Energy Extraterrestrial Neutrinos at the IceCube Detector*, Science 342, 1242856 (2013).
- [105] B. Voigt, *Sensitivity of the IceCube Detector for Ultra-High Energy Electron-Neutrino Events*, Ph.D. thesis, Humboldt U., Berlin (2008).
- [106] P. A. Cerenkov, *Visible radiation produced by electrons moving in a medium with velocities exceeding that of light*, Phys. Rev. 52, 378 (1937).
- [107] S. G. Warren, *Optical constants of ice from the ultraviolet to the microwave*, Appl. Opt. 23(8), 1206 (1984).
- [108] J. D. Jackson, *Classical Electrodynamics*. Wiley (1998).
- [109] I. M. Frank, I. Tamm, *Coherent visible radiation of fast electrons passing through matter*, C. R. Acad. Sci. URSS 14, 109 (1937).
- [110] M. Ackermann, et al., *Optical properties of deep glacial ice at the South Pole*, J. Geophys. Res. 111(D13), D13203 (2006).
- [111] F. Halzen, S. R. Klein, *IceCube: An Instrument for Neutrino Astronomy*, Rev. Sci. Instrum. 81, 081101 (2010).
- [112] A. Roberts, *The Birth of high-energy neutrino astronomy: A Personal history of the DUMAND project*, Rev. Mod. Phys. 64, 259 (1992).
- [113] E. Andres, et al., *The AMANDA neutrino telescope: Principle of operation and first results*, Astropart. Phys. 13, 1 (2000).
- [114] J. Ahrens, et al., *Icecube - the next generation neutrino telescope at the south pole*, Nucl. Phys. Proc. Suppl. 118, 388 (2003).
- [115] A. Achterberg, et al., *First Year Performance of The IceCube Neutrino Telescope*, Astropart. Phys. 26, 155 (2006).
- [116] *The IceCube Public Gallery*, <https://gallery.icecube.wisc.edu>.
- [117] R. Abbasi, et al., *The IceCube Data Acquisition System: Signal Capture, Digitization, and Timestamping*, Nucl. Instrum. Meth. A601, 294 (2009).
- [118] R. Abbasi, et al., *Calibration and Characterization of the IceCube Photomultiplier Tube*, Nucl. Instrum. Meth. A618, 139 (2010).

- 
- [119] R. Abbasi, et al., *IceTop: The surface component of IceCube*, Nucl. Instrum. Meth. A700, 188 (2013).
- [120] R. C. Bay, N. Bramall, P. B. Price, *Bipolar correlation of volcanism with millennial climate change*, Proceedings of the National Academy of Sciences of the United States of America 101(17), 6341 (2004).
- [121] M. Aartsen, et al., *South pole glacial climate reconstruction from multi-borehole laser particulate stratigraphy*, Journal of Glaciology 59(218), 1117 (2013).
- [122] R. Abbasi, et al., *The Design and Performance of IceCube DeepCore*, Astropart. Phys. 35, 615 (2012).
- [123] D. Heereman, *HitSpooling: An Improvement for the Supernova Neutrino Detection System in IceCube*, Ph.D. thesis, Université Libre de Bruxelles (2015).
- [124] S. Schönert, et al., *Vetoing atmospheric neutrinos in a high energy neutrino telescope*, Phys. Rev. D79, 043009 (2009).
- [125] J. L. Kelley, *Event triggering in the IceCube data acquisition system*, AIP Conf. Proc. 1630, 154 (2014).
- [126] S. Tilav, et al., *Atmospheric Variations as Observed by IceCube*, in *Proceedings of the 31st International Cosmic Ray Conference* (2009).
- [127] *SLC hit cleaning*, [https://wiki.icecube.wisc.edu/index.php?title=SLC\\_hit\\_cleaning](https://wiki.icecube.wisc.edu/index.php?title=SLC_hit_cleaning) (2010).
- [128] G. Mie, *Beiträge zur Optik trüber Medien, speziell kolloidaler Metallösungen*, Annalen der Physik 330, 377 (1908).
- [129] M. G. Aartsen, et al., *Measurement of South Pole ice transparency with the IceCube LED calibration system*, Nucl. Instrum. Meth. A711, 73 (2013).
- [130] M. G. Aartsen, et al., *The IceCube Neutrino Observatory Part VI: Ice Properties, Reconstruction and Future Developments*, in *Proceedings, 33rd International Cosmic Ray Conference (ICRC2013)* (2013).
- [131] J. P. Y. Garza, *Measurement of neutrino oscillations in atmospheric neutrinos with the IceCube DeepCore detector*, Ph.D. thesis, Humboldt-Universität zu Berlin (2014).
- [132] M. P. Kowalski, *Search for neutrino-induced cascades with the AMANDA-II detector*, Ph.D. thesis, Humboldt-Universität zu Berlin (2004).
- [133] T. A. Gabriel, et al., *Energy dependence of hadronic activity*, Nucl. Instrum. Meth. A338, 336 (1994).
- [134] *Brief update on PID in DeepCore*, [https://docushare.icecube.wisc.edu/dsweb/Get/Document-69261/20140325\\_jpamdandre\\_LowEnergyPID\\_version2.pdf](https://docushare.icecube.wisc.edu/dsweb/Get/Document-69261/20140325_jpamdandre_LowEnergyPID_version2.pdf) (2014).
- [135] D. Xu, *Search for Astrophysical Tau Neutrinos in Three Years of IceCube Data*, Ph.D. thesis, The University of Alabama (2015).
- [136] J. Ahrens, et al., *Muon track reconstruction and data selection techniques in AMANDA*, Nucl. Instrum. Meth. A524, 169 (2004).
-

- [137] M. G. Aartsen, et al., *Energy Reconstruction Methods in the IceCube Neutrino Telescope*, JINST 9, P03009 (2014).
- [138] G. B. Dantzig, chap. Origins of the Simplex Method, pp. 141–151. ACM, New York, NY, USA (1990).
- [139] F. James, M. Roos, *Minuit: A System for Function Minimization and Analysis of the Parameter Errors and Correlations*, Comput. Phys. Commun. 10, 343 (1975).
- [140] J. Lundberg, et al., *Light tracking for glaciers and oceans: Scattering and absorption in heterogeneous media with Photonics*, Nucl. Instrum. Meth. A581, 619 (2007).
- [141] N. Whitehorn, J. van Santen, S. Lafebre, *Penalized Splines for Smooth Representation of High-dimensional Monte Carlo Datasets*, Comput. Phys. Commun. 184, 2214 (2013).
- [142] J. G. Learned, K. Mannheim, *High-energy neutrino astrophysics*, Ann. Rev. Nucl. Part. Sci. 50, 679 (2000).
- [143] T. Neunhoffer, *Estimating the angular resolution of tracks in neutrino telescopes based on a likelihood analysis*, Astropart. Phys. 25, 220 (2006).
- [144] J. Lünemann, *Suche nach Dunkler Materie in Galaxien und Galaxienhaufen mit dem Neutrinoteleskop IceCube*, Ph.D. thesis, Universität Mainz (2013).
- [145] H. Cramer, *A contribution to the theory of statistical estimation*, Scandinavian Actuarial Journal 1946(1), 85 (1946).
- [146] R. C. Rao, *Information and the accuracy attainable in the estimation of statistical parameters*, Bull. Calcutta Math. Soc. 37, 81 (1945).
- [147] F. Nielsen, *Cramer-Rao lower bound and information geometry*, arXiv preprint (2013).
- [148] R. A. Fisher, *The logic of inductive inference*, Journal of the royal statistical society 98(1), 39 (1935).
- [149] A. F. Heavens, et al., *Generalized Fisher matrices*, Mon. Not. Roy. Astron. Soc. 445(2), 1687 (2014).
- [150] T. DeYoung, *IceTray: A software framework for IceCube*, in *Computing in high energy physics and nuclear physics. Conference Proceedings of CHEP'04, Interlaken, Switzerland*, pp. 463–466 (2005).
- [151] A. N. Tikhonov, *On the stability of inverse problems*, Doklady Akademii Nauk SSSR 39(5), 195 (1943).
- [152] *RESCA - Resolution Estimator for Cascades*, <http://code.icecube.wisc.edu/svn/sandbox/kwiebe/resca/> (2014).
- [153] M. E. Thomadakis, *The architecture of the Nehalem processor and Nehalem-EP SMP platforms*, Resource 3, 2 (2011).
- [154] K. Griest, D. Seckel, *Cosmic Asymmetry, Neutrinos and the Sun*, Nucl. Phys. B283, 681 (1987), [Erratum: Nucl. Phys.B296,1034(1988)].
- [155] A. Gould, *Cosmological density of WIMPs from solar and terrestrial annihilations*, Astrophys. J. 388, 338 (1992).

- 
- [156] J. N. Bahcall, A. M. Serenelli, S. Basu, *New solar opacities, abundances, helioseismology, and neutrino fluxes*, *Astrophys. J.* 621, L85 (2005).
- [157] G. Wikstrom, J. Edsjö, *Limits on the WIMP-nucleon scattering cross-section from neutrino telescopes*, *JCAP* 0904, 009 (2009).
- [158] J. Lundberg, J. Edsjo, *WIMP diffusion in the solar system including solar depletion and its effect on earth capture rates*, *Phys. Rev. D* 69, 123505 (2004).
- [159] R. Catena, P. Ullio, *A novel determination of the local dark matter density*, *JCAP* 1008, 004 (2010).
- [160] F. Nesti, P. Salucci, *The Dark Matter halo of the Milky Way, AD 2013*, *JCAP* 1307, 016 (2013).
- [161] F. Halzen, D. Hooper, *The Indirect Search for Dark Matter with IceCube*, *New J. Phys.* 11, 105019 (2009).
- [162] P. Gondolo, et al., *DarkSUSY: Computing supersymmetric dark matter properties numerically*, *JCAP* 0407, 008 (2004).
- [163] T. Sjostrand, S. Mrenna, P. Z. Skands, *A Brief Introduction to PYTHIA 8.1*, *Comput. Phys. Commun.* 178, 852 (2008).
- [164] C. Rott, T. Tanaka, Y. Itow, *Enhanced Sensitivity to Dark Matter Self-annihilations in the Sun using Neutrino Spectral Information*, *JCAP* 1109, 029 (2011).
- [165] D. Heck, et al., *CORSIKA: A Monte Carlo code to simulate extensive air showers* (1998).
- [166] T. K. Gaisser, *Spectrum of cosmic-ray nucleons, kaon production, and the atmospheric muon charge ratio*, *Astropart. Phys.* 35, 801 (2012).
- [167] D. Chirkin, W. Rhode, *Muon Monte Carlo: A High-precision tool for muon propagation through matter* (2004).
- [168] A. Gazizov, M. P. Kowalski, *ANIS: High energy neutrino generator for neutrino telescopes*, *Comput. Phys. Commun.* 172, 203 (2005).
- [169] H. L. Lai, et al., *Global QCD analysis of parton structure of the nucleon: CTEQ5 parton distributions*, *Eur. Phys. J. C* 12, 375 (2000).
- [170] M. Honda, et al., *Calculation of atmospheric neutrino flux using the interaction model calibrated with atmospheric muon data*, *Phys. Rev. D* 75, 043006 (2007).
- [171] S. Agostinelli, et al., *GEANT4: A Simulation toolkit*, *Nucl. Instrum. Meth. A* 506, 250 (2003).
- [172] S. Euler, *Observation of oscillations of atmospheric neutrinos with the IceCube Neutrino Observatory*, Ph.D. thesis, RWTH Aachen (2014).
- [173] V. Stenger, *Track fitting for DUMAND-II Octagon Array*, Tech. rep., University of Hawaii at Manoa 461 (1990).
- [174] J.-P. Hülß, *Search for neutrinos from the direction of the Galactic Center with the IceCube neutrino telescope*, Ph.D. thesis, Aachen, Tech. Hochsch. (2010).

- [175] O. Richardson, *The emission of electricity from hot bodies*. Longmans, Green and Co, London (1916).
- [176] R. Abbasi, et al., *IceCube Sensitivity for Low-Energy Neutrinos from Nearby Supernovae*, *Astron. Astrophys.* 535, A109 (2011), [Erratum: *Astron. Astrophys.*563,C1(2014)].
- [177] *Photomultiplier Tubes & Assemblies for Scintillation Counting & High-Energy Physics*, [http://www.hamamatsu.com/resources/pdf/etd/High\\_energy\\_PMT\\_TPM00007E.pdf](http://www.hamamatsu.com/resources/pdf/etd/High_energy_PMT_TPM00007E.pdf) (2012).
- [178] H. O. Meyer, *Spontaneous electron emission from a cold surface*, *EPL (Europhysics Letters)* 89(5), 58001 (2010).
- [179] V. Baum, D. Heereman, R. Bruijn, *An improved data acquisition system for supernova detection with IceCube*, in *Proceedings, 33rd International Cosmic Ray Conference (ICRC2013): Rio de Janeiro, Brazil, July 2-9, 2013*, p. 0444 (2013).
- [180] M. Larson, *Simulation and identification of non-Poissonian noise triggers in the IceCube neutrino detector*, Master's thesis, University of Alabama (2013).
- [181] E. Lohfink, *PMT noise and supernova direction determination in IceCube*, Bachelor's thesis, Universität Mainz (2014).
- [182] M. Zoll, *A search for solar dark matter with the IceCube neutrino detector: Advances in data treatment and analysis technique*, Ph.D. thesis, Stockholm University (2016).
- [183] Y. Freund, R. E. Schapire, *A decision-theoretic generalization of on-line learning and an application to boosting*, in *European conference on computational learning theory*, pp. 23–37. Springer (1995).
- [184] B. P. Roe, et al., *Boosted decision trees, an alternative to artificial neural networks*, *Nucl. Instrum. Meth.* A543(2-3), 577 (2005).
- [185] L. Rokach, O. Maimon, *Top-down induction of decision trees classifiers-a survey*, *IEEE Transactions on Systems, Man, and Cybernetics, Part C (Applications and Reviews)* 35(4), 476 (2005).
- [186] A. Hocker, et al., *TMVA - Toolkit for Multivariate Data Analysis*, *PoS ACAT*, 040 (2007).
- [187] *pybdt*, [http://software.icecube.wisc.edu/icerec\\_trunk/projects/pybdt/index.html](http://software.icecube.wisc.edu/icerec_trunk/projects/pybdt/index.html) (2014).
- [188] *SciPy*, <http://www.scipy.org> (2016).
- [189] *scikit-learn: Machine Learning in Python*, <http://scikit-learn.org> (2016).
- [190] N. Smirnov, *On the estimation of the discrepancy between empirical curves of distribution for two independent samples*, *Moscow, Univ., Bull. Math.* 2 (1939).
- [191] G. Krückl, *Improvement of the muon-neutrino energy resolution by using starting tracks*, Master's thesis, Universität Mainz (2015).
- [192] K. Wiebe, A. Steuer, *All-flavor searches for dark matter with the IceCube neutrino observatory*, *Proceedings of Science ICRC2015*, 1224 (2015).
- [193] J. Braun, et al., *Methods for point source analysis in high energy neutrino telescopes*, *Astropart. Phys.* 29, 299 (2008).

- 
- [194] S. Coenders, *IceCube results from point-like source searches using 6 years of through-going muon data*, EPJ Web Conf. 116, 04003 (2016).
- [195] J. T. Kent, *The Fisher-Bingham distribution on the sphere*, Journal of the Royal Statistical Society. Series B (Methodological) pp. 71–80 (1982).
- [196] G. Punzi, *Comments on likelihood fits with variable resolution*, eConf C030908, 002 (2003).
- [197] R. H. Byrd, et al., *A limited memory algorithm for bound constrained optimization*, SIAM Journal on Scientific Computing 16(5), 1190 (1995).
- [198] A. Roodman, *Blind analysis in particle physics*, eConf C030908, TUIT001 (2003).
- [199] *Lepton/neutrino/hadronic shower flux conversion*, <http://copsosx03.fysik.su.se/cgi-bin/edsjo/wimpsim/flxconv.cgi> (2015).
- [200] M. Rameez, T. Montaruli, *Search for Dark Matter annihilations in the Sun using the completed IceCube neutrino telescope*, Proceedings of Science ICRC2015, 1209 (2015).
- [201] M. G. Aartsen, et al., *Search for dark matter annihilations in the Sun with the 79-string IceCube detector*, Phys. Rev. Lett. 110(13), 131302 (2013).
- [202] R. Catena, B. Schwabe, *Form factors for dark matter capture by the Sun in effective theories*, JCAP 1504(04), 042 (2015).
- [203] T. Piffel, et al., *Constraining the Galaxy’s dark halo with RAVE stars*, Mon. Not. Roy. Astron. Soc. 445(3), 3133 (2014).
- [204] K. Choi, C. Rott, Y. Itow, *Impact of the dark matter velocity distribution on capture rates in the Sun*, JCAP 1405, 049 (2014).
- [205] A. M. Serenelli, *New Results on Standard Solar Models*, Astrophys. Space Sci. 328, 13 (2010).
- [206] M. Zoll, *Improved methods for solar Dark Matter searches with the IceCube neutrino telescope*, Proceedings of Science ICRC2015, 1099 (2015).
- [207] M. Rameez, *IceCube searches for neutrinos from dark matter annihilations in the Sun and cosmic accelerators*, Ph.D. thesis, Université Genève (2016).
- [208] K. Choi, et al., *Search for neutrinos from annihilation of captured low-mass dark matter particles in the Sun by Super-Kamiokande*, Phys. Rev. Lett. 114(14), 141301 (2015).
- [209] C. Amole, et al., *Improved dark matter search results from PICO-2L Run 2*, Phys. Rev. D93(6), 061101 (2016).
- [210] K. Hagiwara, et al., *Probing the Weak Boson Sector in  $e^+ e^- \rightarrow W^+ W^-$* , Nucl. Phys. B282, 253 (1987).
- [211] J. F. Gunion, et al., *The Higgs Hunter’s Guide*, Front. Phys. 80, 1 (2000).
- [212] G. Belanger, et al., *micrOMEGAs 3: A program for calculating dark matter observables*, Comput. Phys. Commun. 185, 960 (2014).
- [213] A. Belyaev, N. D. Christensen, A. Pukhov, *CalcHEP 3.4 for collider physics within and beyond the Standard Model*, Comput. Phys. Commun. 184, 1729 (2013).

- [214] A. Djouadi, J.-L. Kneur, G. Moultaka, *SuSpect: A Fortran code for the supersymmetric and Higgs particle spectrum in the MSSM*, Comput. Phys. Commun. 176, 426 (2007).
- [215] A. Arbey, M. Battaglia, F. Mahmoudi, *Constraints on the MSSM from the Higgs Sector: A pMSSM Study of Higgs Searches,  $B_s^0 \rightarrow \mu^+ \mu^-$  and Dark Matter Direct Detection*, Eur. Phys. J. C72, 1906 (2012).
- [216] A. Arbey, et al., *Supersymmetry confronts  $B_s \rightarrow \mu^+ \mu^-$ : Present and future status*, Phys. Rev. D87(3), 035026 (2013).
- [217] M. W. Cahill-Rowley, et al., *More energy, more searches, but the phenomenological MSSM lives on*, Phys. Rev. D88(3), 035002 (2013).
- [218] R. Aaij, et al., *Measurement of the  $B_s^0 \rightarrow \mu^+ \mu^-$  branching fraction and search for  $B^0 \rightarrow \mu^+ \mu^-$  decays at the LHCb experiment*, Phys. Rev. Lett. 111, 101805 (2013).
- [219] V. Khachatryan, et al., *Observation of the rare  $B_s^0 \rightarrow \mu^+ \mu^-$  decay from the combined analysis of CMS and LHCb data*, Nature 522, 68 (2015).
- [220] N. Cabibbo, *Unitary Symmetry and Leptonic Decays*, Phys. Rev. Lett. 10, 531 (1963).
- [221] M. Kobayashi, T. Maskawa, *CP Violation in the Renormalizable Theory of Weak Interaction*, Prog. Theor. Phys. 49, 652 (1973).
- [222] R. Aaij, et al., *Determination of the quark coupling strength  $|V_{ub}|$  using baryonic decays*, Nature Phys. 11, 743 (2015).
- [223] P. Gambino, P. Giordano, *Normalizing inclusive rare B decays*, Phys. Lett. B669, 69 (2008).
- [224] O. Buchmuller, H. Flacher, *Fit to moment from  $B \rightarrow X(c)\bar{l}$  and  $B \rightarrow X(s)\gamma$  decays using heavy quark expansions in the kinetic scheme*, Phys. Rev. D73, 073008 (2006).
- [225] P. Gambino, *Inclusive semileptonic B decays and  $|V_{cb}|$ : In memoriam Kolya Uraltsev*, Int. J. Mod. Phys. A30(10), 1543002 (2015).
- [226] J. Conley, et al., *Supersymmetry Without Prejudice at the LHC*, Eur. Phys. J. C71 (2011).
- [227] D. S. Akerib, et al., *Improved Limits on Scattering of Weakly Interacting Massive Particles from Reanalysis of 2013 LUX Data*, Phys. Rev. Lett. 116(16), 161301 (2016).
- [228] G. Steigman, B. Dasgupta, J. F. Beacom, *Precise Relic WIMP Abundance and its Impact on Searches for Dark Matter Annihilation*, Phys. Rev. D86, 023506 (2012).
- [229] M. Cahill-Rowley, et al., *Complementarity of dark matter searches in the phenomenological MSSM*, Phys. Rev. D91(5), 055011 (2015).
- [230] M. Cahill-Rowley, et al., *Lessons and prospects from the pMSSM after LHC Run I*, Phys. Rev. D91(5), 055002 (2015).
- [231] M. G. Aartsen, et al., *The IceProd Framework: Distributed Data Processing for the IceCube Neutrino Observatory*, J. Parallel Distrib. Comput. 75, 198 (2015).
- [232] *The wimpsim-reader IceTray module*, <http://code.icecube.wisc.edu/projects/icecube/browser/IceCube/projects/wimpsim-reader/trunk> (2014).
- [233] J.-H. Koehne, et al., *PROPOSAL: A tool for propagation of charged leptons*, Computer Physics Communications 184(9), 2070–2090 (2013).